THE INFLUENCE OF CONFORMATIONAL ORDER ON THE EXCITED STATE OF ORGANIC SEMICONDUCTORS

DISSERTATION

zur Erlangung des akademischen Grades
eines Doktors der Naturwissenschaften (Dr. rer. nat.)
im Promotionsprogramm
Fotophysik synthetischer und biologischer multichromophorer Systeme
der Bayreuther Graduiertenschule für Mathematik und Naturwissenschaften

vorgelegt von

Christina Scharsich

geboren in Neubrandenburg, Deutschland

Bayreuth, 2015

Die vorliegende Arbeit wurde innerhalb von drei Jahren und drei Monaten in der Zeit von Oktober 2010 bis Januar 2015 mit Unterbrechungen für Elternzeit am Lehrstuhl für Experimentalphysik II der Universität Bayreuth unter der Betreuung von Prof. Dr. Anna Köhler angefertigt.

Amtierender Direktor der Graduiertenschule: Prof. Dr. Franz X. Schmid

Dissertation eingereicht am: 15.01.2015

Prüfungsausschuss:

Prof. Dr. Anna Köhler (Erstgutachter)

Alles Wissen und alle Vermehrung unseres Wissens endet
nicht mit einem Schlußpunkt, sondern mit Fragezeichen.
Ein Plus an Wissen bedeutet ein Plus an Fragestellungen,
und jede von ihnen wird immer wieder von neuen
Fragestellungen abgelöst.

Hermann Hesse

Table of Contents

1 SUMMARY _____ 1

2 INTRODUCTION _____ 7

3 OBJECTIVE OF THE THESIS _____ 31

4 OVERVIEW OF THE THESIS _____ 33

5 CONTROL OF AGGREGATE FORMATION IN POLY(3-HEXYLTHIOPHENE) BY SOLVENT, MOLECULAR WEIGHT, AND SYNTHETIC METHOD _____ 49

6 ROLE OF STRUCTURAL ORDER AND EXCESS ENERGY ON ULTRAFAST FREE CHARGE GENERATION IN HYBRID POLYTHIOPHENE/SI PHOTOVOLTAICS PROBED IN REAL TIME BY NEAR-INFRARED BROADBAND TRANSIENT ABSORPTION _____ 73

7 THE RED-PHASE OF POLY[2-METHOXY-5-(2-ETHYLHEXYLOXY)-1,4-PHENYLENEVINYLENE] (MEH-PPV): A DISORDERED HJ-AGGREGATE _ 105

8 REVEALING STRUCTURE FORMATION IN PCPDTBT BY OPTICAL SPECTROSCOPY _____ 121

DANKSAGUNG _____ 161

ERKLÄRUNG _____ 163

1 Summary

In the last decades, great progress has been achieved in the field of organic semiconductors. While light emitting diode technologies based on organic materials are already on the market, organic photovoltaics still have to be improved. The prospect of low-cost roll-to-roll fabrication of light, flexible, large area photovoltaic modules brings polymer solar cells into the focus of research. Due to their many degrees of freedom, conjugated polymer chains adopt many different conformations and spatial arrangements. Often they show semicrystalline behavior by forming disordered regions in coexistence with ordered regions where the polymer chains planarize and aggregate.

This thesis covers the aspect of conformation and aggregation in conjugated polymers and their influence on the excited state delocalization and excitonic coupling as well as the aspect of controlling the aggregate formation in conjugated polymers to study its effect on properties fundamental for efficient device performance. These properties include the charge carrier mobility and the process of exciton dissociation in hybrid heterojunctions.

In polymer solar cells and field-effect transistors, the extensively studied poly(3-hexylthiophene) (P3HT) demonstrates the importance of controlling the semi-crystalline behavior for achieving high power conversion efficiency and high charge carrier mobility. In the first part of this thesis, aggregate formation in poly(3-hexylthiophene) is controlled by solvent quality and analyzed quantitatively as a function of molecular weight and synthetic method. The influence of these factors on the photophysical and electrical properties of P3HT was studied by means of absorption measurements both, in solution and thin films, and by field-effect mobility measurements in transistors. Fraction of aggregates formed as well as excitonic coupling and conjugation length within the aggregates were deduced from the absorption spectra, all as a function of solvent quality for molecular weights from 5 to 19 kDa. As a result, control of aggregate formation in solution leads to control of aggregate properties in thin films. In addition, the propensity to aggregation correlates with the field-effect mobility. Thereby, the influence of synthetic method is of importance for low molecular weight samples (up to 11 kDa) where samples with narrow molecular weight distribution obtained from a well-defined synthetic approach reach high field-effect mobilities up to 0.01 cm^2/Vs. For samples of higher molecular weight, synthetic method is of negligible relevance.

In the second part, the process of the debated initial photoconversion for the generation of free charge carriers and charge recombination in a hybrid poly(3-hexylthiophene)/silicon heterojunction is studied using transient absorption spectroscopy with 40 fs time resolution. Control of aggregate formation in P3HT thin

films is employed to investigate regioregular (RR) and regiorandom (RRa) P3HT with enhanced and suppressed aggregation, respectively. Both, in RR and RRa P3HT, instant (< 40 fs) creation of singlet excitons is observed with subsequent dissociation into polarons within 140 fs. This dissociation is significantly enhanced by adding the electron acceptor silicon (Si). While P3HT/Si films with aggregated RR-P3HT experience losses in free charge generation due to nongeminate recombination, in RRa-P3HT/Si films the charge carriers are bound and mainly geminate recombination is observed. In addition, site-selective excitation reveals polymer structural order rather than excess energy to be the key parameter for free charge generation.

The aggregated, red-phase of the semiconducting polymer poly[2-methoxy-5-(2-ethylhexyloxy)-1,4-phenylenevinylene] (MEH-PPV) is the subject of consideration in the third part of this thesis. The peak ratio of the 0-0 to 0-1 photoluminescence (PL) intensity of this phase is enhanced compared to the disordered blue-phase MEH-PPV but, as well as the PL lifetime of red-phase MEH-PPV, is practically independent of temperature as evidenced by Franck-Condon analysis. These experimental trends are accounted for by successfully modeling the red-phase as disordered cofacial dimers of elongated chains by using the HJ-aggregate model expanded to include site-energy disorder of electrons and holes. In order to allow 0-0 emission in such dimers at low temperatures, disorder is required to break symmetry. The calculated PL spectra and the temperature dependence are in excellent agreement with the experimental data and demonstrate that MEH-PPV aggregates act J-like due to a relatively large intrachain exciton bandwidth of 30 meV that is about one order of magnitude greater than the interchain bandwidth.

The last part of this thesis concerns the conjugated polymer poly{[4,4-bis(2-ethylhexyl)-cyclopenta-(2,1-b;3,4-b')dithiophen]-2,6-diyl-alt-(2,1,3-benzo-thiadiazole)-4,7-diyl} (PCPDTBT) that is widely used in polymer solar cells due to its low optical band-gap. Low optical band-gaps enhance the spectral overlap of the solar spectrum with the polymer absorption spectrum resulting in higher power conversion efficiencies in solar cells. The photophysical properties of PCPDTBT in solution and thin films were extensively studied as a function of temperature by means of absorption and photoluminescence measurements combined with Franck-Condon analyses. For PCPDTBT in solution, a phase transition from disordered to aggregated chains with the critical temperature at 300 K is demonstrated. Upon cooling the fraction of aggregates increases up to a saturation value of about 45% that is reached in PCPDTBT thin films at any temperature. In the films, the presence of a low percentage of thermally activated excimer-like states is identified at temperatures above 200 K. These states dominate the PL spectra at high temperatures. Moreover, the photophysical properties of aggregates in PCPDTBT thin films resemble those in solution highlighting the importance of aggregate control for solution processed films and devices.

Therewith, the thesis comprises three relevant conjugated polymers and their immanent aggregation behavior.

Zusammenfassung

In den letzten Jahrzehnten wurden im Bereich der organischen Halbleiter große Fortschritte erzielt. Während die Leuchtdiodentechnologie auf der Grundlage von organischen Materialien bereits auf dem Markt ist, muss die organische Photovoltaik noch weiter verbessert werden. Im Fokus der Forschung stehen dabei Polymersolarzellen, die die kostengünstige Anfertigung von leichten, flexiblen, großflächigen Solarzellenmodulen mittels Rollenvordrucktechnologie versprechen. Aufgrund ihrer vielen Freiheitsgrade können konjugierte Polymere viele verschiedene Konformationen und räumliche Anordnungen einnehmen. Durch die gleichzeitige Ausbildung von ungeordneten und geordneten Bereichen, in denen die Polymerketten planariziert und aggregiert vorliegen, zeigen halbleitende Polymere daher häufig semikristallines Verhalten.

Diese Arbeit behandelt deshalb zum einen die Aspekte der Konformation und Aggregation in konjugierten Polymeren sowie ihren Einfluss auf die Delokalization des angeregten Zustands und die exzitonische Kopplung. Zum anderen beleuchtet sie den Aspekt der gezielt kontrollierten Aggregatbildung in konjugierten Polymeren, um die damit verbundenen Auswirkungen auf leistungsbestimmende Eigenschaften in Solarzellen oder Transistoren zu untersuchen. Die hier untersuchten Eigenschaften umfassen die Ladungsträgerbeweglichkeit sowie den Prozess der Exzitonen-dissoziation in Hybridheteroübergängen.

Das ausführlich untersuchte Polymer Poly(3-hexylthiophen) (P3HT) zeigt die Bedeutung des semikristallinen Verhaltens für Polymersolarzellen und Feldeffekttransistoren auf. Eine gezielte Kontrolle des semikristallinen Verhaltens ermöglicht höhere Energieeffizienzen in Solarzellen sowie hohe Ladungsträger-beweglichkeiten. Im ersten Teil dieser Arbeit wird daher die durch Lösungs-mittelqualität kontrollierte Aggregatbildung in Poly(3-hexylthiophen) in Abhängigkeit vom Molekulargewicht und der Synthesemethode erforscht. Der Einfluss dieser Faktoren auf die photophysikalischen und elektrischen Eigenschaften von P3HT wird mittels Absorptionsmessungen an Lösungen und dünnen Schichten sowie mittels Messungen der Ladungsträgerbeweglichkeit in Transistoren untersucht. Der Anteil der gebildeten Aggregate sowie die exzitonische Kopplung und die Konjugationslänge innerhalb der Aggregate werden aus den Absorptionsspektren in Abhängigkeit der Lösungsmittelqualität und des Molekulargewichtes (5 kDa bis 19 kDa) abgeleitet. Die daraus resultierende Kontrolle der Aggregatbildung in Lösung erlaubt es, die Aggregateigenschaften in dünnen Schichten zu kontrollieren. Zudem korreliert die Neigung der Proben zur Aggregation mit ihrer Ladungsträgerbeweglichkeit. Dabei spielt die Synthesemethode besonders für kleine Molekulargewichte (bis zu 11 kDa) eine wichtige Rolle, denn die Proben mit schmalen Molekulargewichtsverteilungen, die durch wohldefinierte Syntheseansätzen gewonnen werden, erreichen hohe

Ladungsträgerbeweglichkeiten bis zu 0,01 cm²/Vs. Für Proben mit höherem Molekulargewicht bringen wohldefinierte Syntheseansätze keine Vorteile mehr.

Im zweiten Teil der Arbeit wird mittels transienter Absorptionsspektroskopie mit einer Zeitauflösung von 40 fs der Prozess der umstrittenen initialen Photoumwandlung in freie Ladungsträger und deren Rekombination in einem Poly(3-hexylthiophen)/Silizium Hybridheteroübergang untersucht. Dabei wird die Kontrolle über die Aggregatbildung in dünnen P3HT-Schichten benutzt, um regioreguläres (RR) P3HT mit verstärkter Aggregation mit regioregellosem (RRa) P3HT mit unterdrückter Aggregation zu vergleichen. Beide P3HT-Sorten, RR- und RRa-P3HT, zeigen die instantane (< 40 fs) Erzeugung von Singulettexzitonen mit anschließender Dissoziation in Polaronen innerhalb der ersten 140 fs. Diese Dissoziation wird durch die Zugabe des Elektronenakzeptors Silizum (Si) deutlich verstärkt. Während in P3HT/Si-Schichten mit stark aggregiertem RR-P3HT freie Ladungsträger vorliegen, die durch nichtpaarige Rekombination verloren gehen, sind die Ladungsträger in RRa-P3HT/Si-Schichten gebunden und rekombinieren hauptsächlich paarig. Zudem zeigen die Spektren bei unterschiedlichen Anregungsenergien, dass nicht die Überschussenergie, wohl aber die Polymerstruktur, der Schlüsselparameter zur Erzeugung freier Ladungsträger ist.

Im dritten Teil dieser Arbeit steht die aggregierte, rote Phase des halbleitenden Polymers Poly[2-methoxy-5-(2-ethylhexyloxy)-1,4-phenylen-vinylen] (MEH-PPV) im Mittelpunkt der Betrachtung. Das Verhälnis der 0-0 zu 0-1 Peakintensität in der Photolumineszenz (PL) dieser Phase ist wesentlich größer als in der ungeordneten, blauen Phase von MEH-PPV, bleibt aber, wie auch die PL-Lebenszeiten, praktisch Temperatur unabhängig, wie mittels Franck-Condon-Analyse nachgewiesen wird. Diesen experimentellen Befunden wird mit einer Modellierung der roten Phase als ungeordnete Dimere bestehend aus gesteckten, sich gegenüber liegenden Ketten Rechung getragen. Das dafür benutze verbesserte HJ-Aggregatmodell beinhalted hier auch die energetische Lageunordnung der Elektronen und Löcher. Um in solcherart Dimeren bei tiefen Temperaturen eine 0-0-Emission zu erlauben, müssen Symmetrieverbote aufgehoben werden. Dafür ist Unordnung in den Dimeren von Nöten. Die mittels dieser Modellierung berechneten Photolumineszenzspektren und deren Temperaturabhängigkeit stimmen exzellent mit den experimentellen Daten überein und zeigen, dass Aggregate in MEH-PPV J-Charakter mit einer relativ großen Intrakettenexzitonenbandbreite von 30 meV haben. Obwohl ihre Interkettenbandbreite dagegen eine Größenordnung kleiner ist, beinflusst sie essentiell die Peakverältnisse in den Spektren.

Der letzte Teil der Arbeit behandelt das konjugierte Polymer Poly{[4,4-bis(2-ethylhexyl)-cyclopenta-(2,1-b;3,4-b')dithiophen]-2,6-diyl-alt-(2,1,3-benzo-thiadiazol)-4,7-diyl} (PCPDTBT), das umfangreich in Polymersolarzellen aufgrund seiner geringen optischen Bandlücke benutzt wird. Die geringe optische Bandlücke sorgt für eine verbesserte spektrale Übereinstimmung des Sonnenspektrums mit dem Absorptionsspektrum des Polymeres, woraus sich hohe Energieeffizienzen in

Solarzellen ergeben. Die photophysikalischen Eigenschaften von PCPDTBT in Lösung und in dünnen Schichten werden ausführlich und in Abhängigkeit von der Temperatur mittels Absorptions- und Photolumineszenzspektroskopie in Kombination mit Franck-Condon-Analysen unter-sucht. Für PCPDTBT in Lösung wird ein Phasenübergang von einem ungeordneten in einen aggregierten Zustand aufgezeigt. Die kritische Temperatur liegt für diesen Übergang bei 300 K. Der Aggregatanteil steigt dabei bis zu einem Sättigungswert an, der auch in dünnen PCPDTBT-Schichten bei jeder Temperatur erreicht wird. Zudem wird dargelegt, dass in den Schichten ein geringer Prozentsatz an thermisch aktivierten exzimerähnlichen Zuständen oberhalb von 200 K existiert. Diese Zustände dominieren die PL-Spektren bei hohen Temperaturen. Darüber hinaus zeigt sich, dass die photophysikalischen Eigenschaften der PCPDTBT-Aggregate in dünnen Schichten denen in Lösung ähneln, wodurch verdeutlicht wird, wie wichtig die Kontrolle der Aggregate in Lösung für aus Lösung prozessierte Schichten und Geräte ist.

Damit umfasst diese Arbeit drei relevante, konjugierte Polymere and ihr immanentes Aggregationsverhalten.

2 Introduction

2.1 Motivation

Sustainable energy supply is one of the most challenging ambitions today's generation is confronted with. One approach to overcome the reduction in natural resources is the use of solar energy by photovoltaic modules. In addition to conventional inorganic photovoltaic modules that base on silicon, great effort has been made in the last 20 years to develop organic solar cells whose active layers comprise organic semiconductors, e.g. conjugated polymers. However, power conversion efficiencies still have to be improved in order to successfully compete with inorganic photovoltaics.[1]

State-of-the-art polymer solar cells built as triple-junction cells reach power conversion efficiencies up to 11.5%[2] whereas tandem-junction and single-junction cells reach 10.6%[3] and above 9%[4-6], respectively. Recent improvements were achieved by inverting the device architecture to reduce oxidation effects reaching a power conversion efficiency of 10.3%[7] in a single-junction inverted polymer solar cell. However, the company Heliatek® achieved the work record efficiency of 12.0% in OPVs using small molecules in 2013.

Despite the low efficiency compared to inorganic solar cells, organic photovoltaic devices show several key advantages that highlight organic photovoltaics (OPVs) as possible alternative to the inorganic photovoltaic technology. Among these advantages, especially the low weight and flexibility of the photovoltaic modules as well as the low manufacturing costs are emphasized in the community.[8-10] In addition, semitransparency, short energy payback times and possible large scale roll-to-roll fabrication using state-of-the-art printing techniques apply to OPVs.[1, 9, 11, 12]

In contrast to inorganic solar cells that are built mostly from silicon single crystals or polycrystalline materials, semiconducting polymers in OPVs are usually amorphous or polycrystalline. This higher degree of disorder within the organic materials drastically reduces both, the costs and the energy required for production.[13] The order and crystallinity of semiconducting polymers correlates with the exciton and charge transport properties of the material.[11, 14, 15] Hence, control on aggregation and crystallization of the conjugated, electron donating polymer is a key issue to achieve optimum polymer solar cell morphology that contains highly crystalline polymer domains reasonably small to achieve high solar cell performances in a blend heterojunction with an electron acceptor such as fullerenes. Very recently, the temperature-dependent aggregation and morphology behavior of the polymer was

successfully used to reach a power conversion efficiency of 10.8% in a thick-film polymer solar cell.[16]

Generally, semiconducting polymers exhibit many degrees of freedom resulting in many different conformations, spatial arrangements and structures. The concomitant structural disorder induces energetic disorder that affects intermolecular charge transfer since charges experience an energy barrier when moving from ordered to amorphous polymer regions.[17] Moreover, the conformational and aggregation behavior of the conjugated polymer controls the properties of the excited states that can dissociate into free charge carriers in presence of an electron-donor/electron-acceptor interface.[18]

The conformational rearrangement in conjugated polymers is often accompanied by aggregate formation whose influence on the excited state delocalization and intermolecular coupling strongly depends on the polymer. Optical spectroscopy reveals differences between disordered and ordered polymer domains and differences in intermolecular couplings.[19-22] Hence, detailed investigations on excited state characteristics offer insight into aggregate properties that are fundamental for device performances.

The objective of this thesis thus comprises both, the influence of conformation and aggregate formation on the excited state delocalization and excitonic coupling in semiconducting polymers and the control of the polymer excited state characteristics to study their effect on properties essential for device performance. The following sections of this chapter introduce the theoretical background and summarize the well-known concepts by Kasha and recent works by F. C. Spano, J. Gierschner and coworkers on the theoretical model of excitations in organic aggregates. Furthermore, the last section describes the theoretical background of the Franck-Condon analysis which was used to obtain a major part of the results presented in this thesis.

2.2 Kasha's Molecular Exciton Model

The concept of an exciton being a quasi-particle that accounts for the collective response of interacting molecules to an excitation was first introduced by Y. I. Frenkel in 1931.[23] The theoretical classification of excitons by A. S. Davydov distinguishes between free and localized excitons. These cases correspond to the strong-coupling and weak-coupling classification, respectively, which was defined by W. T. Simpson and D. L. Peterson. Their practicable criteria for this classification compare the strength of intermolecular electronic interaction with the strength of intramolecular vibronic coupling. In case $2U/\Delta\varepsilon << 1$ with $2U$ denoting the exciton bandwidth due to intermolecular interaction and $\Delta\varepsilon$ being the Franck-Condon bandwidth of the individual molecule, the strong-coupling regime prevails leading to free excitons. Analogously, the weak-coupling criterion is $2U/\Delta\varepsilon >> 1$ describing localized excitons.[24]

The simplest possible aggregate is a dimer consisting of two interacting molecules. In the strong-coupling limit of Davydov's exciton theory, Kasha presented the exciton band structure of such a molecular dimer and the corresponding selection rules.[25] Figure 1 shows the exciton band structure and the corresponding selection rules for optical transitions to the exciton states for various geometrical arrangements of transition dipoles in a molecular dimer. Regarding the transition dipoles a quasi-classical vector model was applied that approximates the Coulomb type intermolecular interactions with dipole-dipole intermolecular potential term of its multipole expansion. For the vector diagrams in Figure 1, the polarization vector for light absorption is assumed to be parallel to the long axis of the planar molecules.

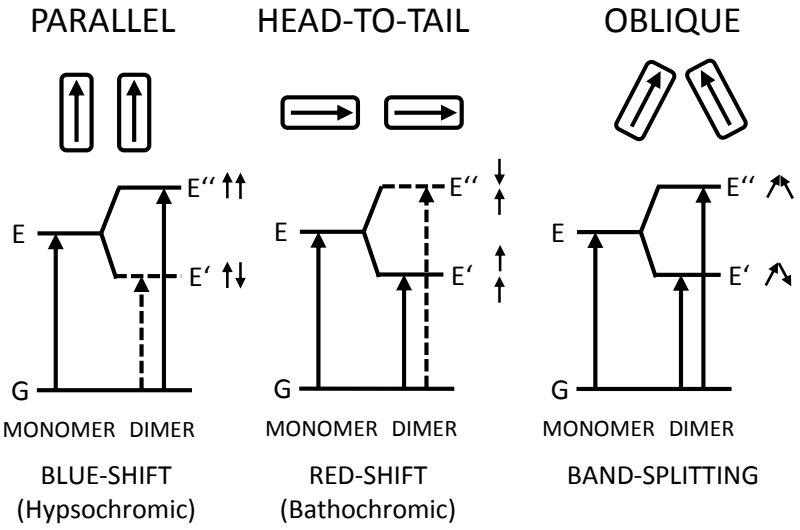

Figure 1: Energy diagrams for exciton band structures and geometrical arrangements of transition dipoles (small arrows) in molecular dimers. The dashed line indicates the forbidden exciton state, the solid line represents the allowed exciton state of each dimer. (From Kasha, 1963.[24])

The exciton state of the dimer is shifted in energy relative to the excited state of the monomer. This energy shift depends on dipole-dipole interaction that can be attractive or repulsive. Thus, in case of a dimer with parallel and in-phase arrangement of transition dipoles, the excited state energy is raised compared to the monomer excited state energy. When the parallel dimer is arranged with transition dipoles out-of-phase, the exciton energy is electrostatically attractive resulting in a lowering of energy in the dimer. In case of head-to-tail dimers the dipole-dipole interaction between dipoles with out-of-phase direction is electrostatically repulsive leading to increased excited state energy whereas the in-phase arrangement yields reduced excited state energy due to its net attractive character.

As for the selection rules corresponding to the arrangement of transition dipoles, the vector sum of these transition dipoles is required. As expected, only in-phase arrangements yield non-zero total transition dipoles. This can easily be understood since the absorbed light has wavelengths much greater than the molecular dimensions resulting in a simultaneous in-phase perturbation of the molecules. In case of oblique arrangement, the excited state splits into two allowed states whose net transition dipole moments show mutually perpendicular polarization. [24]

Applying the selection rules, one finds that the parallel dimer can only be excited into the energetically higher state leading to a hypsochromic shift (blue-shift) compared to the monomer absorption. In case of the head-to-tail arrangement, the optically transition goes from the ground state to the low energy excited state resulting in a bathochromic shift (red-shift) in the absorption spectrum.

In addition to molecular dimers, McRae and Kasha developed selection rules in the exciton model as well as interaction energy expressions in the nearest-neighbor approximation for linear molecular polymers existing of N identical molecular units or chromophores.[26] In the following, a short quantum theoretical treatment of the linear chain model is presented according to Kasha[27].

Assuming a chain of a very large number *N* of identical molecules, the wave function of the ground state can be written as the product of the *N* independent molecule functions:

$$\Psi_G = \psi_1\psi_2\psi_3 \dots \psi_N. \quad (1)$$

The (non-symmetry adapted) excited state wave function of the aggregate then is the following product:

$$\Phi_a = \psi_1\psi_2\psi_3 \dots \tilde{\psi}_a \dots \psi_{N,} \quad (2)$$

with the molecular function of the excited molecule indicated by tilde.

A symmetry-adapted linear combination of the Φ_a yields the *k*-th stationary state wave function of the exciton:

$$\Psi_k = \frac{1}{\sqrt{N}} \sum_{a=1}^{N} c_{ak} \Phi_a. \tag{3}$$

Here, the square of the absolute value of the coefficient c_{ak} describes the probability that the *a*-th molecule in the chain is excited.

If the molecules are distributed uniformly in the chain and their number *N* is very large, end effects can be neglected as valid for periodic boundary conditions and each molecule will have equal probability to be excited. In this case, the coefficients c_{ak} will differ only in their phase factors. Thus, the exciton wave functions can be written as:

$$\Psi_k = \frac{1}{\sqrt{N}} \sum_{a=1}^{N} e^{2\pi i k a/N} \Phi_a, \tag{4}$$

with $k = 0, \pm 1, \pm 2, \ldots N/2$.

Equations (3) and (4) describe the stationary exciton wave functions as a collective excitation of the molecules in the chain. Moreover, they describe excitation nodes ranging from a nodeless to an *N*-noded wave function and the equations show that the *N* stationary states are mutually orthogonal.

Kasha and McRae[26] then calculated the exciton state energies by first-order perturbation theory for the linear chain polymer using a point-dipole point-dipole potential $V_{di\text{-}di}$ as interaction potential representing the intermolecular perturbation of the system. The Hamiltonian for the linear chain polymer is approximated by

$$\mathcal{H} = \sum_{a=1}^{N} \mathcal{H}_a + V_{di-di} = \mathcal{H}_0 + V_{di-di}, \tag{5}$$

with $\mathcal{H}_a$ being the Hamiltonian of the isolated molecules within the linear chain.

In nearest-neighbor approximation the first-order exciton state energies are given by

$$E_k = E_a^0 + 2\left(\frac{N-1}{N}\right)\cos\left(\frac{2\pi k}{N}\right) \int \Phi_a^* V_{di-di} \Phi_{a+1} dt, \tag{6}$$

with $k = 0, \pm 1, \pm 2, \ldots N/2$. The integral in Equation (6) describes the exciton displacement term per pair when accounting merely for nearest-neighbor interactions clearly depending on the geometrical arrangement of the molecules within the linear chain. The electrostatic perturbation induced by the intermolecular dipole-dipole interaction leads to an exciton band consisting of *N* discrete exciton states.

For the exciton bandwidth of a translational chain, i.e. a chain of equally aligned molecules resulting in one molecule per unit cell, it turns out that it is exactly twice

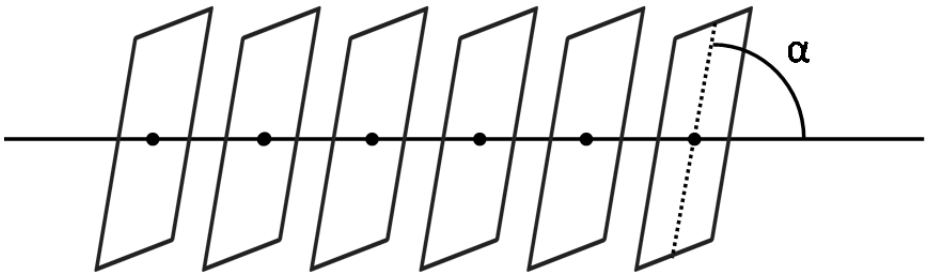

Figure 2: Linear chain polymer consisting of equidistant molecules or chromophores at angle α. (From Kasha, 1976.[27])

the exciton bandwidth of molecular dimers. This can be understood easily, since in the linear chain each molecule has two neighboring molecules and thus the dipole-diploe interactions counts twice in nearest-neighbor approximation. However, a summation beyond nearest-neighbor interaction results in an increase of the exciton displacement term, e.g. by a factor of 2.39 for including eight neighbors on each side.[27]

The arrangements of the interacting molecules in the linear chain determine the selection rules for the transitions. When molecules are arranged face-to-face or in card-pack arrangement with the angle α = 90° (see Figure 2), the molecular aggregate is also called H-aggregate. When the molecules pack at an angle α = 0°, they arrange head-to-tail like which is also called J-aggregate.[28]

Figure 3 shows the exciton band structure diagrams for the face-to-face and the head-to-tail arrangement of transition dipoles. The exciton band is formed by *N* discrete exciton states. The vector representation of the transition dipoles allow the assigning of the transition dipole arrangement to allowed or forbidden transitions as well as their energetic order. In the head-to-tail arrangement case, the lowest-energy exciton state corresponds to the in-phase arrangement of the molecular transition dipoles.

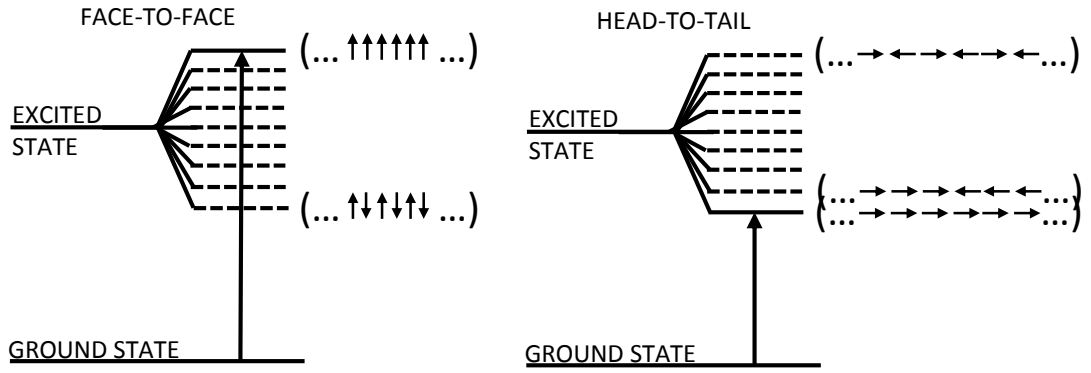

Figure 3: Energy diagrams for exciton band structure in linear molecular polymers for face-to-face and head-to-tail arrangements of the transition dipoles (small arrows). Dashed lines indicate forbidden exciton states, the solid line represents the allowed exciton state of the polymer. (From Kasha, 1963.[24])

Since all transition dipoles are in phase in this case, the exciton wave function of this state is nodeless. Thus, this transition becomes optically allowed. The second lowest-energy exciton state belongs to the exciton wave function with a single excitation node. In this case, the vector sum of the transition dipoles equals zero yielding a forbidden exciton state. The same is true for all higher energy exciton state. The highest-energy exciton state corresponds to an exciton wave function with maximum number of nodes. Thus, the electrostatically interaction is maximally repulsive comparable with the head-to-tail out-of-phase arrangement in the molecular dimer. Analogous considerations for the face-to-face arrangement lead to an allowed exciton state with highest energy.[24] Here again, the face-to-face arrangement (H-aggregate) leads to a blue-shift and the head-to-tail arrangement (J-aggregate) results in a red-shift in the absorption spectrum.

These selection rules explain the often observed narrow absorption band at long wavelength (so-called J-band) for aggregated dye molecules.[29] Here, the absorption is shifted to lower energies compared to the absorption of the individual dye molecules since the transition to the lower-energy exciton states is symmetry-forbidden. The coupling strength is so high that the excitation is fully delocalized as valid for free excitons in the Davydov model. Due to this complete delocalization, the excited molecules experience only minor geometric reorganization. On the basis of the Franck-Condon principle (see section 2.5), the exciton observed shows a pure electronic 0-0 band in absorption.[27]

2.3 Spectral Signatures of H-and J-Aggregates (Spano)

Whereas the considerations on molecular aggregation by M. Kasha include merely the purely electronic excitation, F. C. Spano worked out the impact of simultaneous intermolecular (excitonic) coupling, electron-vibrational coupling and disorder on the spectral signatures of different aggregate types. [30-33] The following section describes the ideas and results recently worked out by Spano.

Spano considered H- and J-aggregates in his work. The latter exhibit head-to-tail orientations and their excitonic coupling is negative resulting in a spectral red-shift. In contrast, H-aggregates consist of molecules in side-by-side orientation. Their excitonic coupling is positive leading to a blue-shift in the spectrum. Whereas H-aggregates show quenched fluorescence compared to the non-aggregated molecules, J-aggregates can be superradiant at low temperatures.[33, 34] Knowing to which extent the Franck-Condon progression is distorted by aggregation of molecules, important information describing the molecular packing can be derived. This information includes the exciton bandwidth, the exciton coherence length, and a parameter describing disorder.[11]

The excitations in conjugated molecules and polymers are so-called Frenkel excitons which exhibit a correlated electron-hole pair that is localized on the same molecule and that can travel in this form through the molecular aggregate or crystal. The Frenkel exciton, often called excitonic polaron, comprises of a vibronically excited molecule surrounded by vibrationally, but not electronically, excited molecules.[33, 35]

To account for these excitations, Spano modeled the excitonic polaron using a multiparticle basis set allowing for single-particle excitations as well as two-particle excitations as depicted in Figure 4. The single-particle excitation $|n,\tilde{\nu}\rangle$ describes a vibronically excited ($\tilde{\nu} \neq 0$) chromophore at site n in the first electronically excited molecular state (S_1) with all other molecules vibrationally and electronically unexcited.

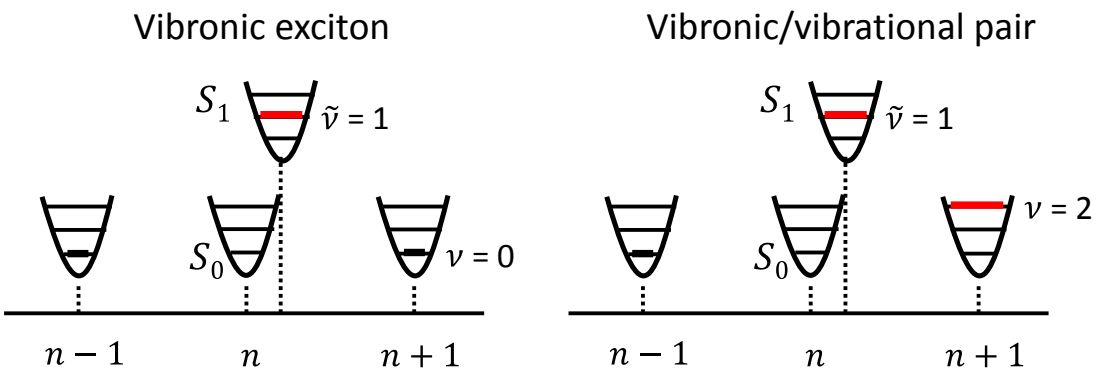

Figure 4: Scheme of the fundamental excitations in organic molecular aggregates. The vibronic exciton is a single-particle excitation. The vibronic/vibrational pair is a two-particle state. (From Spano, 2010.[33])

Thus, the single-particle excitation is just a vibronic exciton. In contrast, the two-particle state $|n, \tilde{\nu}; n', \nu'\rangle$ is a vibronic/vibrational pair consisting of the vibronic exciton at site n and of an additional vibrational excitation ($\nu' \neq 0$) in the ground state (S_0) at a different site n' ($n \neq n'$). The inclusion of two-particle states accounts for the spatial extent of the vibrational distortion field surrounding the central excited molecule.[33]

Generally, there are some basic properties of the optical response arising from the above described excitons. First, only one-particle states couple to the vibrationless ground state and thus contribute to the 0-0 emission. Second, sideband emission evolves from both one- and two particle states. In addition, the wavenumber k is a good quantum number for disorder-free systems. In this case, only excitation of nodeless states with $k = 0$ is optically allowed from the vibrationless ground state. For H-aggregates this state is at the top of exciton band, for J-aggregates at the bottom. In contrast, the dark exciton with $k = \pi$ exhibits N-1 nodes and is at the band bottom for H-aggregates, whereas for J-aggregates this state is at the top of the exciton band.[33]

For his calculations, Spano assumed the ground and the electronically excited state to be harmonic potentials coupled to a single totally symmetric intramolecular vibrational mode with frequency ω_0. This vibration is assumed to be basically the symmetric vinyl stretching and ring breathing mode with $\omega_0 \approx 1400\, cm^{-1}$ that is present in a great number of conjugated molecules and polymers. The shift of the excited state compared to the ground state is described by the Huang-Rhys parameter λ^2 (see also section 2.5) which is close to unity for the $1400\, cm^{-1}$ mode. Moreover, the calculations were carried out using the two-particle approximation and limiting the excitonic coupling to nearest neighbors with

$$J_0 \equiv J_{n,n\pm1} = J_{n\pm1,n}, \tag{7}$$

where $J_{m,n}$ denotes the excitonic coupling which determines the resonant energy transfer from an excited molecule at site m to a molecule at site n.[30, 33]

For his work, Spano employed the following Holstein-type Hamiltonian with site-energy disorder, $\hbar = 1$:

$$H = \omega_0 \sum_n b_n^\dagger b_n + \omega_0 \lambda \sum_n \left(b_n^\dagger + b_n\right)|n\rangle\langle n| + \sum_m \sum_n (J_{mn} + \Delta_m \delta_{mn})|m\rangle\langle n| + D + \omega_{0-0} + \lambda^2 \omega_0. \tag{8}$$

Here, $b_n^\dagger$ and b_n denote the creation and destruction operator for vibrational quanta in the electronic ground state, respectively. State $|n\rangle$ describes the purely electronically excited molecule at site n with all other molecules in the electronic ground state. ω_{0-0} is the transition frequency for the transition between ground state and first excited state that is coupled to the intramolecular vibration ω_0. The first term of the Hamiltonian accounts for the phonon energy, the second term describes the

linear exciton-phonon coupling, and the third term provides the contribution of the excitonic coupling J_{mn} and the diagonal disorder Δ_m. The latter is the molecular transition frequency offset relative to $(D + \omega_{0-0})$ with D being the gas-to-crystal shift. This disorder Δ_m is assumed to be Gaussian distributed and accounts for the disorder in polymer aggregates. Finally, the last term in Equation (8) represents the nuclear relaxation energy.[30]

The further numerical solution of this Hamiltonian shall not be described here. Below, I will focus on the energy diagrams of the exciton bands as well as the resulting spectral signatures of H- and J-aggregates in both, the weak excitonic coupling and strong excitonic coupling regime.

The effect of the aggregation on the exciton energy levels in the weak excitonic coupling regime are shown in Figure 5. Here, the weak excitonic coupling leads to the excitons to split into vibronic bands ($\tilde{\nu} = 0,1, \ldots$). Each $\tilde{\nu}$th band is composed of all one-particle excitations with $\tilde{\nu}$ vibrational quanta in the excited state. For sufficiently large N, periodic boundary conditions can be assumed. Then, the opically allowed, nodeless ($k = 0$) exciton state $|A_{\tilde{\nu}+1}\rangle$ in the $\tilde{\nu}$th vibronic band is situated at the top of the band in H-aggregates and at the band bottom in J-aggregates.[33]

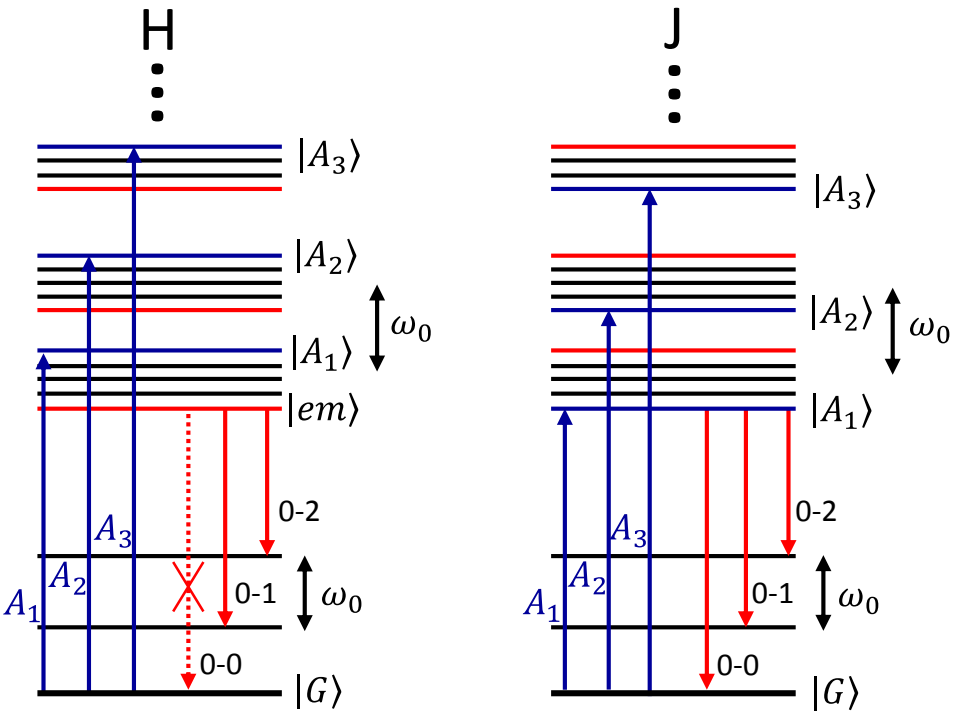

Figure 5: Energy level diagram for the weak excitonic coupling regime in ideal H- and J-aggregates. Nodeless excitons ($k = 0$) are marked blue, while red energy levels correspond to excitons with $k = \pi$. The label A_{n+1} denotes the $0 - n$ molecular transition. Note that not all phonon states of the ground state are shown and that the band gap is not to scale. (From Spano, 2010.[33])

Evidently, the splitting is relative small. Thus, in the weak excitonic coupling regime the transition energies exhibit merely slight blue-shifts and red-shifts in H- and J-aggregates, respectively, when compared to isolated molecules. In this regime, the gas-to-crystal shift may compensate or even exceed the blue-shift in H-aggregates. Furthermore, in polymer H-aggregates the excitonic blue-shift is often smaller than the red-shift due to enhanced planarization of the polymer chains. Hence, the spectral shifts due to aggregation are no reliable measure to determine the H- or J-character of the aggregates.[33]

In H-aggregates the emissive state $|em\rangle$ is the exciton state at the bottom of the $\tilde{\nu} = 0$ vibronic band. Since this emissive state has the wavenumber $k = \pi$, the emission to the vibrationless ground state is optically forbidden. The emission spectrum of ideal H-aggregates (disorder-free) both in the weak and strong excitonic coupling regime thus lacks the 0-0 emission line.[33]

In the weak coupling regime, the consequence of aggregation for the spectral signature in absorption is a ratio of the A_1 and A_2 oscillator strengths, denoted as R_{abs}, that decreases for H-aggregates and increases for J-aggregates compared to the isolated molecule. The magnitude of R_{abs} depends on the first-order interband coupling between vibronic excitons with $k = 0$ from different vibronic bands.[33]

Spano showed that the oscillator strength of the first absorption band A_1 in weakly interacting aggregates is given by

$$\left|\langle G|\widehat{M}|A_1\rangle\right|^2 = e^{-\lambda^2}\mu_{\parallel}^2\left|\sum_n \varphi_n\right|^2\left(1 - \frac{2J_0}{\omega_0}e^{-\lambda^2}\sum_{\nu>0}\frac{\lambda^{2\nu}}{\nu!\,\nu}\right)^2. \tag{9}$$

Here, $\widehat{M}$ is the aggregate transition dipole moment operator. The first two factors of Equation (9) describe the single-molecular oscillator strength with μ being the single-molecule transition dipole moment. The third factor is the expansion coefficient. For cyclic boundary condition, it just equals N, the number of aggregated molecules. For linear aggregates, the expansion coefficient is approximately $0.81\,N$ due to open boundary conditions and finite size effects. Evidently, these first three factors describe how the oscillator strength is enhanced due to aggregation. The last factor in Equation (9) depends on the excitonic coupling J_0 which is positive in H-aggregates and negative in J-aggregates. For the approximate Huang-Rhys parameter of $\lambda^2 = 1$, the factor evolves to $(1 - 0.96\,J_0/\omega_0)^2$. Thus, in H-aggregates this factor reduces the oscillator strength with increasing coupling, while in J-aggregates A_1 is enhanced by excitonic coupling.[30, 33]

The oscillator strength of the second absorption band A_2 is given by

$$\left|\langle G|\widehat{M}|A_2\rangle\right|^2 = \lambda^2 e^{-\lambda^2}\mu_{\parallel}^2\left|\sum_n \varphi_n\right|^2\left(1 - \frac{2J_0}{\omega_0}e^{-\lambda^2}\sum_{\nu\neq 1}\frac{\lambda^{2\nu}}{\nu!\,(\nu-1)}\right)^2. \tag{10}$$

For the assumption of $\lambda^2 = 1$, the last factor of the oscillator strength of A_2 is $(1 + 0.292\,J_0/\omega_0)^2$. In this case, excitonic coupling enhances the intensity of the A_2 band in H-aggregates and reduces A_2 in J-aggregates in the weakly excitonic coupling regime.[30, 33]

The ratio of first two absorption bands, R_{abs}, thus is given by

$$R_{abs} = \frac{\left(1 - \frac{2J_0}{\omega_0} e^{-\lambda^2} \sum_{v>0} \frac{\lambda^{2v}}{v!\, v}\right)^2}{\lambda^2 \left(1 - \frac{2J_0}{\omega_0} e^{-\lambda^2} \sum_{v\neq 1} \frac{\lambda^{2v}}{v!\,(v-1)}\right)^2}. \tag{11}$$

The ratio R_{abs} decreases in case of H-aggregation and increases in case of J-aggregation. Hence, the simple measurement of R_{abs} is a reliable and powerful tool to determine the character of aggregation when compared to the ratio of non-interacting molecules provided that the Huang-Rhys parameter of the single-molecule emitter is known or reasonably approximated.

In addition, R_{abs} is a function of J_0 and thus measuring R_{abs} allows for deducing information on the excitonic coupling strength as well as the exciton bandwidth within the aggregates. The exciton bandwidth is $W = 4|J_0|$ for cyclic boundary conditions that can be assumed for a sufficient large number of molecules forming the aggregate.[33]

As for the photoluminescence spectrum of ideal aggregates at temperature T$= 0$, only emission from the lowest exciton state $|em\rangle$ is allowed. For nonrigid molecules forming H-aggregates, e.g. as valid for polymer aggregates, only the transition from $|em\rangle$ to the vibrationless ground state (0-0) is forbidden. In contrast, sideband emission is present due to coupling to the ground state with vibrational quanta which converses momentum.[33]

Since the radiative decay is proportional to the emission spectral area, the lack of 0-0 emission leads to fluorescence quenching in H-aggregates. Here, two-particle states couple to vibrationally excited ground state, but they do not couple to the vibrationless ground state. Generally, the emission spectrum provides a good measure for the polaron radius.[33]

In J-aggregates, the emitting exciton state is the A_1 state which is optically allowed for absorption. Thus, J-aggregates show a negligible Stokes shift, i.e. the emission shifts similarly to the red as the absorption upon aggregation. Since the emission from the emitting exciton state is allowed, aggregation enhances the emission intensity by a factor of N_{coh} when compared to non-interacting molecules. Here, the coherence number N_{coh} denotes the number of molecules over which the exciton wave function spreads coherently. The emission enhancement is due to the concentration of the oscillator strength in the 0-0 transition and consequently leads to superradiant decay rates. In contrast, the sideband emission is not coherently enhanced. Thus, the ratio of

the first two emission line strengths, R_{em}, directly measures the coherence length within the J-aggregate.[33]

Consider now briefly the strong excitatonic coupling regime. When strong excitonic coupling is present, the absorption spectrum shows an intense absorption peak that is blue-shifted in H-aggregates and red-shifted in J-aggregates. Figure 6 shows the energy level diagrams of H-and J-aggregates in the strong excitonic coupling limit.

The single absorption peak is due to a concentration of the oscillator strength in the transition to the $k = 0$ exciton state which is denoted as $|H\rangle$ and $|J\rangle$ for H-and J-aggregates, respectively. These excitons are nearly free assuming Davydov's classification (see also section 2.2) and have the approximate energy of $\omega_{0-0} + D + \lambda^2\omega_0 + 2J_0$. The excitation in the strong coupling regime exhibits virtually no change in geometry compared to the ground state. In addition, vibronic relaxation is frustrated due to resonant transfer between neighbors. The coupling to vibrations is slightly enhanced by two-particle excitations but still much lower than in the weak-excitonic coupling regime. The latter is also called strong exciton-phonon coupling regime.[30, 33]

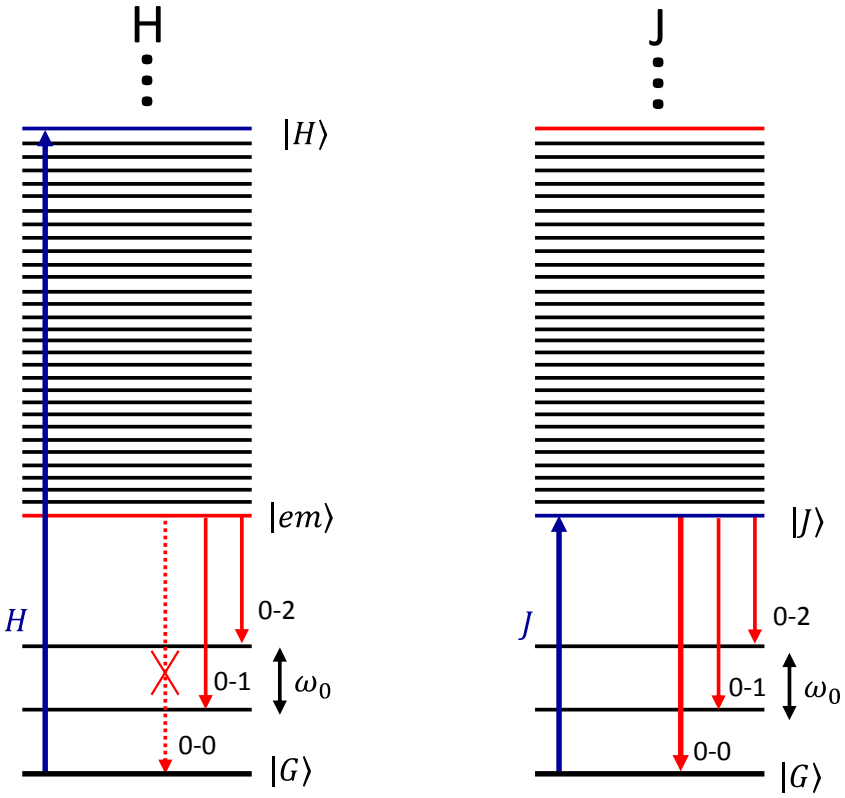

Figure 6: Energy level diagram for the strong excitonic coupling regime in ideal H- and J-aggregates. Nodeless excitons ($k = 0$) are marked blue, while red energy levels correspond to excitons with $k = \pi$. Note that not all phonon states of the ground state are shown and that the band gap is not to scale. (From Spano, 2010.[33])

As already described in section 2.2, the Stokes shift between the emission and absorption spectrum is very large in case of strongly-coupled H-aggregates, since the absorbing exciton $|H\rangle$ and emitting exciton $|em\rangle$ are energetically separated by a large exciton bandwidth. In contrast, no Stokes shift evolves for J-aggregates since the absorbing exciton state $|J\rangle$ is also the emitting state.

So far, only ideal aggregate in absence of disorder were considered. Now the effects of disorder and temperature shall be incorporated according to Spano. Generally, disorder leads to localization and thus affects the coherence numberN_{coh} of the excitons within the aggregates. Thus, the emission in disordered J-aggregates exhibits a reduced 0-0 line strength that directly measures N_{coh} when compared to ideal J-aggregates with $N_{coh} = N$.[33]

Spano focused entirely on the effects of site-energy disorder Δ_n and the effects of temperature on the spectral signatures of H-and J-aggregates in the weakly excitonic coupling regime. Expectedly, site-energy disorder leads to a break in symmetry. Thus, 0-0 emission becomes allowed in H-aggregates, whereas in J-aggregates the 0-0 emission is reduced in intensity significantly. In contrast, the sideband intensities for both aggregate types are only slightly affected by N_{coh} and thus by disorder.[33]

When assuming a Boltzmann distribution of emitting excitons to account for the influence of temperature, the essentially same effects result as for disorder since temperature also reduces the coherence size. Equally, the sideband line strengths do not depend on temperature. Therefore, the emission ratio R_{em} still measures the coherence number N_{coh} even in presence of energy-site disorder or temperature.

Interestingly, for extreme values of disorder the spectral signatures of both, H-and J-aggregates, are washed-out and resemble the emission features of isolated molecules.[33]

2.4 Excitonic Coupling as a Function of Conjugation Length

The excitonic coupling within molecular assemblies and polymer aggregates is a function of several parameters including the number of aggregated molecules or polymer chains, the intermolecular distance, and the conjugation length of the chains.[36, 37]

Using the point-dipole approximation (PDA), D. Beljonne and coworkers showed that the excitonic coupling is enhanced when the size of interacting units increases. In the point-dipole approximation, the interacting molecules are simply modeled as transition dipoles yielding correct excitonic couplings when the extent of the interacting chromophores is much smaller than their separation. In addition to PDA, Beljonne and coworkers also realized quantum-chemical calculations indicating, in contrast to the point-dipole approximation, that an increasing conjugation length leads to a decrease in excitonic coupling.[36] Indeed, first the excitonic coupling increases with conjugation length for oligomer sizes that do not exceed the interchain separation. For conjugation lengths longer than the intermolecular distance, the excitonic coupling decreases with increasing chain length. Thus, the excitonic coupling exhibits a peak behavior as a function of conjugation length. Evidently, for long conjugation lengths the dipole-dipole interactions along the chain when modeling the expanded chain as a series of monomeric transition dipoles cancel each other out and lead to a decrease in excitonic coupling.[38]

In the section 2.3 the quantum-mechanical calculations of weakly-interacting molecular assemblies published by Spano [30 33] were based on the nearest-neighbor approximation that limits the intermolecular interaction to adjacent chains. In contrast, J. Gierschner and coworkers [37] pointed out the importance of non-nearest neighbor interactions and calculated via the quantum-chemical approach the excitonic coupling as a function of conjugation length for a variety of conjugated oligomers and polymers. Here, their results shall be shortly summarized, since these calculations allow for determining the actual conjugation length of the polymer chains within the aggregates when knowing their excitonic coupling.

In consideration of the intermolecular distance in of 4 Å polythiophene aggregates[39], Gierschner and coworkers calculated quantum-chemically using single configuration interaction the excitonic coupling in an infinite one-dimensional stack of thiophenes as a function of thiophene rings. The infinite stack of thiophenes was assumed to consist of 50 molecules since the excitonic coupling is a function of number comprising the stack. However, for large numbers of molecules in the finite stack, the excitonic coupling approaches asymptotically a saturation value that equals the excitonic coupling in the infinite stack.[37] The molecules in the stacks were modeled as perfectly oriented, cofacial oligo- and polythiophenes as a function of chain length. Subsequent to the quantum-chemical calculations, Gierschner and coworkers corrected the values

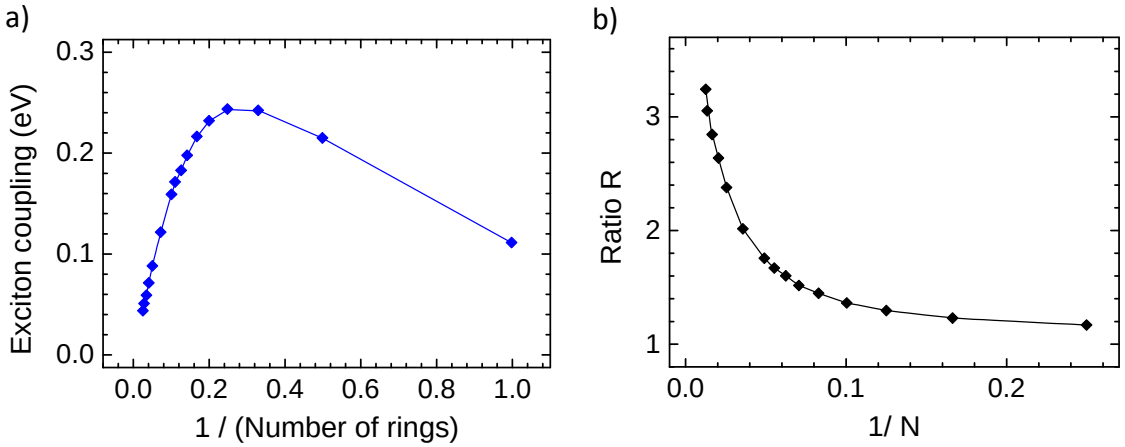

Figure 7: (a) Excitonic coupling V_{stack} as a function of thiophene rings for an infinite stack of polythiophene chains with an interchain distance of 4 Å calculated in the quantum-chemical approach with single configuration interaction and subsequent correction for self-screening. (From Gierschner et al.[37]) (b) Ratio R of excitonic couplings with and without non-nearest neighbor contributions, $R = V_{stack}/V_{NNA}$, as a function of number of double bonds N forming the chain backbone.

of the excitonic coupling for effects of self-screening of the molecules within the molecular assembly by applying a polarizable continuum model. This self-screening affects both the energetic position, also known as gas-to-crystal shift, and the excitonic coupling.[37]

Figure 7(a) shows the result for the excitonic coupling in a quasi-infinite stack of oligo- and polythiophenes as a function of 1/thiophene rings. While for oliogothiophenes up to a length of four thiophene rings the excitonic coupling increases with molecular size, the coupling decreases for longer oligo- and polythiophenes with increasing chain length. From these results, the conjugation length within polythiophene aggregates can be deduced when knowing the excitonic coupling or the exciton bandwidth which can be extracted from the ratio of the first two absorption peaks via Equation (11) by Spano (see section 2.3).

While Spano's calculations based on the nearest-neighbor approximation (NNA), Gierschner included long-range interactions to remote neighboring molecules and compared the resulting excitonic coupling with values calculated with NNA. Figure 7(b) shows the ratio of the excitonic couplings with and without long-range contributions, $R = V_{stack}/V_{NNA}$. Evidently, interactions between remote molecules become more and more important with increasing chain length.

Gierschner and coworkers investigated this ratio of several polymers including phenylene, pheylenevinylene, and phenyleneethynylene in addition to thiophene. They demonstrated that R is independent from the chemical structure. Thus, the importance of non-nearest-neighbor interactions is universal for conjugated polymers.[37]

2.5 Franck-Condon Analysis

Within the Born-Oppenheimer approximation, electron motion is much faster than nuclear motion. A typical frequency of electron motion is $3 \cdot 10^{15} s^{-1}$, whereas nuclear motion typically shows a frequency of $3 \cdot 10^{13} s^{-1}$. Thus, electrons are assumed to adjust instantly to changes in the positions of the nuclei, whereas nuclei are far too slow to follow electronic motion, e.g. as induced by an electric vector of light.[40, 41]

Since the nuclei of a molecule are much more massive and of higher inertia than the electrons, an electronic transition takes place while the nuclei remain essentially stationary. This is the Franck-Condon principle. Thus, an electronic transition is a vertical (or Franck-Condon) transition in a potential energy diagram as a function of configuration coordinate Q as depicted in Figure 9.[41, 42]

After the electronic transition, the nuclei experience a new force field from the electrons, begin to adjust their geometry to that of the excited state and start to vibrate simultaneously. The excited state is represented by S_1 in Figure 9. Generally, a transition between electronic states is most probable when the wave function of vibrational states that describe the nuclear motion most closely resemble each other in the electronic ground and excited state. In this case, the vibrational overlap integral

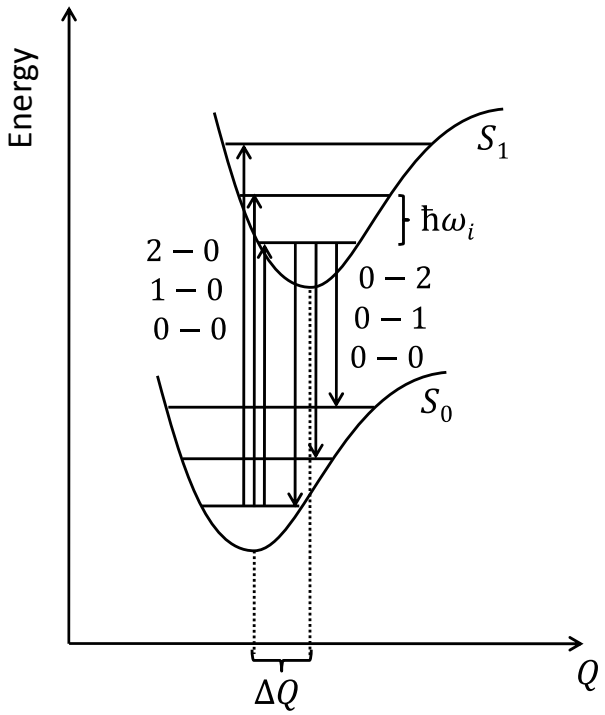

Figure 8: Scheme of vertical absorption ($S_1 \leftarrow S_0\, n-0$) and emission transitions ($S_1 \rightarrow S_0\, 0-n$) between the ground state S_0 and the first excited state S_1 according to the Franck-Condon principle. Q denotes the configurational coordinate, ΔQ is the configurational displacement upon electronic excitation.

$\langle\chi_1|\chi_2\rangle$ is close to unity with χ_1 and χ_2 being the initial and the finial vibrational state, respectively. The rate constant for the transition between the electronic state is proportional to $\langle\chi_1|\chi_2\rangle^2$, the so-called Franck-Condon (FC) factor. The Franck-Condon factor measures a sort of reorganization energy required for the electronic transition to take place. With increasing FC factor, the reorganization energy of the nuclei decreases leading to a higher probability of the transition to occur.[41]

While for the vibrational quantum number $\upsilon = 0$ the vibrational wave function has its maximum at the equilibrium coordinate, for larger υ the vibrational wave functions show their maxima near the classical turning points. In the classical picture, the oscillator spends more time near the turning points than at the equilibrium coordinate where its velocity is highest.[43]

Absorption of a photon starts from the $\upsilon = 0$ level in the ground state which is usually the most populated level. The electronically and vibrationally excitation of the molecule to an upper vibronic state ($\upsilon \neq 0$) of the first electronically excited state takes place in accordance with the highest Franck-Condon factor. After this vertical transition, radiationless relaxation to the lowest vibrational state occurs that brings the nuclei to their equilibrium configuration of the new electronic state. Subsequent emission has a longer wavelength than the exciting light. The energy difference is called the Stokes shift. [41, 42]

The displacement in the configuration of the nuclei denoted as ΔQ describes the difference between the equilibrium configurations of the ground state S_o and the first excited state S_1. Hence, ΔQ determines the wave functional overlap $\langle\chi_1|\chi_2\rangle$ of the vibrational states from both electronic states. For the assumption of harmonic oscillators, the normalized intensities of the according vibrational progression are given by [44]

$$I_n = \frac{Z^n e^{-Z}}{n!}, \tag{12}$$

where Z denotes the Huang-Rhys parameter that describes the coupling strength to the single harmonic oscillator. The Huang-Rhys factor is related to the configurational displacement via [44]

$$Z = \frac{M\omega}{2\hbar}(\Delta Q)^2, \tag{13}$$

with M being the reduced mass and ω being the angular frequency of the harmonic oscillator. Hence, the intensity distribution of the vibrational progression is a Poisson distribution for the vibrational manifold mapping the overlap between the vibrational wavefunctions. The Poissonian is strictly valid only for zero temperature due to the Boltzmann-like population of the vibrational states in the electronic ground state.[42, 44] However, it is sufficient for the purposes of Franck-Condon analysis.

The Huang-Rhys parameter can be extracted from the intensities of the 0-0 and the 0-1 transition since the ratio of I_{0-1}/I_{0-0} evolves to

$$\frac{I_{0-1}}{I_{0-0}} = \frac{Z^1 e^{-Z}}{1!} / \frac{Z^0 e^{-Z}}{0!} = Z. \tag{14}$$

When the two electronic states, S_0 and S_1, exhibit similar configurations in the proximity of their equilibrium positions, no displacement of the potential curves along the configuration coordinate results, i.e. $\Delta Q \approx 0$. Hence, the coupling to the harmonic oscillator vanishes and only the 0-0 transition will be dominant. On the other hand, when ΔQ increases, the vibronic peak position in the spectrum will be shifted to vibronic states of higher energy.[42] Thus, the Huang-Rhys parameter measures roughly the number of vibrations that are created during the relaxation process going from the ground state configuration to the equilibrium configuration of the new electronic state. The according relaxation energy is given by $Z\hbar\omega$ with $\hbar\omega$ being the energy of one vibrational quantum.[44]

Figure 9 illustrates this shift and the effect of coupling strength on the intensity distribution in the spectrum for different values of the Huang-Rhys parameter Z. In addition, the case of $Z = 0$ is shown representing a single 0-0 transition line without coupling to vibrational states due to orthogonality reasons.

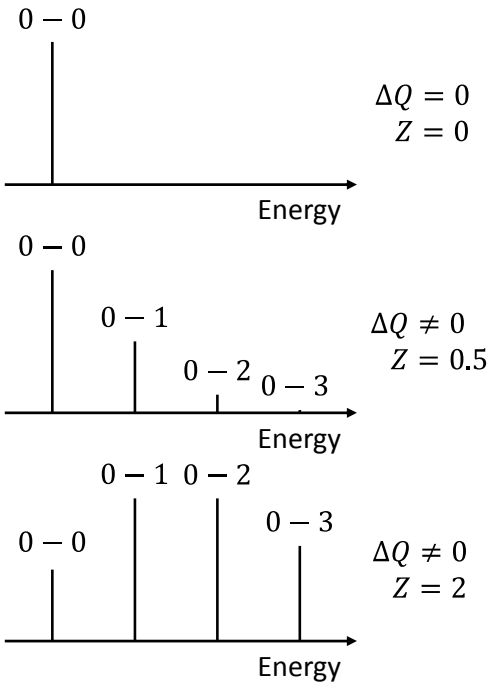

Figure 9: Franck-Condon intensities of vibronic transitions for different configurational displacements ΔQ and different Huang-Rhys parameters Z illustrating the progressional shift to higher energies with increasing Z.

Note, that for a transition involving spin change, the spin wave functions must be altered via spin-orbit coupling to overcome the orthogonality of the spin wave functions in the ground and excited state.

The considerations so far regarding the coupling of the electronic transition to a single oscillator can be generalized to involve two or more vibrational modes i. The total Huang-Rhys parameter then is the sum of the individual Huang-Rhys parameters, $Z = \sum_i Z_i$, and the total relaxation energy becomes $E^{rel} = \sum_i Z_i \hbar\omega_i$ with $\hbar\omega_i$ being the energy of the individual vibrational modes.[44]

The intensity distribution of the transition from state $S_1(0,0,\dots)$ to state $S_0(m,m_2,\dots)$ with n_i being the quantum number of the i-th vibrational mode in the ground state can be modeled as [45]

$$P(\hbar\omega) \propto n^3(\hbar\omega)^3 \sum_{m_i} \prod_i \frac{Z_i^{m_i} e^{-Z_i}}{m_i!} \times \Gamma\delta\left[\hbar\omega - \left(\hbar\omega_0 - \sum_i m_i \hbar\omega_i\right)\right], \qquad (15)$$

where $P(\hbar\omega)$ is the normalized emission spectrum in photons per energy interval, n is the real part of the refractive index at energy $\hbar\omega$. The factor $n^3(\hbar\omega)^3$ accounts for the photon density of states in the medium surrounding the emitter.[46] Γ describes the Gaussian line width function, δ is the Kronecker delta, and ω_0 is the angular transition frequency corresponding to the 0-0 transition.

In the framework of this thesis, I programed a MATLAB routine for the Franck-Condon analysis of absorption and photoluminescence spectra based on Equation (15) and the assumption that the potentials of ground and excited state are harmonic potentials, and thus constant energy of vibrational quanta applies. The program allows for modelling multi-mode transitions that can be used to fit simultaneously two independent polymer phases, e.g. planar and coiled polymer chains. In addition, it is possible to choose from four different line shapes including the Gauss profile, the Lorentz profile, the Voigt profile and an asymmetric line shape. Furthermore, the possibility to vary the 0-0 intensity is included to account for suppression or enhancement due to aggregation effects. In addition, I wrote an OriginC routine to facilitate the time consuming task of importing the fitting data and parameters into Origin.

References

(1) Scharber MC, Sariciftci NS. 2013. Efficiency of bulk-heterojunction organic solar cells. *Progress in Polymer Science* 38, 1929

(2) Chen CC, Chang WH, Yoshimura K, Ohya K, You JB, Gao J, Hong ZR, Yang Y. 2014. An Efficient Triple-Junction Polymer Solar Cell Having a Power Conversion Efficiency Exceeding 11%. *Advanced Materials* 26, 5670

(3) You JB, Dou LT, Yoshimura K, Kato T, Ohya K, Moriarty T, Emery K, Chen CC, Gao J, Li G, Yang Y. 2013. A polymer tandem solar cell with 10.6% power conversion efficiency. *Nature Communications* 4, 1446

(4) Liu SJ, Zhang K, Lu JM, Zhang J, Yip HL, Huang F, Cao Y. 2013. High-Efficiency Polymer Solar Cells via the Incorporation of an Amino-Functionalized Conjugated Metallopolymer as a Cathode Interlayer. *Journal of the American Chemical Society* 135, 15326

(5) He ZC, Zhong CM, Su SJ, Xu M, Wu HB, Cao Y. 2012. Enhanced power-conversion efficiency in polymer solar cells using an inverted device structure. *Nature Photonics* 6, 591

(6) Liao SH, Jhuo HJ, Cheng YS, Chen SA. 2013. Fullerene Derivative-Doped Zinc Oxide Nanofilm as the Cathode of Inverted Polymer Solar Cells with Low-Bandgap Polymer (PTB7-Th) for High Performance. *Advanced Materials* 25, 4766

(7) Liao SH, Jhuo HJ, Yeh PN, Cheng YS, Li YL, Lee YH, Sharma S, Chen SA. 2014. Single Junction Inverted Polymer Solar Cell Reaching Power Conversion Efficiency 10.31% by Employing Dual-Doped Zinc Oxide Nano-Film as Cathode Interlayer. *Scientific Reports* 4, 6813

(8) Zhou HQ, Zhang Y, Seifter J, Collins SD, Luo C, Bazan GC, Nguyen TQ, Heeger AJ. 2013. High-Efficiency Polymer Solar Cells Enhanced by Solvent Treatment. *Advanced Materials* 25, 1646

(9) Leung SF, Gu LL, Zhang QP, Tsui KH, Shieh JM, Shen CH, Hsiao TH, Hsu CH, Lu LF, Li DD, Lin QF, Fan ZY. 2014. Roll-to-roll fabrication of large scale and regular arrays of three-dimensional nanospikes for high efficiency and flexible photovoltaics. *Scientific Reports* 4, 4243

(10) Tan ZA, Li SS, Wang FZ, Qian DP, Lin J, Hou JH, Li YF. 2014. High performance polymer solar cells with as-prepared zirconium acetylacetonate film as cathode buffer layer. *Scientific Reports* 4, 4691

(11) Xiao T, Xu HH, Grancini G, Mai JQ, Petrozza A, Jeng US, Wang Y, Xin X, Lu Y, Choon NS, Xiao H, Ong BS, Lu XH, Zhao N. 2014. Molecular Packing and Electronic Processes in Amorphous-like Polymer Bulk Heterojunction Solar Cells with Fullerene Intercalation. *Scientific Reports* 4, 5211

(12) Riviere GA, Simon JJ, Escoubas L, Vervisch W, Pasquinelli M. 2012. Photo-electrical characterizations of plastic solar modules. *Solar Energy Materials and Solar Cells* 102, 19

(13) Deibel C, Dyakonov V. 2010. Polymer-fullerene bulk heterojunction solar cells. *Reports on Progress in Physics* 73, 096401

(14) Li G, Yao Y, Yang H, Shrotriya V, Yang G, Yang Y. 2007. "Solvent annealing" effect in polymer solar cells based on poly(3-hexylthiophene) and methanofullerenes. *Advanced Functional Materials* 17, 1636

(15) Erb T, Zhokhavets U, Gobsch G, Raleva S, Stuhn B, Schilinsky P, Waldauf C, Brabec CJ. 2005. Correlation between structural and optical properties of composite polymer/fullerene films for organic solar cells. *Advanced Functional Materials* 15, 1193

(16) Liu YH, Zhao JB, Li ZK, Mu C, Ma W, Hu HW, Jiang K, Lin HR, Ade H, Yan H. 2014. Aggregation and morphology control enables multiple cases of high-efficiency polymer solar cells. *Nature Communications* 5, 5293

(17) Noriega R, Rivnay J, Vandewal K, Koch FPV, Stingelin N, Smith P, Toney MF, Salleo A. 2013. A general relationship between disorder, aggregation and charge transport in conjugated polymers. *Nature Materials* 12, 1038

(18) Vandewal K, Albrecht S, Hoke ET, Graham KR, Widmer J, Douglas JD, Schubert M, Mateker WR, Bloking JT, Burkhard GF, Sellinger A, Frechet JMJ, Amassian A, Riede MK, McGehee MD, Neher D, Salleo A. 2014. Efficient charge generation by relaxed charge-transfer states at organic interfaces. *Nature Materials* 13, 63

(19) Sirringhaus H, Brown PJ, Friend RH, Nielsen MM, Bechgaard K, Langeveld-Voss BMW, Spiering AJH, Janssen RAJ, Meijer EW, Herwig P, de Leeuw DM. 1999. Two-dimensional charge transport in self-organized, high-mobility conjugated polymers. *Nature* 401, 685

(20) Heun S, Mahrt RF, Greiner A, Lemmer U, Bässler H, Halliday DA, Bradley DDC, Burn PL, Holmes AB. 1993. Conformational effects in poly(p-phenylene vinylene)s revealed by low-temperature site-selective fluorescence. *Journal of Physics-Condensed Matter* 5, 247

(21) Gurau MC, Delongchamp DM, Vogel BM, Lin EK, Fischer DA, Sambasivan S, Richter LJ. 2007. Measuring molecular order in poly(3-alkylthiophene) thin films with polarizing spectroscopies. *Langmuir* 23, 834

(22) Feller F, Monkman AP. 2000. Optical spectroscopy of oriented films of poly (2,5-pyridinediyl). *Physical Review B* 61, 13560

(23) Pope M, Swenberg CE. 1999. *Electronic Processes in Organic Crystals and Polymers*. New York: Oxford University Press. pp. 39-48

(24) Kasha M. 1963. Energy Transfer Mechanisms and Molecular Exciton Model for Molecular Aggregates. *Radiation Research* 20, 55

(25) Kasha M, Elbayoumi MA, Rhodes W. 1961. Excited State of Nitrogen Base-Pairs and Polynucleotides. *Journal De Chimie Physique Et De Physico-Chimie Biologique* 58, 916

(26) McRae EG, Kasha M. 1958. Enhancement of Phosporescence Ability upon Aggregation of Dye Molecules. *Journal of Chemical Physics* 28, 721

(27) Kasha M. 1976. Molecular excitons in small aggregates. In *Spectroscopy of the Excited State*, ed. B Di Bartolo. New York: Plenum Press

(28) Tsurumi T, Hirayama H, Vacha M, Taniyama T. 2009. In *Nanoscale Physics for Material Science*:152. Boca Raton: CRC Press. pp. 152

(29) Würthner F, Kaiser TE, Saha-Möller CR. 2011. J-Aggregates: From Serendipitous Discovery to Supramolecular Engineering of Functional Dye Materials. *Angewandte Chemie-International Edition* 50, 3376

(30) Spano FC. 2005. Modeling disorder in polymer aggregates: The optical spectroscopy of regioregular poly(3-hexylthiophene) thin films. *Journal of Chemical Physics* 122, 234701

(31) Spano FC. 2006. Absorption in regio-regular poly(3-hexyl)thiophene thin films: Fermi resonances, interband coupling and disorder. *Chemical Physics* 325, 22

(32) Spano FC, Clark J, Silva C, Friend RH. 2009. Determining exciton coherence from the photoluminescence spectral line shape in poly(3-hexylthiophene) thin films. *Journal of Chemical Physics* 130, 074904

(33) Spano FC. 2010. The Spectral Signatures of Frenkel Polarons in H- and J-Aggregates. *Accounts of Chemical Research* 43, 429

(34) Fidder H, Knoester J, Wiersma DA. 1990. Superradiant Emission and Optical Dephasing in J-Aggregates. *Chemical Physics Letters* 171, 529

(35) Schwoerer M, Wolf HC. 2007. *Organic Molecular Solids*. pp 228-233. Weinheim: WILEY-VCH

(36) Beljonne D, Cornil J, Silbey R, Millie P, Bredas JL. 2000. Interchain interactions in conjugated materials: The exciton model versus the supermolecular approach. *Journal of Chemical Physics* 112, 4749

(37) Gierschner J, Huang YS, Van Averbeke B, Cornil J, Friend RH, Beljonne D. 2009. Excitonic versus electronic couplings in molecular assemblies: The importance of non-nearest neighbor interactions. *Journal of Chemical Physics* 130, 6

(38) Beenken WJD. 2009. Excitons in conjugated polymers: Do we need a paradigma change? *Physica Status Solidi a-Applications and Materials Science* 206, 2750

(39) McCullough RD, Tristramnagle S, Williams SP, Lowe RD, Jayaraman M. 1993. Self-orienting head-to-tail poly(3-alkylthiophenes) - New insights on structure-property relationships in conducting polymers. *Journal of the American Chemical Society* 115, 4910

(40) Klessinger M, Michl J. 1995. *Excited States and Photochemistry of Organic Molecules*. pp 34-36. New York: VCH Publishers

(41) Turro NJ, Ramanmurthy V, Scaiano JC. 2010. *Modern Molecular Photochemistry of Organic Molecules*. pp 122-130. Sausalito: University Science Books

(42) Pope M, Swenberg CE. 1999. *Electronic Processes in Organic Crystals and Polymers*. pp 23-29. New York: Oxford University Press

(43) Levine IN. 1975. *Molecular Spectroscopy*. pp 296-306. New York: John Wiley & Sons

(44) Bässler H, Schweitzer B. 1999. Site-selective fluorescence spectroscopy of conjugated polymers and oligomers. *Accounts of Chemical Research* 32, 173

(45) Ho PKH, Kim JS, Tessler N, Friend RH. 2001. Photoluminescence of poly(p-phenylenevinylene)-silica nanocomposites: Evidence for dual emission by Franck-Condon analysis. *Journal of Chemical Physics* 115, 2709

(46) Strickler SJ, Berg RA. 1962. Relationship between Absorption Intensity and Fluorescence Lifetime of Molecules. *Journal of Chemical Physics* 37, 814

3 Objective of the Thesis

The objective of this thesis comprises two related aspects of excited states in conjugated, semiconducting polymers. The first aspect regards the influence of conformation and aggregate formation of the polymer chains on the excited state delocalization and excitonic coupling, the second aspect includes the control of the excited state characteristics to study their effect on properties directly related to device performance. Thereby, control of the excited state characteristics is achieved via control of aggregate formation of the conjugated polymer. The tool of choice for controlling the aggregate formation is simple absorption and photoluminescence measurements as they can be carried out fast and easily even with standard spectrometers.

In the first place, the characterization of the aggregates was always carried out for the semiconducting polymers in solution as a function of various parameters including solvent quality, temperature, molecular weight, and synthetic method of the polymer. As a second step and general aim, polymer thin films and their aggregate behavior relevant for applications were investigated as a function of different processing conditions that lead to aggregates of different natures meaning aggregates with different excitonic couplings, conjugation lengths or energetic disorder and/or leading to different film morphologies.

As for the characterization of conjugated polymer aggregates, the first aim of this thesis is the spectral distinction and subsequent separation of absorption and/or photoluminescence due to aggregates from those due to the non-aggregated phase of the polymer. In order to separate both spectral parts, an extensive program for multi-mode Franck-Condon analyses was developed including the option of simultaneous fitting of two phases as well as modified Franck-Condon fits with variable 0-0 line strength to account for suppressed or enhanced 0-0 radiative decay rates due to aggregation and excitonic coupling. Given the spectral shape of aggregate absorption and photoluminescence, the second aim is the determination of the aggregates' nature and their inherent excitonic couplings or excitonic bandwidths by comparison with theoretical works on excitonic couplings and the resulting spectral properties. Here, the classification of the aggregates as H-or J-aggregates or as mixed HJ-aggregates. Based on this knowledge, this thesis shall give a tool to understand the spectral signatures of the aggregates of the conjugated polymers poly(3-hexylthiophene) (P3HT), poly[2-methoxy-5-(2-ethylhexyloxy)-1,4-phenylenevinylene] (MEH-PPV), and poly{[4,4-bis(2-ethylhexyl)-cyclopenta-(2,1-b;3,4-b')dithiophen]-2,6-diyl-alt-(2,1,3-benzo-thiadiazole)-4,7-diyl} (PCPDTBT) which are widely used in solar cell and field-effect transistor applications.

The second aspect of this thesis is aimed at the application of the knowledge about the aggregate behavior of these semiconducting polymers. Strictly speaking, not only the aggregates themselves are characterized but whole polymer samples and their aggregate formation are controlled to investigate the resulting influence on parameters that control and determine device performance. In case of P3HT such parameters are the charge carrier mobility in field-effect transistors or the exciton dissociation in hybrid heterojunctions with the electron accepting material silicon. Prerequisite for such fundamental research on the influence of the elongation of the excited state on device performance is the knowledge about the amount of aggregates present and their spectral features in absorption or photoluminescence spectra. Thus, further investigations are aimed at the determination of the fraction of aggregates present in solution and in the polymer thin films, respectively.

Eventually, the objective of this thesis is the use of spectral control by means of absorption and photoluminescence measurements to prepare and process different types of polymer aggregates and samples with different amounts of aggregates in order to support fundamental research on device properties that are affected by aggregated polymer chains and the concomitant excited state properties.

4 Overview of the Thesis

Introduction

This thesis examines the role of conformational and structural order in semiconducting polymers primarily on the excited state and subsequently on its related properties such as exciton dissociation, charge generation and charge carrier mobility. The packing behavior including the conjugation length and intermolecular coupling within the polymer aggregates effects significantly the optical and electronic properties of the semiconducting polymer. Thus, the way in which the polymer chains pack and order is relevant for exciton migration, exciton dissociation and charge carrier mobility. Particularly with regard to reaching the industrial level with applications in solar cells and field-effect transistors, a fundamental understanding of the polymer phase behavior and the resulting conjugation length, excitonic and electronic coupling as well as the overall fraction of aggregates present in thin films is necessary.

Particularly, the thesis focuses on the relation between conformational order and optoelectronic properties in terms of simple steady-state absorption and photoluminescence measurements. These types of measurement can be carried out relatively fast and with little effort. However, in combination with theoretical considerations and analyses they offer valuable information about intrinsic properties such as the fraction of aggregates present in the sample, energy transfer, the excitonic coupling or the conjugation length within the aggregates. The latter describe the nature of the aggregates as it is discussed in theory by recent works of F.C. Spano and J. Gierschner.

Furthermore, emphasis is placed on the analysis of semiconducting polymers in solution. In solution, polymer chains are free of spatially constraints thus allowing for examination of the almost unconstrained phase behavior. In many cases, the insight in the aggregation process in solution is necessary to understand the different phases present in the polymer thin films relevant for applications.

The studied polymers comprise poly(3-hexylthiophene) (P3HT), poly[2-methoxy-5-(2-ethylhexyloxy)-1,4-phenylenevinylene] (MEH-PPV) and poly{[4,4-bis(2-ethylhexyl)-cyclopenta-(2,1-b;3,4-b')dithiophen]-2,6-diyl-alt-(2,1,3-benzo-thiadiazole)-4,7-diyl} (PCPDTBT) which are continuously used for photovoltaic applications or field-effect transistors. The chemical structures of these polymers are shown in Figure 10.

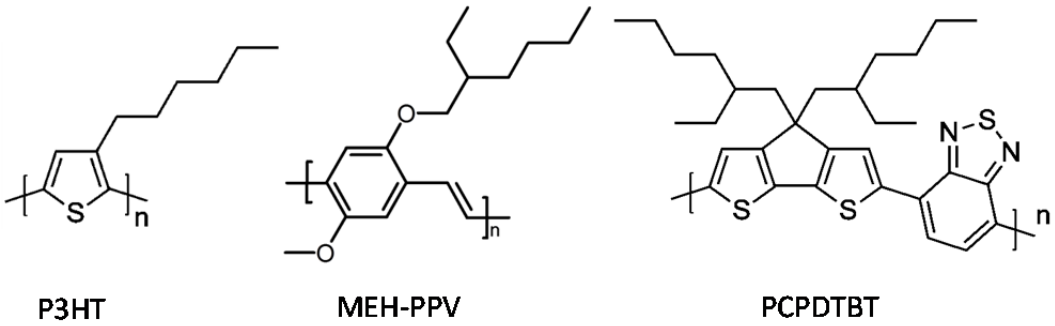

Figure 10: Abbreviations and chemical structures of the semiconducting polymers studied in this thesis.

In the last decade, the extensively studied polymer P3HT illustrated the importance of controlling its semicrystalline behavior for reaching high charge carrier mobilities and high power conversion efficiency in solar cells when combined with an electron accepting material. The control of the packing behavior and the resulting effects on the excited state of P3HT in heterojunctions is clearly dependent on the packing behavior in films of the neat polymer. Thus, an understanding of the phases of P3HT and the excited state related properties provides essential insight into the physical situation of the heterojunction. P3HT is still of enormous importance and probably the most widely studied polymer in the field of organic solar cell research.

First, I studied the aggregation in P3HT upon reduced solvent quality. This work is shown in chapter 5. There are different approaches to reduce the solvent quality. One approach is to add a poor solvent to the polymer in solution and thereby forcing the polymer chains to minimize the interaction with the unfavorable solvent molecules. The aim of the work presented in chapter 5 was the controlled formation of the aggregated phase in P3HT in solution and the characterization of the aggregates formed with regard to photophysical properties as a function of solvent quality and in addition as a function of molecular weight and polydispersity of the polymer. Furthermore, P3HT thin films spin-coated from solutions of different solvent qualities were studied in comparison to P3HT in solution. The results arising from applying the theories from Spano and Gierschner to the absorption spectra of the H-aggregates formed in solution were compared to P3HT thin films spin-coated from solutions with different solvent qualities. The effect of the aggregate formation in the films on the organic field-effect transistor performance was studied since crystallinity, molecular weight, intermolecular coupling and the aggregation of the polymer chains influence the charge carrier mobility within the films.

In chapter 6, I used my knowledge about the conjugation in P3HT aggregates and about the formation of specific fractions of aggregates for the fundamental study on the process of initial photoconversion for generation of free charge carriers in the hybrid P3HT/Si heterojunction. For this study, it was essential to prepare samples with significantly different aggregate fractions. On the basis of the solvent quality

dependent aggregation, two kinds of planar hybrid heterojunctions were prepared. The first one showed strongly depressed aggregation as present in thin films of regiorandom P3HT. The second type exhibited considerably aggregation with low excitonic coupling and thus long conjugation length within the aggregates as deduced from the spectral shape of the absorption (see chapter 5). The fraction of aggregates of both sample types differed by a factor of two. The enhanced aggregation in the second type of samples was prepared by adding a small amount of poor solvent to induce pre-aggregates already in solution prior to the spin-coating process onto the silicon substrates. Basically, the different types of hybrid heterojunctions were used to study the fundamental process of light absorption, the formation of free charge carriers and their subsequent transport to the electrodes. The work helps to clarify controversial questions, e.g. the unresolved question whether free charge carriers or excitons, dissociating into free charge carriers, are initially generated by light absorption. Moreover, the role of excess energy and the role of the polymer structural order on the charge generation in hybrid solar cells were studied. In addition, the work provides a correlation between structure of the polymer chains presented by different degrees of aggregation and the observed geminate/nongeminate recombination.

The findings outstanding for the solar cell research community that are presented in chapter 6, stress the importance of the phase behavior of the semiconducting polymers and our knowledge of the underlying properties of the aggregates. Chapter 7 presents another semiconducting polymer, namely MEH-PPV, used as well in research on organic photovoltaics. The experimental part of the work is based on a second approach to reduce the solvent quality in polymer solutions. Recent work showed that MEH-PPV undergoes a phase transition from a coiled state to an aggregated state and that the polymer can adopt consequently two different conformations. Here, our work focuses on the aggregated, low-energy, phase of MEH-PPV since absorption and photoluminescence spectra of this phase feature a distinctive asymmetry as it was observed for J-aggregates. I studied the photophysical properties of the red phase of MEH-PPV by means of Franck-Condon analyses as a function of temperature. In comparison to quantum mechanical calculations in the framework of Spano's HJ-aggregate model, chapter 7 presents the nature of the MEH-PPV aggregates.

On the way to efficient solar cells, emphasis is recently laid on low-bandgap polymers whose absorption leads to photon collection in the red part of the solar spectrum resulting in higher power conversion efficiencies compared to conventional semiconducting homo-polymers. A prominent representative of this group is PCPDTBT, a co-polymer consisting of the alternating groups dithiophene being electron donating and benzo-thiadiazole being electron accepting. In chapter 8, the aggregation and structure formation in PCPDTBT and their effect on the excited state are studied. The formation of aggregates in PCPDTBT is again induced by cooling the solution to reduce continuously the solvent quality. This way, we are able to observe

the aggregation process and the photophysical properties of the aggregates formed with the highest possible degree of freedom. The knowledge of the aggregation process in solution is transferred to PCPDTBT thin films relevant for photovoltaic applications. The absorption and photoluminescence spectra of films with two distinct morphologies were analyzed by means of Franck-Condon analyses as a function of temperature. In this way, we discover low-energy emissive trap sites in the PCPDTBT films and trace their possible origin.

The following sections present an overview of the individual works composing this thesis.

Control of Aggregate Formation in Poly(3-hexylthiophene) by Solvent, Molecular Weight, and Synthetic Method

The formation of aggregates in P3HT in solution depends on the solvent, the molecular weight and the synthetic method and thus on the resulting polydispersity of the sample. Since the interplay of these factors controls the device performance in applications, our study was aimed at a quantitative understanding how these parameters control the resulting electronic properties of the polymer. Therefore, we measured absorption of P3HT in solution and in thin films along with the resulting field-effect mobility in thin film transistors. The parameter of synthetic method refers, on the one hand, to P3HT tailor-mode to a specific molecular weight. These samples were synthesized according to the catalyst transfer polymerization reaction method and have thus a very low polydispersity index (< 1.2). In the chapter, they are referred to as “defined P3HT”. The second synthetic method we focused on was the early McCullough route with subsequent fractionation with different solvents to obtain samples of different molecular weight. The polydispersity index of these samples is much higher compared to the defined P3HT samples. They are referred to as “extracted P3HT”.

The absorption was measured of P3HT in solution. The good solvent used was chloroform, the poor solvent ethyl acetate (EtAc) was added. The spectra show increasing low-energy absorption with increasing fraction of poor solvent due to aggregate absorption. To determine the fraction of aggregates present in the solutions, we separated the part of the spectrum arising from aggregate absorption from the part arising from coiled chain absorption. In order to subtract the coiled chain absorption from the spectra showing contributions of both phases, we scaled the absorption spectrum of the coiled chains to the high energy shoulder of the absorption spectrum. The calculated fraction of aggregates is based on the fraction of aggregate absorption and takes into account that the oscillator strength changes when going from the coiled to the aggregated state. However, the fraction of aggregates reflects the propensity to aggregation of the P3HT sample considered.

The spectral shape of the aggregate absorption allowed further analysis to extract the excitonic coupling between the polymer chains within the aggregates. Based on the theoretical work for weakly interacting H-aggregates by Spano, we extracted the excitonic coupling from the ratio of the first two peaks in the aggregate absorption. The results are shown in Figure 11(a). Apparently, the excitonic coupling depends on the amount of poor solvent.

On the basis of the theoretical work by Gierschner, the conjugation length of the aggregated P3HT chains can be calculated from the excitonic coupling. The longer the conjugation length of the polymer chains, the lower the resulting excitonic coupling. A comparison of the derived conjugation length with the degree of polymerization determined by matrix-assisted laser desorption ionization time of flight mass spectroscopy (MALDI-TOF MS) leads to conclusions about the extension of the conjugation over the polymer chain. Whereas the defined polymer chains with low molecular weight are fully extend, the conjugation lengths for polymer samples with higher molecular weight are significantly below the degree of polymerization. In combination with the fraction of aggregates present in solution, we can derive a scenario for the packing behavior of the polymer chains in aggregates for different molecular weights and different fractions of poor solvent. A scheme of these packing behaviors is shown in Figure 11(b). The same method does not apply for the extracted P3HT samples, since it is not possible to determine a reliable chain length due to their high polydispersity. Up to this point, the results are based solely on spectroscopic measurements in combination with the adequate theories of excitonic coupling provided by Spano and Gierschner.

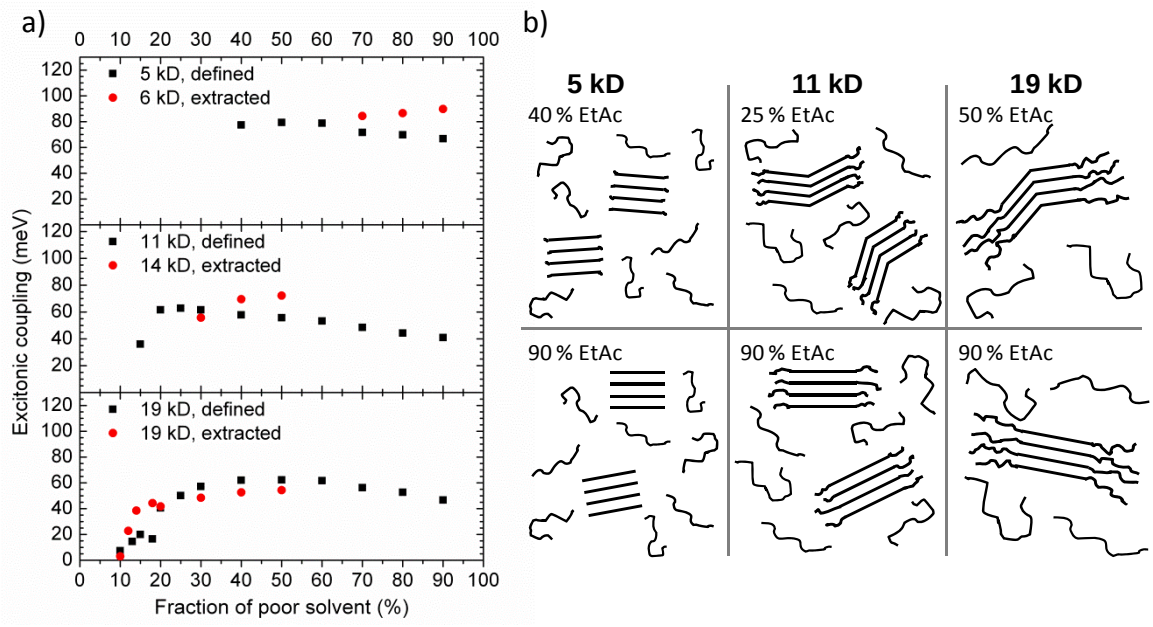

Figure 11: (a) Excitonic coupling within aggregates of defined and extracted P3HT as a function of the fraction of poor solvent. The molecular weight increases from top to bottom. (b) Scheme of possible scenarios for the packing behavior of defined P3HT for different molecular weights and different fractions of the poor solvent EtAc.

In addition to the study of P3HT in solution, we tested whether the results obtained for the aggregates in solution can be transferred to P3HT thin films spun from solutions containing poor solvent fractions and thus already containing aggregates. We measured the absorption of the P3HT thin films. The analysis of these spectra revealed very similar excitonic couplings of the defined P3HT samples compared to the aggregates found in solution. Thus, we can indeed control the nature of the aggregates formed in P3HT thin films via control of solvent quality in case of defined P3HT.

To clarify to which extent the use of defined P3HT is advantageous for the charge carrier mobility, we measured P3HT field-effect transistors. Here, the polymer was simply spin-coated from 100% chloroform solutions without any subsequent post-treatment of the device. Apart from the expected increase in saturation mobility with increasing molecular weight, we found that the defined P3HT samples with 5 kDa and 11 kDa show significantly higher charge carrier mobilities than their extracted counterparts. However, already for a molecular weight of 19 kDa this difference in charge carrier mobility vanishes. Both samples, independent of synthetic method, reach charge carrier mobilities of 10^{-2} cm/Vs. This is in accordance with the results for the solution aggregates that did not show any significant differences in fraction of aggregates and excitonic coupling when comparing the defined and extracted P3HT samples with 19 kDa. Thus, complex synthetic approaches for P3HT with high molecular weights have no advantage over the early McCullough route in device performance.

Role of Structural Order and Excess Energy on Ultrafast Free Charge Generation in Hybrid Polythiophene/Si Photovoltaics Probed in Real Time by Near-Infrared Broadband Transient Absorption

A polymer solar cell operates by the sequence of light absorption, exciton diffusion to a donor-acceptor interface and subsequent separation of the excitation into free electron and hole that then need to be extracted to the electrodes. In this chapter, we focus on the mechanism of exciton dissociation and how electrical charge is actually generated in hybrid solar cells. We address the following questions. What exactly happens at the donor-acceptor heterojunction when Coulomb bound electron-hole pairs created by light absorption separate at this interface? Which molecular parameters control their separation? And is the initial electron hole pair really Coulomb bound right from the beginning? The latter has recently been questioned since free charge carriers were observed in solar cells within 100 fs after excitation which was the limit of time resolution.

The hybrid heterojunctions we studied here with a novel broadband (UV-Vis-NIR) transient absorption spectroscopy setup used silicon as electron acceptor. In silicon the electron delocalizes well and is well screened. Furthermore, silicon does not have any signals over the whole spectral range of interest we studied with our ultrafast pump-probe spectroscopy setup in contrast to the frequently used PCBM or C60. The used polymer acting as electron donor in our hybrid heterojunctions is P3HT. In addition to P3HT/Si bulk heterojunctions, we prepared two distinct types of bilayer samples with polycrystalline silicon as electron acceptor layer. For the first type, regiorandom (RRa) P3HT was spin-coated from good solvent onto the (Si-)substrate resulting in mostly disordered chains with short conjugation lengths. For the second type, regioregular (aggRR) P3HT was spin-coated from a solution containing a low fraction of poor solvent resulting in enhanced aggregation and long conjugation lengths. The long conjugation length and high order of the planar chains is manifested in a structured, red absorption as shown in Figure 12(a). The polymer was spin-coated only partially onto the substrate, thus we were able to optically excite the P3HT alone, the silicon alone, and the P3HT on top of the silicon.

Our transient absorption spectroscopy setup included a pump beam with a full width of half maximum of 15 fs that was tunable over the range of 450 nm to 750 nm. The probe beam had a time resolution of 40 fs and was tunable from 300 nm to 1200 nm. For the identification of the transient absorption signal due to polarons, we measured the steady-state polaron absorption by doping P3HT thin films with the strong oxidant iron-chloride. This way, we were able to distinguish the ground state bleach, the polaron signal and the exciton signal in the transient absorption spectrum.

The analysis of the absorption spectra of the disordered RRa-P3HT and the ordered aggRR-P3HT reveals a fraction of aggregates of 20% for the RRa-P3HT and 40% for the aggRR-P3HT. The influence of this difference is striking. After 300 fs in neat P3HT, there is an enhanced polaron formation in aggRR-P3HT compared to the more

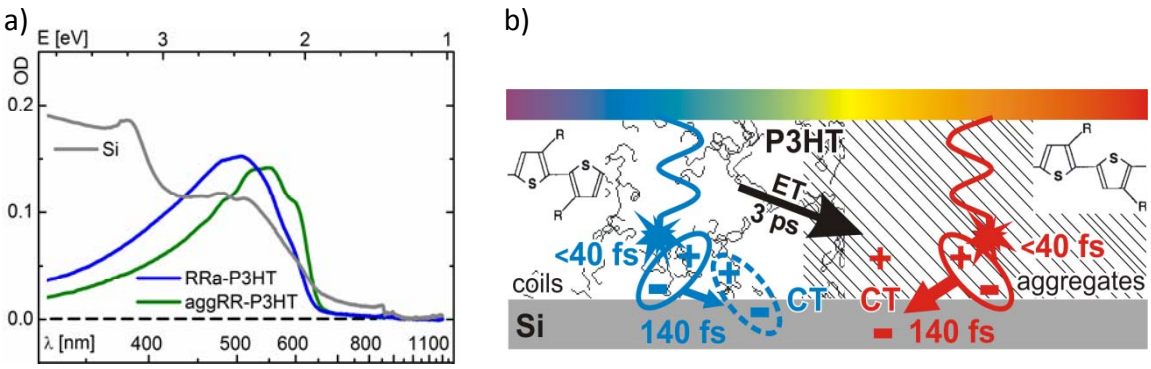

Figure 12: (a) Absorption spectra of thin films of neat regiorandom P3HT (RRa-P3HT), regioregular P3HT aggregated with low fractions of poor solvent (aggRR-P3HT), and neat polycrystalline silicon (Si). (b) Scheme of primary photoinduced processes and their lifetimes in hybrid P3HT/Si thin film heterojunctions.

disordered counterpart RRa-P3HT. In fact, in the P3HT/Si heterojunction the polaron yield in aggRR-P3HT is twice as high as in RRa-P3HT. In addition, we observed an increased polaron signal and a simultaneous decrease in exciton signal when adding Si to the P3HT. Evidently, silicon acts indeed as electron acceptor thereby causing the dissociation of the neutral, Coulomb bound, exciton. In summary, the ultrafast electron transfer from P3HT to silicon strongly depends on the polymer structural order.

To test this result, we studied the initial polaron yield at about 300 fs in a bulk heterojunction consisting of a blend film of regioregular P3HT with medium aggregate fraction and silicon nanocrystals as a function of pump wavelength ranging from 450 nm to 600 nm. At 600 nm, disordered chains do not absorb while planar, aggregated chains absorb. The polaron yield for excitation in the blue spectral range, where the absorption is dominated by the coiled chains, is lower by a factor of two compared to the resulting polaron yield for the red range of the spectrum. Even though the excitation energy in the blue is higher, the resulting polaron yield is much lower. This clearly proofs that polymer structural order and not excess energy is the key criterion for free charge generation in P3HT/Si photovoltaics.

As for the question whether the charges are initially free, we analyzed the transient absorption signals from the neutral excited state at 1000 nm, the positively charged polaron in P3HT at 660 nm and the ground state bleach at 550 nm in regard to their evolution in time. Remarkably, absorption from the exciton shows immediately when the ground state is bleached, i.e. after 40 fs. Moreover, we find that the exciton signal decays initially with a time constant of 140 fs while the polaron signal shows a delayed rise with a rise time of again 140 fs and reaches its maximum after 300 fs. Thus, we monitored the dissociation of the excitons as primary photoexcitations into positive and negative free charges. Figure 12(b) shows a summary of the primary photoinduced processes and their lifetimes in the hybrid P3HT/silicon heterojunction.

Furthermore, we investigated whether the electron is still bound or free when it has been transferred to the silicon. As for this question, we studied the intensity dependence of the polaron decay. In the disordered RRa-P3HT, the polaron decay is completely independent of the pump power. This means, the decay is independent on the number of polarons generated. It is therefore a monomolecular process and a clear signal of geminate recombination. This is only possible when the charges are still Coulomb bound. In contrast, the polaron decay in films with aggregated aggRR-P3HT gets faster for increasing pump intensities suggesting a bimolecular nongeminate recombination and decay. Clearly, the charges must be free for nongeminate recombination. This confirms the key role of polymer structural order on the ultrafast free charge generation in hybrid P3HT/Si photovoltaics.

The Red-Phase of Poly[2-methoxy-5-(2-ethylhexyloxy)-1,4-phenylenevinylene] (MEH-PPV): A Disordered HJ-Aggregate

The soluble poly(phenylene-vinylene) derivate MEH-PPV has been widely studied in thin films as well as in solution and even as single molecules. Recent studies showed that MEH-PPV in solution can undergo a phase transition when cooled below 200 K. Here, we studied the spectroscopic properties of the red phase of MEH-PPV in solution as a function of temperature ranging from 180 K down to 5 K. This low energy, red, phase was associated with polymer chains assembling into aggregates.

The theoretical works by Kasha and coworkers on H- and J- aggregation showed already that aggregation and the inherent electronic interaction between molecules lead to delocalization of the excited state inducing an energy shift in absorption compared to isolated molecules and differing radiative decay rates due to symmetry reasons of the lowest energy exciton. Here, we introduced an enhanced HJ-aggregate model including electron and hole site disorder to investigate the impact of disorder on the temperature dependence of the 0-0/0-1 photoluminescence line strength in MEH-PPV aggregates. Our theoretical model treats the simplest aggregate being a dimer of two cofacial MEH-PPV polymer chains and yields information on the effect of disorder and intermolecular coupling on the photoluminescence spectrum, the absorption spectrum, the radiative decay rate and on the exciton coherence length along the polymer chain.

Our experimental studies on MEH-PPV in solution as a function of temperature showed that the 0-0/0-1 peak ratio in photoluminescence of aggregated red-phase MEH-PPV is significantly enhanced compared to the 0-0/0-1 ratio of the disordered blue-phase of MEH-PPV. Furthermore, this ratio of the 0-0 to 0-1 peak PL intensity as well as the photoluminescence lifetime is temperature independent for the whole temperature range between 180 K and 5 K in which the red-phase MEH-PPV was present. In order to identify the spectroscopic features in PL and absorption, we reproduced the spectra considering three different torsional and vibrational modes by means of multi-mode Franck-Condon analyses. Figure 13(a) shows the experimental data and the corresponding Franck-Condon fits of the photoluminescence and absorption of MEH-PPV in solution at 80 K. The sum of the Huang-Rhys factors of the three modes yields the total effective Huang-Rhys factor that is modelled in our theoretical calculations on MEH-PPV dimers as a single effective mode.

First, we calculated the dispersion curves for a single MEH-PPV chain revealing an exciton bandwidth, ΔE_{intra}, of 200 meV associated with the lowest energy intrachain exciton. In addition, interchain interactions with an with interchain coupling J_{inter} cause the intrachain exciton band to split into an antisymmetric and a symmetric band. As characteristic of H-aggregates, absorption is allowed only into the symmetric band that is at higher energies than the corresponding antisymmetric band.

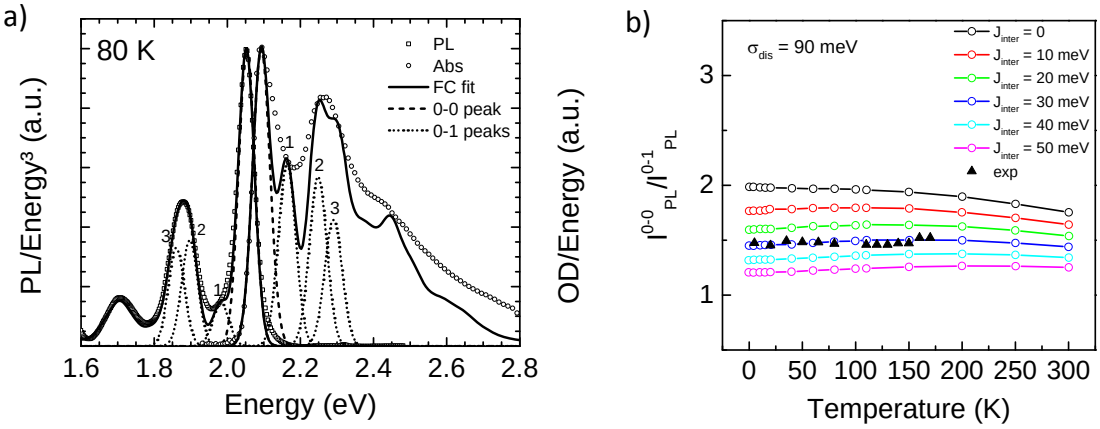

Figure 13: (a) Franck-Condon analysis of the absorption and photoluminescence spectra of MEH-PPV in solution at 80 K. The absorption spectrum (circles) was divided by ħω, the emission spectrum (squares) was divided by $(\hbar\omega)^3$. The Franck-Condon fit is shown as solid line, the 0-0 peak and 0-1 peaks of the three modes considered are shown as dashed and dotted lines, respectively. (b) 0-0/0-1 PL ratio numerically calculated as a function of temperature for MEH-PPV dimers with a disorder of σ_{dis} = 90 meV for different interchain couplings, J_{inter}. Experimental values are shown as triangles.

Since the calculated intrachain exciton bandwidth is substantially larger than the measured line width of 32 meV at 80 K, we further investigated motional narrowing which is a typical signature in J-aggregates. From this analysis, we found that disorder σ_{dis} = 90 meV is necessary to reproduce the measured line width. This is the value of disorder we used for further calculations. The numerically calculated absorption and photoluminescence spectra then reproduced nicely the experimental linewidth and Stokes shift. The spectra were calculated for different values of interchain coupling. While for the absorption spectra the ratio of the oscillator strengths of the 0-0 and 0-1 peaks decreases only slightly with increasing J_{inter}, the impact of interchain interaction on the 0-0/0-1 ratio in photoluminescence is far more dramatic. More effective destructive interference between the emitting chains with increasing J_{inter} leads to a considerable drop in the PL 0-0 peak intensity as it is characteristic for H-aggregates.

A further investigation comprised the numerically calculated 0-0/0-1 PL ratio of MEH-PPV dimers as a function of temperature. The 0-0/0-1 PL ratios were calculated for three different values of interchain coupling (J_{inter} = 0, 10 meV, 30 meV) each with three different values of disorder (σ_{dis} = 0, 11 meV, 22 meV). For isolated chains (J_{inter} = 0), the PL ratio is largest at low temperature and decreases steadily with increasing temperature. For dimers with interchain interaction the PL ratio first increases and above the HJ transition temperature decreases with increasing temperature. Thus, the behavior is characteristic of H-aggregates at low temperatures and J-like at high temperatures. Note that for disorder-free chains the PL ratio is zero at 0 K due to symmetry reasons. Considering the effect of disorder, the overall impact is on the

temperature dependence of the 0-0/0-1 PL ratio. For the higher, relevant value of σ_{dis} = 90 meV, the PL ratio as well as the radiative decay rate is practically temperature independent for all values of interchain coupling. Figure 13(b) shows numerically calculated 0-0/0-1 PL ratio as a function of temperature for different values of the interchain coupling J_{inter} as well as the measured values. Good agreement between theory and experiment was achieved for interchain couplings of 30 meV.

As a final point, we calculated the exciton coherence length along the polymer chain within the MEH-PPV dimer as a function of temperature. In contrast to the 0-0/0-1 PL ratio and the radiative decay rate, the exciton coherence length along the polymer chain is temperature dependent and decreases with increasing temperature due to disorder-induced localization. Interestingly, increasing interchain coupling leads to an increasing coherence length along the chain at T = 0 K probably due to the ability of excitons to sidestep traps along the chain. The coherence length in our MEH-PPV dimer at T = 0 K is approximately eight phenylene-vinylene repeat units.

To summarize, the aggregated red phase of MEH-PPV reproduce best the measured photoluminescence and absorption spectral line shapes when described as a weakly coupled, disordered HJ-aggregates in which the interchain splitting ($\Delta E_{inter} \approx 0.012$ eV) is roughly an order of magnitude smaller than the lowest energy exciton bandwidth ($\Delta E_{intra} \approx 0.2$ eV). Generally, the photophysical response results from a competition of J-like and H-like behavior. The first is due to intrachain interactions, the latter due to interchain interactions. Remarkably, the measured temperature independence of the PL lifetime and the 0-0/0-1 PL peak ratio is in stark contrast to the predictions of the HJ-aggregate model when disorder is absent. Incorporating disorder into the model decreases the PL ratio at high temperatures as characteristic for J-aggregates and increases the PL ratio at low temperatures since disorder destroys the symmetry needed for perfect destructive interference as valid for H-aggregates.

Revealing Structure Formation in PCPDTBT by Optical Spectroscopy

The tendency of a semiconducting polymer to aggregate is a key factor in controlling its charge carrier mobility and in controlling the propensity of the excited states to dissociate at the interface with an electron accepting material. Thus, investigations on structure formation and aggregate behavior are fundamental for device applications. Here, we studied the structure formation of the low-bandgap polymer PCPDTBT which reached power conversion efficiencies up to 5.5% in bulk heterojunction cells with PCBM.

To reveal the aggregate behavior of PCPDTBT in presence of the highest possible degree of freedom, we first studied spectroscopically as a function of temperature

PCPDTBT in solution where the chains can adopt their favorable conformation without major constraints. As a second step, we extended our absorption and photoluminescence studies to PCPDTBT thin films with two distinct morphologies.

We cooled down PCPDTBT in solution, and measured absorption as well as photoluminescence at different temperatures between 340 K and 180 K. Figure 14(a) shows the resulting absorption. For temperatures below 320 K, the structured absorption of an additional low energy state and an isosbestic point evolve. Equally in photoluminescence, two distinct emissions can be identified. The absorption and PL spectra of a concentration series at room temperature showed the increase of this low energy phase with increasing concentration confirming that this spectral feature is due to an aggregated phase consisting of interacting polymer chains. Thus, PCPDTBT in solutions clearly undergoes a phase transition from a disordered, coiled phase with unstructured absorption to a planarized and aggregated phase with clearly structured absorption as it's well-known for other conjugated polymers such as P3HT, PFO and MEH-PPV. In contrast to these polymers, the critical temperature of the phase transition of PCPDTBT is already at 300 K and thus effecting the structure formation in all solution processed devices.

We performed thorough multi-mode Franck-Condon analyses including five different Raman modes to separate the absorption and the photoluminescence of both phases. This way, we determined the energetic distance between both phases to be 180 meV. In addition, the spectral shape of aggregate photoluminescence and absorption showed neither specific H- or J-type character. Thus, we conclude that PCPDTBT forms rather strongly disordered aggregates. A further result of the separation of coiled and aggregate absorption is the present fraction of both phases. Figure 14(b) shows the fraction of aggregates as a function of temperature. At temperatures below 240 K, it reaches a saturation value of 45% which is comparable to those of P3HT or MEH-PPV.

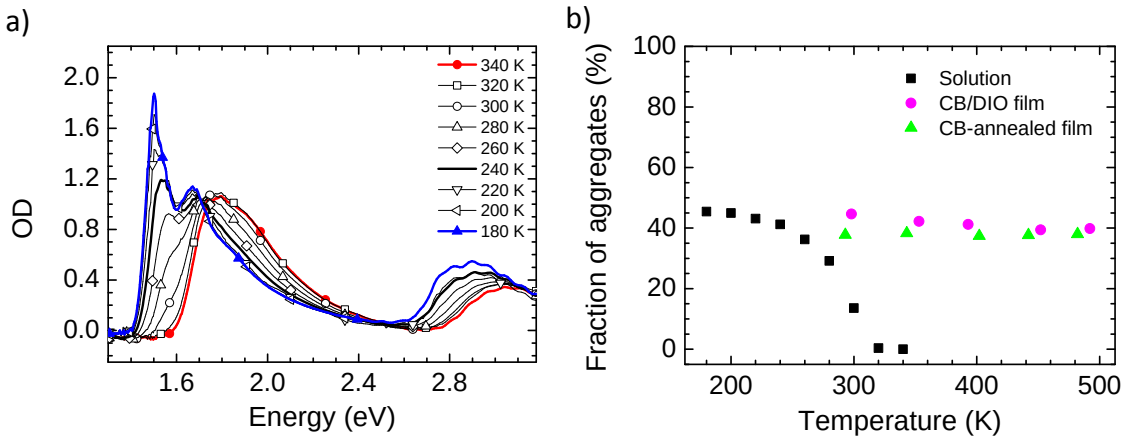

Figure 14: (a) Optical density of PCPDTBT in solution for different temperatures between 340 K and 180 K. (b) Fraction of aggregates for PCPDTBT in solution (squares), CB/DIO film (circles), and CB-annealed film (triangles) as a function of temperature.

Our investigation of PCPDTBT thin films comprised the CB/DIO film type that was spin-coated from a chlorobenzene (CB) solution with 2 wt% of the high-boiling point additive diiodooctane (DIO) and the CB-annealed film type that was spin-coated from chloroform and afterwards solvent (CB) annealed. These processing conditions dramatically affect the resulting film morphology. Whereas in the CB/DIO films randomly oriented aggregates prevail that show a lamellar structure with a distance of 4 Å between the polymer backbones, the CB-annealed films form spherulites and terraces consisting of dimers arranged in herringbone structure with 7 Å between the backbones.

Comparing the PCPDTBT film absorption with the absorption of the solution, we found a continuous red-shift of the absorption maximum for the films instead of evolving an additional peak upon cooling as valid for the solution. Although the 0-0 peak of the aggregates is less pronounced in the film absorption, the CB/DIO film and PCPDTBT in solution at 240 K show very similar absorption spectra. In contrast, the absorption of the CB-annealed film is at higher energies, suggesting that lamellar aggregates present in solution at room temperature act as nucleation points during the spin-coating process. Franck-Condon analyses of the PCPDTBT film absorption spectra yield fractions of aggregates independent from temperature as shown in Figure 14(b).

As for the photoluminescence of the films, only emission from the PCPDTBT aggregates was measured due to efficient energy transfer from the coiled to the aggregated phase. In addition, the PL spectra showed a substantial red shift upon cooling, thus arising the question of spectral diffusion. Therefore, we analyzed the low temperature absorption and PL of CB/DIO film by means of Franck-Condon analysis to extract the energetic difference between the 0-0 transition in PL and the center of the density of states $\Delta\varepsilon(T)$ as well as the linewidth $\sigma(T)$ as a function of temperature. The plot of $\Delta\varepsilon(T)/\sigma(T)$ as a function of kT/σ was in good agreement with the theoretical values for individual chromophores. Evidently, within these PCPDTBT aggregates the same temperature dependent dynamics of exciton diffusion is present as for individual chromophores.

Again, PCPDTBT aggregates in thin films show no features specific for H- of J-aggregates. Solely, the CB-annealed film is energetically shifted to higher energies compared to the CB/DIO film. This shift can be explained by differences in polarization in the two distinct morphologies. The CB/DIO film has a more compact packing of the polymer chains resulting in an energy shift to lower energies compared to the CB-annealed film with herringbone structure.

Looking at the changes in PL with temperature, we renormalized the PL spectra to the 0-0 line as determined from Franck-Condon analyses. This renormalization showed enhanced low energy emission increasing with temperature above 150 K. To identify these emissivebstates, we tried to reproduce the PL spectra with Franck-Condon fits. The spectra can be reproduced either by using an increasing single vibrational mode

with simultaneous change in the 0-0 line strength when increasing the temperature or by using a broad low emissive state modeled by a broad Gaussian peak without any simultaneous changes of the 0-0 line strength. Since the first scenario is physically not convincing, we presumed this low energy emission to emerge from the presence of a low percentage of broad low energy emissive states that get more and more populated with increasing temperature and thus increasing diffusion length. These states were not present in solution.

In addition to further identify the low energy emissive states in the PCPDTBT thin films, we measured the lifetime at room temperature where a major part of the PL is due to these states. The lifetimes for both film types did not differ and were about 250 ps. Furthermore, the quantum yield of the films is very low (below 0.1%) and thus the non-radiative decay rate is three orders of magnitude higher than the radiative decay rate. The radiative decay rate is comparable with rates for excimers published by Gierschner and Park. We explained the discrepancies in the non-radiative decay rates by the energy-gap law that predicts very high non-radiative decay rates for low-bandgap materials. Thus, we assumed the low emissive states to be excimers that are likely to form due to structural defects especially at grain boundaries.

To summarize, the low-bandgap material PCPDTBT undergoes a phase transition upon cooling in solution. Above the critical temperature of 300 K, the polymer chains adopt a randomly coiled conformation, below this temperature up to 45% of the chains aggregate and adopt a more planarized conformation. These aggregates can be transferred to the film where they act as nucleation points during the spin-coating process. In the PCPDTBT thin films, the same maximum fraction of about 42% can be obtained. In addition, these films exhibit a small percentage of low-energy trap sites which get populated at temperatures above 150 K.

Individual Contributions to Joint Publications

This thesis comprises of four completed works of which three are published in peer-reviewed journals. The fourth work is ready to be submitted for publication. The following section clarifies my individual contributions to the papers.

Chapter 6

This work is published in *Journal of Polymer Science Part B: Polymer Physics 2012, 50, 442–453, DOI: 10.1002/polb.23022*, under the title

"Control of Aggregate Formation in Poly(3-hexylthiophene) by Solvent, Molecular Weight, and Synthetic Method"

by Christina Scharsich, Ruth H. Lohwasser, Michael Sommer, Udom Asawapirom,

Ullrich Scherf, Mukundan Thelakkat, Dieter Neher, and Anna Köhler

Based on data taken in the framework in my diploma thesis, I performed the analysis of the spectra, calculated the excitonic coupling and did the entire interpretation of the spectra. I carried out additional experimental measurements. Furthermore, I wrote the manuscript.

Chapter 7

This work is published in *Journal of the American Chemical Society 2011, 133, 18220–18233, DOI: 10.1021/ja207887q*, under the title

"Role of Structural Order and Excess Energy on Ultrafast Free Charge Generation in Hybrid Polythiophene/Si Photovoltaics Probed in Real Time by Near-Infrared Broadband Transient Absorption"

by Daniel Herrmann, Sabrina Niesar, Christina Scharsich, Anna Köhler, Martin Stutzmann, and Eberhard Riedle

I did the sample preparation of the organic part of the planar hybrid heterojunctions with two distinct aggregate characters. I measured the steady-state absorption spectra of both polythiophene film types and did the modified Franck-Condon analyses. I determined the fraction of aggregate within these films. In addition, I doped the polythiophene by means of a strong oxidant and measured the steady-state

absorption of the polythiophene polaron in thin films. Furthermore, I wrote minor parts of the manuscript.

Chapter 8

This work is published in *Journal of Chemical Physics 2013, 139, 114903, DOI: 10.1063/1.4819906*, under the title

"The Red-Phase of Poly[2-methoxy-5-(2-ethylhexyloxy)-1,4-phenylenevinylene]

(MEH-PPV): A Disordered HJ-Aggregate"

by Hajime Yamagata, Nicholas J. Hestand, Frank C. Spano, Anna Köhler,

Christina Scharsich, Sebastian T. Hoffmann, and Heinz Bässler

I implemented the simultaneous fitting of two Franck-Condon progressions in our fitting routine and did the Franck-Condon analyses with two phases of the MEH-PPV absorption and photoluminescence spectra. I analyzed the Franck-Condon parameters used for fitting as a function of temperature. In addition, I measured the photoluminescence lifetime as a function of temperature. Furthermore, I wrote minor parts of the manuscript.

Chapter 9

This work is prepared for submission under the title

"Revealing Structure Formation in PCPDTBT by Optical Spectroscopy"

by Christina Scharsich, Florian S. U. Fischer, Kevin Wilma, Richard Hildner, Sabine Ludwigs, and Anna Köhler

I measured the absorption and photoluminescence spectra at different temperatures as well as the quantum yield of PCPDTBT in solution and in thin films. I did the Franck-Condon analyses of the spectra and analyzed all data. Furthermore, I interpreted the results and wrote the manuscript.

5 Control of Aggregate Formation in Poly(3-hexylthiophene) by Solvent, Molecular Weight, and Synthetic Method

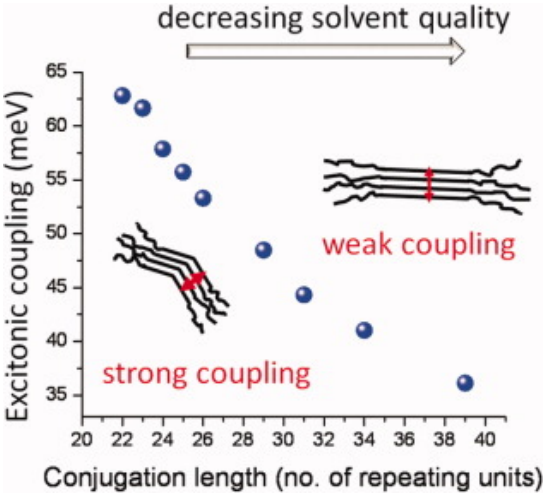

Christina Scharsich, Ruth H. Lohwasser, Michael Sommer, Udom Asawapirom, Ullrich Scherf, Mukundan Thelakkat, Dieter Neher, Anna Köhler

Published in

Journal of Polymer Science Part B: Polymer Physics

DOI: 10.1002/polb.23022

Reprinted with permission from J. Poly. Sci. B: Polymer Physics 2012, 50, 442–453

Control of Aggregate Formation in Poly(3-hexylthiophene) by Solvent, Molecular Weight, and Synthetic Method

Christina Scharsich,[1] Ruth H. Lohwasser,[2] Michael Sommer,[2] Udom Asawapirom,[3]* Ullrich Scherf,[3] Mukundan Thelakkat,[2] Dieter Neher,[4] Anna Köhler[1]

[1]Organic Semiconductors, Experimental Physics II, Department of Physics and Bayreuth Institute of Macromolecular Science (BIMF), University of Bayreuth, Bayreuth 95440, Germany

[2]Applied Functional Polymers, Macromolecular Chemistry I, Department of Chemistry, University of Bayreuth, Bayreuth 95440, Germany

[3]Macromolecular Chemistry Group, Bergische Universität Wuppertal, Wuppertal 42097, Germany

[4]Soft Matter Physics, Institute of Physics and Astronomy, University of Potsdam, Potsdam 14476, Germany

Correspondence to: Anna Köhler (E-mail: anna.koehler@uni-bayreuth.de)

Received 26 July 2011; revised 7 November 2011; accepted 22 November 2011; published online 13 December 2011
DOI: 10.1002/polb.23022

ABSTRACT: Aggregate formation in poly(3-hexylthiophene) depends on molecular weight, solvent, and synthetic method. The interplay of these parameters thus largely controls device performance. In order to obtain a quantitative understanding on how these factors control the resulting electronic properties of P3HT, we measured absorption in solution and in thin films as well as the resulting field effect mobility in transistors. By a detailed analysis of the absorption spectra, we deduce the fraction of aggregates formed, the excitonic coupling within the aggregates, and the conjugation length within the aggregates, all as a function of solvent quality for molecular weights from 5 to 19 kDa. From this, we infer in which structure the aggregated chains pack. Although the 5 kDa samples form straight chains, the 11 and 19 kDa chains are kinked or folded, with conjugation lengths that increase as the solvent quality reduces. There is a maximum fraction of aggregated chains (about 55 ± 5%) that can be obtained, even for poor solvent quality. We show that inducing aggregation in solution leads to control of aggregate properties in thin films. As expected, the field-effect mobility correlates with the propensity to aggregation. Correspondingly, we find that a well-defined synthetic approach, tailored to give a narrow molecular weight distribution, is needed to obtain high field effect mobilities of up to 0.01 cm^2/Vs for low molecular weight samples (=11 kDa), while the influence of synthetic method is negligible for samples of higher molecular weight, if low molecular weight fractions are removed by extraction. © 2011 Wiley Periodicals, Inc. J Polym Sci Part B: Polym Phys 50: 442–453, 2012

KEYWORDS: conformational analysis; conjugated polymers; crystallization; films; interaction parameter; molecular weight distribution/molar mass distribution; nucleation; photophysics; structure; UV–vis spectroscopy

INTRODUCTION The optical and electronic properties of regioregular poly(3-hexylthiophene) (rrP3HT) are relevant for many applications in the field of organic semiconductors such as solar cells and field-effect transistors. Regioregular P3HT is known to show high mobilities that provide promising application on the industrial level.[1–4] For this reason, the focus is often placed on the charge carrier mobility in P3HT thin films. It is well-known that several parameters affect the charge carrier mobility, such as the degree of crystallization, the molecular weight of P3HT chains, and the intermolecular coupling between these chains.[4–7] Especially, the aggregation of polymer chains plays an important role in the performance of organic field effect transistors (OFETs) and organic solar cells.[8] Indeed, the number and the nature of the aggregates are of central importance for these applications. Properties such as conjugation length, intermolecular coupling within the aggregates as well as the packing behavior of the polymer chains and disorder affect the applicable optic and electronic properties of P3HT.[9–11] Another important parameter is the polydispersity of the polymer chains, which depends strongly on the synthetic approach. It was shown that low molecular weight polythiophene with low polydispersity forms highly ordered structures in thin films.[12] Despite investigations on phase control in polymer films, the relation between molecular weight, polydispersity, and aggregation behavior of chains is still not fully understood.[13]

**Present address:* National Nanotechnology Center (NSTDA), 130 Thailand Science Park, Phahonyothin Rd., Klong 1 Klong Luang, Pathumthani 12120, Thailand.

Additional Supporting Information may be found in the online version of this article.

TABLE 1 Molecular Weights (MW) of Defined P3HTs Directly Synthesized to Get Well-Controlled Molecular Weights

Poly(3-hexylthiophene)	M_n [Da]	M_w [Da]	PDI	M_n	DP
Based on	GPC	GPC	GPC	MALDI-TOF MS	MALDI-TOF MS
5 kDa	5,100	6,300	1.22	3,200	19
11 kDa	11,300	15,200	1.11	7,100	43
19 kDa	18,600	21,600	1.16	12,400	74

M_n, number-average molecular weight; M_w, weight-average molecular Weight; PDI = M_w/M_n, polydispersity index; DP, degree of polymerization, i.e. the number of repeating units.

Here, we investigate the effect of molecular weight as well as the effect of synthetic approach to P3HT on the aggregate formation. We obtain information on the fraction of aggregates and on the packing behavior of P3HT chains within aggregates by combining spectroscopic methods with the theoretical works by Spano[9] and Gierschner et al.[11] Furthermore, we observe variations in excitonic coupling within P3HT aggregates and use this information to clarify to which extent the results obtained in solution can be transferred to P3HT thin films. We find that the synthetic approach affects the packing behavior of P3HT chains with low molecular weight. A synthesis defined to a specific molecular weight results in more accurate aggregates in both solution and thin films and thus in better FET performance. When going to higher molecular weights, these differences disappear, which implies that specific synthetic approaches to obtain defined high molecular weights, such as catalyst transfer polymerization, are not necessary. The early McCoullough route with subsequent extraction of low molecular weight fractions is sufficient to obtain comparable performances.

EXPERIMENTAL

The poly(3-hexylthiophene) samples differ in molecular weight and belong to two groups of different synthetic approach. The first group of poly(3-hexylthiophene)s was synthesized according to the catalyst transfer polymerization reaction method.[14,15] These compounds, listed in Table 1, were tailor-made to their specific molecular weight. They have a very sharp molecular mass distribution and thus a very low polydispersity index (PDI). The number-average molecular weights (M_n) and the weight-average molecular weights (M_w) were measured by two methods. We used gel permeations chromatography (GPC) in tetrahydrofuran (THF) with polystyrene as calibration standard as well as matrix-assisted laser desorption ionization-time of flight mass spectroscopy (MALDI-TOF MS). Both methods are known to be associated with some experimental error. The molecular weight determined by MALDI-TOF MS is significantly lower than the one obtained from GPC measurements, because calibration against the polystyrene standard overestimates the molecular weight of rigid polymers.[16] The degree of polymerization, DP, refers to the number of repeat units, and it is derived from the molecular weight as determined by MALDI-TOF, though we note that an uncertainty of about two repeat units remains. Throughout this article, the compounds in this group are referred to as "defined P3HT."

The second group of poly(3-hexylthiophene)s was synthesized according to the original McCullough route[17] that does not allow for molecular weight control and that leads to broad molecular weight distributions.[18] In order to obtain different molecular weight samples, the initial molecular mass distribution was fractionated with different solvents as listed in Table 2. Molecular mass distributions of the different samples were again obtained via GPC measurements with polystyrene standard. The compounds from this group are below referred to as "extracted P3HT." We consider the average degree of polymerization of each extracted compound to be similar to the DP of the corresponding defined compounds, because the M_n values of the defined and extracted samples are comparable in pairs.

Solutions were prepared from a ratio of good to moderately poor solvents, denoted subsequently as *A*:*B*, where *A* gives the volume fraction of good solvent and *B* the corresponding volume fraction of poor solvent, each as percent. Both solvents had a similar boiling point (bp) to eliminate different behaviors of volatilization. The good solvent for all compounds was chloroform ($CHCl_3$; bp = 61 °C), whereas the moderately poor solvent was ethyl acetate (EtAc; bp = 77 °C). As both the boiling points are close enough, only the influence of solubility was studied. The worse solubility of P3HT in ethyl acetate results from its slightly higher polarity when compared with chloroform. The difference in Hildebrandt solubility parameter is not large (9.10 $cal^{0.5}$ $cm^{-1.5}$ for EtAc versus 9.21 $cal^{0.5}$ $cm^{-1.5}$ for $CHCl_3$), yet it is sufficient to induce planarization (as evidenced further below by the absorption spectra). Importantly, the solubility of P3HT in the solvent mixtures at room temperature remains sufficiently high to ensure that the solution remains visibly clear, without any noticeable changes in the absorption spectra over a period of 24 h. This is necessary to ensure the absorption spectra are not altered due to the effects of light scattering or changes of concentration due to a fall-out of

TABLE 2 Poly(3-hexylthiophene) Fractionated from a Broad Molecular Mass Distribution Sample with Different Solvents

Poly(3-hexylthiophene) Fractionated With	M_n [Da]	M_w [Da]	PDI
Hexane	5,600	6,600	1.18
Dichloromethane	13,800	20,400	1.48
Chloroform	19,000	25,600	1.35

Molecular weights measured with GPC (M_n, number-average molecular weight; M_w, weight-average molecular weight; PDI = M_w/M_n, polydispersity index).

larger aggregates. Although the solutions do not change on the time scale of our experiments, they are not in thermal equilibrium, as detailed in the Supporting Information. This is in agreement with findings by Xu et al. on solvent-induced crystallization of related poly(thiophene)s using a mixture of chlorobenzene (solvent) and anisole (poor solvent).[19]

All solutions within one series had the same concentration. The defined compounds were studied at a concentration of 0.25 mg/mol, whereas the solutions of the extracted P3HT samples had a concentration of 0.10 mg/mol. For each molecular weight of the defined compounds, additional absorption measurements have also been carried out on a few samples at a concentration of 0.10 mg/mol. This control experiment confirmed that the slight difference in concentration between the two series does not have any significant effect. In order to keep the concentrations within each series constant, every single solution within each solution series was prepared separately in new and isopropanol-rinsed dark sample glasses. Thereby, the P3HT was first completely dissolved in $CHCl_3$ before the fraction of EtAc, the poor solvent, was added. The absorption of the solutions was measured in 1 mm-quartz cuvettes with a Varian Carry UV/Vis spectrometer in a standard double-beam transmission alignment. The absorption of thin films was measured with the same Varian Carry UV/Vis spectrometer by means of the diffuse reflectance accessory (integrating sphere). P3HT films were spin coated from solution with a concentration of 15 mg/mL at a constant speed of 1500 rpm on Spectrosil B, a silica glass substrate. Prior to spin coating, the substrate was cleaned with common solvents such as acetone and isopropanol.

Organic field effect transistors were prepared in a bottom-gate, top-source/drain geometry under nitrogen atmosphere from solutions with a concentration of 10 mg/mL. The substrates were n-doped silicon plates with a grown layer of insulating silicon dioxide of ~300 nm thickness. Substrates were silanized using hexamethyldisilazane (HDMS) vapor for 1 h at 90 °C and 3 h at 60 °C. Prior to silanization, the substrate surface was cleaned thoroughly with several common solvents and treated with oxygen plasma for 5 min at a power of 200 W. Thereafter, the substrates were annealed under nitrogen atmosphere at 130 °C for 1 h and cooled down slowly to room temperature. After spin coating, 100-nm-thick gold electrodes were evaporated on top of the P3HT layer. The resulting field effect transistors had a channel width $W = 14.85$ cm, a channel length $L = 100$ μm, and a capacitance of the insulating layer per unit area $C_i = 11.9$ nF/cm^2. The charge carrier mobilities were determined from a plot of the square root of the drain current in the saturation regime using

$$I_{DS,sat} = \frac{WC_i}{2L}\mu_{sat}(V_G - V_T)^2,$$

with V_T being the threshold voltage.

RESULTS

Figure 1 shows the absorption of rrP3HT in solutions of constant concentration. The solvent was a mixture of chloroform and ethyl acetate with increasing ratios of ethyl acetate. The latter is a moderately poor solvent for P3HT and is thus used to induce planarization/aggregation. Measurements were done for samples of three different molecular weights and made by two different synthetic approaches: rrP3HTs directly synthesized to get a specific molecular weight (5, 11, and 19 kDa) and rrP3HT extracted from a large molecular mass distribution to get different molecular weight fractions (6, 14, and 19 kDa).

For both, defined and extracted P3HT samples, we observe two absorption features, an unstructured peak centered around 2.80 eV and a band with structure at lower energy (three peaks at about 2.05, 2.20, and 2.40 eV). The low-energy band increases in intensity with increasing fraction of poor solvent. Simultaneously, the ratio of the 0-0 vibrational peak at 2.05 eV to the 0-1 vibrational peak at 2.20 eV changes. With increasing molecular weight, the contribution of the low energy band to the overall spectrum increases. Furthermore, the high-energy band shifts slightly from 2.85 to 2.75 eV when going from 5/6 kDa to higher molecular weights. In contrast to the defined P3HT, the absorption of the high-energy band of the extracted P3HT with 6 kDa shifts to lower energies (2.80 eV) with increasing fraction of poor solvent before the low-energy band appears. The high-energy band has been identified as arising from coiled chains that form amorphous regions. The structured low-energy band is associated with absorption from planar chains that form weakly interacting H-aggregates.[6,9]

Although these spectra contain absorption due to both, aggregated and coiled chains, it is possible to extract the absorption spectra of the aggregated chains. As detailed in the Supporting Information, this is obtained by taking the spectra obtained in 100% chloroform solution (where the chains are fully dissolved and coiled), scaling it to the high-energy shoulder of the solution spectra (containing the absorption of aggregated and coiled chains), and subtracting it. We have also deduced the relative oscillator strength that describes the change in oscillator strength when going from a nonplanar chain as present in solution to a planar polymer chain in the aggregate, using the approach by Clark et al.[20] This procedure is described further in the Supporting Information.

When the change in oscillator strength is known, the fraction of aggregated chains in the solution (as a total of the overall number of chains) can be derived from the fraction of absorption due to aggregated chains. This is shown in Figure 2. We observe that for the defined P3HT sample with 5 kDa aggregation starts at 50% of poor solvent and increases linearly with decreasing solvent quality up to a fraction of 35% of aggregates. The difference to the extracted sample with comparable molecular weight is considerable. The latter does not aggregate below 70% of poor solvent and reaches only a fraction of 10% of aggregates at 90% of ethyl acetate. For the samples with 11 and 14 kDa, respectively, the aggregation starts much earlier. The defined sample shows aggregation at 15% of poor solvent and higher. Its fraction of

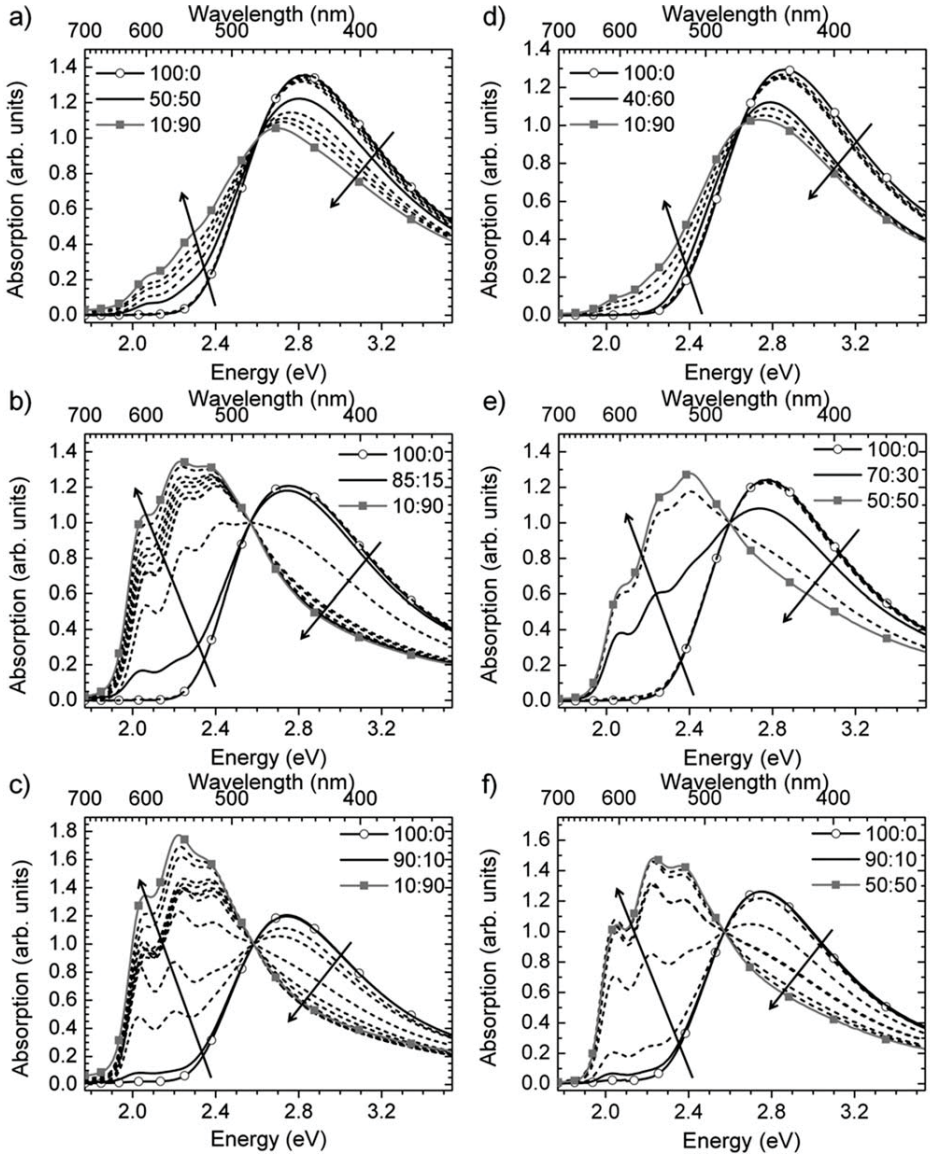

FIGURE 1 Absorption spectra of solutions with ratios of good:poor solvent ($CHCl_3$:EtAc). Dashed lines show increments of about 10% of poor solvent. Solutions with maximum and minimum fraction of good solvent used are indicated as lines with open and solid symbols, respectively. The black solid line highlights the solvent fraction at which the onset of aggregation takes place. Adjacent graphs show samples of comparable molecular weight. Left column: Defined P3HTs with molecular weight (a) 5 kDa, (b) 11 kDa, (c) 19 kDa. Right column: Extracted P3HTs with molecular weight (d) 6 kDa, (e) 14 kDa, (f) 19 kDa.

aggregates increases steeply and reaches a saturation value of about 55%, whereas the extracted sample with 14 kDa starts to aggregate at 20% of poor solvent and shows fraction of aggregates below the defined sample. For the 19 kDa samples from the defined and extracted synthetic approaches, aggregation starts at 10% of poor solvent and reaches as well a maximum value of about 50%. No difference in aggregate fraction between the defined and extracted P3HT with 19 kDa can be seen. The interesting feature to note is that for none of the samples the fraction of aggregated chains exceeds 55%, even when 90% ethyl acetate is used. In other words, a substantial part of the chains remains dissolved. A 100% ethyl acetate solution becomes turbid, indicating the formation of larger agglomerated structures. The earlier onset of aggregation for P3HT with higher molecular weight, that is, longer chains, is consistent with Flory-Huggins theory that predicts less solubility for longer polymer chains.[21]

From Figure 2, it is evident that a substantial fraction of the chains forms aggregates in solution. It is known that such aggregates that are present in solution can later serve as nucleation points for aggregate formation in the film when prepared by spin-coating.[13] To get a more thorough understanding on the nature of these aggregates, we now consider the spectral shape of the aggregate absorption. The aggregate absorption (derived as outlined in the Supporting

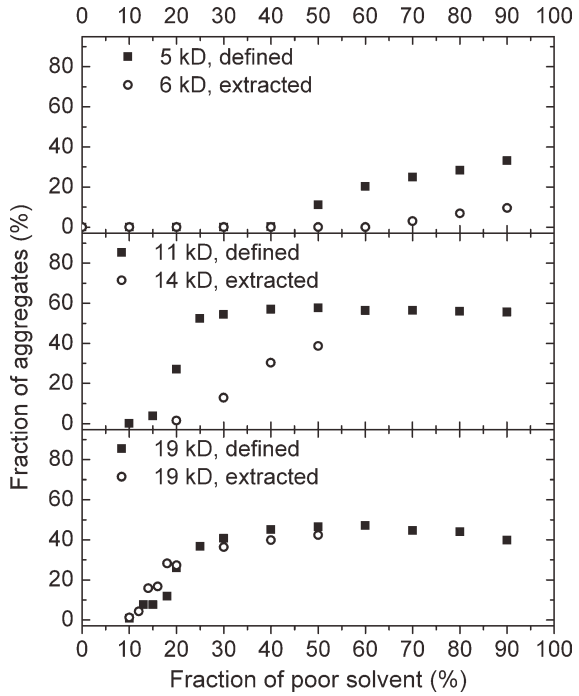

FIGURE 2 The fraction of aggregates present in solution as a function of poor solvent fraction for defined and extracted P3HT. The molecular weight increases from top to bottom.

Information), normalized to 0-1 peak, is shown in Figure 3 for the defined P3HT samples. Very similar spectra can be obtained for the extracted samples. From Figure 3, we see, first, that the relative height of the 0-0 absorption peak increases with molecular weight. Second, the ratio of the 0-0 to 0-1 absorption peak changes significantly with solvent quality. For the 5 kDa sample the 0-0 intensity increases with increasing fraction of poor solvent. For the 11 and 19 kDa samples, the 0-0 intensity first increases and then decreases with increasing fraction of ethyl acetate. The absorption spectra of the weakly interacting H-aggregates can be analyzed in a framework for excitonic coupling in weakly interacting H-aggregates that has been developed by Spano.[9,22] According to this model, the relative height of the 0-0 peak is a measure for the degree of excitonic coupling present in the aggregate. The very high 0-0 peak (0-0/0-1 ratios larger than unity) observed for the 19 kDa sample at 90:10 EtAc:$CHCl_3$ mixtures (line with open symbols in Fig. 3) thus implies excitonic coupling is largely absent, even though the chain must adopt conformations that are already partially planarized as evidenced by the low energy of the 0-0 peak. In contrast, excitonic coupling is particularly strong for the 50:50 mixture (black line) and then reduces somewhat when adding more ethyl acetate. Quantitatively, the 0-0/0-1 absorption peak ratio relates to the excitonic coupling J as follows

$$\frac{A_{0-0}}{A_{0-1}} = \frac{n_{0-0}}{n_{0-1}} \frac{\left(1 - \frac{J}{\omega_0} e^{-S} \sum_{v>0} \frac{S^v}{v!v}\right)^2}{S\left(1 - \frac{J}{\omega_0} e^{-S} \sum_{v\neq 1} \frac{S^v}{v!(v-1)}\right)^2},$$

where S is the Huang Rhys parameter of the single emitter and ω_0 is its effective vibrational energy, $n_{0\text{-}0}$ and $n_{0\text{-}1}$ refer to the refractive index at the position of $A_{0\text{-}0}$ and $A_{0\text{-}1}$. To allow for an exact analysis, we have taken photoluminescence spectra and applied a Franck-Condon analysis in order to derive S and ω_0. Through this analysis, we found S to be 0.90 (5 kDa sample) and 0.84 (11 and 19 kDa samples) and ω_0 to be 1390 cm^{-1}. Full details of the Franck-Condon analysis are given as Supporting Information.

Using this approach, we obtained the excitonic couplings shown in Figure 4. We first consider the defined P3HT samples. For all compounds, we observe an initial rise of the excitonic coupling up to a peak followed by a decrease. For the 5 kDa sample, the rise is not visible, only the decrease. For the extracted P3HT samples with 6 and 14 kDa, the excitonic coupling is slightly higher than for the comparable defined samples, whereas the defined and extracted samples with 19 kDa show no significant difference in excitonic coupling. The excitonic coupling within the P3HT aggregates depends clearly on the fraction of the poor solvent and thus

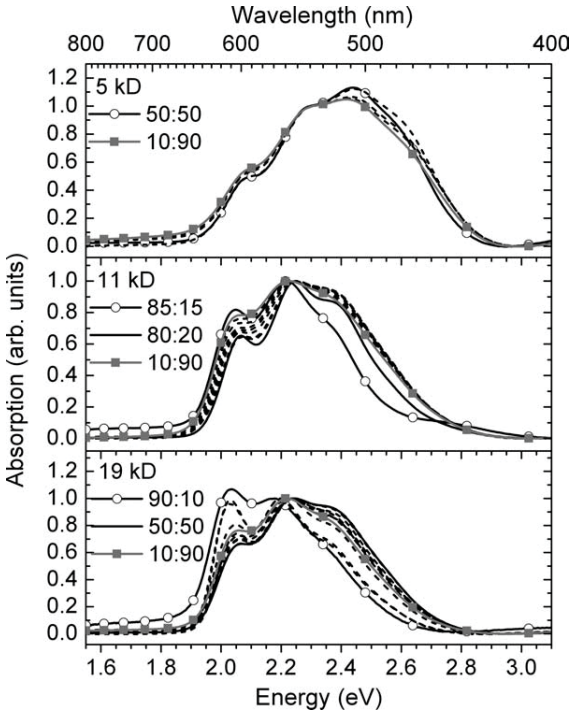

FIGURE 3 The absorption spectra of aggregates in solutions of defined P3HT. The spectra are normalized to the second absorption peak and presented for different fractions of poor solvent. The given ratios denote the volume fractions of good: poor solvent ($CHCl_3$:EtAc). The dashed lines show increments of about 10% of poor solvent. Lines with open and solid symbols indicate samples with the minimum and maximum amount of poor solvent used. With increasing fraction of poor solvent, the relative intensity of the second absorption peak decreases up to the fraction indicated by the black line. From then onwards, it increases again. The molecular weight increases from top to bottom.

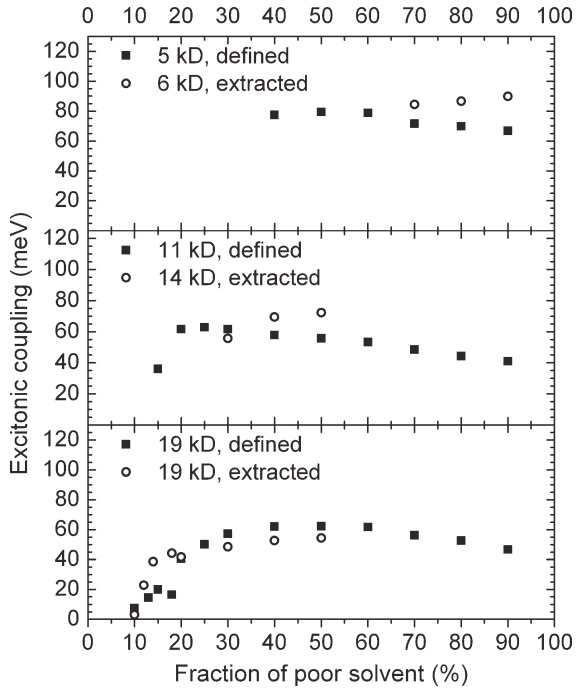

FIGURE 4 The excitonic coupling as function of poor solvent fraction for aggregates of defined and extracted P3HTs. The molecular weight increases from top to bottom. The excitonic coupling is calculated from the ratio of the first two absorption peaks according to Spano's model[9] for weakly interacting H-aggregates.

on solvent quality. We attribute this to a conjugation length dependence of the excitonic coupling. It is well-known that the strength of intermolecular coupling is related to the extent of the conjugated system. The breakdown of the point-dipole model for polymers is due to extended conjugations. Although for a point-dipole, the coupling between chains increases with conjugation length, this is not the case for very extended π-systems. Thus, a longer conjugation length implies a lower excitonic coupling and vice versa.[10]

By means of the theoretical work of Gierschner et al. who calculated the excitonic coupling in thiophene-based conjugated polymers as a function of repeating units, we derive the conjugation lengths within the aggregates of the defined and extracted P3HT as a function of poor solvent fraction.[11] The excitonic coupling in regioregular P3HT is lower than the coupling in polythiophene without any side chains calculated by Gierschner et al. This leads to an overestimation of the conjugation length in rrP3HT, which was corrected by a factor of 0.8. This factor takes into account that the conjugation length of the 5 kDa sample cannot exceed the degree of polymerization of the polymer chains known from MALDI-TOF MS. Figure 5(a) shows the resulting conjugation length as a function of poor solvent for defined and extracted P3HT samples. In addition, the corresponding position of the 0-0 absorption peak, taken from Figure 3, as well as the ratio of the first two absorption peaks is presented in Figure 5(b).

We find that the 5/6 kDa samples have more or less constant conjugation lengths with increasing fraction of poor solvent, and that the extracted sample shows a shorter conjugation length than the defined P3HT sample. The defined samples with 11 and 19 kDa show a minimum conjugation length at 25 and 50% of poor solvent, respectively, followed by a steady increase of conjugation length with decreasing solvent quality. Although the extracted sample with 19 kDa shows a similar behavior to the 19 kDa defined sample, the conjugation lengths of the 14 kDa extracted sample has again a shorter conjugation length than the 11 kDa defined sample. To assess the correlation to the degree of polymerization (DP), relative DP values were calculated from MALDI-TOF molecular weights. We like to point out that the 5/6 kDa samples show conjugation lengths in the region of their degree of polymerization, whereas the samples with higher molecular weight form aggregates whose conjugation length is much lower than their degree of polymerization in the saturation region of the fraction of aggregates. Moreover, the positions of the 0-0 absorption peaks correlate nicely with the conjugation lengths calculated from the excitonic coupling, given by the ratio of the 0-0/0-1 absorption peak intensity, that is, the position of the first absorption peak shifts to maximum energy for solutions where the conjugation length calculated from the vibrational intensities is at a minimum. We note that these are two independently derived quantities.

From our investigations we know the fraction of aggregates (Fig. 2), their conjugation length (Fig. 5) and the degree of polymerization. Thus it is possible to infer information about the conformation of the aggregates. Our conclusions about the resulting conformations of the defined P3HT samples are summarized in Figure 6.

For the 5 kDa sample, we consider the polymer chains within the aggregates to be completely planarized and conjugated. The aggregates coexist with still dissolved chains in the solution even when 90% of poor solvent is used. This picture is based on the fact that the conjugation length derived from the spectral analysis corresponds to the degree of polymerization obtained by the MALDI-TOF MS. Additionally, it is supported by a moderate fraction of aggregates which does not saturate for high amount of poor solvent. The still dissolved chains are likely to be the shorter ones in the overall distribution.

For the 11 and 19 kDa samples, there are some key features to be noticed. In all cases the length of the conjugated segments is shorter than the total degree of polymerization [see Fig. 5(a)]. Thus, in principle, a polymer chain may comprise of one planarized segments and additional coiled segments or several planarized segments which are separated. This separation may be caused by coiled segments or simply by twists, kinks or folds.

Keeping this in mind, we now consider the 11 kDa sample for 25% of poor solvent and more. At 25% of poor solvent, the conjugation length for each conjugated segment is about 22 repeating units which correspond to 50% of the degree

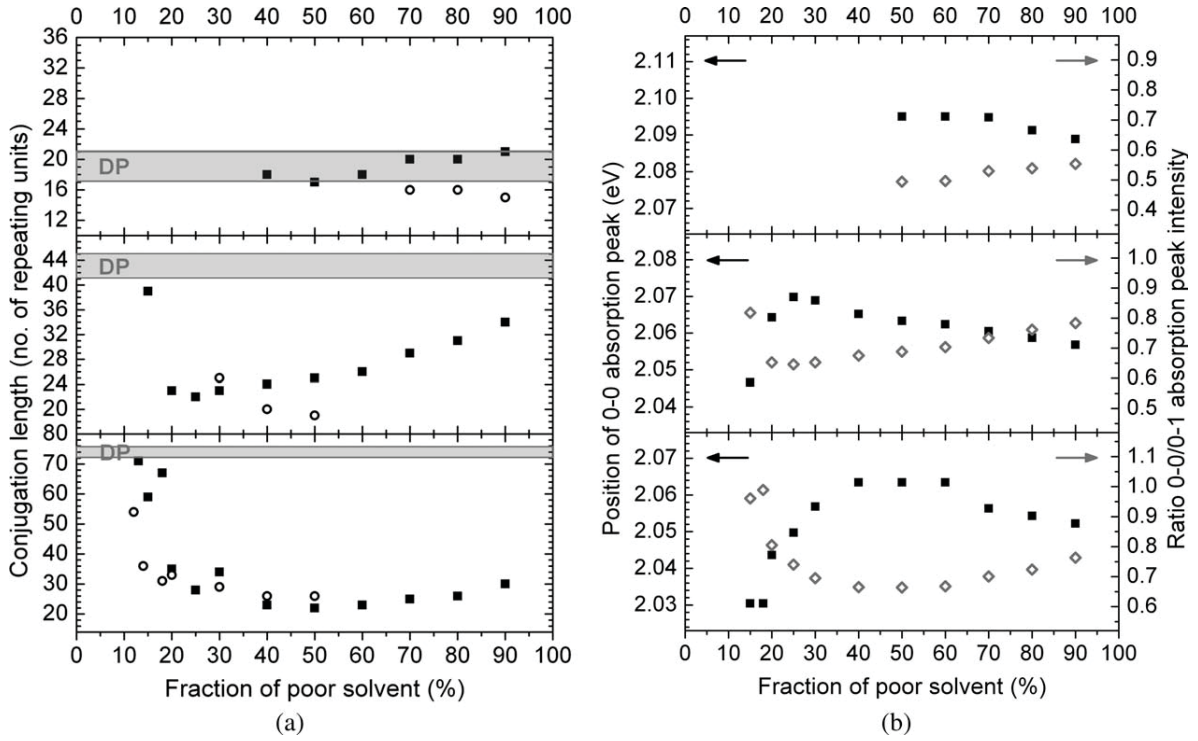

FIGURE 5 (a) The conjugation length derived from the excitonic coupling for chains of defined (solid squares) and extracted (open circles) P3HT, given as the number of thiophene repeating units. The grey bar indicates the degree of polymerization, determined from MALID-TOF with an error of ±2 repeat units, for reference. The molecular weight increases from top to bottom showing the pairs of 5/0.6 kDa, 11/14 kDa, and 19/19 kDa. (b) The position of the 0-0 absorption peak (solid symbols) and the ratio of the first to absorption peaks (open symbols) as a function of poor solvent fraction for the extracted P3HT samples with $M_n = 5$ kDa (top), 11 kDa (center), and 19 kDa (bottom).

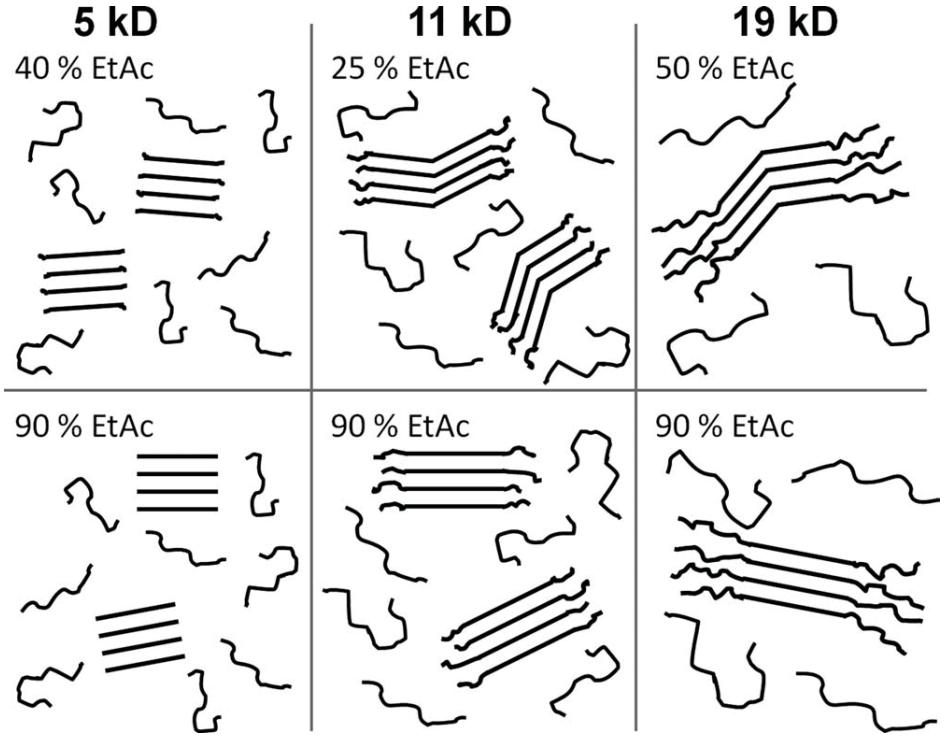

FIGURE 6 Possible scenarios for the packing behavior of defined P3HT chains for different molecular weights and different fractions of poor solvent.

TABLE 3 Excitonic Coupling for Films of Defined and Extracted P3HT Spun from Solutions with Different Ratios of Good: Poor Solvent ($CHCl_3$: EtAc)

	M_n [Da]	$CHCl_3$: EtAc	Excitonic Coupling (meV)
Defined P3HT	5,100	100:0	70
		80:20	70
	11,300	100:0	55
		85:15	45
	18,600	100:0	35
		85:15	55
Extracted P3HT	5,600	100:0	60
		80:20	70
	13,800	100:0	40
		80:20	45
	19,000	100:0	55
		80:20	35

The excitonic couplings were determined by means of the model by Spano for weakly interacting H-aggregates.

of polymerization. In principle, this still allows one or two conjugated segments in one polymer chain. When increasing the fraction of poor solvent, the conjugation length enlarges up to 34 repeating units being 80% of the DP. This implies that for higher amounts of poor solvents there is only one conjugated segment for each chain within the aggregates. On the other hand, the fraction of aggregates does not enlarge equally with the conjugation length but remains constant at (55 ± 5)%.

We now consider two scenarios.

1. If we assume that, at 25% of poor solvent, there is only one planarized segment per chain then 50% of each chain within the aggregates is still dissolved. Overall, the solution consists of (55% ± 5%) aggregated segments with the remainder being dissolved segments. In this scenario, the dissolved segments are then formed by half of each chain within the aggregates and some additional fully dissolved chains. Let us now consider a fraction of 90% of poor solvent in this scenario. At 90% of poor solvent, 80% of each chain within the aggregates is conjugated. Thus, only 20% of each chain within the aggregates can contribute to the fraction of dissolved segments in the solution. Compared to the situation with 25% of poor solvent, the overall fraction of aggregated segments in solution, and thus also of dissolved segments in solution, has not changed. As only 20% of each chain within the aggregates are dissolved, there must be more fully dissolved chains in the solution to make up the same total fraction of dissolved segments in solution than at 20% of poor solvent. An increase in the number of fully dissolved chains with increasing fraction of poor solvent, however, seems unlikely. Let us now turn to the second possible case.
2. Consider there are two planarized segments at 25% of poor solvent. By the same reasoning we find that much more fully dissolved chains are present at 25% than at 90% of poor solvent. This seems more realistic.

Therefore, by comparing the degree of polymerization, the conjugation length and the fraction of aggregated segments present in solutions made with different fractions of poor solvent, we infer that the 11 kDa sample adopts a conformation comprising predominantly two planarized segments at low fraction of poor solvent and one planarized segment at high fraction of poor solvent.

Very similar considerations are valid for the 19 kDa sample, for which a conjugation length of 22 repeat units (as found for 50% ethyl acetate) allows for two or three planarized segments. For 90% ethyl acetate, where the conjugation length is 30 repeating units, there can be only one or two planarized segments.

In addition to studying P3HT solutions, we want to know whether the results obtained for P3HT aggregates in solution can be transferred to P3HT films that were spun from solution already containing aggregates due to poor solvent fractions. Therefore, we measured the absorption of the P3HT thin films (see Supporting Information). The same quantitative analysis of the ratio of the first two absorption peaks as for the absorption spectra of the P3HT solutions leads to the excitonic coupling within the aggregates according to the work of Spano. These excitonic couplings for the film aggregates are listed in Table 3. We see that the aggregates of the defined P3HT in the film show very similar excitonic couplings as the aggregates found in solution for maximum aggregation (see Fig. 4). Therefore, we consider the aggregates in the defined P3HT films to be of the same nature as the aggregates in solution near maximum aggregation, or to be the same aggregates grown from aggregates in solution acting as nucleation points. Thus, we can control the

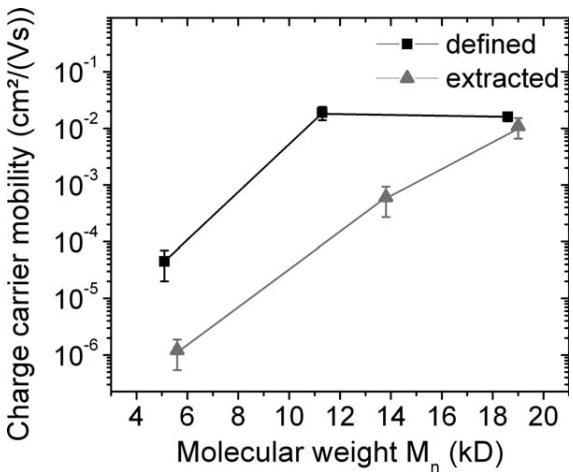

FIGURE 7 Charge carrier mobilities of defined and extracted P3HT samples as a function of molecular weight M_n. Films were spun from 100% chloroform solutions.

formation of aggregates in the film via a control of solvent quality. This is true only for the defined P3HT samples.

As this control only applies for defined P3HT samples, we studied whether this advantage can be transferred also to charge carrier mobilities within the films. For this reason, we measured P3HT thin film transistors prepared from 100% chloroform solutions simply by spin coating without any post-treatment of the devices such as annealing. The resulting saturation mobilities are shown in Figure 7 as a function of molecular weight. Both, the extracted and the defined samples, show increasing charge carrier mobilities with increasing molecular weight. This effect is well-known and was expected. Furthermore, the defined samples with lower molecular weight (5 and 11 kDa) reach significantly higher charge carrier mobilities than their comparable extracted samples. However, already for the samples with 19 kDa, this difference in charge carrier mobility vanishes. Both samples, defined and extracted, reach charge carrier mobilities of 10^{-2} cm/Vs.

DISCUSSION

The Formation of P3HT Aggregates in Solution

P3HT is well-known to exist in two distinct conformations, that is a random coil conformation leading to an amorphous film, and a planarized conformation giving rise to aggregates and films with corresponding crystalline inclusions. There have been various approaches to force poly(3-hexylthiophene) chains to aggregate. Several preparation parameters affect the solubility of polymer chains and thus the formation of aggregates, such as temperature, concentration or quality of the solvent used.[23–25] Clark et al. used solutions with high concentrations of P3HT whose temperature dependent solubility lead to polymer aggregates at sufficiently low temperatures.[6,20] A similar approach to induce aggregates in P3HT solutions was chosen by Liu et al. who investigated the crystallization behavior of P3HT in respect to crystallization temperature, polymer concentration and molecular weight of the samples.[26] Likewise, Berson et al. and Oosterbaan et al. used highly concentrated and initially heated solutions of P3HT to induce P3HT nanofibers in the chilled solution and thus controlled the organization of the polymer chains.[27,28] In contrast to that, Zhao et al. used ultrasonic oscillation to promote the formation of P3HT aggregates.[29] Treatments such as thermal annealing, solvent vapor annealing, or the usage of high boiling point solvents enhance the order of the polymer chains within the aggregates.[28] The approach by Park et al. refrained from any additional treatments. Park et al.[30] made thin-film transistors from solutions containing small amounts of a nonsolvent with poly(3-hexylthiophene)s of molecular weights in the range of $M_n = 35–45$ kg/mol.

In our studies, we aimed at inducing aggregates in P3HT of molecular weights in the range of $M_n = 5–19$ kg/mol in solution by varying the quality of the solvent. We studied the effect of different fractions of poor solvent, from 0 to 90%, within the P3HT solutions with respect to molecular weight dependence and the influence of the synthetic approach. The induced aggregates in solution were analyzed carefully to obtain the fraction of polymer chains, which were aggregated due to low solvent quality. To relate the fraction of aggregate absorption to the actual fraction of aggregates, the relative oscillator strength was introduced that describes the relative increase in oscillator strength comparing a coiled P3HT chain with a planarized chain in an aggregate. This method was presented by Clark et al. in Ref. 31, where a relative oscillator strength of 1.39 ± 0.10 was obtained for solutions going from 70 °C to room temperature. In our investigations, we found a dependence of the relative oscillator strength on the fraction of poor solvent. To be precise, our investigations showed a minimum value for the relative oscillator strength in solutions with 30–50% of poor solvent. For higher amounts of poor solvent the oscillator strength increases slightly. This is direct evidence for an increase of conjugation length within the aggregates since oscillator strength is proportional to the squared transition dipole moment which increases linear with the dipole length.[32]

As for the fraction of aggregates, we showed that there is a limit to the maximum fraction of the polymer chains that can be forced to planarize and aggregate, even if 90% of poor solvent is used. This maximum fraction is about 50–60% for the 11 and 19 kDa samples. This is in the order of the fraction of aggregated chains in solution induced by cooling published by Clark et al. being $39\% \pm 10\%$.[20] Obviously, there must be thermodynamic reasons that prevent the formation of entirely crystalline aggregates that would then precipitate from solution. One such factor may relate to the entropy of the system. For synthetic reasons, the connection between the first and the second 3-alkyl thiophenes unit is not head-to-tail, but instead it is head-to-head, inducing some disorder in each single chain.

As for the defined 5 kDa sample, the onset of aggregation was lowered compared to the extracted 6 kDa sample that did not show any aggregation below 70% of poor solvent. The defined 5 kDa sample starts to aggregate already at 50% of poor solvent. Equally, the onset of aggregation is at higher fraction of poor solvent for the extracted 14 kDa sample compared to the corresponding defined sample. Since the extracted sample was fractionized out of a very broad molecular mass distribution, the extracted sample consists of just those shorter chains that stopped growing during synthesis. It has been reported that this can result in lower regioregularity and thus in a relatively strong steric hindrance within the material.[18] Moreover, the extracted samples usually have a broader polydispersity. The late onset of aggregation for extracted P3HT compounds with molecular weight below 19 kDa is thus comparable with the effect of a lower order on the packing of polymer chains. The higher the disorder, the lower is the crystallinity and the less ordered is the packing of the P3HT chains.[33,34] No effect of synthetic approach on aggregation onset as well as on aggregate fraction can be seen for the 19 kDa sample, because all chains with a smaller molecular weight are extracted out.

The Conjugation-Length Dependence of Excitonic Coupling

Considering the nature of the aggregates induced in solution, we showed that the excitonic coupling within the aggregates

is a function of solvent quality. We interpret this dependency as a conjugation length-dependent dipole coupling as investigated theoretically by Gierschner et al.[11] Indeed, the excitonic coupling of the aggregates in solution as a function of solvent quality show a maximum value for the defined 11 and 19 kDa samples that correlates with a minimum in the conjugation length of the P3HT chains within the aggregates as evidenced through the minimum in the relative oscillator strength. In addition, the positions of the 0-0 absorption peaks in the isolated aggregate absorption spectra shift as a function of solvent quality, in agreement with the calculated conjugation lengths for these aggregates, giving direct experimental confirmation for the conjugation-length dependence of the excitonic coupling predicted theoretically (Fig. 5). This is indeed remarkable. For Förster-type energy transfer, the dependence of the dipole-coupling mechanism on the extent of the conjugated system is well documented through measurements of energy transfer rates.[35,36] In contrast, experimental evidence for the manifestation of this effect in the case of excitonic coupling in aggregates is found only rarely.

In addition, we demonstrate that the excitonic coupling and accordingly the conjugation length depends on molecular weight and synthetic approach. We show that the defined synthetic approach results in higher conjugation lengths for P3HT compounds of molecular weights below 19 kDa compared with extracted compounds, whereas for higher molecular weights, the synthetic approach is not relevant if low molecular weight fractions are extracted out. Although the effect of synthetic approach has not been studied yet, other effects, for example, the temperature dependence of the excitonic coupling in P3HT films were described in the literature. It is well known that temperature affects the conformation of P3HT chains. Pingel et al. showed that aggregates in P3dHT films have temperature dependent excitonic couplings.[37] Furthermore, Clark et al. published a study on the effect of the boiling point of the solvent, which affects the rate with which the film dries after spinning from solution.[20] Basically, the higher the solvent boiling point the lower is the resulting excitonic coupling and the higher is the obtained fraction of aggregates. This is in accordance with AFM results from Chang et al. who presented long P3HT ribbons in films spun from a high boiling point solvent.[1] In contrast to these studies, we did not post-treat our samples to enhance the change in excitonic coupling and conjugation length. The resulting change in excitonic coupling in our study is merely due to thermodynamic effects that force the polymer chains to minimize their interaction with the surrounding solvent molecules and thus start aggregation with decreasing solvent quality.[38]

The Packing Behavior of P3HT Aggregates in Solutions and Thin Films

Combining the calculated conjugation length with the corresponding fraction of aggregates, we obtain a model for the packing behavior of the polymer chains in solution. We have found that the organization of P3HT chains depends not only on molecular weight but also on solvent quality. In particular, there is a solvent-dependent change in packing. Higher fractions of poor solvent lead to planarization of the aggregated middle sections of the polymer chains. For example, we conclude that the 5 kDa sample packs as nonfolded chains. In contrast, the 11 and 19 kDa sample form aggregates with kinks or even folded chains at lower fractions of poor solvent, while they form nonfolded chains at high fractions of poor solvent. This scenario is consistent with current understanding of the polymer crystallization process.[25]

This result further agrees with observations made by Liu et al. on the packing behavior of P3HT within nanofibers.[26] By means of high-resolution transition electron microscopy, they obtained information on the width of nanoribbons. In combination with the contour length of the P3HT chains, this allows concluding on the packing behavior of the chains contained. Liu et al. showed for nanoribbons made of P3HT with $M_n = 9.3$ and 19.9 kDa (M_n-values corrected for GPC overestimation) that the low molecular weight sample packs indeed as nonfolded chains while chains in the high molecular weight sample have to be folded.[26] This is also consistent with studies of Wu et al. on a series of P3HT with molecular weights of 5–19 kDa.[39]

We also note that according to our results, the aggregates of the 5 kDa compounds consist of completely planar chains implying that their conjugation length is equivalent to the full contour length of 7.5 nm. A comparable low molecular weight sample with $M_n = 5.7$ kDa was recently studied by Brinkmann and Rannou. They reported on the packing behavior and the semicrystalline structures in P3HT and showed that the low molecular weight sample packs in crystalline lamellar of 7–8 nm width.[40] This value confirms the conjugation length we obtained for the 5 kDa sample. Thus, although our conclusions concerning the packing behavior of P3HT chains were based merely on spectroscopic studies, they are confirmed by the results on P3HT morphology from other groups.

For defined P3HT samples, we were able to transfer the aggregate interaction (excitonic coupling and conjugation length) obtained in solution into the thin film structure prepared by spin-coating. For example, in solution, the fraction of poor solvent controls the intermolecular coupling within the aggregates. For defined P3HT samples, we have found equal excitonic couplings in both, thin film aggregates and aggregates in solution. Thus, the aggregates induced in solution by changing the solvent quality are either the same aggregates found in the resulting film after spin-coating or they act at least as starting points for nucleation and growth. Therefore, a control over the excitonic coupling and conjugation length within aggregates in the resulting films is given by the control of the solvent quality.

Considering the charge carrier mobility in P3HT thin films, it is well known that the presence of aggregates or crystalline regions controls the mobility. Several aspects of this have been studied, among them the effect of crystallinity,[39,41] the effect of the boiling point of the solvent,[42,43] the effect of film thickness,[44] the effect of the concentration of the solution[30] and the effect of the organization of the P3HT chains

in the film.[27] Our investigations concerning the charge carrier mobility in P3HT thin films focus on changes due to different molecular weights and different synthetic approaches. In addition to the well-known molecular weight dependence of charge carrier mobility, we observe a direct correlation between the fraction of aggregates in solution (Fig. 2) and the resulting thin film mobility (Fig. 7). For the defined and extracted 19 kDa samples, the onset of aggregation in solution occurs early (at 10% poor solvent), and in both cases similarly high fraction of aggregates up to 50% are obtained. The same is true for the defined 11 kDa sample, where aggregates can take up even 60% in solution. For these three samples, the same charge carrier mobilities exceeding 10^{-2} cm^2/Vs are obtained. For the extracted 14 kDa sample, aggregation in solution takes place less easily, as evidenced by the higher fraction of poor solvent required and by the lower fractions of aggregates obtained. Concomitantly, the charge mobility is more than an order of magnitude lower than for the corresponding 11 kDa defined sample. Aggregation is even more difficult for the 5 kDa defined sample, translating equally in a reduced mobility until finally for the 6 kDa extracted sample there is hardly any aggregation present in solution, and concomitantly the charge carrier mobility ranges at 10^{-6} cm^2/Vs. These changes in FET mobility cannot be attributed to differences in the excitonic coupling within the aggregates. Experimentally, comparison with Figure 4 shows that the changes in excitonic coupling with molecular weight and synthetic approach are less drastic. Furthermore, there is no a priori reason why a dipole-interaction based excitonic coupling should necessarily correlate with an exchange-interaction based charge transfer mechanism.

The observed correlation between the fraction of aggregates in solution and the thin film mobility may assist towards understanding the widely observed increase of charge carrier mobility with molecular weight.[2,4] The reasons for the increase of mobility with molecular weight are still discussed. Zen et al. suggest that the increasing fraction of crystalline domains with increasing molecular weight controls the charge carrier mobility.[41] In contrast, Brinkmann and Rannou suggest that an increasing fraction of bridging chains with increasing molecular weight increases the probability of charge transport through the less conductive amorphous domains of the film.[45] Both approaches are based on the idea that the charge transport through the film is limited by amorphous domains. Recently, Lan and Huang published a theoretical study that implies that charge carrier mobilities below 10^{-2} cm^2/Vs are controlled by the number of crossing points between the crystalline domains, whereas mobilities above this value correspond to present bridging chains between the ordered domains.[46]

The correlation we found between the fraction of aggregates in solution and the resulting thin film charge carrier mobility supports the arguments by Zen et al, at least for the range of molecular weights considered here. We observe the same high mobility for samples with very different molecular weight, that is, 11 kDa and with 19 kDa, yet with the same propensity to aggregation.[41] While the degree of aggregation in solution clearly does not need to translate into an equal aggregation in the film, it can serve as an indication of the propensity of the sample towards aggregation. The 11 and 19 kDa chains have about 44 and 74 repeat units, respectively. When forming aggregates in solution at a medium fraction of poor solvent (i.e., a moderate driving force towards aggregation), both have a conjugation length of about 22 repeat units, implying one or at most two kinks in the chain. Thus, or a chain as short as 11 kDa, bridging chains between different crystallites are hard to imagine. Moreover, one would expect more bridging chains for the 19 kDa chain. As both samples show the same mobility this implies that either there are no bridging chains, or they do not contribute to the overall chain mobility. This argument is further strengthened by the fact that the mobility of 10^{-2} cm^2/Vs we obtain for the defined 11 kDa sample is the same mobility that is obtained by Kline et al.[2] for 40 kDa samples, where bridging chains would be conceivable.

The authors thank Patrick Pingel and Rene Kalbitz for the FET measurements. Funding by the Graduiertenkolleg 1640 and SPP 1635 of the Deutsche Forschungsgemeinschaft is gratefully acknowledged. RHL thanks the Elite Netzwerk Bayern for a stipend according the Bayrisches Eliteförderungsgesetz.

REFERENCES AND NOTES

1 Chang, J. F.; Sun, B. Q.; Breiby, D. W.; Nielsen, M. M.; Solling, T. I.; Giles, M.; McCulloch, I.; Sirringhaus, H. *Chem. Mater.* **2004,** *16*, 4772–4776.

2 Kline, R. J.; McGehee, M. D.; Kadnikova, E. N.; Liu, J. S.; Frechet, J. M. *J. Adv. Mater.* **2003,** *15*, 1519–1522.

3 McCullough, R. D.; Tristramnagle, S.; Williams, S. P.; Lowe, R. D.; Jayaraman, M. *J. Am. Chem. Soc.* **1993,** *115*, 4910–4911.

4 Zen, A.; Pflaum, J.; Hirschmann, S.; Zhuang, W.; Jaiser, F.; Asawapirom, U.; Rabe, J. P.; Scherf, U.; Neher, D. *Adv. Funct. Mater.* **2004,** *14*, 757–764.

5 Chang, J. F.; Clark, J.; Zhao, N.; Sirringhaus, H.; Breiby, D. W.; Andreasen, J. W.; Nielsen, M. M.; Giles, M.; Heeney, M.; McCulloch, I. *Phys. Rev. B* **2006,** *74*, 115318.

6 Clark, J.; Silva, C.; Friend, R. H.; Spano, F. C. *Phys. Rev. Lett.* **2007,** *98*, 206406.

7 Reid, O. G.; Malik, J. A. N.; Latini, G.; Dayal, S.; Kopidakis, N.; Silva, C.; Stingelin, N.; Rumbles, G. *J. Polym. Sci. Part B: Polym. Phys.* **2012,** *50,* 27–37.

8 Herrmann, D.; Niesar, S.; Scharsich, C.; Köhler, A.; Stutzmann, M.; Riedle, E. *J. Am. Chem. Soc.* **2011,** *133,* 18220–18233.

9 Spano, F. C. *J. Chem. Phys.* **2005,** *122*, 234701.

10 Beljonne, D.; Cornil, J.; Silbey, R.; Millie, P.; Bredas, J. L. *J. Chem. Phys.* **2000,** *112*, 4749–4758.

11 Gierschner, J.; Huang, Y. S.; Van Averbeke, B.; Cornil, J.; Friend, R. H.; Beljonne, D. *J. Chem. Phys.* **2009,** *130*, 044105.

12 Pingel, P.; Zen, A.; Neher, D.; Lieberwirth, I.; Wegner, G.; Allard, S.; Scherf, U. *Appl. Phys. A: Mater. Sci. Process.* **2009,** *95*, 67–72.

13 Khan, A. L. T.; Banach, M. J.; Köhler, A. *Synth. Met.* **2003,** *139*, 905–907.

14 Sheina, E. E.; Liu, J. S.; Iovu, M. C.; Laird, D. W.; McCullough, R. D. *Macromolecules* **2004,** *37*, 3526–3528.

15 Lohwasser, R. H.; Thelakkat, M. *Macromolecules* **2011,** *44*, 3388–3397.

16 Conjugated Polymers: Theory, Synthesis, Properties, and Characterization; Skotheim, T. A.; Reynolds, J. R., Eds.; CRC Press, Taylor & Francis Group: Boca Raton, Florida, **2007.**

17 Loewe, R. S.; Khersonsky, S. M.; McCullough, R. D. *Adv. Mater.* **1999,** *11*, 250–253.

18 Trznadel, M.; Pron, A.; Zagorska, M.; Chrzaszcz, R.; Pielichowski, J. *Macromolecules* **1998,** *31*, 5051–5058.

19 Xu, W. T.; Li, L. G.; Tang, H. W.; Li, H.; Zhao, X. L.; Yang, X. N. *J. Phys. Chem. B* **2011,** *115*, 6412–6420.

20 Clark, J.; Chang, J. F.; Spano, F. C.; Friend, R. H.; Silva, C. *Appl. Phys. Lett.* **2009,** *94*, 163306.

21 Die Kunststoffe—Chemie, Physik, Technologie; Carlowitz B., Ed.; Carl Hanser Verlag: München, **1990.**

22 Brown, P. J.; Thomas, D. S.; Kohler, A.; Wilson, J. S.; Kim, J. S.; Ramsdale, C. M.; Sirringhaus, H.; Friend, R. H. *Phys. Rev. B* **2003,** *67*, 064203.

23 Polymer Crystallization: Observations, Concepts and Interpretations; Reiter G., S. J. -U., Ed.; Springer: Berlin, **2003.**

24 Progress in Understanding of Polymer Crystallization; Reiter G., S. G., Ed.; Springer: Berlin, **2007.**

25 Hu, W. B.; Frenkel, D. In Interphases and Mesophases in Polymer Crystallization III; Springer-Verlag Berlin: Berlin, **2005. pp 1–35.**

26 Liu, J. H.; Arif, M.; Zou, J. H.; Khondaker, S. I.; Zhai, L. *Macromolecules* **2009,** *42*, 9390–9393.

27 Berson, S.; De Bettignies, R.; Bailly, S.; Guillerez, S. *Adv. Funct. Mater.* **2007,** *17*, 1377–1384.

28 Oosterbaan, W. D.; Vrindts, V.; Berson, S.; Guillerez, S.; Douheret, O.; Ruttens, B.; D'Haen, J.; Adriaensens, P.; Manca, J.; Lutsen, L.; Vanderzande, D. *J. Mater. Chem.* **2009,** *19*, 5424–5435.

29 Zhao, K.; Xue, L. J.; Liu, J. G.; Gao, X.; Wu, S. P.; Han, Y. C.; Geng, Y. H. *Langmuir* **2010,** *26*, 471–477.

30 Park, Y. D.; Lee, H. S.; Choi, Y. J.; Kwak, D.; Cho, J. H.; Lee, S.; Cho, K. *Adv. Funct. Mater.* **2009,** *19*, 1200–1206.

31 Clark, J. EPAPS Document, EAPPLAB94058913 (= Supporting Information to Ref. 20).

32 Turro, N. J. Modern Molecular Photochemistry; University Science Books: Sausalito, California, **1991.**

33 Kim, Y.; Cook, S.; Tuladhar, S. M.; Choulis, S. A.; Nelson, J.; Durrant, J. R.; Bradley, D. D. C.; Giles, M.; McCulloch, I.; Ha, C. S.; Ree, M. *Nat. Mater.* **2006,** *5*, 197–203.

34 Sirringhaus, H.; Brown, P. J.; Friend, R. H.; Nielsen, M. M.; Bechgaard, K.; Langeveld-Voss, B. M. W.; Spiering, A. J. H.; Janssen, R. A. J.; Meijer, E. W.; Herwig, P.; de Leeuw, D. M. *Nature* **1999,** *401*, 685–688.

35 Beljonne, D.; Curutchet, C.; Scholes, G. D.; Silbey, R. J. *J. Phys. Chem. B* **2009,** *113*, 6583–6599.

36 Beljonne, D.; Pourtois, G.; Silva, C.; Hennebicq, E.; Herz, L. M.; Friend, R. H.; Scholes, G. D.; Setayesh, S.; Mullen, K.; Bredas, J. L. *Proc. Natl. Acad. Sci. USA* **2002,** *99*, 10982–10987.

37 Pingel, P.; Zen, A.; Abellon, R. D.; Grozema, F. C.; Siebbeles, L. D. A.; Neher, D. *Adv. Funct. Mater.* **2010,** *20*, 2286–2295.

38 Hamley, I. W. Introduction to Soft Matter; Polymers, Colloids, Amphiphilies and Liquid Crystals; Wiley: Chichester, **2006.**

39 Wu, Z. Y.; Petzold, A.; Henze, T.; Thurn-Albrecht, T.; Lohwasser, R. H.; Sommer, M.; Thelakkat, M. *Macromolecules* **2010***, 43*, 4646–4653.

40 Brinkmann, M.; Rannou, P. *Macromolecules* **2009,** *42*, 1125–1130.

41 Zen, A.; Saphiannikova, M.; Neher, D.; Grenzer, J.; Grigorian, S.; Pietsch, U.; Asawapirom, U.; Janietz, S.; Scherf, U.; Lieberwirth, I.; Wegner, G. *Macromolecules* **2006,** *39*, 2162–2171.

42 Cheng, H. L.; Lin, J. W.; Jang, M. F.; Wu, F. C.; Chou, W. Y.; Chang, M. H.; Chao, C. H. *Macromolecules* **2009,** *42*, 8251–8259.

43 Surin, M.; Leclere, P.; Lazzaroni, R.; Yuen, J. D.; Wang, G.; Moses, D.; Heeger, A. J.; Cho, S.; Lee, K. *J. Appl. Phys.* **2006,** *100*, 033712.

44 Joshi, S.; Grigorian, S.; Pietsch, U.; Pingel, P.; Zen, A.; Neher, D.; Scherf, U. *Macromolecules* **2008,** *41*, 6800–6808.

45 Brinkmann, M.; Rannou, P. *Adv. Funct. Mater.* **2007,** *17*, 101–108.

46 Lan, Y. K.; Huang, C. I. *J. Phys. Chem. B* **2009,** *113*, 14555–14564.

Supporting Information to:

On the Control of Aggregate Formation in Poly(3-hexylthiophene) by Solvent, Molecular Weight and Synthetic Method

Christina Scharsich[1], Ruth Lohwasser[2], Michael Sommer[2], Udom Asawapirom[3§], Ullrich Scherf[3], Mukundan Thelakkat[2], Dieter Neher[4], Anna Köhler[1*]

[1]*Organic Semiconductors, Experimental Physics II, Department of Physics, University of Bayreuth, Bayreuth 95440, Germany.*

[2]*Applied Functional Polymers, Macromolecular Chemistry I, Department of Chemistry, University of Bayreuth, Bayreuth 95440, Germany*

[3]*Macromolecular Chemistry, Bergische Universität Wuppertal, Wuppertal 42097, Germany*

[4]*Soft Matter Physics, Institute of Physics and Astronomy, University of Potsdam, Potsdam 14476, Germany*

e-mail: anna.koehler@uni-bayreuth.de

Absorption spectra of aggregated chains

This section describes how we derived the absorption spectra of chains in the aggregated state. To induce poly(3-hexylthiophene) chains to aggregate, we prepared solutions with different ratios of good:poor solvent (chloroform:ethyl acetate). The measured absorption of these solutions is caused by coexisting coiled and aggregated chains. The resulting isosbestic point (see Fig. 1 in the manuscript) indicates that there are only these two species of chains, namely dissolved, and thus coiled, polymer chains and planarized, aggregated chains. The latter show structured and red-shifted absorption compared to the coiled chains.

Figure 1 illustrates exemplarily for each molecular weight compound how the absorption spectra of the aggregated chains were extracted from the measured total spectra. The shape of the absorption spectrum of well dissolved, coiled P3HT was

measured in 100% chloroform solution and scaled to fit the high energy shoulder of the examined solution spectrum without changing its position. This scaled spectrum of the coiled chains was then subtracted yielding the absorption spectrum due to pure aggregates present in the according solution.

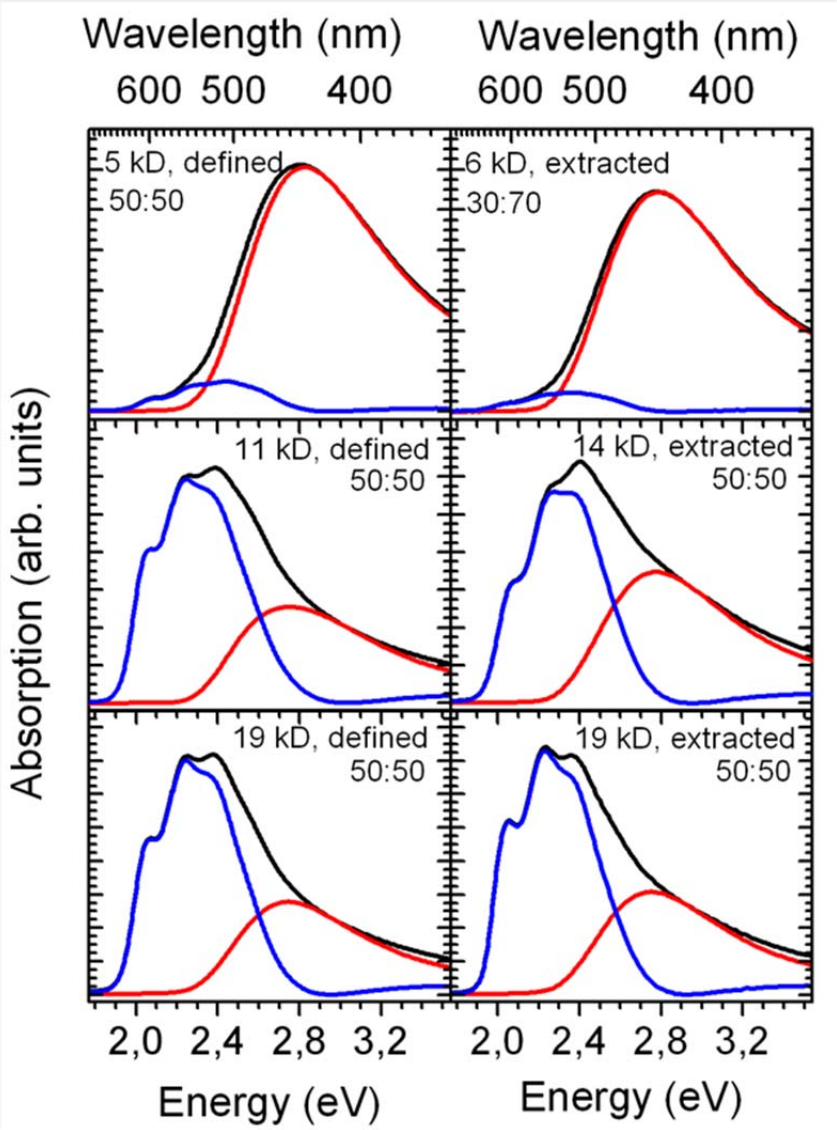

Figure 1

Measured absorption spectra for solutions with good:poor solvent ($CHCl_3$:EtAc) (black line) containing coexisting coiled and aggregated chains. The absorption of well dissolved, coiled P3HT in 100% chloroform (red line) was scaled to fit the high energy shoulder of the solution spectrum. The spectrum of the coiled chains was then subtracted yielding the absorption due to aggregates (blue line).

Determination of relative oscillator strength

For our interpretation, we need to know the fraction of chains that are aggregated. Above, we have derived which fraction of absorption is due to aggregates. However, the fraction of aggregate absorption is not equal to the fraction of aggregates, since the chain may have different oscillator strength in the coiled form and in the aggregated form. The relative oscillator strength describes the change in oscillator strength when going from coiled to aggregated P3HT chains. Knowledge of this relative oscillator strength is therefore necessary to determine the fraction of aggregates from the area of the aggregate absorption.

To determine the relative oscillator strength, we followed the procedure by Clark et al.[1] Figure 2 illustrates the procedure. As outlined above, the total absorption spectrum (blue solid line) can be deconvoluted into the absorption caused by dissolved, coiled chains (black dashed line) and the absorption caused by aggregated chains (blue dashed line). The change in absorption of the coiled chains, ΔA_{coiled}, corresponds to the difference between the spectrum from 100% coiled chains (black solid line) and the fraction of absorption by the coiled chains in the measured spectrum (black dashed line). In the left part of Figure 2, ΔA_{coiled} is indicated by the shaded area.

The corresponding increase in absorption of the aggregated chains, $\Delta A_{aggregate}$, is given by the absorption of the aggregated chains formed (blue dashed line). $\Delta A_{aggregate}$ is shown as shaded area in the right part of Figure 2. Any difference between the

decrease of absorption by coiled chains and the increase in absorption by aggregated chains must arise from a change in relative oscillator strength F as follows.

$$F = -\frac{\Delta A_{aggregate}}{\Delta A_{coiled}} \quad (1)$$

The resulting change in relative oscillator strength F for solutions with different ratios of good:poor solvent (chloroform:ethyl acetate) for the defined and extracted poly(3-hexylthiophene) compounds is summarized in Figure 3. Clark et al. obtained a relative oscillator strength of (1.39 ± 0.10) for commercial P3HT in solution going from 70° C to

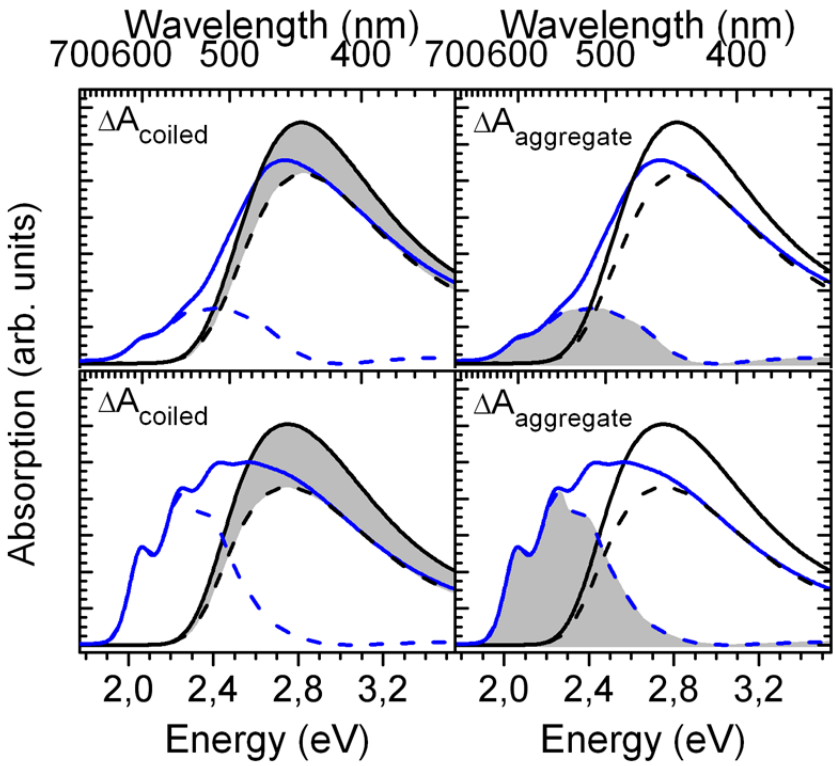

Figure 2

Exemplarily absorption spectra for P3HT solutions with solvent induced aggregate absorption (blue solid line) indicating the change in oscillator strength between coiled and aggregated chains (grey areas). The absorption of 100% well dissolved, coiled chains is presented as solid black line. The dashed lines show the absorption due to

aggregated (dashed blue line) and coiled (dashed black line) chains, respectively. Top figures show absorption of 30:70 ($CHCl_3$:EtAc) solution of the defined 5 kD sample and bottom figures show 80:20 ($CHCl_3$:EtAc) solution of the 11 kD sample.

room temperature. This is in good agreement with the relative oscillator strength we obtained for the solutions of the 19 kD samples with 25% of poor solvent and higher.

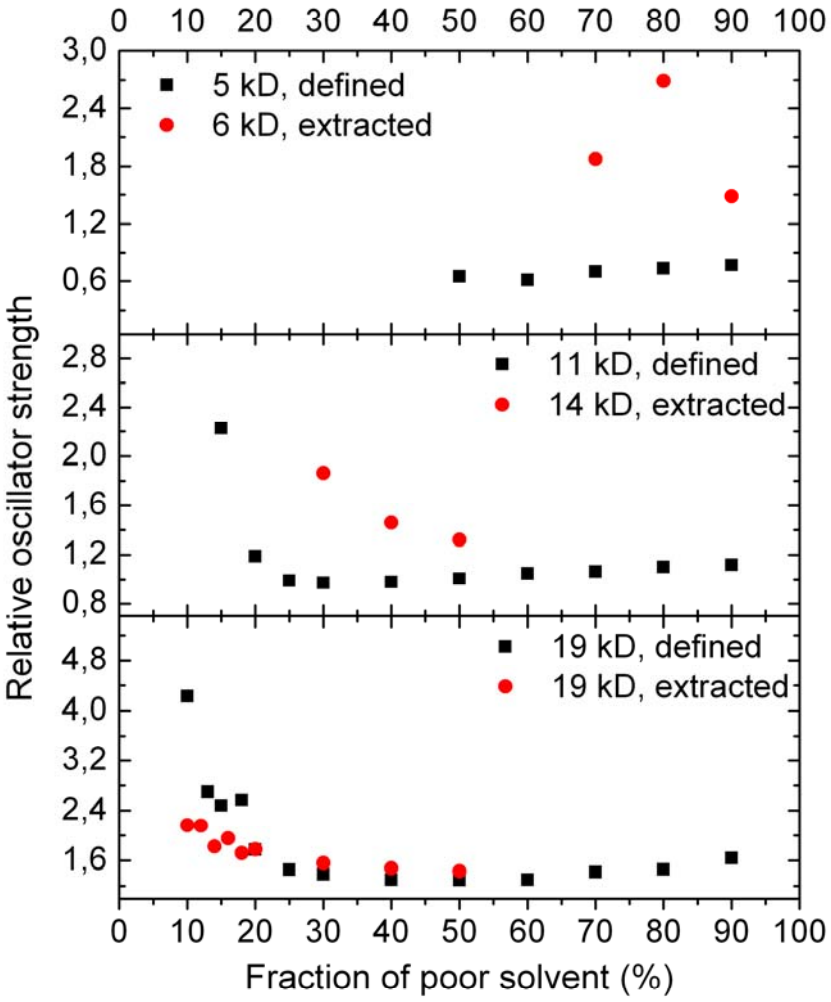

Figure 3

The relative oscillator strength between coiled and aggregated P3HT chains as function of poor solvent fraction for defined and extracted P3HT as indicted in the figure. The molecular weight increases from top to bottom.

Franck-Condon analysis

The quantitative analysis of the P3HT aggregate absorption yields the excitonic coupling J between the polymer chains within these aggregates. According to the work of Spano[2], the coupling is determined by the ratio of the first two absorption peaks, $A_{0\text{-}0}/A_{0\text{-}1}$, as follows

$$\frac{A_{0-0}}{A_{0-1}} = \frac{n_{0-0}}{n_{0-1}} \frac{\left(1-\frac{J}{\omega_0}e^{-S}\sum_{\nu>0}\frac{S^{\nu}}{\nu!\nu}\right)^2}{S\left(1-\frac{J}{\omega_0}e^{-S}\sum_{\nu\neq 1}\frac{S^{\nu}}{\nu!(\nu-1)}\right)^2},$$

where ω_0 is the effective vibrational energy of the single emitter and S its Huang Rhys parameter, $n_{0\text{-}0}$ and $n_{0\text{-}1}$ refer to the refractive index at the position of $A_{0\text{-}0}$ and $A_{0\text{-}1}$. Thus, the correct determination of the excitonic coupling J requires the knowledge of Huang Rhys parameter S and the effective vibrational energy ω_0 of the single, i.e. non-aggregated, emitter. Both parameters can be extracted from a Franck-Condon analysis of the photoluminescence of the single emitter (a non-aggregated chain). Therefore, we measured photoluminescence spectra of dilute P3HT solutions in 100% chloroform. Figure 4 shows the experimental photoluminescence data (blue symbols).

For the analysis of the excitonic coupling J, we need only a vibrational energy for an *effective* oscillation. Thus, a single mode Franck-Condon analysis is sufficient. In a Franck-Condon analysis, the photoluminescence spectrum is modeled as a sum of Gaussian shaped transitions, Γ, from the first excited state $S_1(m=0)$ to the ground state $S_0(m)$ with m=1,2,3,… being the vibration quantum number.[3] The fitting procedure demands a normalization of the photoluminescence signal P(ħω) given by

$$\frac{P(\hbar\omega)}{n^3\,(\hbar\omega)^3\,I_{0-0}} = \sum_m \frac{S^m}{m!}\Gamma\delta[\hbar\omega - (\hbar\omega_0 - m\,\hbar\omega_i)], \quad (2)$$

where $I_{0\text{-}0}$ is the intensity of the emission from the 0-0 vibrational level of the first excited state to the 0-0 vibrational level of the ground state. The integer m denotes the excitation level of the vibration with energy $\hbar\omega_i$ and n is the refractive index of the surrounding material at photon energy $\hbar\omega$. Here, the material surrounding the single emitters was the solvent, chloroform. Its refractive index was calculated from the Cauchy parameters published by Samoc.[4]

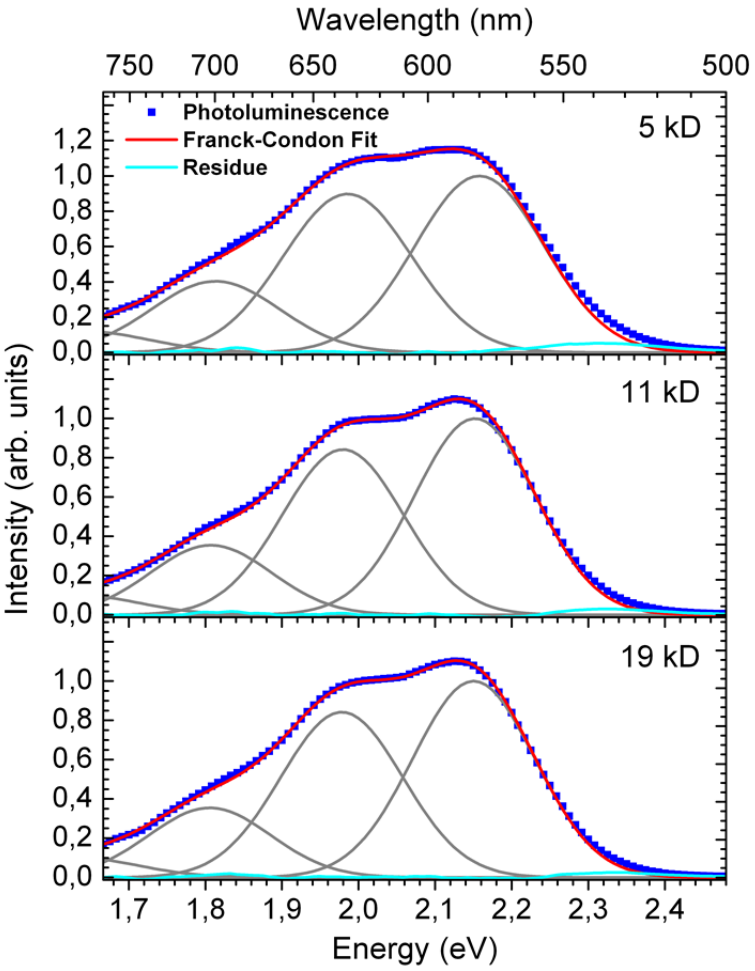

Figure 4

Single mode Franck-Condon fits (red line) for the single emitter emission spectra in dilute solution for defined P3HT. The molecular weight increases from top to bottom. The experimental data (blue symbols) were fitted with Gaussian functions (grey lines) at four vibration levels. The residue is presented as cyan line.

The Franck-Condon fits according to equation 2 were calculated using four vibrational levels (m= 0, 1, 2, 3, 4) of the effective oscillator $\hbar\omega_0$ and yield the fitting parameters summarized in Table 1. The Franck-Condon fits (red line in Figure 4) reproduce the experimental data with high accuracy. Thus, the resulting parameters S and ω_0 enable a precise calculation of the free excitonic coupling J.

P3HT	**S**	**ω_0**	**σ**
5 kD	0.90	1390 cm^{-1}	0.084 eV
11 kD	0.84	1390 cm^{-1}	0.079 eV
19 kD	0.84	1390 cm^{-1}	0.080 eV

Table 1

Fitting parameters of the Franck-Condon analyses for the poly(3-hexylthiophene) (P3HT) single emitter photoluminescence spectra: Huang Rhys parameter S, energy of effective oscillation ω_0 and Gaussian standard deviation σ.

Absorption spectra of thin films

We want to investigate whether the results obtained for P3HT aggregates in solution can be transferred to P3HT films that were spun from solution already containing aggregates due to poor solvent fractions. Therefore, we studied the absorption of the P3HT thin films, shown in Figure 5 normalized to the 0-1 absorption peak for the defined P3HT samples. The absorption spectra of the films show both, a structured

absorption due to aggregated chains at low energies and absorption around 2.8 eV and higher due to non-aggregated coiled chains in amorphous regions. We find that films spun from solutions containing fractions of poor solvent have higher 0-0 absorption indicating aggregates with lower excitonic coupling and thus higher conjugation length. Similar absorption spectra can be obtained for the extracted P3HT samples as well.

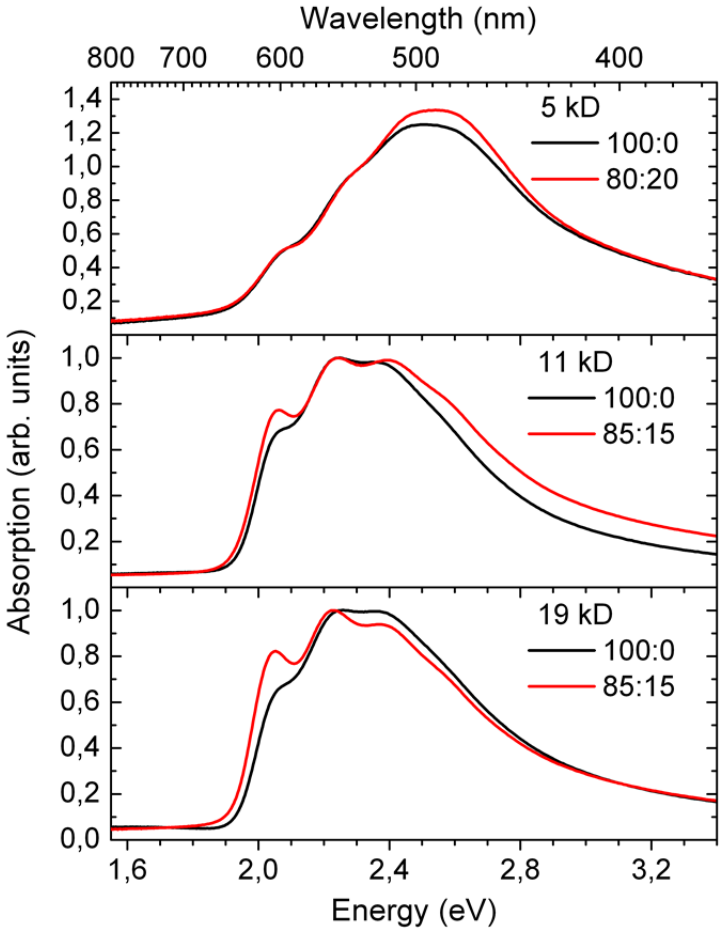

Figure 5

Absorption spectra of thin films made from defined P3HT, normalized to the second absorption peak. Films were spun from solutions with ratios of good:poor solvent ($CHCl_3$:EtAc) as indicted in the figure.

Assessment of thermal equilibrium state in solution

The absorption spectra of P3HT in a solvent mixture of chloroform and ethyl acetate do not show any changes on a 24 hour timescale. We therefore wanted to know whether the conformation obtained in such a solution corresponds to a thermal equilibrium state. To probe this, P3HT was dissolved in a chloroform:ethyl acetate 50:50 mixture at a concentration of 0.25 mg/ml prepared in two different ways. In the first approach, P3HT was fully dissolved in chloroform. Then, the necessary amount of ethyl acetate was added at once. In the second approach, P3HT was again fully dissolved in chloroform, but the necessary amount of ethyl acetate was added very slowly (0.4 ml/h) in small amounts while stirring using an automated syringe. The absorption spectra resulting from the two modes of preparation are different, with larger aggregates falling out of solution in the second mode of preparation. From this difference we infer that that the solutions prepared by the first mode are not in a thermal equilibrium state.

References

1. Clark, J.; Chang, J. F.; Spano, F. C.; Friend, R. H.; Silva, C. Applied Physics Letters 2009, 94, 3.

2. Spano, F. C. Journal of Chemical Physics 2005, 122, -.

3. Ho, P. K. H.; Kim, J. S.; Tessler, N.; Friend, R. H. Journal of Chemical Physics 2001, 115, 2709-2720.

4. Samoc, A. Journal of Applied Physics 2003, 94, 6167-6174.

6 Role of Structural Order and Excess Energy on Ultrafast Free Charge Generation in Hybrid Polythiophene/Si Photovoltaics Probed in Real Time by Near-Infrared Broadband Transient Absorption

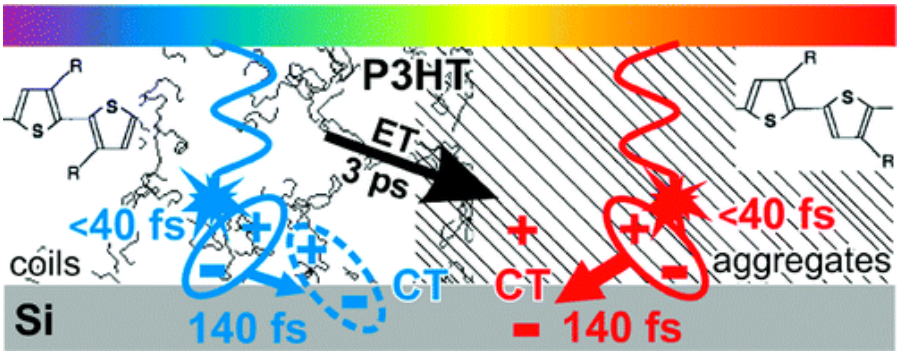

Daniel Herrmann, Sabrina Niesar, Christina Scharsich,
Anna Köhler, Martin Stutzmann, Eberhard Riedle

Published in

Journal of the American Chemical Society

DOI: 10.1021/ja207887q

Reprinted with permission from J. Am. Chem. Soc. 2011, 133, 18220–18233

JACS
JOURNAL OF THE AMERICAN CHEMICAL SOCIETY

ARTICLE

pubs.acs.org/JACS

Role of Structural Order and Excess Energy on Ultrafast Free Charge Generation in Hybrid Polythiophene/Si Photovoltaics Probed in Real Time by Near-Infrared Broadband Transient Absorption

Daniel Herrmann,[†] Sabrina Niesar,[‡] Christina Scharsich,[§] Anna Köhler,[§] Martin Stutzmann,[‡] and Eberhard Riedle*[,†]

[†]Lehrstuhl für BioMolekulare Optik, Ludwig-Maximilians-Universität München, Oettingenstraße 67, 80538 München, Germany

[‡]Walter Schottky Institut, Technische Universität München, Am Coulombwall 4, 85748 Garching, Germany

[§]Lehrstuhl EP II, Universität Bayreuth, Universitätsstraße 30, 95440 Bayreuth, Germany

Supporting Information

ABSTRACT: Despite the central role of light absorption and the subsequent generation of free charge carriers in organic and hybrid organic−inorganic photovoltaics, the precise process of this initial photoconversion is still debated. We employ a novel broadband (UV−Vis−NIR) transient absorption spectroscopy setup to probe charge generation and recombination in the thin films of the recently suggested hybrid material combination poly(3-hexylthiophene)/silicon (P3HT/Si) with 40 fs time resolution. Our approach allows for monitoring the time evolution of the relevant transient species under various excitation intensities and excitation wavelengths. Both in regioregular (RR) and regiorandom (RRa) P3HT, we observe an instant (<40 fs) creation of singlet excitons, which subsequently dissociate to form polarons in 140 fs. The quantum yield of polaron formation through dissociation of delocalized excitons is significantly enhanced by adding Si as an electron acceptor, revealing ultrafast electron transfer from P3HT to Si. P3HT/Si films with aggregated RR-P3HT are found to provide free charge carriers in planar as well as in bulk heterojunctions, and losses are due to nongeminate recombination. In contrast for RRa-P3HT/Si, geminate recombination of bound carriers is observed as the dominant loss mechanism. Site-selective excitation by variation of pump wavelength uncovers an energy transfer from P3HT coils to aggregates with a $1/e$ transfer time of 3 ps and reveals a factor of 2 more efficient polaron formation using aggregated RR-P3HT compared to disordered RRa-P3HT. Therefore, we find that polymer structural order rather than excess energy is the key criterion for free charge generation in hybrid P3HT/Si solar cells.

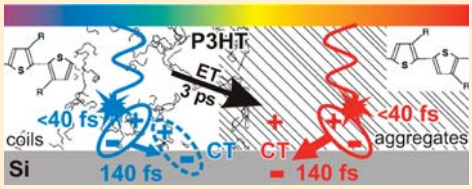

1. INTRODUCTION

Thin film solar cells constitute one of the future technological solutions for sustainable energy supply. A particularly promising route is offered by solar cells made from organic semiconductors or inorganic semiconducting nanoparticles.[1−4] In recent years, hybrid solar cells based on an organic semiconductor in conjunction with an inorganic nanoscale material are considered as an alternative to purely organic solar cells, as they allow achieving additional functionality by combining the advantages of the two materials.[5−9] In comparison to polymers, inorganic semiconductors offer a broader spectral range of absorption, particularly in the NIR spectral range, a higher charge carrier mobility, and a better thermal and morphological stability. At the same time, their application in the form of nanoparticles enables the possibility of band gap tuning for sufficiently small nanoparticle diameters and the technological advantages of purely organic solar cells, such as low-cost solution processing, roll-to-roll assembly, or processing onto flexible substrates, are maintained. In the literature, various composites based on Si, ZnO, TiO_2, CdSe, and a few other nanomaterials are currently of scientific interest.[6−15]

However, in hybrid and organic solar cells, a detailed fundamental understanding of the processes of light absorption, formation of free polarons, and the subsequent transport of these charges to the electrodes, which are central to their operation, is lacking. In purely organic solar cell devices, these photophysical processes have been shown to depend strongly on the morphology of the heterojunction[16] so that the device efficiency can be improved significantly by the processing conditions of the film.[17−19] The widely used and highly attractive polymer poly(3-hexylthiophene) (P3HT) can form two distinct morphological phases associated with different chain conformations. If the P3HT chain adopts a random coil conformation, the resulting film is amorphous. The associated absorption spectrum is unstructured with a maximum centered around 450 nm (about 2.8 eV). This disordered structure prevails for regiorandom P3HT (RRa-P3HT). In regioregular P3HT (RR-P3HT), the polymer chains can planarize and assemble to form weakly coupled H-aggregates,[20,21] which arrange in closely (a few angstroms) packed two-dimensional lamellar structures via π-stacking.[22−25] Their spectroscopic signature is a well-structured absorption spectrum with a 0−0 vibronic peak around 600 nm (about 2.0 eV).[21]

Received: June 1, 2011
Published: September 26, 2011

Such aggregates are partially formed when RR-P3HT is embedded in a poor solvent or in a film after spin-coating from solution. RR-P3HT is a semicrystalline polymer whose degree of crystallization can be controlled by processing conditions. While it became clear that the charge carrier mobility is enhanced in aggregated P3HT chains,[26,27] studies on the role of the aggregated or coiled conformation in the process of charge carrier generation and separation in organic devices have been emerging only recently.[16]

For the design and operation of a solar cell, it is therefore of crucial importance to understand the influence of morphology on each of the individual photophysical steps. In organic semiconductors, there is widespread agreement about the photoconversion process. The elementary step is light absorption to generate excited states of a donor, followed by diffusion of the excitation to the internal interface formed by a donor adjacent to an acceptor and the decisive electron transfer from the excited donor to the acceptor forming a Coulombically bound electron−hole pair. Ideally, this is followed by their dissociation into free charges that move away from the interface, preferentially not suffering bimolecular recombination before being collected at the respective electrodes. Moreover, there is agreement that in purely organic blends the process of charge carrier generation takes place on an ultrafast time scale in the range of 100 fs.[16,28−31]

However, the exact mechanism of charge separation is still debated for purely organic solar cells and still in an early phase for hybrid composites. For P3HT in combination with [6,6]phenyl-C_{61}-butyric acid methyl ester (PCBM), which has been demonstrated to achieve power conversion efficiencies of around 5%,[32] there are suggestions that Frenkel-type excitons are the primary photoexcitations that dissociate into free charges.[16,29,30] There are indications that the charge separation takes place more efficiently for blends of RR-P3HT:PCBM than for RRa-P3HT:PCBM.[16] In contrast, prompt polaron formation during laser excitation was considered for neat P3HT and RRa-P3HT:PCBM.[30,33] For the polymer PCDTBT in combination with PCBM, there are also contradicting interpretations in discussion. On the one hand, it has been suggested that light absorption may directly create mobile electrons and holes by interband $\pi-\pi^*$ transitions which would subsequently evolve into Coulombically bound excitons in less than 1 ps.[31] Similarly, for a composite of a PPV derivative with PCBM, the primary photoexcitation has been suggested to be an ultrafast electron transfer on the time scale of 45 fs.[28] On the other hand, ultrafast exciton dissociation to form free charges was also considered very recently for PCDTBT:PCBM blends.[34] For hybrid donor−acceptor materials, detailed ultrafast spectroscopic investigations are still in an early phase. The question, whether light absorption initially creates free charge carriers or excitons, is central to the understanding of light harvesting in organic and hybrid systems. A problem in resolving this issue pertains to the experimental limits of time resolution and spectral range that are accessible to optical probing. Here, we have developed a novel ultrabroadband transient absorption spectroscopy setup with a time resolution of 40 fs covering the entire broad spectral range from 415 to 1150 nm without interruption. This allows us to monitor both the kinetics of the decay of the primary excitation and its evolution into a charge pair state in thin hybrid films.

In our studies, we focus on composites of P3HT in combination with silicon which is a particularly promising inorganic acceptor for several reasons. It unifies an almost unlimited abundance with environmentally friendliness, allowing for its widespread use. Silicon additionally provides high electron affinity and allows for rapid electron delocalization and screening after charge transfer which may prevent back transfer and enables fast transport away from the interface. Because of the higher dielectric constant of silicon compared to PCBM, this effect should be even more pronounced as in purely organic films, thus rendering silicon a very promising alternative to PCBM for photovoltaic devices and fundamental studies. Proof-of-principle investigations of charge transfer in hybrid P3HT/Si systems were recently performed using electron spin resonance (ESR).[9] Prototype devices exhibited a relatively high open-circuit voltage of 0.75 V,[10] and power conversion efficiencies of around 1% have been achieved.[8] However, no detailed spectroscopic understanding has been available so far. Because of its current availability in crystalline, nanocrystalline, and amorphous forms, silicon serves as a model system with fundamental implications for various other hybrid or organic material systems. In particular, the exciton dissociation mechanism and therefore the photophysics of charge generation and separation can be studied more clearly in silicon-based devices. The reason for this is that these processes are difficult to assess in the widely studied P3HT/PCBM composite, since the various PCBM transient signals from the visible to NIR[35] superimpose with the transient absorption by the polaron and exciton of P3HT.

In our study, we employ Si nanocrystals (Si-ncs) and polycrystalline silicon (poly-Si) as the electron acceptor in order to study both film geometries of interest, bulk heterojunctions and planar heterojunctions. For the development of efficient commercial solar cells, the bulk heterojunction structure is favored, since it offers a particularly large donor−acceptor interface. The efficiency of planar heterojunctions is limited by the smaller interfacial area, yet the two-dimensional interface area avoids recombination associated with interrupted percolation pathways and cross-currents of electrons and holes. However, as our studies primarily focus on the fundamental principles of the photophysics (charge generation and separation), our devices are optimized for an unambiguous data interpretation. To address the dependence of charge carrier separation on polymer structural order, both disordered RRa-P3HT and semicrystalline RR-P3HT were used.

Our pump−probe setup allows us to directly monitor in real time the process of charge generation in hybrid thin film P3HT/Si heterojunctions, here at room temperature in the absence of an applied external field. For both RR- and RRa-P3HT, we observe an instant creation of singlet excitons that subsequently dissociate to form polarons on an ultrafast time scale. We observe that the yield of polaron formation through exciton dissociation is significantly enhanced by adding Si as electron acceptor. Furthermore, we find that the yield of polaron formation and the degree of Coulombic binding of the corresponding polaron pairs formed in P3HT/Si depend on the polymer structural order, with efficient free charge carrier generation in RR-P3HT/Si and geminately bound charge carriers formed in RRa-P3HT/Si.

2. SAMPLE PREPARATION AND SUMMARY OF EXPERIMENTAL METHODS

2.1. Sample Preparation. In this work, three different types of poly(3-hexylthiophene) with varying degree of aggregation were used. For fundamental studies of interactions between disordered and ordered regions of P3HT, films of a RR-P3HT (BASF SE, Sepiolid P 100, regioregularity ∼95%, M_w = 50 000 g/mol, M_w/M_n = 2.2) were prepared by spin-coating from chloroform ($CHCl_3$) solutions with a concentration of 7.5 mg/mL onto precleaned glass substrates. The same polymer was dissolved in spectroscopically pure chloroform, toluene, and 1,2-dichlorobenzene with concentrations of 0.075 mg/mL and filled

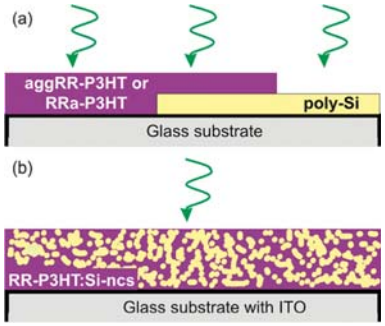

Figure 1. Sample architecture of hybrid P3HT/Si thin film: (a) planar heterojunction and (b) bulk heterojunction on glass substrates.

in 1 mm fused silica cuvettes for the transient absorption spectroscopy of P3HT in solution.

P3HT/Si thin film heterojunctions with varied morphology were prepared as planar heterojunctions (PHJs, Figure 1a) and bulk heterojunctions (BHJs, Figure 1b). For the PHJs with varied polymer structural order, RRa-P3HT (University of Bayreuth, Germany, M_w = 40 000 g/mol, M_w/M_n = 2.4) dissolved in chloroform (5 mg/mL), and RR-P3HT (Rieke Metals, M_w = 39 000 g/mol, M_w/M_n = 2.0) dissolved in 98% chloroform and 2% ethyl acetate (EtAc) (5 mg/mL) was used. The former was synthesized by treating thiophene with $FeCl_3$.[36] For the latter, ethyl acetate as nonideal solvent for P3HT was admixed to enhance the aggregation of the RR-P3HT molecules,[37−39] which is therefore referred to as aggRR-P3HT. All sample preparations were performed under argon atmosphere.

Silicon nanocrystals (Si-ncs) were synthesized in a low-pressure microwave plasma reactor by decomposition of silane.[40] The pressure of the process gases and the microwave power determine the mean diameter of the Si-ncs. Phosphorus doping of the Si-ncs was achieved by adding phosphine during growth and increases the carrier mobility in the Si-ncs. The nominal doping concentration is defined by the phosphine flow and the flow of the total precursor gas. The Si-ncs used in this work have a mean diameter of 4 and 18 nm and nominal doping concentrations of 5×10^{20} and 6.5×10^{19} cm^{-3}, respectively. The standard deviation of the particle diameter is typically $\sigma \approx 1.4$ nm.

Blend films of RR-P3HT and Si-ncs with a weight ratio of 5:1 were spin-coated under nitrogen atmosphere from solutions in chloroform (concentration 7.5 mg/mL) to form RR-P3HT:Si-ncs BHJs (Figure 1b). For the intended application as a solar cell, 15 mm × 15 mm × 1.1 mm aluminoborosilicate with an approximately 110 nm thick conductive indium tin oxide layer (ITO, Delta Technologies, R_s = 5−15 Ω) was used as a substrate. Before spin-coating, the substrates were cleaned by subsequent ultrasonic treatment in acetone and isopropanol for 10 min each. A typical sample layer thickness of 100 nm was achieved. The thin film samples were sealed against air by using fused silica coverslips (150 μm thin) and silicone sealant.

The refractive index of the Si-ncs was previously measured to be about 2.0 with only a slight monotonic decrease with wavelength. The refractive index of the blend films can be expected to be close to the one of a neat P3HT film, which has a reported index of around 1.7−2.0.[41] Consequently no significant change of the Fresnel losses upon mixing of the two materials is expected and the weak excitation should also not lead to a transient change.

Polycrystalline silicon (poly-Si) films were prepared by silver-induced layer exchange (AgILE).[42] For a resulting poly-Si film thickness of 30 nm, an amorphous silicon precursor layer (50 nm) was grown on top of a 30 nm silver layer on a fused silica substrate. The crystallization was performed at 800 °C for 10 h under nitrogen atmosphere. Afterwards, the silver was etched away with a 1:1 mixture of hydrogen peroxide and ammonia solution at 100 °C. We prepared PHJs of 40 nm RRa-P3HT or aggRR-P3HT and 30 nm poly-Si (aggRR-P3HT/poly-Si PHJ and RRa-P3HT/poly-Si PHJ, Figure 1b) under nitrogen atmosphere. To be able to perform TA spectroscopy of the individual materials and of the heterojunctions, the poly-Si covers only a part of the substrate (Figure 1a). Furthermore, we removed a stripe of the P3HT on the Si side using a cotton tip with chloroform. A summary of the sample structures used is given in Table 1.

Table 1. List of Samples Used in This Work along with Their Abbreviations

sample	abbreviation
RR-P3HT (BASF), spun from $CHCl_3$	RR-P3HT
RRa-P3HT (Bayreuth), spun from $CHCl_3$	RRa-P3HT
RR-P3HT (Rieke), spun from $CHCl_3$/EtAc	aggRR-P3HT
silicon nanocrystals	Si-ncs
polycrystalline silicon	poly-Si
RR-P3HT:Si-ncs bulk heterojunction	RR-P3HT:Si-ncs BHJ
RRa-P3HT/poly-Si planar heterojunction	RRa-P3HT/poly-Si PHJ
aggRR-P3HT/poly-Si planar heterojunction	aggRR-P3HT/poly-Si PHJ

2.2. Summary of Experimental Methods. Details about the basic optical and morphologic characterization of the thin film samples and the novel ultrafast transient absorption spectrometer are given in the Supporting Information. To investigate the nature of the photoexcitations and their inherent kinetics after visible excitation, we used an ultrafast 1 kHz pump−probe setup with a probe range of 290−740 nm.[43] The visible excitation with 15 fs pulses in the range from 450 to 720 nm is accomplished by a noncollinear optical parametric amplifier (NOPA).[44,45] We expand the probe range to 415−1150 nm by the combination of two supercontinuum generation stages and a NIR-OPA operated at 1180 nm, allowing for broadband UV−Vis-NIR TA spectroscopy with 40 fs time resolution (Figure S3). This OPA was seeded with a supercontinuum from a YAG crystal[46] and generated the Vis−NIR probe continuum in a CaF_2 crystal. The pump and probe were focused towards the sample to a 210 and 110 μm $1/e^2$ beam diameter that allows ensemble averaging over the finely grained morphology of the thin films to mimic their usage as photovoltaic device and to ensure low local excitation densities.

3. RESULTS AND DISCUSSION

3.1. Structural Implications of Regioregularity and Solvent. In our study, we aim to understand the process of charge carrier generation in the polymer P3HT and in the hybrid system formed by P3HT in combination with silicon. P3HT is a semicrystalline polymer whose degree of aggregation depends on the degree of regioregularity of the chain as well as on the solvent used. In order to assess the role of aggregated P3HT chains in the charge generation process, we employed samples with different degrees of regioregularity and spun from different solvents, as summarized in Table 1. The resulting structure of the films was carefully monitored via atomic force microscopy (AFM). The corresponding topographical images in 2D and 3D plots are shown in Figures 2a−c and Figure S1 and reveal a varied aggregation: While RRa-P3HT exhibits a rather long spatial coherence length (Figure 2a, Figure S1a), aggRR-P3HT possesses a fine structure (Figure 2c, Figure S1b). RR-P3HT is between these two extremes (Figure 2b).

The differences can be understood by regarding the different processing conditions. In the case of aggRR-P3HT, we have used chloroform as the main solvent, which exhibits a lower (61 °C)

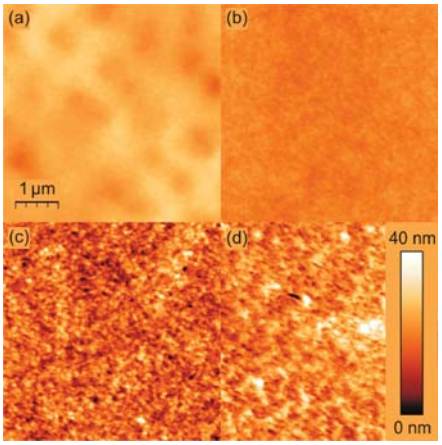

Figure 2. Topographical AFM images of spin-coated films of (a) RRa-P3HT (rms roughness R_q = 2.2 nm), (b) RR-P3HT (R_q = 1.2 nm), (c) aggRR-P3HT (R_q = 5.4 nm) directly on glass substrate as well as (d) aggRR-P3HT on top of a 30 nm thin polycrystalline Si layer (R_q = 6.3 nm). For (c) and (d), 2% ethyl acetate was mixed with the chloroform solution to enhance the aggregation of the RR-P3HT molecules.

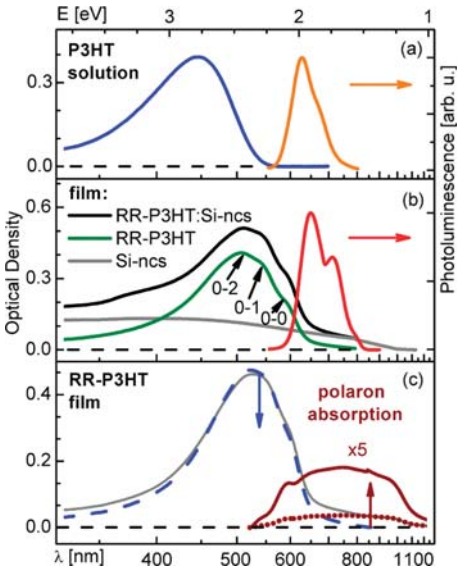

Figure 3. Absorbance and photoluminescence spectra of P3HT in (a) dilute chloroform solution and (b) of RR-P3HT film. The absorbances of Si-ncs and RR-P3HT:Si-ncs (5:1) BHJ as film are also shown. (c) Absorbance spectra of RR-P3HT (blue dashes), oxidized RR-P3HT film after adding $FeCl_3$ (solid gray curve) and P3HT film polaron absorption (brown dots and brown solid curve).

boiling point as the nonideal solvent ethyl acetate (77 °C). The already partially aggregated polymer falls out of solution before the main solvent is fully dissipated and before the film has fully dried, leading to enhanced aggregation evident in the fine structure of the AFM data. Comparison of Figure 2c and Figure 2d further reveals that when spin-coating aggRR-P3HT directly on poly-Si instead of glass, the fine structure indicating the aggregation is maintained.

3.2. Optical Characterization. The amount of aggregation present in a P3HT sample manifests itself not only in the AFM

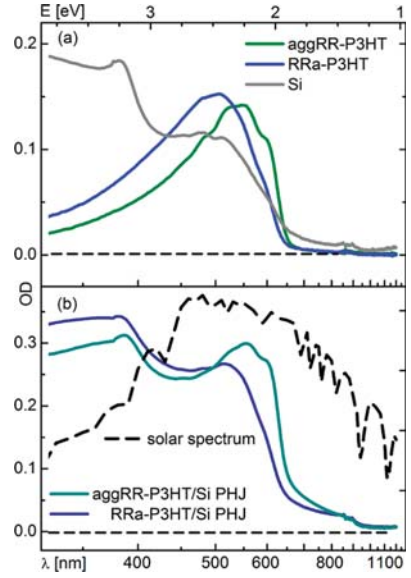

Figure 4. (a) Absorbance spectra of neat RRa-P3HT, RR-P3HT + ethyl acetate (aggRR-P3HT), and neat poly-Si and (b) the corresponding P3HT/poly-Si PHJs samples compared with the solar spectrum.

characteristics but also in the optical spectra. Figure 3 shows the absorbance (OD) and photoluminescence (PL) spectra of RR-P3HT in the dilute chloroform solution and for thin film samples used in this work. In dilute solution with a good solvent such as chloroform, RR-P3HT is known to adopt a random coil conformation with a distribution of short conjugation lengths. This results in a structureless absorbance that has its maximum at 446 nm and in a red-shifted more structured PL with peaks at 627 and 688 nm (Figure 3a). The PL originates from the longest polymer segments after relaxation of the initial photoexcitation. In film, the RR-P3HT chains can planarize to form weakly interacting H-aggregates that are embedded in a matrix of amorphous coiled P3HT chains. The resulting absorption thus consists of a superposition of absorption by coiled chains and absorption by planar, highly conjugated and aggregated chains.[21] Consequently, the absorption is shifted to longer wavelengths, is broadened, and shows vibronic peaks at 518, 558, and 608 nm (Figure 3b) due to the 0−2, 0−1, and 0−0 transitions, respectively, in agreement with literature data.[21] The corresponding PL also contains vibronic structure with peaks at 650, 712, and 800 nm (mainly the C═C symmetric stretching mode, 1452 cm^{-1}).

By considering the intensity of absorption between 400 and 500 nm and by considering the vibrational structure around 600 nm through a modified Franck-Condon analysis as described in refs 21 and 47, it is possible to derive the amount of aggregates present in a film (Figure S2). Figure 4a shows the absorption spectra of the two limiting cases given in our study, that is, RRa-P3HT and aggRR-P3HT. The absorption of poly-Si is also shown for comparison. Analyzing the P3HT absorption in this fashion, with the assumption that the absorption coefficient of aggregated chains is 1.39 times that of coiled chains,[47] yields a percentage of (38 ± 5)% aggregates for the aggRR-P3HT sample and of (24 ± 5)% aggregates for the RRa-P3HT sample (Figure S2). RRa-P3HT possesses less aggregation and a reduced conjugation length compared to RR-P3HT, which was attributed to the adverse steric repulsive interactions between the hexyl side chains and the sulfur.[17,48] Figures 3b and 4b illustrate that when

the P3HT is intermixed with Si-ncs or spun on top of poly-Si, the absorption spectrum is given by a superposition of the individual components. Thus, in agreement with the AFM data, spinning a film on top of a silicon substrate does not seem to affect the amount of aggregates formed. Figure 4b further demonstrates the good match of the heterojunction absorption against the solar irradiation spectrum that is essential for efficient solar cells.

In order to study the process of charge generation in these material systems, we do not only need to know how many aggregated or coiled chains are present in the P3HT but also require a spectroscopic signature for charges in P3HT films. P3HT thin films can be chemically oxidized employing a strong oxidant.[25,49] Figure 3c shows the absorbance spectrum of thus oxidized RR-P3HT thin films after dipping into 20 ppm solution of iron(III) chloride ($FeCl_3$) in acetonitrile (CH_3CN) for 1 min followed by rinsing with acetonitrile to remove excess oxidant. From the raw spectrum of the treated film we obtain the P3HT polaron ($P3HT^+$) absorption as follows. The treatment with $FeCl_3$ decreases the known absorbance of the neutral P3HT molecule (blue dashes) and increases absorbance in the range from about 560 to 1150 nm (brown dots). Partial saturation occurs at treatment longer than 2 min. The difference between the blue dashed line scaled to the peak of the gray solid curve in Figure 3c and the gray solid curve reveals the RR-P3HT film polaron absorption (brown dots and brown solid line). It ranges from about 560 to 1150 nm with a characteristic shape and increases again up to the mid-infrared spectral region. The same oxidation was performed for RRa- and aggRR-P3HT, and the results are shown in Figure 5. Comparable but, because of reduced conjugation length, slightly shifted results of the cation absorption are obtained for P3HT in solution where chemical oxidation was introduced via adding pentachloroantimonate (Figure S6, see details in Supporting Information). Similar oxidation experiments as the ones presented here have been reported and yielded very similar spectra.[25,49,50]

The polaron absorption spectrum, that we obtain in the P3HT films (Figure 3c), closely matches the subgap polaron absorption bands obtained by CW photoinduced absorption (PA) measurements as reported in recent publications.[7,11,25,51,52] Therefore, we use our measured polaron absorption spectra for the individual P3HT types for comparison with the transient absorption spectra throughout the whole work.

3.3. Primary Photoexcitations. The thoroughly characterized samples and the systematic variation of their composition allow the study of the excitations formed after illumination. To directly probe the nature of the primary photoexcitations and the inherent photovoltaic conversion processes in hybrid P3HT/Si layers, we performed ultrafast pump−probe (transient absorption, TA) spectroscopy. The thin film samples were designed to enable direct comparison between neat P3HT, neat Si, and the P3HT/Si heterojunction in ultrafast TA spectroscopy at the same experimental conditions by moving the relevant sample regions into the pump−probe region. We chose pump and probe beam diameters at the sample that allow for ensemble averaging over the finely grained morphology of the thin films to mimic their usage as photovoltaic device and to ensure low excitation fluence ($9\,\mu J/cm^2$ at 518 nm) comparable to the solar exposure. The low excitation fluence was also chosen to prevent modulation of the transient signatures due to a thermally induced spectral blue shift, which might occur at high excitation fluences.[53]

Figure 5 shows typical Vis−NIR TA spectra for aggP3HT/poly-Si PHJ, RRa-P3HT/poly-Si PHJ, and RR-P3HT:Si-ncs BHJ (red solid curves) compared with the TA spectra of the corresponding neat polymer film (black solid curves). Spectra were recorded for the full range from 10 ps prior to the pump pulse up to 2 ns after the pump pulse (see Figure S11). Spectra taken at 300 fs, 20 ps, and 1-2 ns pump−probe delay are shown. The spectra are composed of negative ΔOD signals in the spectral region of the P3HT film absorption between 415 and 630 nm because of ground state bleach (GSB) and positive signals at longer wavelengths due to photoinduced absorption (PIA), i.e. excitons and polarons.

In order to directly compare the transient spectra and the kinetics of the charged species of the various neat P3HT with the corresponding P3HT/Si heterojunctions, the *same number of initial photoexcitations* needs to be considered. Small deviations in this number of initial photoexcitations occur in the experiment due to small variations in film quality, film thickness, and thus absorption or due to small changes in pump beam size and pump energy between the various samples. The integral over the GSB area equals the product of the excitation density times the strength of the first electronic transition of P3HT regardless of small variations of Franck-Condon activity due to differing morphologies of P3HT in the various samples.[54] The integral therefore represents a good relative measure of the number of initial photoexcitations. We use the transient spectrum of the aggRR-P3HT film as reference. The TA spectra of the other polymers and PHJs are each scaled by a small factor (0.7−1.3) for the whole data set of 250 time steps and 512 wavelengths. As a result, all spectra yield the same GSB area integral at the earliest usable time delay. We found that any delay time between 0 and 80 fs gives the same result. This procedure allows for considering the same number of initial photoexcitations in the films. Any changes in the optical density (ΔOD in %) that would be seen under reference conditions are then solely inherent to the different nature of the sample.

For each measurement, the pairwise difference between TA spectra of the heterojunction and the neat polymer is calculated (green solid curves). For comparison, the particular P3HT film polaron absorption spectrum (blue dashes) is included. The GSB of aggRR-P3HT and RR-P3HT clearly reveals the characteristic vibronic structure of the P3HT aggregate, in particular at 1-2 ns after excitation, which does not show a spectral shift during the delay times covered in the TA measurements. In Figure 5, we further observe the relative signal ratio between the 0−0 and 0−1 GSB peak to change over time and, most importantly, the GSB at 500 nm to reduce with time. As detailed further below in section 3.6.1 and in the Supporting Information, this is a signature that energy transfer takes place from coiled chains to aggregated chains.

Since the GSB is due to those P3HT chains which are not in the electronic ground state, it directly monitors the total number of photoexcitations such as excitons or polarons still present at a given delay time. The broadband PIA signals with positive ΔOD (compare Figure 5) are adjacent to the GSB and exceed the NIR detection range. We compare the PIA for the hybrid heterojunctions (red solid curves) to the corresponding neat polymer (black solid curves) and the difference spectra for each pair with the chemically obtained P3HT film polaron absorption spectrum. We find that the difference spectra match the P3HT film polaron absorption spectra in the range of about 620−850 nm. The comparison also reveals a region of enhanced PIA through adding Si to P3HT. From this we conclude that combining P3HT with silicon results in the generation of

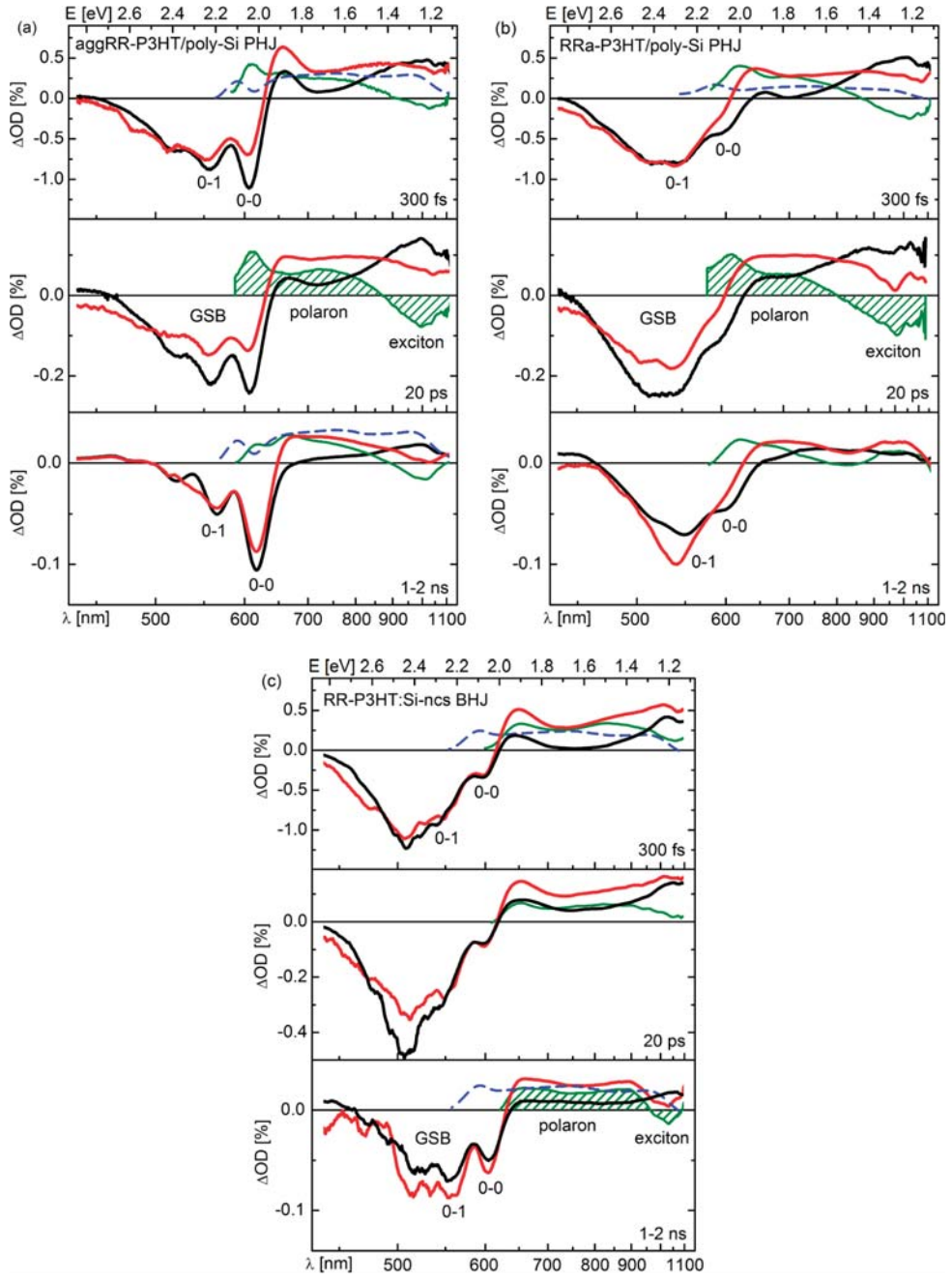

Figure 5. Transient absorption of (a) aggRR-P3HT/poly-Si PHJ, (b) RRa-P3HT/poly-Si PHJ and (c) RR-P3HT:Si-ncs BHJ for 300 fs, 20 ps and 1−2 ns pump−probe delay. The spectra are scaled to the same number of initial photoexcitations. The P3HT polaron absorption (blue dashes) and the difference (green solid curve) between neat P3HT (black solid curve) and P3HT/Si (red solid curve) are compared. Excitation: 518 nm, 9 μJ/cm^2.

additional P3HT cations, i.e. polarons. In the neat P3HT film, this polaron absorption also seems to be present, albeit at a significantly reduced level. From a comparison of the signal magnitude at 660 nm in the neat P3HT film and in the hybrid heterojunction we infer that the polaron yield in the P3HT/Si heterojunctions is more than a factor of 2 higher. Clearly, there must be ultrafast electron transfer from P3HT to Si in PHJ and BHJ morphologies. Consequently, Si is a promising electron acceptor for hybrid photovoltaic devices, in accordance with results by LESR.[9]

We now focus on the PIA spectra in the range of 900−1100 nm. In this range, the difference spectrum, given by the green solid curve in Figure 5, does not match the polaron absorption spectrum (blue dots). In agreement with previous investigations,[16,25,29,30] we assign the photoinduced absorption in this spectral range to absorption by singlet excitons. To support this assignment, we performed TA measurements of RR-P3HT in various dilute solutions, where the intermolecular distance is high. We found that under these conditions, P3HT cation formation does not take place (Figure S7, see details in Supporting Information).

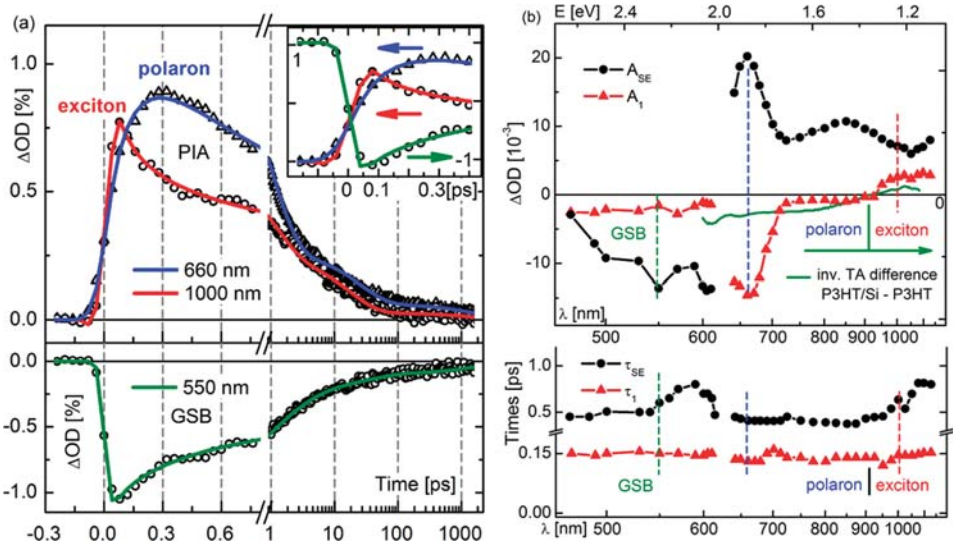

Figure 6. (a) Experimental TA signals (open symbols) as function of the pump−probe delay with corresponding fits (solid curves) of GSB (green), singlet exciton (red), and polaron (blue) for the aggRR-P3HT/poly-Si PHJ. The fit parameters are listed in Table 2. (b) PIA band single-channel fit amplitudes and time constants for the 140 fs component (red triangles) and the 1 ps component (black dots). The dashed lines are the signals taken for (a). The band assignment (inverted green curve) from Figure 5a agrees with the separation of polaron and exciton signatures via the fit amplitudes of the 140 fs component.

The singlet exciton leads to stimulated emission and undergoes intersystem crossing on the nanosecond time scale to a triplet state with a characteristic transition at 1.49 eV (830 nm). The energetic position of the P3HT triplet transition confirms and adds to recent experimental and theoretical investigations.[16,55] In addition to confirming the assignment of the singlet and triplet excitons, this measurement also implies that excitation dissociation does not occur efficiently on a single polymer chain.

Moreover, the difference spectrum between the hybrid system and the neat P3HT in Figure 5 shows a reduced PIA in the range of 900−1150 nm, which suggests that adding silicon to P3HT rapidly reduces the number of singlet excitons. The time evolution of the TA signals will be analyzed in detail further below. No transient signatures of stimulated emission (SE) or a triplet state are detected in any of the film measurements. This observation and the concomitant increase of polaron absorption and reduction of exciton absorption when P3HT is combined with silicon suggest the dissociation of singlet excitons as a path for polaron formation. We therefore conclude that the enhancement of polaron yield in P3HT by adding Si is due to an ultrafast electron transfer from P3HT (electron donor) to Si (electron acceptor) for all morphologies, namely PHJ and BHJ. We note that no transient signatures could be detected for the neat Si films or for excitation of the P3HT/Si heterojunctions with a pump wavelength of 720 nm, which is outside the P3HT absorption (Figures 3b and 4a). This shows that the observed effect of enhanced polaron absorption and reduced exciton absorption is due to electron transfer from excited P3HT to Si and not due to optical effects such as a transient change of index of refraction in Si.

So far we have assigned the various features of the TA spectra to photoexcitations, and the general observations pertained to all sample structures. We now consider the quantitative differences that arise between the various samples. In agreement with previous work,[16,29,33] we find some polaron formation to occur also for the neat P3HT films. Taking the signal magnitude around 660 nm as a measure for the amount of polaron formation, we find the initial yield to decrease in the order aggRR-P3HT, RR-P3HT, and RRa-P3HT. This is also the order in which the amount of aggregated chains in the film decreases (Figure 2). Therefore, the obtained clear discrimination between the TA spectra of the three types of P3HT matches the distinct differences in the corresponding optical and structural properties. We thus associate a higher polaron yield with an enhanced degree of aggregation and extended conjugation, enabling highly delocalized excitations and charge carriers with high mobility.[24,25]

This effect of the P3HT structural order on the polaron yield is also manifested in the hybrid heterojunctions. Comparison of the polaron absorption signal (at 660 nm; see red curve in Figure 5) indicates about a factor of 2 more efficient initial polaron formation for aggRR-P3HT/poly-Si PHJ compared to RRa-P3HT/poly-Si PHJ. We attribute this finding to the higher degree of conjugation, pronounced exciton delocalization, and an increased mobility of charge carriers which enable a more efficient charge transfer. A possibly more favorable free energy of charge generation through improved band alignment for ordered P3HT chains remains to be investigated.[56] Recent results state a rise only of the HOMO energy level and no change of the LUMO level through chain ordering.[57] For a possible photovoltaic application, we compared RR-P3HT:Si-ncs BHJs with aggRR-P3HT/poly-Si PHJs. The polaron yield is higher and their lifetime is slightly longer in aggRR-P3HT/poly-Si PHJ than in RR-P3HT:Si-ncs BHJ as becomes evident through comparison of the TA spectra in Figure 5a,c. The former can be attributed to the intermediate P3HT type used in the BHJ. The latter is assigned to Si dangling bond defects in Si-ncs which act as recombination centers. To address this, we are currently working on postgrowth treatments, e.g., HF etching, vacuum annealing, and surface functionalization, which improve the surface and defect properties.[58] Moreover, interrupted percolation paths in the current BHJ morphology can also lead to enhanced recombination and limit the efficiency, as not the entire amount of photoinduced charge carriers can move to the electrodes. To overcome this, the fabrication of a defined BHJ morphology via nanoimprinting is a promising approach.

In summary, our TA measurements point out that polymer structural order plays a significant role in hybrid solar cells, though Si can significantly enhance the initial polaron yield even in the disordered RRa-P3HT (Figure 5b). Below, it will be investigated whether bound polaron pairs or mobile charge carriers are formed in the P3HT/Si heterojunctions.

3.4. Temporal Evolution of the Charge Generation Process. Having identified the features of GSB (about 415−620 nm), polaron absorption (about 620−900 nm), and singlet-exciton absorption (900−1150 nm), we now consider their inherent kinetics in a quantitative fashion. Figure 6a shows the evolution of the TA signals for the GSB (at 550 nm), the polaron absorption (at 660 nm), and the singlet exciton absorption (at 1000 nm) of aggRR-P3HT/poly-Si PHJ on a time scale up to 2 ns with a time resolution of 40 fs. From Figure 6a, a few observations can be made immediately. First, the GSB and the singlet exciton absorption reach their maximum signal with a rise time of 40 fs (see also the inset), i.e., within the experimental resolution. This observation is important, as it implies that the exciton is formed *directly upon photoexcitation*. Second, the polaron absorption signal shows a *delayed* rise. It reaches its maximum at about 300 fs. This rise of the polaron signal is matched by a corresponding initial decay of the singlet exciton absorption signal. This suggests that the singlet exciton, formed by absorption, decays to form polarons. Third, the ultrafast time evolution of the GSB and the singlet exciton absorption signal is very similar. This can be readily understood by an additional ultrafast nonradiative decay mechanism of at least some of the excited P3HT molecules. A minimal rate model that allows relaxation of the exciton into the polaron by dissociation and to the P3HT ground state by nonradiative decay directly renders the result that the yield of each channel is given by the ratio of the individual rate to the sum of both.[59] The spectroscopic signal is additionally weighted by the respective extinction coefficients. The exciton serves as a reservoir, and the same femtosecond kinetics is observed for the decay of the exciton signal and the recovery of the GSB.[59] Nonradiative electronic decay on the femtosecond time scale is now widely reported for a large variety of molecular systems[60−64] and believed to be frequently mediated by conical intersections.[65,66] Whether a conical intersection is also responsible for the observed ultrafast nonradiative decay in P3HT films has to be clarified in the future. It has recently been established in conjugated polymers that exciton localization occurs in tens of femtoseconds and leads to nonemissive states.[67,68] Single-molecule spectroscopy has correlated the ultrafast relaxation to aggregated regions of the polymer.[69]

To further substantiate the conclusion that the polarons are formed from the excitons, we have fitted the decay of the transient data. Already a visual interpretation of the kinetic traces shows that there is the ultrafast signal change as discussed above and an additional slower component. It is possible to model the decay of the GSB and the singlet exciton absorption as a stretched exponential (SE) curve. A stretched exponential decay is expected for films that possess an ensemble of ordered and disordered regions and a correspondingly broad distribution of decay times.[70,71] As we are particularly interested in the initial signal changes, we treat the ultrafast component separately by fitting the GSB and the singlet exciton absorption according to the function

$$\Delta OD = A_1 \exp(-t/\tau_1) + A_{SE} \exp(-t/\tau_{SE})^{\beta} + \text{const} \qquad (1)$$

We also use eq 1 to fit the polaron absorption signal. The polaron decay will also be characterized by a distribution of relaxation times, because of various on-chain and interchain recombination paths. Therefore, the use of a stretched exponential fit for the decay kinetics is justified.[71] The fit curves obtained are indicated as solid colored curves in Figure 6a. The fit parameters A_1, A_{SE}, τ_1, τ_{SE} are listed in Table 2 for the ΔOD signals at 660 nm (polaron), 1000 nm (exciton), and 550 nm (GSB). The exponent β was found to be 0.5 in all cases. Figure 6b illustrates how these fit parameters vary as a function of probe wavelength across the entire detected spectral range.

Table 2. Fit Parameters: Amplitudes and Time Constants for the Transient Species in Figure 6

parameter	polaron (660 nm)	exciton (1000 nm)	GSB (550 nm)
A_1	-14.6×10^{-3}	2.6×10^{-3}	-1.6×10^{-3}
τ_1 (ps)	0.14	0.14	0.14
A_{SE}	20.2×10^{-3}	7.1×10^{-3}	-13.6×10^{-3}
τ_{SE} (ps)	0.41	0.63	0.6

We find that the singlet exciton absorption and the GSB both decay with a similar first ultrafast time constant of 140 fs, followed by a slower decay, for which the combination of $\tau_{SE} \approx 0.6$ ps and $\beta = 0.5$ yields an average decay time $\langle\tau\rangle$ of about 1.2 ps. We find the *same* time constant of 140 fs for the delayed buildup of the polaron signal, followed by a decay characterized by an average decay time $\langle\tau\rangle$ of about 0.8 ps. The fact that the rise of the polaron population is correlated with a simultaneous decay of the exciton population is strong evidence that the polarons are created through the dissociation of singlet excitons.[72]

From the overview of the fit parameters in Figure 6b, we see that the time constants found in our fits stay rather constant over the entire spectral range of the individual transient species. Moreover, the fastest time constant τ_1 is present over the entire probe spectral range. This implies that the chosen model describes the intrinsic dynamics properly. The variations of the τ_{SE} decay time between the transient species can be attributed to different recombination processes for polarons and excitons as well as energy transfer processes between coils and aggregates suggested above and demonstrated in more detail below. The amplitudes for the ultrafast 140 fs component (A_1) and the slower component (A_{SE}) have the same sign in the spectral region describing the singlet exciton absorption, that is, from 900 to 1150 nm and beyond. For shorter probe wavelengths, when the polaron absorption is probed, the amplitude A_1 for the 140 fs component changes sign, as it no longer describes an absorption decay but rather the delayed rise of the polaron absorption. This evident correlation between singlet exciton decay and polaron rise further strengthens our interpretation. Similar kinetics are observed for neat P3HT, RRa-P3HT/poly-Si PHJ, and RR-P3HT:Si-ncs BHJ, independent of pump polarization orientation. At 6 ns, the GSB shows 5% of its initial signal magnitude that we assign to long-lived photoexcitations, which can readily be harvested in a solar cell. At this point we want to emphasize that the samples were optimized for ultrafast TA measurements and not for optimum solar cell performance, where reduced recombination can be achieved via various methods as detailed in the introduction and the conclusion sections.

For an absorbed number of photons of 2.6×10^9 per pulse at an excitation of 9 μJ/cm^2 at 518 nm, we obtain an excited state areal density of 2.4×10^{13} cm^{-2} (Table 3, see details in Supporting Information). The polaron cross section of $(3.4 \pm 2) \times 10^{-16}$ cm^2, the polaron molar extinction coefficient of

Table 3. Parameters of the P3HT/Si Heterojunction with 9 μJ/cm^2 Excitation at 518 nm

parameter	
absorbed photons	2.6×10^9/pulse
areal density of excitations (cm^{-2})	2.4×10^{13}
polaron cross section (cm^2)	$(3.4 \pm 2) \times 10^{-16}$
initial charge density (cm^{-3})	6×10^{18}

Table 4. Initial Quantum Yields of Charges in Neat P3HT and aggRR-P3HT/poly-Si PHJ

Sample	P3HT$^+$	P3HT$^-$	P3HT + E	Si$^-$
aggP3HT	0.17	0.17	0.83	0
aggP3HT/Si	0.38	0.13	0.62	0.25

$(4 \pm 1) \times 10^4$ L mol^{-1} cm^{-1}, and the initial charge density of 6×10^{18} cm^{-3} obtained from our measurement series are similar to previous investigations of RR-P3HT:PCBM BHJ at comparable excitation fluence.[16,30,73]

With the interpretation that photoexcitation generates excitons that subsequently decay into polarons, it is possible to estimate the maximum yield of polarons formed initially by considering the relative magnitudes of the TA signals at 300 fs given in Figure 5. Details of the calculations can be found in the Supporting Information. While we estimate a maximum quantum yield of 17% for the formation of the P3HT$^+$ polaron in a neat film of aggRR-P3HT, this value raises to 38% in the planar heterojunction (aggRR-P3HT/poly-Si PHJ) in combination with a maximum Si$^-$ yield of 25% (Table 4). We note that in the heterojunction device, the P3HT layer covering the silicon has a film thickness of only 40 nm so that excitons are created close to the donor−acceptor interface. The significant enhancement of exciton dissociation in the presence of silicon implies that silicon performs very well as an electron accepting material. The charge yield points to efficient electron transfer and a spatial exciton delocalization in ordered P3HT of about 10 nm, in agreement with previous investigations.[74,75]

The obtained polaron yields are similar to RR-P3HT:PCBM studied previously,[29] which raises the hope for aggRR-P3HT/Si heterojunctions to achieve comparable power conversion efficiencies as existing and even commercially available thin film solar cells based on RR-P3HT:PCBM BHJs.[32]

3.5. Charge Recombination Processes. So far we have substantiated the discussion of the yield and the time scale of the exciton dissociation into polarons. Now we address the issue of whether the positive and negative polarons formed are still Coulomb-bound as a geminate pair or whether they are free charge carriers. This question is crucial for the efficient operation of photovoltaic devices. There is no obvious reason why the TA spectra of bound polarons should be very different from those of free polarons. We are therefore not able to distinguish between bound and free polarons on the basis of the TA spectra. However, it is possible to distinguish the two species by considering their recombination kinetics. We expect a pair of geminately bound positive and negative polarons to recombine (radiatively or nonradiatively) with each other, i.e., monomolecularly. Their decay should therefore not be affected by the overall number density of bound polaron pairs that are formed upon photoexcitation. Further, the number density of bound polaron pairs formed should not impact on the singlet exciton population, thus leaving the decay kinetics of the singlet exciton absorption or the GSB unaltered. In contrast, if exciton dissociation results in the generation of free, i.e., nongeminate, positive and negative polarons, then these charges can only recombine when they meet each other, i.e., by bimolecular charge−charge annihilation. The probability of meeting the oppositely charged polaron thereby increases with the number density of polarons formed.[16,73] Further, singlet excitons can recombine through quenching by free polarons, and the probability for this exciton-charge annihilation also increases with the number density of free polarons.[16,76,77] Thus, in summary, for geminately bound polarons we expect the decay transients of polaron absorption, singlet exciton absorption, and GSB to be independent of excitation fluence, while we expect accelerated decays with increasing excitation fluence for free polarons generated upon singlet exciton dissociation.

To study the role of delocalization and the nature of the recombination processes in P3HT/Si heterojunctions, we record Vis−NIR TA spectra up to 2 ns delay with increased excitation fluences from 4 to 60 μJ/cm^2. The absorption signals of the corresponding relevant transient species in aggRR-P3HT/poly-Si PHJ (Figure 7a), RRa-P3HT/poly-Si PHJ (Figure 7b), and RR-P3HT:Si-ncs BHJ (Figure S8) are normalized against their individual initial maximum. This allows the study of the recombination rate as a function of excitation fluence. For the RRa-P3HT/poly-Si PHJ sample we find the decay kinetics to be independent of excitation fluence. Consequently, the polarons formed in a PHJ of silicon with RRa-P3HT are predominantly Coulomb-bound. In contrast, we find enhanced decay rates with increasing excitation fluence for aggRR-P3HT/poly-Si PHJ, suggesting the predominant formation of free polarons. The same observation is made for RR-P3HT:Si-ncs BHJs (Figure S8). In Figure 7a the enhanced decay rate leads to an apparent shift of the maximum of polaron absorption to earlier times, covering the delayed polaron rise.

Consequently, in the aggRR-P3HT/poly-Si PHJ and the RR-P3HT:Si-ncs BHJ photoinduced ultrafast generation of free charges is obtained, which opens the route for efficient charge extraction from the active layer in the hybrid devices. In fact, it was recently shown that the competition between extraction and bimolecular recombination of mobile charges determines the dependence of the photocurrent on the applied bias and therefore the fill factor in RR-P3HT:PCBM BHJ devices.[78,79]

It is worthwhile to briefly reflect on these results. For the RRa-P3HT/poly-Si PHJ, photoexcitation near the hybrid interface results in excitons that are mostly localized on coiled chains. An electron is then transferred to the poly-Si with a time constant of 140 fs, leaving behind a P3HT$^+$ cation, i.e., a positive polaron. In silicon, the electron can be expected to be well delocalized because of the high dielectric screening. However, on the coiled P3HT chain, the conjugation length is low and the energetic disorder is high. As a result, the positive polaron is localized in the sense that its coherence length and its mobility are low. It seems that the presence of a more "pointlike" and moreover "immobile" positive charge on the P3HT prevents the formation of free polarons. In a certain way, the situation is comparable to that of a point charge in front of a metal that feels an attractive force. In contrast for the aggRR-P3HT/poly-Si PHJ, a significant fraction of the excitations are created on planar, aggregated chains that are characterized by a high conjugation length and low energetic disorder. After charge transfer, the delocalized electron in the silicon is thus interacting with a positive polaron that not only is

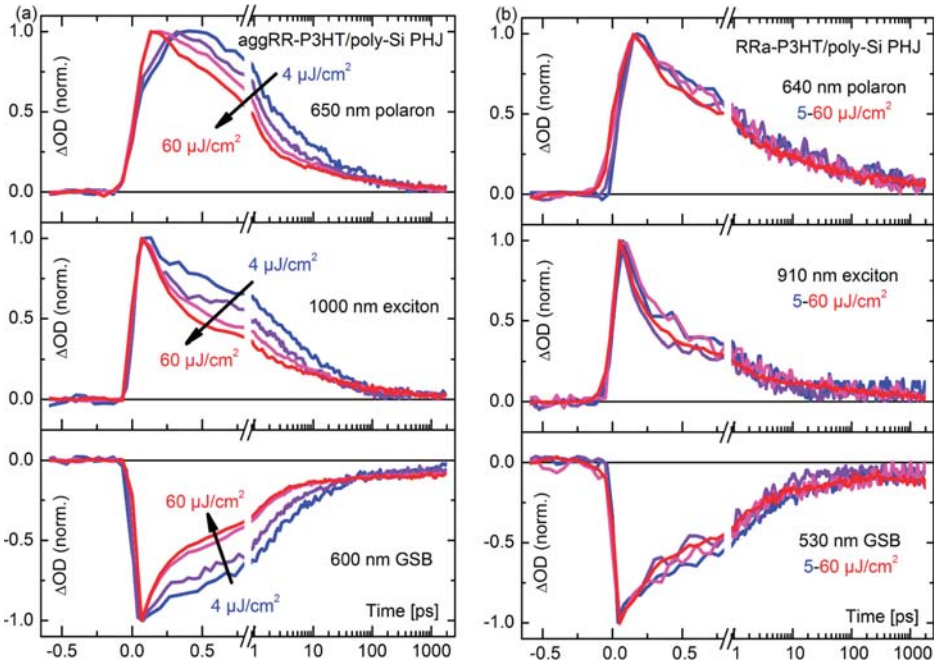

Figure 7. (a) Decay of TA signals for increased excitation fluences (4, 10, 40, and 60 μJ/cm^2 at 518 nm) reveals bimolecular nongeminate recombination in the case of aggRR-P3HT/poly-Si PHJ. (b) Decay of TA signals for increased excitation fluences (5, 20, 40, and 60 μJ/cm^2 at 518 nm) reveals monomolecular geminate recombination in the case of RRa-P3HT/poly-Si PHJ.

comparatively delocalized but also has a high initial mobility due to the low disorder. Such a polaron might move away from the hybrid interface, for example, by spectral diffusion to slightly longer conjugated segments, thereby overcoming the weak Coulomb attraction to the delocalized electron in the silicon and thus leading to the formation of a free pair of positive and negative charge. This finding is also supported by anisotropy measurements (Figure S10). It seems that a key issue in exciton dissociation is the delocalization, the dielectric screening, and the mobility of both the electron *and* the hole. Thus, a significant implication of the polymer structural order for hybrid and organic solar cells becomes evident and can be understood on a microscopic level.

Our interpretation of the results is based on the concept of singlet exciton dissociation into bound or free polaron pairs that we support by Figures 5 and 6. From the excitation fluence of 4 μJ/cm^2, where bimolecular annihilation sets in, we derive a mean excitation spacing of more than 6 nm in aggRR-P3HT and RR-P3HT, assuming an isotropic distribution of photoexcitations within the pump−probe volume. This finding reveals that despite the 6 nm (~15 thiophene repeating units) separation between the initial photoexcitations, the subsequent bimolecular interactions due to the generated mobile polarons can still take place pointing to high charge carrier mobility and rather spatially delocalized excitations, in agreement with other TA measurements for conjugated polymers,[29,74] and supporting the degree of delocalization indicated from our quantum yield calculations mentioned above.

It was previously suggested that polarons in conjugated polymers may also be generated from higher excitonic states accessed by sequential excitation or by exciton−exciton annihilation.[33,80−82] These delocalized "hot exciton" charge-transfer states are supposed to exhibit a higher dissociation probability via enhanced electron−hole separation and charge mobility.[75,83,84] These additional processes cannot, however, be the dominant polaron formation pathway in the present work for several reasons. First, the polaron formation happens with a 140 fs time, which is too fast for bimolecular annihilation processes.[16,77,82] Second, sequential excitations during the pump pulse come into play only at very high excitation fluences starting at 100−400 μJ/cm^2.[81,82] Third, the polarons show the same intensity dependence as the excitons (Figure S9) and are thus generated from singlet excitons.

3.6. Variation of Excitation Wavelength.

3.6.1. Energy Transfer. We have seen that the conformation of the polymer chain has a major impact on the nature of the photogenerated charges. The number of excitations created on coiled chains or on aggregated chains is determined not only by the choice of P3HT regioregularity and solvent but also by the choice of excitation wavelength. Figure 8 shows ultrafast UV−Vis TA spectra of neat RR-P3HT thin films at 60 fs, 300 fs, 13 ps, and 140 ps with excitation at 450 nm (blue solid curve) and 600 nm (red solid curve). The spectra are normalized against the GSB so that signal changes solely inherent to the variation of the pump wavelength can be studied. The transient absorption spectra contain signatures of GSB (425−625 nm) and of polaron absorption (>625 nm). The inverted RR-P3HT film absorption spectrum (OD, green solid curve) is scaled to the RR-P3HT GSB peaks. The calculated difference spectra between the GSB and the inverted thin film absorption are shown as dashed curves for both excitation wavelengths (TA − OD, dashed). These difference spectra are then compared to the scaled absorption spectrum of RR-P3HT in dilute chloroform solution (OD, cyan solid line).

At 60 fs, the GSB of the RR-P3HT film is significantly broader when excited at 450 nm than for excitation at 600 nm. Immediately after excitation with 600 nm, the GSB of the film lacks the spectral components equivalent to the absorption spectrum in dilute chloroform solution. In dilute chloroform solution, polymers form coils as the chains curl up. Thus, at 60 fs after excitation, only planar

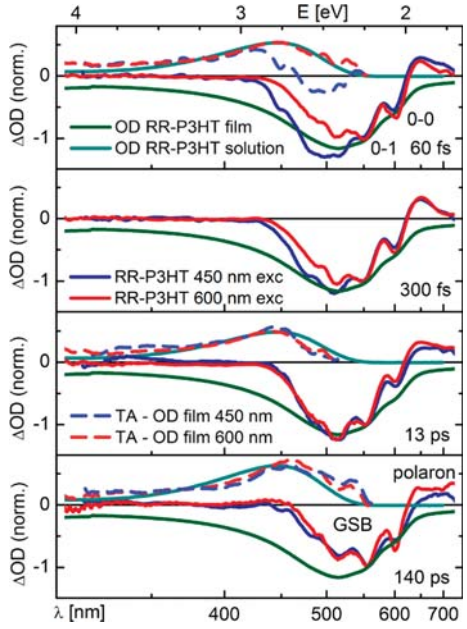

Figure 8. UV−Vis TA spectra of RR-P3HT thin film at 60 fs, 300 fs, 13 ps, and 140 ps with excitation at 450 nm (solid blue curve) and at 600 nm (solid red curve). The inverted absorption spectrum of RR-P3HT thin film (OD, green solid curve) is scaled to the RR-P3HT GSB peaks to extract the differences (TA − OD, corresponding dashed curves) between the transient spectra and the film absorption, which are compared to the absorption spectrum of RR-P3HT in dilute chloroform solution (OD, cyan solid curve).

aggregated chains are excited by light with 600 nm, while both coiled and aggregated chains are excited by light with 450 nm. This distinct difference between the spectra obtained for excitation with 450 nm and with 600 nm stays visible up to 13 ps. At 13 ps, the film GSB coincides for both pump wavelengths. The difference between the GSB at 13 ps and the inverted film absorption spectrum corresponds to the absorption spectrum of P3HT coils except for some weak low energy tail around 480 nm.

At 140 ps after excitation, the GSB shows even clearer vibrational structure and the difference between GSB and inverted film absorption spectrum reveals spectral parts missing in the GSB which are even beyond the coil absorption spectrum. This indicates further slow energy migration within the aggregates toward more planar and extended conjugated segments, e.g., via torsional relaxation or excitation energy transfer (EET).[85,86] Thus, the GSB beyond 13 ps reveals the absorption spectrum due to RR-P3HT aggregates only, which is taken from the 140 ps case for Figure 9. It can be seen that aggregate absorption ranges from 460 to 625 nm.

For excitation at 600 nm, the GSB at 60 fs and the GSB at 140 ps are identical except for the changes in the 0−0 peak intensity already discussed in the context of Figure 5. In contrast, for excitation at 450 nm, the GSB loses the higher energy contributions that are attributed to coiled chains. We attribute this behavior to an energy transfer from unordered (coils) to ordered domains (aggregates, planar segments) in RR-P3HT films, as also indicated in the TA measurements of the PHJs and the BHJ above. Parts a and b of Figure 3 show that the PL of RR-P3HT in dilute solution (coils) overlaps with the absorption spectrum of RR-P3HT thin films, which is a prerequisite for efficient electronic energy transfer.[68,70] With excitation of the RR-P3HT film at

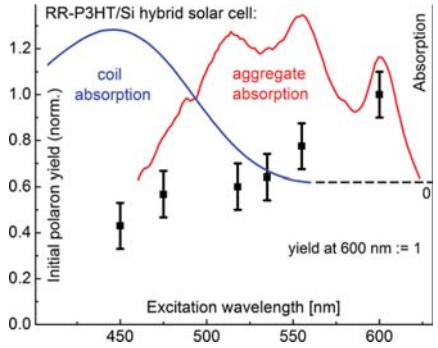

Figure 9. Dependence of initial polaron yield (black squares) on excitation wavelength for RR-P3HT/Si heterojunctions. Selective excitation of coiled (blue curve) vs aggregated (red curve) RR-P3HT domains reveals greater than a factor of 2 more efficient charge separation if exciting directly the aggregated RR-P3HT domains.

450 nm, both coils and aggregates are addressed; however, the coils undergo downhill energy transfer to the aggregated regions. An analysis of the ratio between the GSB intensity at 480 nm for excitation at 450 and at 600 nm reveals a forward $1/e$ energy transfer time of about 3 ps (Figure S5, see more details in the Supporting Information). It is interesting to note that this is the same time constant as observed for the energy transfer from glassy phase to a planarized phase in poly(9,9-dioctylfluorene).[37]

3.6.2. Role of Excess Energy. Figure 8 allows us to distinguish the absorption range of coils and aggregates. For excitation wavelengths above 500 nm one predominantly addresses the aggregated RR-P3HT regions. For excitation above 550 nm one exclusively addresses the aggregated RR-P3HT regions. Furthermore, with excitation wavelengths below 500 nm one predominantly addresses the coiled RR-P3HT regions. We can therefore selectively excite ordered or disordered regions of P3HT films. Variation of the excitation wavelength thus provides an alternative approach to control whether coiled or aggregated chains are initially excited. We use this to further corroborate our results obtained on the morphology dependence of the polaron yield. Figure 9 shows the initial polaron yield at about 300 fs as a function of the excitation wavelength at the hybrid heterojunction with the intermediately aggregated RR-P3HT. For comparison, the absorption spectra of coiled and of aggregated P3HT chains (taken as the GSB at 140 ps from Figure 8) are also shown.

For this experiment, the pump pulse was adjusted to central wavelengths of 450, 475, 518, 535, 555, and 600 nm and pulse durations of about 15 fs with the same experimental pump−probe conditions. For directly comparing the transient spectra of hybrid RR-P3HT/Si heterojunctions excited at different wavelengths, the transient spectra were scaled according to the individual initial P3HT GSB (internal standard). In this case, comparing the initial polaron absorption magnitudes of the various TA spectra can reveal changes in polaron yield solely inherent to the different excitation wavelengths while considering the same number of initial photoexcitations in the P3HT/Si heterojunction.

Figure 9 reveals an enhancement of more than a factor of 2 of initial polaron yield by increasing the excitation wavelength from 450 to 600 nm. The trend was obtained independently on the device structure, i.e., for PHJ and BHJ geometries. The error bars result from multiple measurements of several hybrid RR-P3HT/Si samples under the nominally same experimental conditions.

The increase by a factor of 2 matches the enhancement of the polaron yield which was observed in Figure 5a,b by comparing highly aggregated aggRR-P3HT/poly-Si PHJ with RRa-P3HT/poly-Si PHJ. In the latter case, P3HT coils were predominant. Our findings are an extension of previous TA investigations where the degree of aggregation was varied via thermal annealing.[19] In conclusion, we record the same factor of 2 more efficient charge generation in aggregated polymer-based hybrid heterojunctions compared to the unaggregated version by two different and independent methods: (i) by using different P3HT configurations and therefore solely changing the structural order in the P3HT film (Figure 5) and (ii) by solely changing the excitation wavelength and therefore selectively exciting defined P3HT regions (Figure 9). If excess photon energy was necessary for the exciton dissociation process, we would expect a high initial polaron yield for excitation at 450 nm and a lower polaron yield for 600 nm excitation. The fact that we observe exactly the opposite tendency clarifies that excess photon energy is not required; however, structural order is essential. Whether this order enhances charge separation by increasing the initial charge carrier mobility or by improving the overall energetics or by both remains an intriguing question for further research.

4. CONCLUSIONS AND IMPLICATIONS FOR HYBRID AND ORGANIC PHOTOVOLTAIC DEVICES

We have comprehensively studied the nature of primary photoexcitations and their inherent dynamics in neat P3HT and in hybrid P3HT/Si thin films by ultrabroadband (UV−Vis−NIR) transient absorption (TA) spectroscopy with 40 fs time resolution and varied excitation wavelength. Hybrid heterojunctions with 30 nm thin polycrystalline Si layers or Si nanocrystals were processed with P3HT of varied polymer structural order and film geometry. The spatial and optical properties of planar and bulk heterojunctions show that Si does not change the P3HT structure and leads to a broad film absorption range from the UV to 1100 nm needed for efficient light-harvesting.

Scheme 1 summarizes the primary photoinduced processes in hybrid P3HT/Si thin film heterojunctions. In the TA experiments, we can identify the transient signatures of P3HT polarons (620−900 nm) and singlet excitons (900−1150 nm). Our measurements reveal singlet excitons in P3HT as primary photoexcitation with a subsequent ultrafast electron transfer from P3HT to Si as inherent photovoltaic conversion process for all employed hybrid heterojunctions. The addition of Si to RR-P3HT or RRa-P3HT significantly enhances the polaron yield in the active layer

These experiments show that silicon is a particularly favorable electron acceptor because of the highly efficient charge delocalization. Moreover, the higher dielectric constant, compared to the state-of-the-art electron acceptor PCBM, allows for an improved screening of the electron, preventing back transfer. Besides these advantages compared to organic semiconductors, Si is abundantly available and offers the possibility of selective surface modifications and thus interface engineering.

In neat P3HT and in P3HT/Si heterojunctions, we reveal a *delayed* polaron formation compared to singlet excitons, which appear within the experimental time resolution of 40 fs. The population of polarons has a maximum at about 300 fs after excitation. Thus, charge generation is probed in *real time*, revealing a 140 fs rise time for polarons, which is found to correlate with the initial 140 fs decay of the singlet excitons in P3HT. We conclude that the

Scheme 1. Primary Photoinduced Processes in Hybrid P3HT/Si Thin Film Heterojunctions

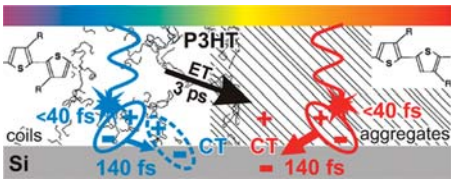

correlated decay of the exciton population and the rise of the polaron population indicate polaron formation via singlet exciton dissociation. In particular we stress that there is no significant polaron population immediately after excitation, i.e., after 40 fs. The ultrafast charge transfer (CT) process implies a strong exchange integral of the excited state orbitals of electron donor and acceptor.

This result demonstrates that the observation of ultrafast charge carrier generation is not in contradiction to the initial formation and subsequent dissociation of a singlet exciton, in contrast to recent suggestions made for the mechanism of charge carrier generation in the blend of the low band gap polymer PCDTBT with PCBM.[31] Their argument essentially pertains to the fact that free charges can be observed as fast as 100 fs after photoexcitation. Similar interpretations for a MDMO-PPV:PCBM blend have been made earlier.[28] This issue, whether light absorption immediately creates free charge carriers *or* excitons, is central to the understanding and optimization of photoconversion in organic and hybrid solar cells. A problem in resolving this issue pertains to the experimental limits of time resolution and spectral range that are available for optical probing. Here we have developed a novel ultrabroadband gap-free TA spectroscopy setup with a time resolution of 40 fs over the entire spectral range from 415 to 1150 nm. This allows us to monitor *both* the decay of the primary excitation and its evolution into a charge pair state.

We have investigated the difference in the polaron formation process for RRa-P3HT, where only a small part of the film is composed of aggregates and for RR-P3HT containing an increased fraction of aggregates. TA measurements with varied excitation fluence clarify that in hybrid P3HT/Si heterojunctions with aggregated P3HT exciton dissociation predominantly leads to free charge carriers, which can in principle be extracted as photocurrent. This is evident from the fact that in RR-P3HT/Si planar as well as in bulk heterojunctions we observe an increasing recombination rate of polarons with increasing excitation fluence, indicating bimolecular nongeminate recombination of charges outside the Coulombic capture radius. These recombination rates indicate that besides the primary photoconversion processes, the charge transport and extraction at the electrodes are crucial issues toward more efficient hybrid photovoltaic devices. Although we have already performed initial systematic studies on the reduction of Si dangling bond defects in the Si-ncs,[58] which act as recombination centers, the charge transport and extraction need to be further addressed in future work. However, power conversion efficiencies of 1% have been shown recently with the first P3HT:Si-ncs blends.[8] Combined with an optimized charge transport and extraction at the electrodes, their efficiency is expected to increase.

In contrast, for RRa-P3HT/Si, where there is initially a higher proportion of excitons on coiled P3HT chains, the decay rate is

independent of the excitation fluence, suggesting monomolecular geminate recombination of bound carriers, making it less suitable for photovoltaics from the photophysical perspective. Geminate recombination was recently also found for polymer−polymer blends and seems to be one of the main obstacles to be overcome for photovoltaic applications.[77,87] We attribute this difference between RRa- and RR-P3HT to a more localized hole in RRa-P3HT leading to localized charge carriers in RRa-P3HT/Si as opposed to highly delocalized charge carriers in RR-P3HT/Si revealing that high polymer structural order is a necessity for free charge generation in P3HT/Si.

Quantitatively, we can demonstrate that using aggregated P3HT leads to a *factor of 2 higher polaron yield* compared to employing disordered P3HT in photovoltaics, by two different and independent methods: (i) by using different P3HT configurations and therefore solely changing the structural order in the P3HT film and (ii) by solely changing the excitation wavelength and therefore selectively exciting defined P3HT regions. Combined with results from a modified Franck−Condon analysis, we find that the polaron yield in P3HT/Si increases disproportionally with increasing degree of aggregation in P3HT. Moreover, we find that supplying excess energy does *not* assist the charge carrier separation, whereas our results indicate that ultrafast generation of free charges is *more* dependent on polymer structural order. We argue that the larger conjugation length, low energetic disorder, and the concomitant higher initial charge carrier mobility in the planar aggregated P3HT compared to the short conjugation length in coiled P3HT favor the dissociation process into free charge carriers. Additionally, we observed that downhill energy transfer (ET) from coiled to aggregated chains takes place with a time constant of 3 ps.

For this reason, purely organic and hybrid photovoltaic devices using P3HT should employ highly aggregated P3HT. The loss of high-energy polymer absorption can be compensated by stacking heterojunctions in tandem or even multiple solar cells using conjugated polymers with different band gaps.[88,89] Detailed investigations of the optimum Si-nc band gap for charge transfer remains for future research. The present ultrafast spectroscopic studies combined with ongoing P3HT/Si-ncs device optimization in terms of surface and defect properties of the Si-ncs as well as of the film morphology raise the hope to realize efficient P3HT/Si photovoltaic devices.

■ ASSOCIATED CONTENT

Supporting Information. Basic optical and structural characterization of P3HT: 3D AFM images of the samples and modified Franck−Condon analysis, description of the TA spectrometer, formulas of optical densities, cross sections and excitation densities, raw TA data for comparison, energy transfer from amorphous P3HT to aggregated P3HT, quantum yields, P3HT cation absorption spectrum in solution, TA measurements of P3HT in dilute solutions, bimolecular recombination, anisotropy measurements, exemplary 2D gap-free TA maps. This material is available free of charge via the Internet at http://pubs.acs.org.

■ AUTHOR INFORMATION

Corresponding Author
riedle@physik.uni-muenchen.de

■ ACKNOWLEDGMENT

The authors thank H. Bässler (Universität Bayreuth, Germany) for very fruitful discussions, P. Rupp and M. Bradler for experimental support, R. Tautz for help with the P3HT oxidation in solution, M. Algasinger and T. Antesberger for synthesizing the poly-Si, H. Wiggers for providing the Si-ncs, and J. Gmeiner for the synthesis of RRa-P3HT. D.H. is grateful to Studienstiftung des Deutschen Volkes. S.N. is thankful to the Karl-Max von Bauernfeind-Verein and the International Graduate School "Material Science for Complex Interfaces (CompInt)" of the Technische Universität München, Germany. C.S. and A.K. are thankful to the Graduiertenkolleg 1640 of the DFG. E.R. acknowledges funding from the SFB 749.

■ REFERENCES

(1) Thompson, B. C.; Fréchet, J. M. J. *Angew. Chem., Int. Ed.* **2008**, *47*, 58–77.
(2) Brabec, C. J.; Sariciftci, N. S.; Hummelen, J. C. *Adv. Funct. Mater.* **2001**, *11*, 15–26.
(3) Park, S. H.; Roy, A.; Beaupré, S.; Cho, S.; Coates, N.; Moon, J. S.; Moses, D.; Leclerc, M.; Lee, K.; Heeger, A. J. *Nat. Photonics* **2009**, *3*, 297–303.
(4) Gur, I.; Fromer, N. A.; Geier, M. L.; Alivisatos, A. P. *Science* **2005**, *3*, 462–465.
(5) Jabbour, G. E.; Doderer, D. *Nat. Photonics* **2010**, *4*, 604.
(6) Huynh, W. U.; Dittmer, J. J.; Alivisatos, A. P. *Science* **2002**, *295*, 2425–2427.
(7) Oosterhout, S. D.; Wienk, M. M.; van Bavel, S. S.; Thiedmann, R.; Koster, L. J. A.; Gilot, J.; Loos, J.; Schmidt, V.; Janssen, R. A. J. *Nat. Mater.* **2009**, *8*, 810–824.
(8) Liu, C.-Y.; Holman, Z. C.; Kortshagen, U. R. *Nano Lett.* **2009**, *9*, 449–452.
(9) Dietmueller, R.; Stegner, A. R.; Lechner, R.; Niesar, S.; Pereira, R. N.; Brandt, M. S.; Ebbers, A.; Trocha, M.; Wiggers, H.; Stutzmann, M. *Appl. Phys. Lett.* **2009**, *94*, 113301.
(10) Niesar, S.; Dietmueller, R.; Nesswetter, H.; Wiggers, H.; Stutzmann, M. *Phys. Status Solidi A* **2009**, *206*, 2775–2781.
(11) Beek, W. J. E.; Wienk, M. M.; Janssen, R. A. J. *Adv. Funct. Mat.* **2006**, *16*, 1112–1116.
(12) Briseno, A. L.; Holcombe, T. W.; Boukai, A. I.; Garnett, E. C.; Shelton, S. W.; Fréchet, J. M. C.; Yang, P. *Nano Lett.* **2010**, *10*, 334–340.
(13) Liu, J.; Kadnikova, E. N.; Liu, Y.; McGehee, M. D.; Fréchet, J. M. J. *J. Am. Chem. Soc.* **2004**, *126*, 9486–9487.
(14) Liu, J.; Tanaka, T.; Sivula, K.; Alivisatos, A. P.; Fréchet, J. M. J. *J. Am. Chem. Soc.* **2004**, *126*, 6550–6551.
(15) McDonald, S. A.; Konstantatos, G.; Zhang, S.; Cyr, P. W.; Klem, E. J. D.; Levina, L.; Sargent, E. H. *Nat. Mater.* **2005**, *4*, 138–142.
(16) Howard, I. A.; Mauer, R.; Meister, M.; Laquai, F. *J. Am. Chem. Soc.* **2010**, *132*, 14866–14876.
(17) Kim, Y.; Cook, S.; Tuladhar, S. M.; Choulis, S. A.; Nelson, J.; Durrant, J. R.; Bradley, D. D. C.; Giles, M.; McCulloch, I.; Ha, C.-S.; Ree, M. *Nat. Mater.* **2006**, *5*, 197–203.
(18) Peet, J.; Kim, J. Y.; Coates, N. E.; Ma, W. L.; Moses, D.; Heeger, A. J.; Bazan, G. C. *Nat. Mater.* **2007**, *6*, 497–500.
(19) Clarke, T.; Ballantyne, A. M.; Nelson, J.; Bradley, D. D. C.; Durrant, J. R. *Adv. Funct. Mater.* **2008**, *18*, 4029–4035.
(20) Spano, F. C. *J. Chem. Phys.* **2005**, *122*, 234701.
(21) Clark, J.; Silva, C.; Friend, R. H.; Spano, F. C *Phys. Rev. Lett.* **2007**, *98*, 206406.
(22) McCullough, R. D.; Tristram-Nagle, S.; Williams, S. P.; Lowe, R. D.; Jayaraman, M. *J. Am. Chem. Soc.* **1993**, *115*, 4910–4911.
(23) Chen, T.-A.; Wu, X; Rieke, R. D. *J. Am. Chem. Soc.* **1995**, *117*, 233–244.
(24) Sirringhaus, H.; Brown, P. J.; Friend, R. H.; Nielsen, M. M.; Bechgaard, K.; Langeveld-Voss, B. M. W.; Spiering, A. J. H.; Janssen, R. A. J.; Meijer, E. W.; Herwig, P.; de Leeuw, D. M. *Nature* **1999**, *401*, 685–688.
(25) Österbacka, R.; An, C. P.; Jiang, X. M.; Vardeny, Z. V. *Science* **2000**, *287*, 839–842.

(26) Chang, J.-F.; Clark, J.; Zhao, N.; Sirringhaus, H.; Breiby, D. W.; Andreasen, J. W.; Nielsen, M. M.; Giles, M.; Heeney, M.; McCulloch, I. *Phys. Rev. B* **2006**, *74*, 115318.
(27) Mauer, R.; Kastler, M.; Laquai, F. *Adv. Funct. Mater.* **2010**, *20*, 2085–2092.
(28) Brabec, C. J.; Zerza, G.; Cerullo, G.; De Silvestri, S.; Luzzati, S.; Hummelen, J. C.; Sariciftci, S. *Chem. Phys. Lett.* **2001**, *340*, 232–236.
(29) Piris, J.; Dykstra, T. E.; Bakulin, A. A.; van Loosdrecht, P. H. M.; Knulst, W.; Trinh, M. T.; Schins, J. M.; Siebbeles, L. D. A. *J. Phys. Chem. C* **2009**, *113*, 14500–14506.
(30) Guo, J.; Ohkita, H.; Benten, H.; Ito, S. *J. Am. Chem. Soc.* **2010**, *132*, 6154–6164.
(31) Banerji, N.; Cowan, S.; Leclerc, M.; Vauthey, E.; Heeger, A. J. *J. Am. Chem. Soc.* **2010**, *132*, 17459–17470.
(32) Brabec, C. J.; Gowrisankar, S.; Halls, J. J. M.; Laird, D.; Jia, S.; Williams, S. P. *Adv. Mater.* **2010**, *22*, 3839–3856.
(33) Guo, J.; Ohkita, H.; Benten, H.; Ito, S. *J. Am. Chem. Soc.* **2009**, *131*, 16869–16880.
(34) Etzold, F.; Howard, I. A.; Mauer, R.; Meister, M.; Kim, T.-D.; Lee, K.-S.; Baek, N. S.; Laquai, F. *J. Am. Chem. Soc.* **2011**, *133*, 9469–9479.
(35) Grancini, G.; Polli, D.; Fazzi, D.; Cabanillas-Gonzalez, J.; Cerullo, G.; Lanzani, G. *J. Phys. Chem. Lett.* **2011**, *2*, 1099.
(36) Yoshino, K.; Hayashi, S.; Sugimoto, R. *Jpn. J. Appl. Phys.* **1984**, *23*, L899.
(37) Khan, A. L. T.; Sreearunothai, P.; Herz, L. M.; Banach, M. J.; Köhler, A. *Phys. Rev. B* **2004**, *69*, 085201.
(38) Campbell, A. R.; Hodgkiss, J. M.; Westenhoff, S.; Howard, I. A.; Marsh, R. A.; McNeill, C. R.; Friend, R. H.; Greenham, N. C. *Nano Lett.* **2008**, *8*, 3942–3947.
(39) Scharsich, C; Lohwasser, R.; Asawapirom, U.; Scherf, U.; Thelakkat, M.; Köhler, A. Manuscript submitted, **2011**.
(40) Knipping, J.; Wiggers, H.; Rellinghaus, B.; Roth, P.; Konjhodzic, D.; Meier, C. *J. Nanosci. Nanotechnol.* **2004**, *4*, 1039–1044.
(41) Germack, D. S.; Chan, C. K.; Kline, R. J.; Fischer, D. A.; Gundlach, D. J.; Toney, M. F.; Richter, L. J.; DeLongchamp, D. M. *Macromolecules* **2010**, *43*, 3828–3836.
(42) Scholz, M.; Gjukic, M.; Stutzmann, M. *Appl. Phys. Lett.* **2009**, *94*, 012108.
(43) Megerle, U.; Pugliesi, I.; Schriever, C.; Sailer, C. F.; Riedle, E. *Appl. Phys. B: Lasers Opt.* **2009**, *96*, 215–231.
(44) Wilhelm, T.; Piel, J.; Riedle, E. *Opt. Lett.* **1997**, *22*, 1494–1496.
(45) Riedle, E.; Beutter, M.; Lochbrunner, S.; Piel, J.; Schenkl, S.; Spörlein, S.; Zinth, W. *Appl. Phys. B: Lasers Opt.* **2000**, *71*, 457–465.
(46) Bradler, M.; Baum, P.; Riedle, E. *Appl. Phys. B: Lasers Opt.* **2009**, *97*, 561–574.
(47) Clark, J.; Chang, J.-F.; Spano, F. C.; Friend, R. H.; Silva, C. *Appl. Phys. Lett.* **2009**, *94*, 163306.
(48) Xu, B.; Holdcroft, S. *Macromolecules* **1993**, *26*, 4457–4460.
(49) Singh, R. K; Kumar, J.; Singh, R.; Kant, R.; Rastogi, R. C.; Chand, S.; Kumar, V. *New J. Phys.* **2006**, *8*, 112.
(50) Schueppel, R.; Schmidt, K.; Uhrich, C.; Schulze, K.; Wynands, D.; Brédas, J. L.; Brier, E.; Reinold, E.; Bu, H.-B.; Baeuerle, P.; Maennig, B.; Pfeiffer, M.; Leo, K. *Phys. Rev. B* **2008**, *77*, 085311.
(51) Jian, X. M.; Österbacka, R.; Korovyanko, O.; An, C. P.; Horovitz, B.; Janssen, R. A. J.; Vardeny, Z. V. *Adv. Funct. Mater.* **2002**, *12*, 587–597.
(52) van Hal, P. A.; Christiaans, M. P. T.; Wienk, M. M.; Kroon, J. M.; Janssen, R. A. J. *J. Phys. Chem. B* **1999**, *103*, 4352.
(53) Albert-Seifried, S; Friend, R. H. *Appl. Phys. Lett.* **2011**, *98*, 223304.
(54) Klessinger, M.; Michl, J. *Excited States and Photochemistry of Organic Molecules*; VCH Publishers, Inc.: New York, 1995; p 36.
(55) Köhler, A.; Bässler, H. *Mater. Sci. Eng., R* **2009**, *66*, 71–109.
(56) Ohkita, H.; Cook, S.; Astuti, Y.; Duffy, W.; Tierny, S.; Zhang, W.; Heeney, M.; McCulloch, I.; Nelson, J.; Bradley, D. D. C.; Durrant, J. R. *J. Am. Chem. Soc.* **2008**, *130*, 3030–3042.
(57) Tsoi, W. C.; Spencer, S. J.; Yang, L.; Ballantyne, A. M.; Nicholson, P. G.; Turnball, A.; Shard, A. G.; Murphy, C. E.; Bradley, D. D. C.; Nelson, J.; Kim, J.-S. *Macromolecules* **2011**, *44*, 2944–2952.
(58) Niesar, S.; Stegner, A. R.; Pereira, R. N.; Hoeb, M.; Wiggers, H.; Brandt, M. S.; Stutzmann, M. *Appl. Phys. Lett.* **2010**, *96*, 193112.
(59) Houston, P. L. *Chemical Kinetics and Reaction Dynamics*; Dover Publications, Inc.: Mineola, NY, 2001; pp 56−58.
(60) Middleton, C. T.; de La Harpe, K.; Su, C.; Law, Y. K.; Crespo-Hernández, C. E.; Kohler, B. *Annu. Rev. Phys. Chem.* **2009**, *60*, 217.
(61) Polli, D.; Altoè, P.; Weingart, O.; Spillane, K. M.; Manzoni, C.; Brida, D.; Tomasello, G.; Orlandi, G.; Kukura, P.; Mathies, R. A.; Garavelli, M.; Cerullo, G. *Nature* **2010**, *467*, 440.
(62) Chudoba, C.; Lutgen, S.; Jentzsch, T.; Riedle, E.; Woerner, M.; Elsaesser, T. *Chem. Phys. Lett.* **1995**, *240*, 35.
(63) Sobolewski, A. L.; Domcke, W.; Hättig, C. *J. Phys. Chem. A* **2006**, *110*, 6301.
(64) Petersson, J.; Eklund, M.; Davidsson, J.; Hammarström, L. *J. Am. Chem. Soc.* **2009**, *131*, 7940.
(65) Domcke, W.; Yarkony, D. R.; Köppel, H. *Conical Intersections: Electronic Structure, Dynamics & Spectroscopy (Advanced Series in Physical Chemistry)*; World Scientific Publishing Co., Inc.: Singapore, 2004.
(66) Köppel, H.; Domcke, W.; Yarkony, D. R. *Conical Intersections: Theory, Computation and Experiments (Advanced Series in Physical Chemistry)*; World Scientific Publishing Co., Inc.: Singapore, 2011.
(67) Ruseckas, A.; Wood, P.; Samual, I. D. W.; Webster, G. R.; Mitchell, W. J.; Burn, P. L.; Sundström, V. *Phys. Rev. B* **2005**, *72*, 115214.
(68) Hwang, I.; Scholes, G. D. *Chem. Mater.* **2011**, *23*, 610–620.
(69) Lin, H.; Tian, Y.; Zapadka, K.; Persson, G.; Thomsson, D.; Mirzov, O.; Larsson, P.-O.; Widengren, J.; Scheblykin, I. G. *Nano Lett.* **2009**, *9*, 4456.
(70) Laquai, F.; Park, Y.-S.; Kim, J.-J.; Basché, T. *Macromol. Rapid Commun.* **2009**, *30*, 1203–1231.
(71) Movaghar, B.; Grünewald, M.; Ries, B.; Bässler, H.; Würtz, D. *Phys. Rev. B* **1986**, *33*, 5545–5554.
(72) Gulbinas, V.; Zaushitsyn, Y.; Sundström, V.; Hertel, D.; Bässler, H.; Yartsev, A. *Phys. Rev. Lett.* **2002**, *89*, 107401.
(73) Shuttle, C. G.; O'Regan, B.; Ballantyne, A. M.; Nelson, J.; Bradley, D. D. C.; Durrant, J. R. *Phys. Rev. B* **2008**, *78*, 113201.
(74) Dogariu, A.; Vacar, D.; Heeger, A. J. *Phys. Rev. B* **1998**, *58*, 10218–10224.
(75) Köhler, A.; dos Santos, D. A.; Beljonne, D.; Shuai, Z.; Brédas, J,-L.; Kraus, A.; Müllen, K.; Friend, R. H. *Nature* **1998**, *392*, 903–906.
(76) Ferguson, A. J.; Kopidakis, N.; Shaheen, S. E.; Rumbles, G. *J. Phys. Chem. C* **2008**, *112*, 9865–9871.
(77) Howard, I. A.; Hodgkiss, J. M.; Zhang, X.; Kirov, K. R.; Bronstein, H. A.; Williams, C. K.; Friend, R. H.; Westenhoff, S.; Greenham, N. C. *J. Am. Chem. Soc.* **2010**, *132*, 328–335.
(78) Shuttle, C. G.; Hamilton, R.; O'Regan, B. C.; Nelson, J.; Durrant, J. R. *Proc. Natl. Acad. Sci. U.S.A.* **2010**, *107*, 16448–16452.
(79) Mauer, R.; Howard, I. A.; Laquai, F. *J. Phys. Chem. Lett.* **2010**, *1*, 3500–3505.
(80) Frolov, S. V.; Bao, Z.; Wohlgenannt, M.; Vardeny, Z. V. *Phys. Rev. Lett.* **2000**, *85*, 2196–2199.
(81) Stevens, M. A.; Silca, C.; Russell, D. M.; Friend, R. H. *Phys. Rev. B* **2001**, *63*, 165213.
(82) Silva, C.; Dhoot, A. S.; Russell, D. M.; Stevens, M. A.; Arias, A. C.; MacKenzie, J. D.; Greenham, N. C.; Friend, R. H. *Phys. Rev. B* **2001**, *64*, 125211.
(83) Arkhipov, V. I.; Emelianova, E. V.; Bässler, H. *Phys. Rev. Lett.* **1999**, *82*, 1321–1324.
(84) Zenz, C.; Lanzani, G.; Cerullo, G.; Graupner, W.; Leising, G.; Scherf, U.; DeSilvestri, S. *Synth. Met.* **2001**, *116*, 27–30.
(85) Parkinson, P.; Müller, C.; Stingelin, N.; Johnson, M. B.; Herz, L. M. *J. Phys. Chem. Lett.* **2010**, *1*, 2788–2792.
(86) Westenhoff, S.; Beenken, W. J. D.; Friend, R. H.; Greenham, N. C.; Yartsev, A.; Sundström, V. *Phys. Rev. Lett.* **2006**, *97*, 166804.
(87) Hodgkiss, J. M.; Campbell, A. R.; Marsh, R. A.; Rao, A.; Albert-Seifried, S.; Friend, R. H. *Phys. Rev. Lett.* **2010**, *104*, 177701.
(88) Kim, J. Y.; Lee, K.; Coates, N. E.; Moses, D.; Nguyen, T.-Q.; Dante, M.; Heeger, A. J. *Science* **2007**, *317*, 222–225.
(89) Gilot, J.; Wienk, M. M.; Janssen, R. A. J. *Appl. Phys. Lett.* **2007**, *90*, 143512.

Supporting Information to:

Role of Structural Order and Excess Energy on Ultrafast Free Charge Generation in Hybrid Polythiophene/Si Photovoltaics Probed in Real Time by Near-Infrared Broadband Transient Absorption

Daniel Herrmann[1], Sabrina Niesar[2], Christina Scharsich[3], Anna Köhler[3], Martin Stutzmann[2], and Eberhard Riedle[1]

[1]*Lehrstuhl für BioMolekulare Optik, Ludwig-Maximilians-Universität München, Oettingenstr. 67, 80538 München, Germany.*

[2]*Walter Schottky Institut, Technische Universität München, Am Coulombwall 4, 85748 Garching, Germany*

[3]*Lehrstuhl EP II, Universität Bayreuth, Universitätsstr. 30, 95440 Bayreuth, Germany*

Contact Information:

Prof. Eberhard Riedle, LMU München

Phone: +49(0)89/2180-9210
Email: riedle@physik.uni-muenchen.de

Prof. Martin Stutzmann, TU München

Phone: +49(0)89/289-12760

Email: Stutz@wsi.tum.de

Prof. Anna Köhler, University of Bayreuth

Phone: +49(0)921/55-2600

Email: anna.koehler@uni-bayreuth.de

Basic Optical and Structural Characterization of P3HT

The basic optical characterization of the thin film samples was done by UV-Vis-NIR absorbance measurements recorded with a Perkin Elmer Lambda 750 spectrophotometer. To differentiate between absorption and scatter, some spectra were recorded with a Perkin Elmer Lambda 900 equipped with an integrating sphere. Visible photoluminescence spectra were recorded with a Spex Fluorolog 2 fluorimeter. To gain knowledge on the morphology of the samples atomic force microscopy (AFM) images were taken with a Veeco MultiMode Nanoscope V microscope in tapping mode (Figs. 2,S1). The scan size was 10 µm x 10 µm.

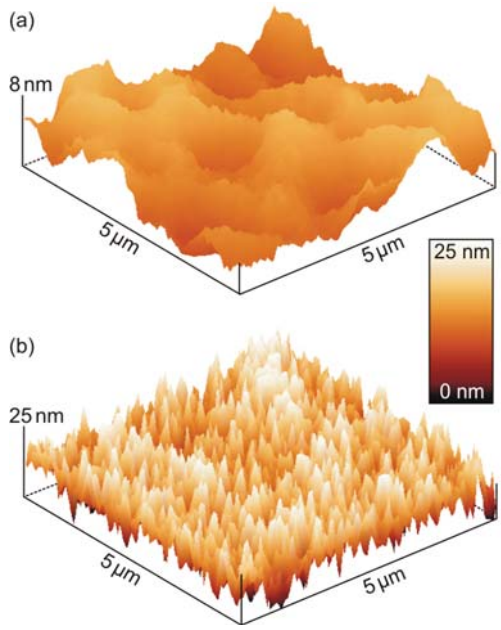

Figure S1. Corresponding topographical 3D AFM images of spin-coated films of (a) RRa-P3HT and (b) aggRR-P3HT on fused silica.

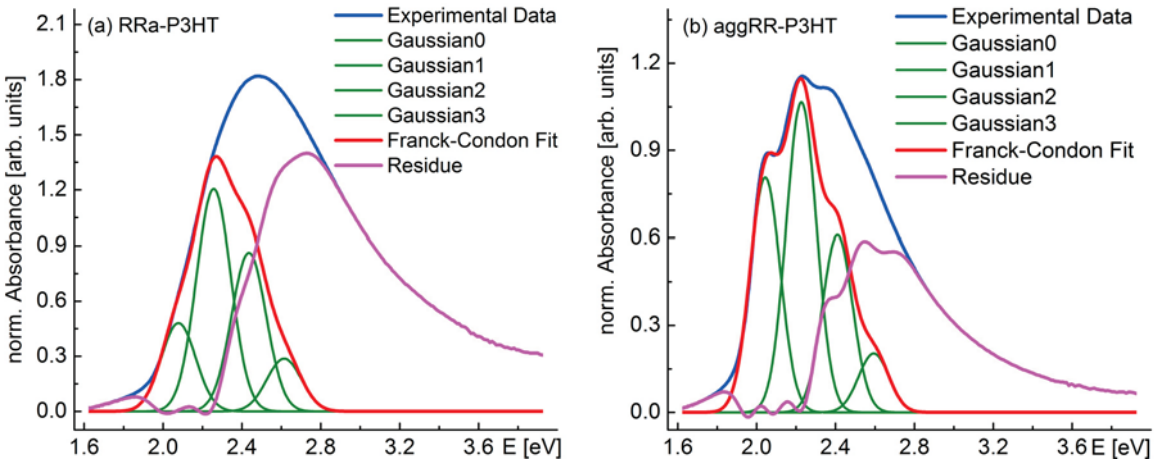

Figure S2. Modified Franck-Condon fit to the absorption spectra of (a) RRa-P3HT and (b) aggRR-P3HT taken from Fig. 4(a).

With the assumption that the absorption coefficient of aggregated chains is 1.39 times that of coiled chains [S1,S2], a percentage of (38 ± 5)% aggregates for the aggRR-P3HT sample and of (24 ± 5)% aggregates for the RRa-P3HT sample can be derived with a modified Franck-Condon fit to the absorbance spectra as indicated in Fig. S2.

Description of the TA Spectrometer

To investigate the nature of the photoexcitations and their inherent kinetics after visible excitation we used a novel pump-probe spectrometer that allows for ultrafast broadband (UV-Vis-NIR) transient absorption (TA) experiments at room temperature with a time resolution of 40 fs. The UV-Vis part of the setup employing a Ti:Sa chirped-pulse amplifier system (CPA 2001, ClarkMXR) with 1 kHz repetition rate as common fundamental light source for pump and probe generation has been described previously. It was extended to allow the investigation of thin film samples and to expand the detection range into the NIR (Fig. S3). A single-stage noncollinear optical parametric amplifier (NOPA) was used as pump source providing ultrashort pump pulses with tunable wavelength. The NOPA allows a very broad tuning of the pump wavelength providing the possibility of a selective excitation from 450 to 760 nm. For the P3HT-based samples investigated in this work, excitation wavelengths of 450, 518, 535, 555, 600 and 720 nm were selected.

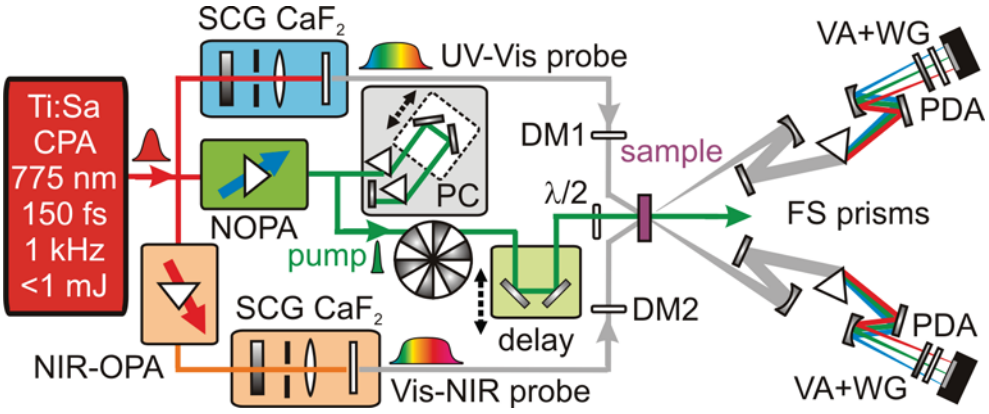

Figure S3. Experimental layout of the novel ultrafast UV-Vis-NIR TA pump-probe spectrometer. NOPA: noncollinear optical parametric amplifier, SCG: supercontinuum generation, PC: prism compressor, DM: dichroic mirror, VA: variable attenuator, WG: wire-grid polarizer, PDA: photodiode array.

The NOPA pulses were compressed with a fused silica prism compressor (PC) and showed a Fourier-limited 15 fs FWHM pulse duration, measured at the sample position with a second-

harmonic generation scanning autocorrelator. The pump energy was adjusted to 4-60 nJ using a combination of an achromatic λ/2 waveplate and broadband wire-grid polarizer (Moxtek Inc.). The energy stability was typically 1.5% RMS. A chopper wheel in the pump beam blocked every second excitation pulse such that changes in the optical density (ΔOD) of the sample could be recorded. The pump beam was led through a 2 ns delay stage. A λ/2 waveplate in front of the sample was used to adjust the linear pump polarization relative to the linear probe polarization.

The UV-Vis and a Vis-NIR broadband probe source were employed in subsequent measurements. For gap-free TA measurements up to the NIR spectral range, a novel probe setup was developed employing a combination of two supercontinuum generation (SCG) stages and OPA (Fig. S3). First in a NIR-OPA, approximately 1 μJ light from the Ti:Sa amplifier was focused into a 4 mm YAG crystal to generate a supercontinuum with high NIR content [46]. The SC was subsequently amplified at 1180 nm in a collinear OPA stage employing a 3 mm long type-I BBO crystal (phase-matching angle: 20°) and pumped by the fundamental light from the Ti:Sa. Second, about 1-2 μJ of the amplified signal at 1180 nm were focused into a 5 mm long circularly translated CaF_2 crystal for SCG. After passing a short pass dichroic mirror (DM) deposited on a 1 mm fused silica substrate to block the intense light around 1180 nm and an OD filter, the broadband probe ranged from 415 to 1150 nm limited by the transmission of the DM.

The pump and probe were weakly focused into the sample leading to a 210 μm and 110 μm $1/e^2$ beam diameter at the sample, respectively. The weak focusing leads to an ensemble averaging over the finely grained morphology of the thin films to mimic their usage as photovoltaic device and to ensure low local excitation densities. We routinely verified that the samples did not degrade due to the prolonged illumination by the pump pulses and only observed signal degradation when storing the samples over several months at ambient conditions in the lab.

A broadband multichannel detection of the TA signals employing a fused silica (FS) prism polychromator and a silicon photodiode array (PDA) based camera with 512 pixels is used. Typically, a probe noise below 2% and a probe detection sensitivity of $\Delta OD \sim 10^{-4}$ over the entire spectral range were achieved. Selected measurements were repeated on later days and with additional samples of the same nominal composition. No differences were found within experimental accuracy.

All TA measurements were performed from -10 ps up to 2 ns delay in small steps and additionally at fixed delays of 3, 4, and 6 ns. 3 runs with averaging over 1500 pump on/off

couples per delay step were recorded and averaged. The pump beam was led through a carefully aligned 2 ns delay stage with a maximum pump pointing deviation at the sample of 2 µm over the whole delay range. The vertically aligned sample was not moved during the recordings and could be adjusted in all directions. The spectral resolution at the detector was better than 3 nm/pixel. To minimize pump straylight originating from the solid film samples, a broadband wire-grid polarizer (WG) was placed in front of the detector. This WG was aligned with maximum transmission for the probe polarization and the pump polarization was adjusted to be perpendicular to the probe polarization in this case.

For accurate calibration of the time zero, the raw data was corrected for the chirp of the probe pulses by adjusting the zero time at half rise of the signals. Additionally, we could show that the pump-probe setup is interferometrically stable and thus offers the alternative to employ a periodic modulation due to spectral interference between pump straylight and probe to extract the delay via Fourier-transformation. We have explicitly compared both options and found that the deviation of their result is negligible and enable calibration of the zero delay with a few-fs accuracy. Overall, the time resolution of the ultrabroadband TA measurements was 40 fs, in particular because we do not need to measure over the spectral region of the SCG fundamental where a time jump is present in the broadband probe pulse. This is considerably better than for measurements with solutions due to the effective lack of a group velocity mismatch contribution in the 100 nm thin films.

Formulas of Optical Densities, Cross-sections and Excitation Densities

The Beer-Lambert law is a linear relationship between absorbance change ΔOD (optical density, OD) and photoinduced concentration change Δc of the corresponding species generated upon photoexcitation (e.g. polarons) with its inherent molar extinction coefficient ε_M in L mol^{-1} cm^{-1}

$$\Delta OD(t) = \varepsilon_M \cdot \Delta c(t) \cdot l = -\log(T(t)/T_0), \quad (1)$$

where l is the sample thickness. The transient change in optical density ΔOD is linked to the transmission T after photoexcitation and T_0 without excitation. T and T_0 are recorded during the TA measurements.

The carrier concentration c in mol/L is connected to the carrier density n in cm^{-3} via

$$c = \frac{1000}{N_A} n, \qquad (2)$$

where N_A is Avogadro's constant. Therefore the polaron molar extinction coefficient can be derived from the TA data

$$\varepsilon_M = \frac{\Delta OD_{300\text{fs}}}{[\text{P3HT}^+]_{300\text{fs}} \cdot l} \cdot \frac{N_A}{1000}, \qquad (3)$$

where for the carrier density, the initial photoinduced charge density $[\text{P3HT}^+]_{300\text{fs}}$ at the maximum of the polaron signal (at 300 fs) is taken. For its calculation, the polaron cross-section is needed.

From the TA data we can estimate the polaron cross-section σ

$$\sigma = \frac{\Delta T}{T \cdot N}, \qquad (4)$$

where N is the areal density of excited states. N is equal to the pump photon number per square centimeter multiplied by the fraction of photons absorbed, which is determined by the absorbance of the sample at the pump wavelength. Employing the polaron cross-section, we determine the initial charge density $[\text{P3HT}^+]_{300\text{fs}}$ at the maximum of the polaron signal

$$\text{n(t=300 fs)}=[\text{P3HT}^+]_{300\text{fs}} = \frac{|\Delta T / T|_{300\text{fs}}}{\sigma \cdot l}, \qquad (5)$$

where $|\Delta T/T|_{300\text{fs}}$ is the initial magnitude of the polaron TA signal at 300 fs.

The cross-section is related to the absorption coefficient α in m^{-1} and the extinction coefficient via

$$\sigma = \frac{\alpha}{n} = \frac{\varepsilon_M \cdot c}{\log(e) \cdot n} = \frac{\varepsilon_M \cdot 1000}{\log(e) \cdot N_A}. \qquad (6)$$

Raw TA Data for Comparison

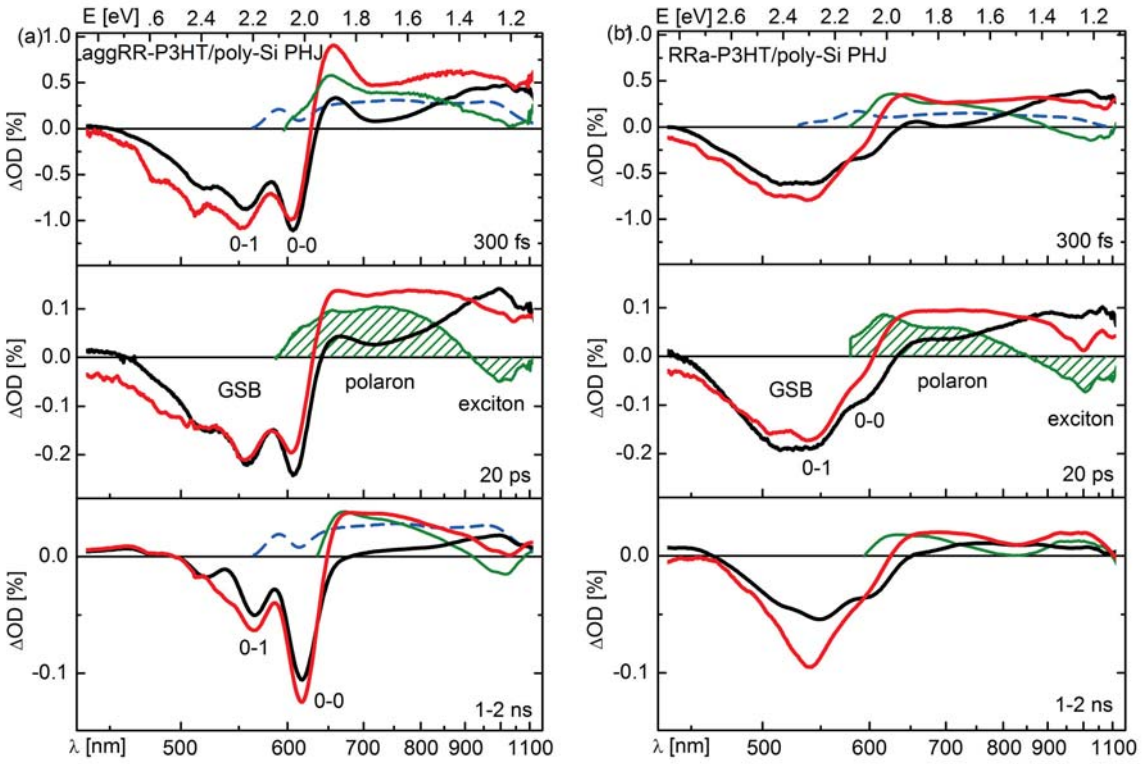

Figure S4. (a) Raw TA spectra of pure aggRR-P3HT (black) and aggRR-P3HT/poly-Si PHJ (red). (b) Raw TA spectra of pure RRa-P3HT (black) and RRa-P3HT/poly-Si PHJ (red). All at the nominal same excitation of 9 μJ/cm^2 at 518 nm. The difference spectra (green) are compared to the individual P3HT film polaron absorption spectrum (blue dashes).

Energy Transfer from amorphous P3HT to aggregated P3HT

When considering the vibrational structure displayed in Fig. 5 of the manuscript for different delay times, we observe that the ratio 0-0 to 0-1 decreases until 13 ps and subsequently increases again. In addition, the relative intensity of the GSB signal around 500 nm reduces with time. These changes imply that some dynamic process must take place in P3HT after photoexcitation. We recall that the P3HT absorption spectrum, and similarly the GSB spectrum, arises from a superposition of contributions of coils (around 450-500 nm) and aggregates (around 600 nm). In addition, within the aggregate absorption spectrum, a high 0-0 peak signal implies planar chains with long conjugation length and with weak excitonic coupling to their neighbors, while a lower 0-0 peak suggests chains with somewhat shorter

conjugation length and concomitantly stronger excitonic coupling [S3]. Furthermore, the reduction of the relative GSB intensity around 500 nm with time suggests that the ground state of the coiled chains recovers faster than the ground state of the aggregated chains, for example by energy transfer from coiled to aggregated chains. To quantify on which timescale this energy transfer takes place, we have displayed the ratio between the GSB intensity at 480 nm for excitation at 450 nm to excitation at 600 nm (Fig. S5), using the data displayed in Fig. 8 of the manuscript. This ratio reaches a constant value after about 13-20 ps. Fig. S5 reveals a forward 1/e energy transfer time of about 3 ps. It is interesting to note that the same 1/e time of 3 ps had been found for the energy transfer from a glassy phase to a planarized phase in the blue-light-emitting poly(9,9-dioctylfluorene) [S4].

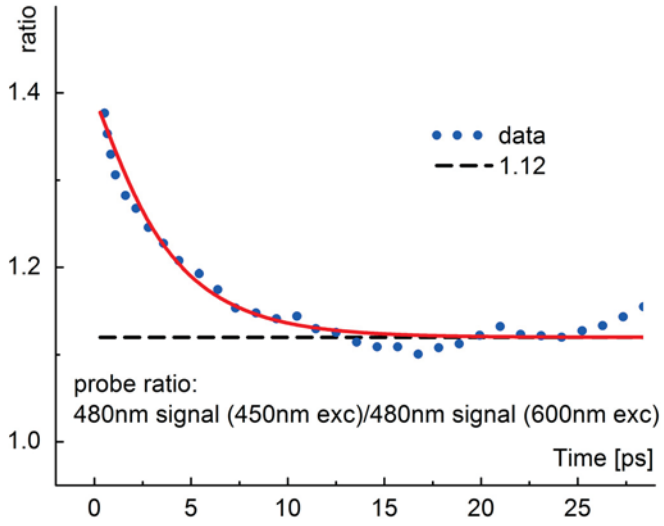

Figure S5. The ratio of 480 nm GSB signal for 450 nm to the 480 nm GSB signal for 600 nm excitation shows a 1/e energy transfer time from coils to aggregates of 3 ps derived from a monoexponential fit. The energy transfer is completed at around 13-20 ps.

In order to analyse the temporal changes in the 0-0 intensity shown in Fig. 6 of the manuscript in full quantitative detail, the contributions from coiled and aggregated chains would need to be deconvoluted. This is beyond the scope of this paper. However, the change from a relatively high 0-0 peak (300 fs) to a lower one (20 ps) and again to a high 0-0 peak (1-2 ns) is obvious. It suggests the excitation to be initially delocalized, then more localized and subsequently again more delocalized. Whether these changes are due to structural rearrangements of polymer chains such as torsional relaxation [S5], or whether they are due to spectral diffusion to more conjugated chain segments, or due to a combination of both effects[S6], cannot be distinguished on the basis of these data.

Quantum Yields

The PIA is determined by singlet-excitons and polarons in P3HT. The maximum quantum yields of charges can be derived from the TA spectra in Fig. 5, accounting for the observed photovoltaic conversion pathways shown in Scheme S1 [S7].

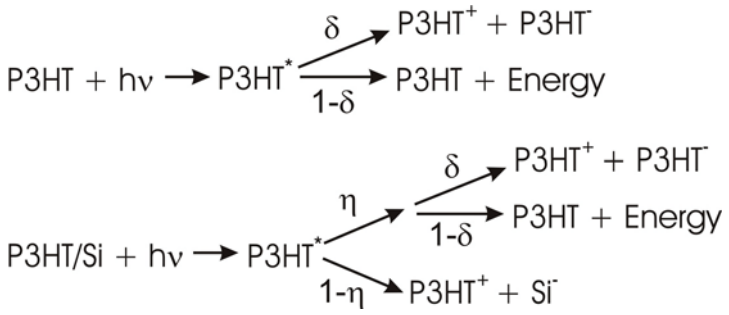

Scheme S1. Yields of transient species generated by photoexcitation of pure P3HT and P3HT/Si heterojunctions.

According to our findings, exciting pure P3HT with pump photons in the absorption range initially leads to the formation of singlet-excitons. These Frenkel-type excitons can dissociate into positive ($P3HT^+$) and negative ($P3HT^-$) P3HT polarons with quantum yield δ and the remaining photoexcitations can decay to the ground state with yield 1- δ through release of vibrational energy (P3HT + Energy). In the P3HT/Si heterojunction, a proportion η of the photons is absorbed so far away from the hybrid heterojunction as to lead to the same result as in pure P3HT. The remaining fraction (1- η) of photons is absorbed near a P3HT/Si interface to yield ultrafast electron transfer to the Si with 140 fs forward transfer time. To determine the quantum yields (Tab. S1), we consider the TA signal magnitude at 300 fs due to excitons in aggRR-P3HT/poly-Si PHJ, which typically has about 0.75 times the magnitude as for pure aggRR-P3HT. Therefore, the fraction of photoexcitations that initially do not sense the Si component is taken as η=0.75. The maximal magnitude of the TA signal due to polarons at 300 fs is typically about 2.2 times that for pure P3HT, which results in $\delta = \frac{1-\eta}{2.2-\eta} = 0.17$.

Sample	$P3HT^+$	$P3HT^-$	P3HT+E	Si^-
aggP3HT	0.17	0.17	0.83	0
aggP3HT/Si	0.38	0.13	0.62	0.25

Table S1. Initial quantum yields of charges in pure P3HT and aggRR-P3HT/poly-Si PHJ

TA Measurements of RR-P3HT in Dilute Solutions

To identify the PIA of singlet-excitons, we performed TA measurements of RR-P3HT in dilute solutions of toluene, chloroform and 1,2-dichlorobenzene, where the intermolecular distance is too high for P3HT cation formation (Fig. S7). In this condition, the inherent lifetime of singlet-excitons can be studied. It is found to be significantly increased compared to the film, enabling their radiative decay (SE) and ISC to the triplet state on the ns timescale.

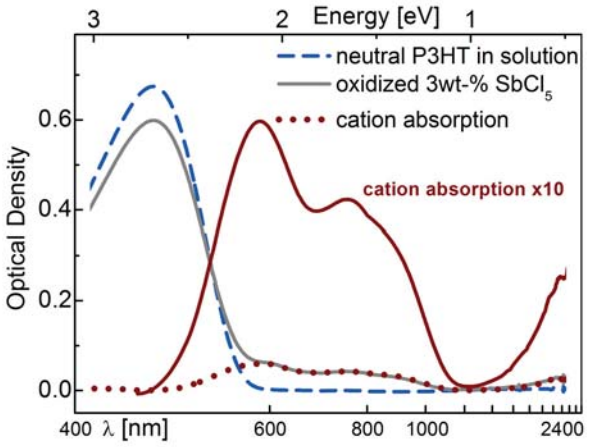

Figure S6. (a) Absorbance spectra of pure P3HT (blue dashes), chemically oxidized P3HT in 1,2-dichlorobenzene solution after adding 3wt-% pentachloroantimonate ($SbCl_5$) (solid grey curve) and P3HT cation absorption (brown).

P3HT in solution can be chemically oxidized employing a strong oxidant to obtain the P3HT cation signature. Fig. S6 shows the absorbance spectrum of chemically oxidized P3HT in 1,2-dichlorobenzene solution after adding 3wt-% pentachloroantimonate ($SbCl_5$). From this we obtained the P3HT cation ($P3HT^+$) absorption spectrum as follows. Adding $SbCl_5$ decreases the absorbance of the neutral P3HT molecule (blue dashes) and increases the cation absorbance (brown dots). Saturation occurs at adding 10wt-% $SbCl_5$. The difference between the blue dashed line scaled to the peak of the gray solid curve in Fig. S6 and the gray solid curve reveals the P3HT cation absorption (brown dots and brown solid line) ranging from 470 to about 1200 nm and increasing again up to the mid-infrared spectral region. The absorption spectrum of RR-P3HT in dilute solution (Fig. S6) shows reduced conjugation and hindered aggregation compared to RR-P3HT film (Fig. 3(b)) [S3].

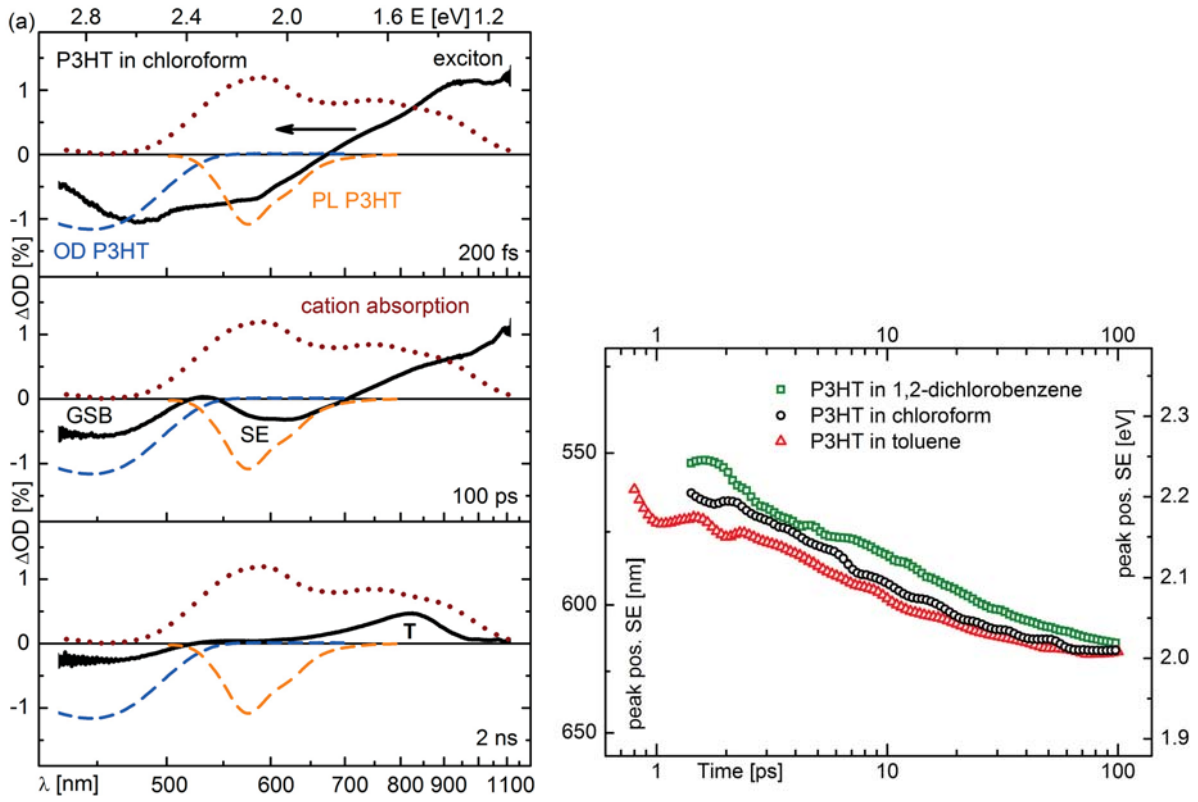

Figure S7. (a) TA spectra (black solid curves) of RR-P3HT dissolved in chloroform at 200 fs, 100 ps and 2 ns. The cation absorption spectrum (brown dots) as well as the P3HT absorption (blue dashed curve) and PL spectra (orange dashed curve) are scaled to the transient absorption spectrum to identify GSB, SE and singlet-/triplet-exciton absorption. Excitation: 15 μJ/cm^2 at 475 nm. (b) Time evolution of the SE center spectral position for P3HT in 1,2-dichlorobenzene (green squares), chloroform (black circles) and toluene (red triangles).

Fig. S7(a) shows TA spectra (black solid curves) of RR-P3HT in dilute solutions of chloroform at 200 fs, 100 ps and 2 ns with low excitation fluence of 15 μJ/cm^2 at 475 nm pump wavelength. In order to cancel out effects of molecule orientation in solution on the dynamics, the polarization direction of the linearly polarized pump pulse was adjusted at the magic angle of 54.7° with respect to that of the probe pulse. For comparison, the P3HT absorption (blue solid curve) and PL (orange solid curve) spectra as well as the P3HT cation absorption spectrum are incorporated in Fig. S7(a). The TA spectra reveal signatures of GSB and SE (ΔOD<0) as well as signatures of PIA (ΔOD>0) at the expected spectral positions. The GSB shows a more rapid decay at longer probe wavelengths (lower energy), which we attribute to a faster decay of excited longer conjugations that are less stabilized by interchain interactions [S3]. Fig. S7 shows that the SE spectrally shifts with time towards lower probe photon energy (longer probe wavelength) by about 0.22 eV until it vanishes at around 1 ns,

whereas the total shift depends on the solvent polarity. We note that only broadband probe detection of the TA signals allows for observing this relaxation process which other-wise would be misinterpreted as a decay process in case of single-wavelength probe detection. We assign this effect to funneling of intrachain excitons to lower-energy sites [S5], torsional relaxation of the polymer backbone in the excited state [S5,S6] and solvation effects [S8,S9].

It should be noted, that no signatures of P3HT cation absorption are present in Fig. S7(a). The early PIA signature above 750 nm (1.65 eV) in Fig. S7 is assigned to singlet-exciton absorption in agreement with the results of Fig. 5, taking into account the energetic shift of the signals between film and solution. At around 2 ns, a distinct PIA peak at 1.49 eV (830 nm) remains, which stays constant at least up to 6 ns (the maximum investigated delay). Consequently, this signature can be assigned to a PIA of a P3HT triplet state, which confirms and adds to recent theoretical predictions [S10]. We attribute this observation to intersystem crossing (ISC) with a ~1 ns-1 rate from the singlet-exciton to the triplet state [S11,S12].

Bimolecular Recombination

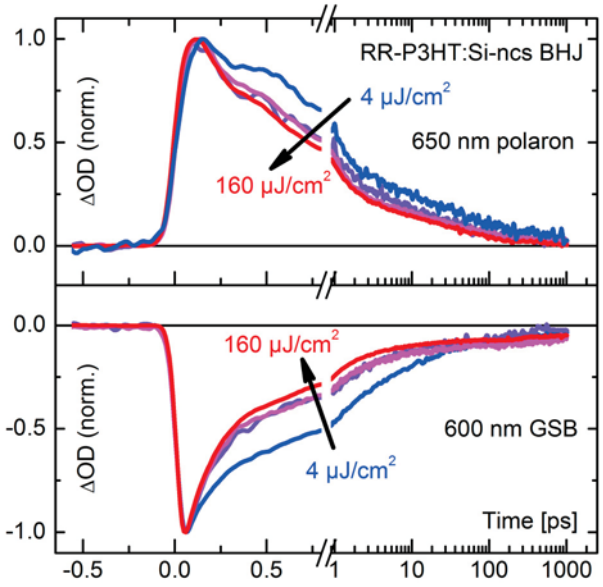

Figure S8. (a) Decay of TA signals for increased excitation fluences (4, 30, 60 and 160 µJ/cm^2 at 480 nm) reveals bimolecular nongeminate recombination in case of RR-P3HT:Si-ncs BHJ.

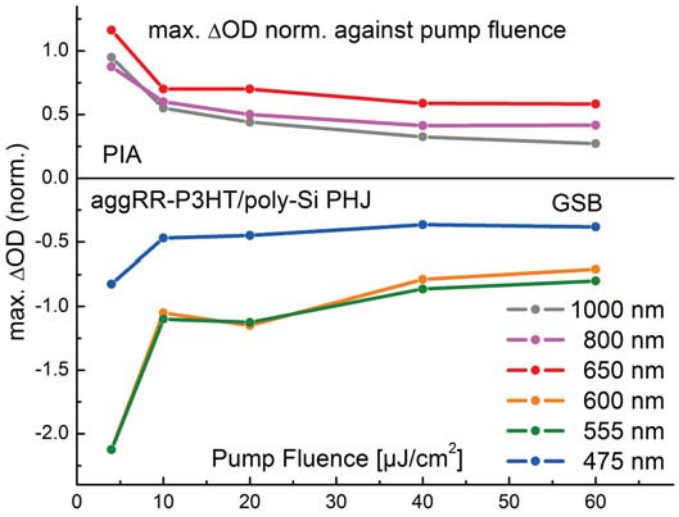

Figure S9. Transient signal magnitudes normalized with respect to excitation fluence plotted against the excitation fluence for aggRR-P3HT/Si PHJ excited at 518 nm. The polarons (650, 800 nm) show the same intensity dependence as the excitons (1000 nm) and are thus generated from excitons.

Time-dependent Anisotropy

The TA spectra in Fig. 5 were recorded with perpendicular (pp) pump and probe polarization to allow for optimum straylight suppression. To study the time-dependent anisotropy r(t) of polarons and singlet-excitons via Eq. 15, additional traces were recorded with both polarizations parallel (pa) to each other.

$$r(t) = \frac{\Delta OD_{pa} - \Delta OD_{pp}}{\Delta OD_{pa} + 2 \cdot \Delta OD_{pp}} = 0.2 \cdot (3 \cdot \cos^2 \theta - 1) \qquad (15)$$

From the anisotropy, the the transition dipole orientation angle θ can be derived. The excitation fluence was kept low at 9 μJ/cm^2. Fig. S10(a) compares the anisotropy spectra of pure aggRR-P3HT (green solid curve) and aggRR-P3HT/poly-Si PHJ (blue solid curve) with the corresponding TA spectrum of pure aggRR-P3HT (black dashes) all at 300 fs with 518 nm excitation. Fig. S10(b) shows the time-dependent anisotropy decay of the transient species.

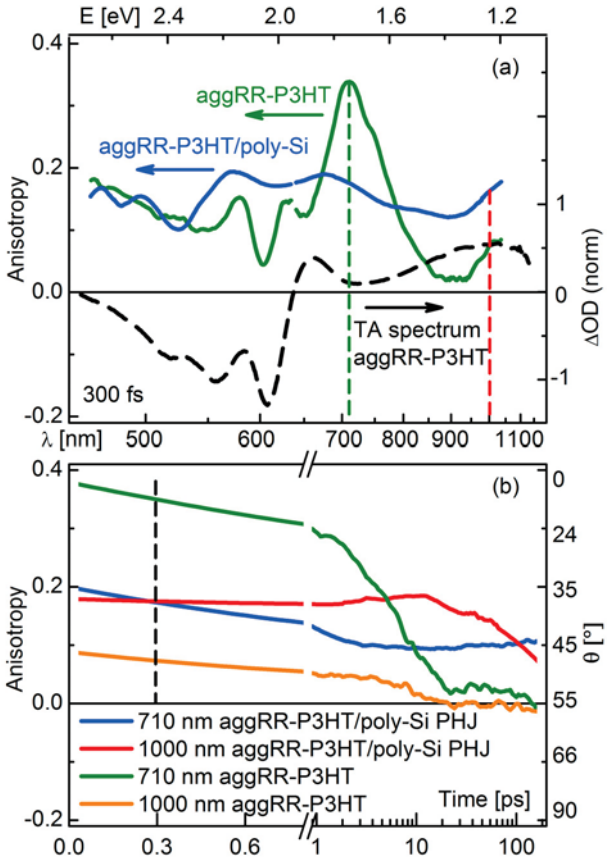

Figure S10. (a) Anisotropy spectrum at 300 fs of pure aggRR-P3HT (green solid curve) and aggRR-P3HT/poly-Si PHJ (blue solid curve) compared to the corresponding normalized TA spectrum (black dashes) of pure aggRR-P3HT (Fig. 6(a)). (b) Transient anisotropy decay and corresponding transition dipole reorientation angle θ of polaron (710 nm) and singlet-exciton (1000 nm).

In case of pure aggRR-P3HT, the anisotropy at 710 nm probe wavelength within the characteristic polaron band is r = 0.39 immediately after photoexcitation, which corresponds to parallel pump and probe transition dipole moments. Subsequently, the anisotropy decays to r = 0.20 at 4 ps and levels off at r ~ 0.02 after 20 ps (Fig. S10(b)). The anisotropy at the characteristic exciton band (1000 nm) is r = 0.10 immediately after photoexcitation (Fig. S10(b)), subsequently decays to r = 0.05 at 1 ps and finally completely vanishes at 20 ps, which might indicate a random relative orientation of pump and probe transition dipole moments. The anisotropy spectrum of pure aggRR-P3HT at 300 fs reveals a distinct peak from 620 to 910 nm, which matches the spectral range of polaron absorption in Fig. 5(a). We therefore assign the distinct peak around 710 nm with high anisotropy to polarons in pure aggRR-P3HT that are localized on a chain and completely loose their initial polarization

memory within 20 ps through energy migration [S13]. We attribute this anisotropy decay to hopping of charge carriers with a characteristic 1/e hopping time of 7 ps.

On the other hand, the anisotropy spectrum of the aggRR-P3HT/poly-Si PHJ at 300 fs reveals no distinct feature. The anisotropy at the characteristic polaron band (710 nm) in case of the aggRR-P3HT/poly-Si PHJ is r = 0.19 immediately after photoexcitation. Subsequently, the anisotropy decays to r = 0.13 at 1 ps and r = 0.10 at 20 ps, where it saturates (Fig. S10(b)). Fig. 7(a) reveals that the ultrafast charge transfer between aggRR-P3HT and Si leads to generation of mobile charge carriers. We therefore conclude that the ultrafast loss of anisotropy for polarons in the aggRR-P3HT/poly-Si PHJ compared to aggRR-P3HT is attributable to this ultrafast charge transfer leading to a rapid loss of polarization memory and uncorrelated charges. It should be noted that an excess electron in the inorganic semiconductor Si possesses a highly delocalized wavefunction.

Exemplary 2D Gap-free TA Maps

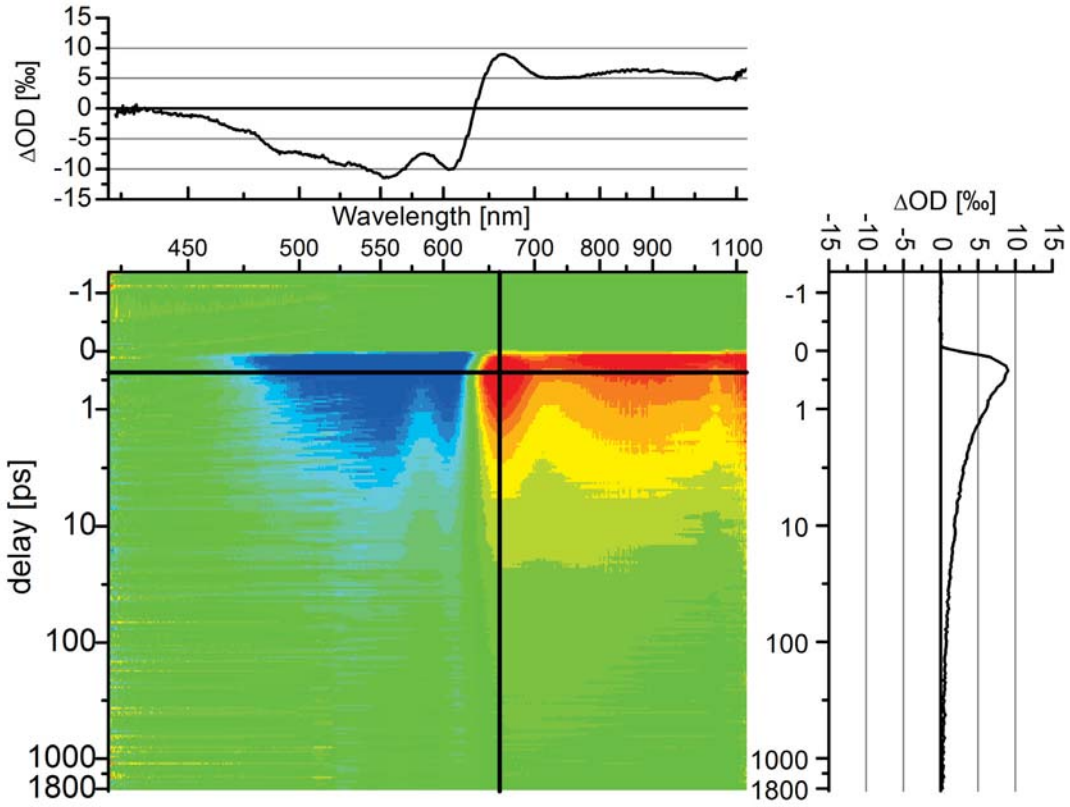

Figure S11(a). 2D map and lineouts for the TA measurement of aggRR-P3HT/Si PHJ excited at 518 nm with 9 μJ/cm^2.

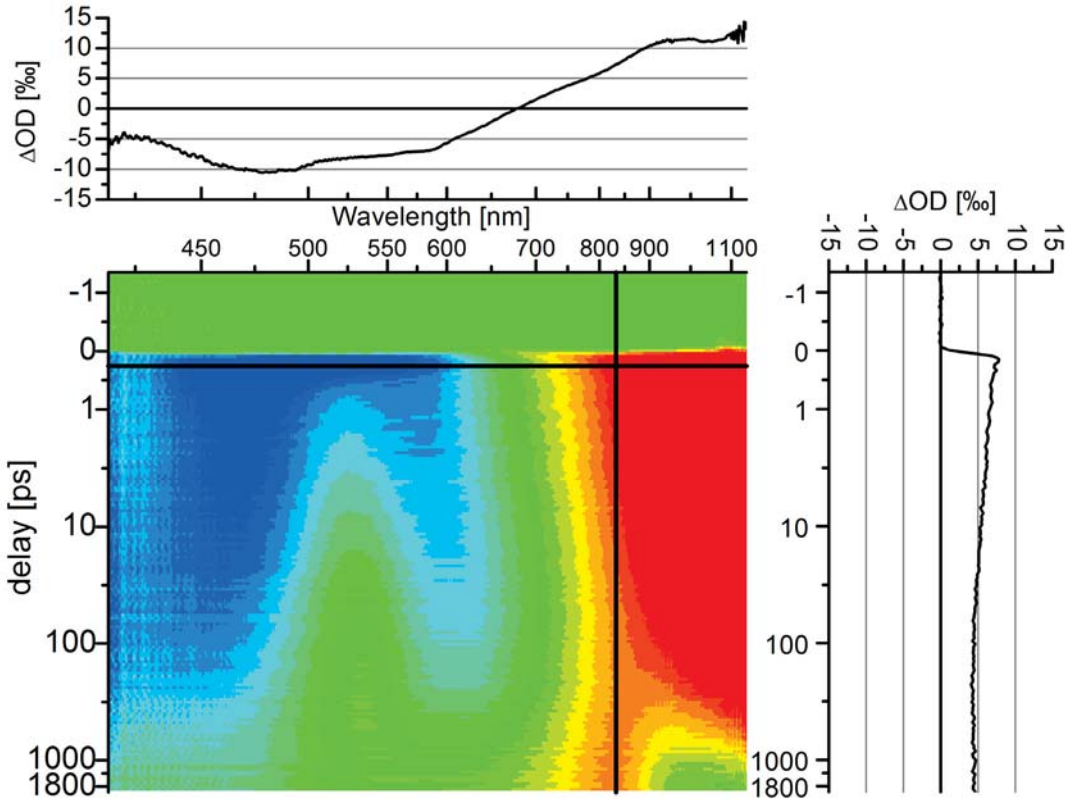

Figure S11(b). 2D map and lineouts for the TA measurement in Fig. S7(a).

(S1) Clark, J.; Chang, J.-F; Spano, F. C.; Friend, R. H.; Silva, C. Appl. Phys. Lett. **2009**, 94, 163306.

(S2) Scharsich, C; Lohwasser, R.; Asawapirom U.; Scherf U.; Thelakkat, M.; Köhler, A. (2011, submitted).

(S3) Clark, J.; Silva, C.; Friend, R. H.; Spano, F. C Phys. Rev. Lett. **2007**, 98, 206406.

(S4) Khan, A. L. T.; Sreearunothai, P.; Herz, L. M.; Banach, M. J.; Köhler, A. Phys. Rev. B **2004**, 69, 085201.

(S5) Parkinson, P.; Müller, C.; Stingelin, N,; Johnson, M. B.; Herz, L. M. J. Phys. Chem. Lett. **2010**, 1, 2788-2792.

(S6) Westenhoff, S.; Beenken, W. J. D.; Friend, R. H., Greenham, N. C.; Yartsev, A.; Sundström, V. Phys. Rev. Lett. **2006**, 97, 166804.

(S7) Piris, J.; Dykstra, T. E.; Bakulin, A. A.; van Loosdrecht, P. H. M.; Knulst, W.; Trinh, M. T.; Schins, J. M.; Siebbeles, L. D. A. J. Phys. Chem. C **2009**, 113, 14500-14506.

(S8) Horng, M. L.; Gardecki, J. A.; Papazyan, A.; Maroncelli, M. J. Phys. Chem. **1995**, 99, 17311-17337.

(S9) Reynolds, L.; Gardecki, J. A.; Frankland, S. J. V.; Horng, M. L.; Maroncelli, M. J. Phys. Chem. **1996**, 100, 10337-10354.

(S10) Köhler, A.; Bässler, H. Mater. Sci. Engineering R **2009**, 66, 71–109.

(S11) Kraabel, B.; Moses, D.; Heeger, A. J. J. Chem. Phys. **1995**, 103, 5102-5108.

(S12) Grebner, D.; Helbig, M.; Rentsch, S. J. Phys. Chem. **1995**, 99, 16991-16998.

(S13) Guo, J.; Ohkita, H.; Benten, H.; Ito, S. J. Am. Chem. Soc. **2009**, 131, 16869-16880.

7 The Red-Phase of Poly[2-methoxy-5-(2-ethylhexyloxy)-1,4-phenylenevinylene] (MEH-PPV): A Disordered HJ-Aggregate

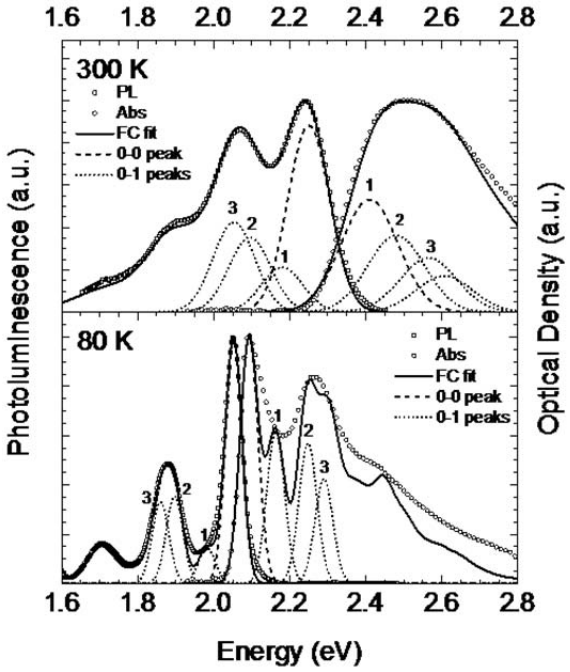

Hajime Yamagata, Nicholas J. Hestand, Frank C. Spano, Anna Köhler, Christina Scharsich, Sebastian T. Hoffmann, Heinz Bässler

Published in

Journal of Chemical Physics

DOI: 10.1063/1.4819906

Reproduced with permission from J. Chem. Phys. 2013, 139, 114903

The red-phase of poly[2-methoxy-5-(2-ethylhexyloxy)-1,4-phenylenevinylene] (MEH-PPV): A disordered HJ-aggregate

Hajime Yamagata,[1] Nicholas J. Hestand,[1] Frank C. Spano,[1] Anna Köhler,[2] Christina Scharsich,[2] Sebastian T. Hoffmann,[2] and Heinz Bässler[2]
[1]*Department of Chemistry, Temple University, Philadelphia, Pennsylvania 19122, USA*
[2]*Experimental Physics II, Department of Physics and Bayreuth, Institute of Macromolecular Science (BIMF), University of Bayreuth, Bayreuth 95440, Germany*

(Received 7 June 2013; accepted 19 August 2013; published online 18 September 2013)

The ratio of the 0-0 to 0-1 peak intensities in the photoluminescence (PL) spectrum of red-phase poly[2-methoxy-5-(2-ethylhexyloxy)-1,4-phenylenevinylene], better known as MEH-PPV, is significantly enhanced relative to the disordered blue-phase and is practically temperature independent in the range from T = 5 K to 180 K. The PL lifetime is similarly temperature independent. The measured trends are accounted for by modeling red-phase MEH-PPV as disordered π-stacks of elongated chains. Using the HJ-aggregate Hamiltonian expanded to include site disorder amongst electrons and holes, the absorption and PL spectra of cofacial MEH-PPV dimers are calculated. The PL 0-0/0-1 line strength ratio directly responds to the competition between intrachain interactions which promote J-aggregate-like behavior (enhanced PL ratio) and interchain interactions which promote H-aggregate-like behavior (attenuated PL ratio). In MEH-PPV aggregates, J-like behavior is favored by a relatively large intrachain exciton bandwidth – roughly an order of magnitude greater than the interchain bandwidth – and the presence of disorder. The latter is essential for allowing 0-0 emission at low temperatures, which is otherwise symmetry forbidden. For Gaussian disorder distributions consistent with the measured (inhomogeneous) line widths of the vibronic peaks in the absorption spectrum, calculations show that the 0-0 peak maintains its dominance over the 0-1 peak, with the PL ratio and radiative lifetime practically independent of temperature, in excellent agreement with experiment. Interestingly, interchain interactions lead only to about a 30% drop in the PL ratio, suggesting that the MEH-PPV π-stacks – and strongly disordered HJ-aggregates in general – can masquerade as single (elongated) chains. Our results may have important applications to other emissive conjugated polymers such as the β-phase of polyfluorenes. © *2013 AIP Publishing LLC*. [http://dx.doi.org/10.1063/1.4819906]

I. INTRODUCTION

Energy and charge transport in conjugated polymer films continues to be an active area of research, driven largely by the promise of highly efficient plastic solar cells and light-emitting diodes.[1–3] Relatively recent research[4–8] has shown that polymer photophysics can be understood using the ideas developed by Kasha and co-workers[9–12] for understanding absorption and fluorescence in molecular J- and H-aggregates. The classification of H- vs. J-aggregation was a key development in understanding the relationship between morphology and photophysical function in molecular assemblies. Electronic interactions between molecules induce delocalized excited states, or Frenkel excitons, creating a red-shift (blue-shift) of the main absorption peak in J-(H-) aggregates when compared to isolated molecules in solution. Radiative properties are also affected quite differently in the two aggregate types: in J-(H-) aggregates the symmetry of the lowest energy exciton dictates enhanced (depressed) radiative decay rates relative to the monomer.

The J-aggregate model for a *single* polymer chain has been successfully used to understand singlet exciton fluorescence in polydiacetylenes (PDAs)[8] as well as triplet exciton phosphorescence in a Pt-containing phenylene-ethynylene polymer.[13] The PDA derivatives referred to as 3BCMU and 4BCMU are ideal test objects for studying the spectroscopy of one-dimensional systems because they can be prepared as isolated, perfectly ordered π-bonded chains with macroscopic dimension.[14–16] Absorption and fluorescence spectra of "red-phase" 3-BCMU-PDA feature a remarkable asymmetry regarding the vibronic coupling to the lowest optically allowed singlet exciton state; in the photoluminescence (PL) spectrum, the ratio of the 0-0 and first side band (0-1) vibronic peak intensities (with the latter corresponding to the 1400 cm^{-1} vinyl stretching mode) far surpasses the analogous absorption ratio at low temperatures; for example, when T = 13 K the PL 0-0/0-1 ratio is approximately 10^2, about an order of magnitude greater than the corresponding ratio in the absorption spectrum (0-0/0-1) measured at T = 15 K.[15] Moreover, the PL ratio is strongly temperature dependent, diminishing by about a factor of three when warmed from T = 13 K to 80 K.[16] The PL ratio directly probes delocalization of the exciton states, tractable in terms of J-aggregate model developed earlier.[17] In this model, the ratio of line strengths, $I_{PL}^{0-0}/I_{PL}^{0-1}$, scales directly with the number of coherently coupled monomer units in the 1^1Bu exciton; hence, the decrease

of $I_{PL}^{0-0}/I_{PL}^{0-1}$ with temperature measured in PDA reflects thermally induced localization. Interestingly, the absorption ratio directly tracks the exciton *bandwidth*[18] (as opposed to coherence length probed by the PL ratio), establishing a fundamental difference between the two spectra and leading to the aforementioned asymmetry.

Several previous theoretical works[19–21] have shown that the Huang-Rhys (HR) factor for a single polymer chain decreases with increasing chain length, effectively accounting for the increase in the PL ratio, $I_{PL}^{0-0}/I_{PL}^{0-1}$, with the number of monomer repeat units. However, such theories are based on the adiabatic approximation, which support the same HR factor for absorption and emission (i.e., mirror image symmetry). Treating the vibrations dynamically, as is done here and in our former works using Holstein-based Hamiltonians,[17,18] shows that generally it is not possible to describe the vibronic progressions in absorption and emission with the same HR factor; there is no mirror image symmetry in absorption and emission.

When two polymer chains interact within a π-stack, the PL ratio is sensitive to the exciton delocalization along the chain and between chains. However, the positive coupling between chains, as exists in a H-aggregate, leads to a destructive *interference* in the interchain exciton coherence, as opposed to the constructive interference existing within a chain (and typical of J-aggregates). The destructive interference causes $I_{PL}^{0-0}/I_{PL}^{0-1}$ to decrease upon aggregation, exactly opposite to what is expected in J-aggregates;[17,18] in the limit of no disorder and low temperature perfect destructive interference between the chain emitters in H-aggregates leads to the disappearance of just the 0-0 peak within the vibronic progression.[18] This destructive interference is consistent with a high wave vector exciton at the band bottom, the defining characteristic of H-aggregates.

Polymer π-stacks are therefore hybrid "HJ-aggregates" with photophysical properties determined by a competition between intrachain coupling inducing J-like behavior, and interchain coupling inducing H-like behavior.[22] The competition is strongly influenced by morphology, through the nature and magnitude of the diagonal and/or off-diagonal disorder.[23] In poly[3-hexylthiophene] - or P3HT - prevailing H-like behavior has been observed in spin cast films,[5–7] where the H-aggregate model has been very successful in accounting for photophysical properties, while prevailing J-type behavior has recently been observed in nanofibers,[23] where stronger intrachain interactions, consistent with reduced intrachain disorder, leads to much larger 0-0/0-1 PL ratios. It is straightforward to conjecture whether or not other π-conjugated polymers that are not perfectly ordered but feature some topological (static) disorder can display J-dominant or H-dominant behaviors.

In this work, we apply the concept of HJ-aggregates to the well-studied polymer, poly[2-methoxy-5-(2-ethylhexyloxy)-1,4-phenylenevinylene] (MEH-PPV), which has been widely investigated in solution and spin-cast films[24–29] as well as single molecules.[28–37] Recent work by three of us[27] showed that MEH-PPV chains dissolved in methyltetrahydrofuran (MeTHF) undergo a phase transition at approximately 200 K. Above this temperature, the polymer exists in a disordered coil morphology referred to as the blue phase. As the solution is cooled through the transition temperature, the polymer assembles into aggregates (the "red-phase") in which polymer chains are substantially elongated causing a red shift of the absorption and fluorescence spectra relative to the spectra of more disordered chains. Interestingly, the 0-0/0-1 PL ratio is substantially *larger* in the aggregated form, exactly opposite to what is found in spin-cast P3HT aggregates, and defying the predictions of the simple H-aggregate model.

The goal of the current work is to study the spectroscopic properties of red-phase MEH-PPV as a function of temperature, systematically covering a temperature range down to 5 K. An initial increase of the ratio with temperature would indicate dominant H-like behavior, as observed in spin-cast P3HT films[5,7] while a decrease of the ratio with temperature would indicate J-like behavior, as was observed for isolated PDA chains.[16] We are particularly interested in the impact of disorder on the temperature dependence of the 0-0/0-1 PL line strength. To this end, we have enhanced the HJ-aggregate model introduced in Ref. 22 to include electron and hole site disorder.

A very elegant earlier work by Collison *et al.*[26] showed that the room-temperature PL spectral line shape of MEH-PPV dissolved in a toluene/hexane solvent mixture can be understood using a two-emitter model; the vibronic progression arising from isolated disordered chains is superimposed on a red-shifted vibronic progression arising from aggregates. Collison *et al.*[26] concluded that although the red-phase corresponds to aggregates, the spectral line shapes are consistent with single (elongated) chains. Single-molecule studies have also associated the red-shifted spectrum with aggregates[30] but emphasizing that the photophysics can be understood in terms of single elongated chromophores.[30,31] How is it then possible to reconcile the profound effect of aggregation on the PL line shape of spin-cast P3HT films with the apparently mild effect of aggregation on red-phase MEH-PPV? By measuring the temperature dependence of the PL line shape in red-phase MEH-PPV aggregates down to 5 K, and interpreting the results in terms of the disordered HJ-aggregate model, we show here that interchain interactions are certainly not negligible in MEH-PPV aggregates and that the PL line shape properly reflects a competition between intrachain and interchain forces tempered by the presence of substantial disorder.

II. EXPERIMENTAL METHODS

Absorption and photoluminescence spectra were taken from MEH-PPV (ADS, $M_w = 1000$ kD) in MeTHF solution at a concentration of 5×10^{-5} mol/l using, for absorption, a home-built setup consisting of a tungsten lamp, the sample in a fused silica 1 mm cuvette inside a continuous-flow temperature-controlled cryostat, a monochromator, and a silicon diode connected to a lock-in amplifier. For photoluminescence spectra, a PicoQuant laser diode at 405 nm was used to excite the sample and an Oriel Instaspect IV CCD-camera attached to a spectrograph was used to record the spectrum. Photoluminescence lifetimes were measured by time-correlated single photon counting (TCSPC) using a FluoTime

200 time-resolved spectrometer by PicoQuant. For excitation, a PDL 800-D pulsed diode laser with a wavelength of 405 nm was used, the detector was a MCP-PMT by Hamamatsu and the data acquisition unit was the PicoHarp 300 TCSPC system. The time resolution of the setup is about 70 ps.

For an analysis of the spectra, the ratio between the intensity of the 0-0 and 0-1 peaks in the absorption and PL spectra needs to be known precisely. We have modeled the absorption spectrum, $\bar{A}(\hbar\omega)$, and the PL spectrum, $\bar{S}(\hbar\omega)$, as Franck-Condon (FC) transitions involving several intramolecular vibrational modes, i, according to[38]

$$\bar{A}(\hbar\omega) = n(\hbar\omega)\sum_{\{m_i\}}\prod_i I_{0\to m_i} \times \Gamma\left[\hbar\omega - \left(\hbar\omega_{0-0} + \sum_i m_i\,\hbar\omega_i\right)\right], \quad (1a)$$

$$\bar{S}(\hbar\omega) = n^3(\hbar\omega)^3\sum_{\{m_i\}}\prod_i I_{0\to m_i} \times\Gamma\left[\hbar\omega - \left((\hbar\omega_{0-0} - \sum_i m_i\,\hbar\omega_i\right)\right], \quad (1b)$$

where ω_i is the frequency of the ith mode, $m_i = 0,1,2,\ldots$ is the number of vibrational quanta in the ith mode, and the set of integers $\{m_i\}$ identifies a particular combination peak, for example, $\{0, 0, \ldots, 0\}$ pertains to the "0-0" peak with energy $\hbar\omega_{0-0}$. Γ is the Gaussian line shape function with constant standard deviation σ. The intensities $I_{0\to m_i}$ of the vibronic transitions 0-m_i are related to the Huang-Rhys parameter S_i for a particular mode i via $I_{0-m_i} = e^{-S_i}S_i^{m_i}/m_i!$. The linear (cubic) dependence in Eq. (1a) (Eq. (1b)) on the refractive index n of the surrounding medium and on the frequency arises from considering the influence of the photon density-of-states in the medium surrounding the emitter on its absorption rate (emission coefficient).[39]

III. EXPERIMENTAL RESULTS

We have recently shown that MEH-PPV in moderately dilute MeTHF solution undergoes a phase transition from a disordered, coiled conformation to a conformation containing extended chain segments that are characterized by a red-shifted absorption and emission.[27] The transition from the disordered, "blue" phase to the ordered, "red" phase can be induced by a change in temperature. Both conformations have been observed for a variety of experimental conditions, including even measurements on single-molecules and core-shell-structures.[26–31,33–37,40]

Fig. 1 shows the absorption and emission spectra for MEH-PPV in MeTHF solution at 300 K, where the polymer chain is coiled, and at 80 K, where the extended red phase prevails. One may notice that at 300 K, the absorption and emission spectra appear to be of comparable shape, except for the size of the inhomogeneous broadening. In contrast, at 80 K the 0-1 peak in emission centered on 1.90 eV is much lower than the corresponding peak at about 2.25 eV in absorption. Such a feature has been predicted as a signature for a J-aggregate[8] and it has also been observed for perfectly ordered systems such as crystalline polydiacetylene.[15] The difference in vibrational peak intensities can be assessed using a FC analysis. We stress that at this level such an analysis is approximate, as it does not account for the changes that the FC progression undergoes upon aggregation. The 0-n vibronic peak intensities are affected differently by aggregation,[4,5] the most dramatic example being the uniquely attenuated 0-0 peak in the PL spectrum of H-aggregates. Such effects will be considered in Secs. V and VI.

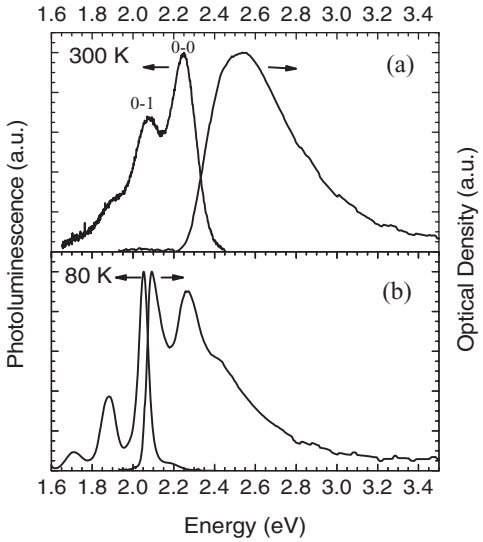

FIG. 1. Absorption and emission intensity of MEH-PPV in MeTHF, taken at 300 K (a) and at 80 K (b), as a function of photon energy.

Figs. 2(a) and 2(b) show the normalized absorption and emission of the blue phase and red phase, respectively, along with the Franck-Condon fit. The luminescence spectra have been corrected for the cubic dependence of the radiative decay rate on photon frequency, and the linear dependence on

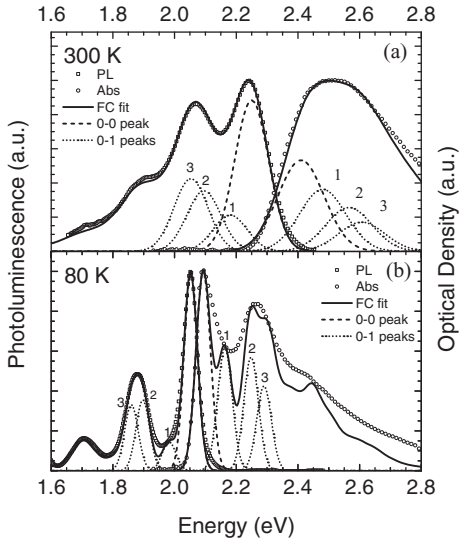

FIG. 2. Franck-Condon analysis to the spectra at 300 K (a) and at 80 K (b). The emission spectra (squares) were divided by ω^3, the absorption spectra (circles) were divided by ω. The solid line shows the Frank-Condon-fit. The 0-0 peak and the 0-1 peaks of the 3 modes considered, labeled 1-3, are shown as dashed and dotted lines, respectively.

photon frequency of the absorption was accounted for in the absorption spectra.[39] For the Franck-Condon analysis, we considered the three modes at 70 meV, 155 meV, and 192 meV that can be resolved in the emission spectrum taken at 5 K (see Fig. 4 further below). The 192 meV mode reflects a carbon-carbon stretching vibration, the 155 meV mode is associated with a coupled carbon-carbon stretching/carbon-hydrogen bending motion, and the 70 meV mode is likely to involve some torsional or librational motion.

The analysis of the 300 K spectra (Fig. 2(a)) shows that the experimental spectra can be well reproduced with these 3 modes. The line width σ is narrower in emission (σ = 55 meV) than in absorption (σ = 75 meV), consistent with energy transfer after absorption from a distribution of excited conjugated segments to the longer ones. The total "effective" Huang-Rhys factor, $S = S_1 + S_2 + S_3$, is S = 1.10 in emission and S = 1.45 in absorption, i.e., it is comparable, differing by only a factor of 1.3. From the intensities of the vibrational modes in Fig. 2(a), one sees that upon absorption, the electronic transition couples most prominently to the low-energy torsional mode at 70 meV. In contrast, the luminescence involves mainly the modes associated with carbon-carbon stretching motions.

In the red phase prevailing at 80 K, the coupling to the low-energy torsional modes is also dominant in absorption, yet very low in emission. However, in contrast to the coiled phase at 300 K, the total values for the effective Huang-Rhys factors differ strongly, by about a factor of 2, with S = 0.78 in emission and S = 1.61 in absorption. Moreover, the linewidths for emission (σ = 22 meV) and absorption (σ = 24 meV) are narrowed by more than a factor of two compared to the blue phase at 300 K. We note that the FC fit for absorption does not account for the extra asymmetric broadening of the vibronic peaks observed in experiment. Such an asymmetry may arise from a distribution of conjugation lengths.

The evolution of the effective Huang-Rhys factors as a function of temperature for the red phase is shown in Fig. 3(a). For the luminescence, they are constant over the entire temperature range investigated for the red phase. In absorption, the overall amount of geometric distortion also remains constant. Considering the contribution of the different modes shows, however, a continuous reduction with decreasing temperature of the 70 meV mode associated with torsional motion and a concomitant increase of the carbon-carbon stretching mode at 192 meV. This redistribution may suggest a further planarization in the chain conformation upon cooling. Analogous to the Huang-Rhys factors, the fluorescence lifetimes (Fig. 3(b)) are also constant. A factor that changes, however, is the Gaussian linewidth σ (Fig. 3(c)). It reduces by nearly a factor of 2 when going from 120 K to 5 K. This narrowing of the emission spectra is accompanied by further bathochromic shift, as evident in Fig. 4.

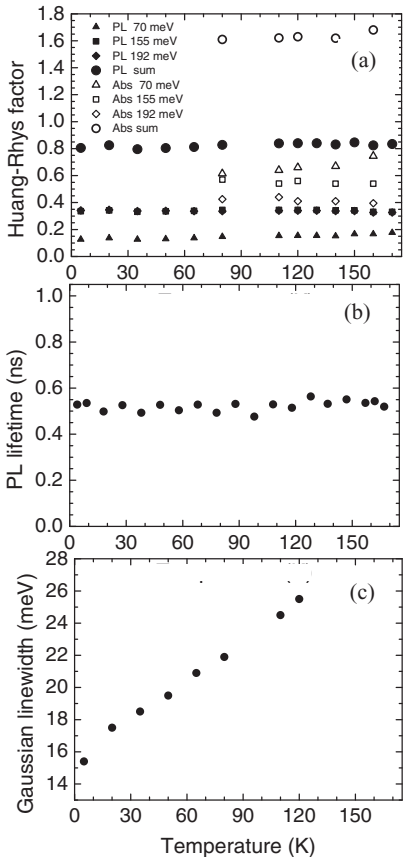

FIG. 3. The evolution of different photoluminescence parameters in the red phase as a function of temperature: (a) The effective Huang-Rhys factor for the modes at 70 meV, 155 meV, and at 192 meV as well as their combined values ("sum") taken from the emission spectra ("PL") and taken from the absorption spectra ("Abs"), (b) the fluorescence lifetime, and (c) the standard deviation σ of the Gaussian linewidth for the 0-0 $S_0 \rightarrow S_1$ transition.

IV. MEH-PPV DIMERS: THE DISORDERED HJ-AGGREGATE MODEL

In the following, we will show that the basic photophysical features observed for red-phase MEH-PPV can be understood using the HJ-aggregate model developed in Ref. 22, enhanced to include electron/hole site-energy disorder. We treat the simplest aggregate – a dimer, consisting of two cofacial MEH-PPV chains, each containing N repeat units. Vibronic coupling of the 1^1B_u intrachain exciton to the three vibrational modes identified in Sec. III are accounted for by coupling to a single *effective* mode, with energy, $\hbar\omega_0 = 0.174$ eV (1400 cm^{-1}), which is the approximate spacing between the first two vibronic peaks in the 80 K absorption spectrum in Fig. 1. Since the HJ model resolves exciton motion along a given chain (as well as between chains), the relevant HR

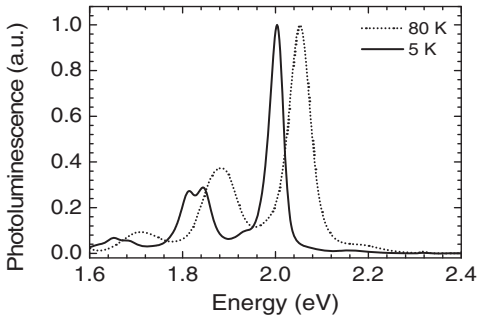

FIG. 4. Comparison of the fluorescence spectrum at 80 K and at 5 K.

factor for the effective mode relates to a single phenylene-vinylene repeat unit, where only the HOMO and LUMO levels are retained in our course-grained approach. Hence, for a neutral Frenkel-like excitation corresponding to a HOMO-LUMO transition within a given monomer the HR factor was set to $\lambda_0^2 = 2$, consistent with the value extrapolated from the measured HR factors in a series of OPVn molecules, where n = number of phenyl groups.[19] (In Ref. 19, the HR factors deduced from the measured PL spectra increase with decreasing n to a value of approximately 1.5 for stilbene.) The HJ model also allows for charge-separated states. Hence, for the cationic (half-filled HOMO) and anionic (half-filled LUMO) monomers, we took slightly smaller values for the HR factors, $\lambda_+^2 = \lambda_-^2 = 1.5$, consistent with the expected softening of the vibronic coupling.

In the disordered HJ-aggregate model, the Hamiltonian for two coupled polymer chains is written as

$$H = H_1 + H_2 + H_{12} + H_{dis}. \tag{2}$$

Here, H_s (s = 1,2) represents the sth chain with no disorder present, H_{12} represents the interchain interaction, and H_{dis} accounts for disorder. With each chain modeled as a one-dimensional semiconductor with vibronic coupling, H_s takes the form[8]

$$\begin{aligned} H_s = {} & e_e + e_h + \sum_n \left[t_e c_{n,s}^\dagger c_{n+1,s} + t_h d_{n,s}^\dagger d_{n+1,s} + h.c. \right] \\ & + \sum_{n,r} V(r) c_{n,s}^\dagger c_{n,s} d_{n+r,s}^\dagger d_{n+r,s} \\ & + \hbar\omega_0 \sum_n b_{n,s}^\dagger b_{n,s} \\ & + \hbar\omega_0 \sum_n \{\lambda_0 (b_{n,s}^\dagger + b_{n,s}) + \lambda_0^2\} c_{n,s}^\dagger c_{n,s} d_{n,s}^\dagger d_{n,s} \\ & + \hbar\omega_0 \sum_{n,r\neq 0} \{\lambda_- (b_{n,s}^\dagger + b_{n,s}) + \lambda_+ (b_{n+r,s}^\dagger + b_{n+r,s}) \\ & + \lambda_-^2 + \lambda_+^2\} c_{n,s}^\dagger c_{n,s} d_{n+r,s}^\dagger d_{n+r,s}. \end{aligned} \tag{3}$$

A full description of H_s is given in Ref. 8. Essentially, H_s is limited to the subspace containing a single electron and a single hole within MOs built from the coupled HOMOs and LUMOs from each phenylene-vinylene unit. $c_n^\dagger (d_n^\dagger)$ and $c_n (d_n)$, respectively, create and annihilate an electron (hole) in the LUMO (HOMO) of the nth unit cell. The summations in Eq. (3) run over all N repeat units. The electron (hole) transfer integral t_e (t_h) couples neighboring LUMOs (HOMOs). Maintaining charge conjugation symmetry, we take $t_e = t_h = -t$ (with $t > 0$) as for a direct bandgap semiconductor.[41] $V(r)$ is the Coulombic interaction between electron and hole separated by $|r|$ unit cells,

$$V(0) = -U \qquad U > 0, \tag{4a}$$

$$V(r) = -V_1/|r| \qquad V_1 > 0. \tag{4b}$$

Hence, $e_e + e_h - U$ is the energy required to create a (singlet) e/h pair within a given unit cell, while $U - V_1$ is the energy barrier for charge separation between adjacent unit cells. To describe the binding well, we took U = 1.0 eV and V_1 = 0.5 eV, essentially the same parameters as those used by Wu and Conwell[41] for describing MEH-PPV (but without vibronic coupling). However, whereas t = 1.0 eV was used in Ref. 41, we chose t = 0.5 eV, in order to obtain the best reproduction of the absorption spectral line shape (see below).

The band of phonons deriving from the effective phenylene-vinylene-stretching mode is taken to be dispersionless with frequency $\omega_0 \approx 0.175$ eV/$\hbar$ (i.e., Einstein phonons). Their influence on the total energy is contained in the last three summation terms in Eq. (3). $b_n^\dagger$ (b_n) creates (destroys) a vibrational quantum in the ground state (S_0) nuclear potential well corresponding to the absence of electrons and holes in monomer n (i.e., a filled HOMO level). The second to last summation term accounts for elongation along the vibrational coordinate when the nth monomer is excited to the neutral state S_1 containing a single e/h pair. The corresponding nuclear potential, S_1 is shifted relative to S_0 and is characterized by a HR factor λ_0^2 (= 2). The shifts in the nuclear potentials corresponding to cation and anion excitations are represented by the HR factors, λ_+^2 and λ_-^2, respectively, appearing in the last summation term ($\lambda_+^2 = \lambda_-^2 = 1.5$). Our model assumes that all four (unit cell) potential wells are harmonic with identical curvature.

The electronic interactions between chains is given by

$$H_{12} = \sum_{n=1,N} J_{inter} \{ |n,1\rangle\langle n,2| + |n,2\rangle\langle n,1| \}. \tag{5}$$

Here, a simplified form of the Coulombic, interchain coupling J_{inter} is assumed in which the interactions are limited to adjacent (same n) repeat units on opposing chains. The basis functions are defined with $|n,s\rangle \equiv c_{n,s}^\dagger d_{n,s}^\dagger |g\rangle$ (s = 1,2), where $|g\rangle$ is the pure electronic dimer ground state in which all $2N$ monomers are unexcited (filled HOMO levels). In reality, a given monomer on one chain interacts with *all* monomers on another via through-space coupling. The absorption spectrum depends only on the $k = 0$ interaction sum, denoted as $\tilde{J}_{inter}(k = 0)$, which is the sum of interactions between all monomer repeat units on one chain and a given monomer repeat unit on the other. In our simplified Hamiltonian we have, $\tilde{J}_{inter}(k = 0) = J_{inter}$, and therefore view J_{inter}, as the *effective* through-space interaction between the two chains.

Finally, in order to incorporate disorder, which is necessary to account for the temperature dependencies of the PL spectral line shape and radiative decay rate (see Sec. VI), we assume a simple model accounting for the transition frequency deviation, $\Delta_{n,s}^e (\Delta_{n,s}^h)$ for an electron (hole) on the nth repeat unit of the sth chain. Such offsets are measured against the mean electron or hole energies, e_e and e_h, respectively, and are Gaussian distributed random variables with the distribution given by

$$P(\Delta) = \frac{1}{\sqrt{2\pi}\sigma_{e,h}} e^{-\Delta^2/2\sigma_{e,h}^2}. \tag{6}$$

In Eq. (6), Δ represents the electron or hole energy offset at a particular site and $\sigma_{e,h}$ is the width of the distribution, taken to be the same for electrons and holes. In what follows, we do not assume any spatial correlation in the frequency offsets, i.e., $\langle \Delta_{n,s}^{e(h)} \Delta_{n',s'}^{e(h)} \rangle = \delta_{n,n'} \delta_{s,s'} \sigma_{e,h}^2$. Note that because all excited states contain a single electron and a single hole, the standard

deviation in the excitation energy is actually $\sqrt{2}\sigma_{e,h}$. In what follows, we denote this quantity as $\sigma_{dis} \equiv \sqrt{2}\sigma_{e,h}$.

Introducing disorder in this manner leads to an explicit form for the Hamiltonian representing the last term in Eq. (2),

$$H_{dis} = \sum_{n,s} \left(\Delta^{e}_{n,s} c^{\dagger}_{n,s} c_{n,s} + \Delta^{h}_{n,s} d^{\dagger}_{n,s} d_{n,s}\right). \tag{7}$$

Since our Hamiltonian (2) is defined in the subspace containing a single electron and a single hole, all local basis states will be detuned by the sum of an electron detuning plus a hole detuning, independent of whether the electron and hole occupy the same site (as in a Frenkel-like excitation) or different sites (as in a charge-separated state). A more sophisticated model would distinguish these two cases with possibly different disorder widths.[42]

The Hamiltonian in Eq. (2) is represented in the multiparticle basis set, including up to 3-particle states which can either be Frenkel-like states or Charge-Separated (CS) states.[8,43] Here, an n-particle excitation involves n monomer repeat units which are excited either electronically or purely vibrationally, under the constraint that there is always a single electron and single hole excitation. For example, a three particle state can contain a Frenkel-like excitation on one site (electron/hole pair) and two purely vibrational excitations on two other neutral sites. (Pure vibrational excitations consist of a repeat unit with a filled HOMO but with one or more vibrational quanta in the S_0 nuclear potential specific to that site.) A three-particle state can also consist of a charge separated pair occupying two sites, with an additional vibrationally excited neutral site. In this work, we retain only the CS states in which the electron and hole exist within a single chain. (Hence, we neglect polaron pair states.) The multiparticle states can be further classified as entirely intrachain or mixed inter/intrachain states. In the latter, excitations are distributed over the two chains, as would exist, for example, in a 3-particle CS state where the electron/hole pair exists on one chain while a pure vibrational excitation resides on the opposite chain. In the calculations to follow, we cap the total number of vibrational quanta in a multiparticle state at six, regardless of whether the state is Frenkel-like or CS. Once the Hamiltonian is expressed in the multiparticle basis set, numerical methods are used to obtain all eigenstates and energies.

It is useful to first characterize the excitons on a fully symmetric dimer, i.e., without disorder. The relevant Hamiltonian, $H - H_{dis}$, was analyzed in detail in Ref. 22. Application of periodic boundary conditions along the polymer backbone, allows all eigenstates to be described with a dimensionless wave vector k (= 0, $\pm 2\pi/N$, $\pm 4\pi/N$, ...) along the chain as well as their symmetry (+,−) with respect to the dividing reflection plane. Hence, the dimer Hamiltonian $H - H_{dis}$ can be factored into blocks, identified as (k,+) and (k,−) where the sign indicates the symmetry with respect to reflection. The αth eigenstate in block (k,j) with $j = +,-$ is denoted as $|\Psi_{k,j,\alpha}\rangle$ and has energy $\varepsilon_{k,j,\alpha}$. Eigenstates with $\alpha = 1,2,\ldots$ increase in energy and involve increasing admixtures of states with more vibrational quanta.

Because J_{inter} is taken to be positive, consistent with H-aggregation, the lowest energy exciton is antisymmetric (−). However, along the chain the wave vector remains $k = 0$, as in a linear J-aggregate. Hence, the lowest energy exciton has hybrid J/H character. It is identified by the quantum numbers, ($k = 0,-, \alpha = 1$), and, by Kasha's rule, is the primary emitting state in a disorder-free dimer at low temperatures. When the interchain coupling is weak, the zeroth-order emitting exciton is given by

$$|\Psi_{k=0,-,\alpha=1}\rangle^{(0)} = \frac{1}{\sqrt{2}}\{|\psi_{k=0,\alpha'=1}\rangle_1 |G\rangle_2 - |\psi_{k=0,\alpha'=1}\rangle_2 |G\rangle_1\}, \tag{8}$$

where $|\psi_{k=0,\alpha'=1}\rangle_s$ (s = 1,2) is the lowest energy exciton on the sth chain – the (vibrationally dressed) 1^1B_u exciton as described in detail in Ref. 8 – and $|G\rangle_s$ is the vibrationless ground state on chain s. For the parameters chosen to model a *single* MEH-PPV chain, analysis of H_1 in Eq. (3) shows that the 1^1B_u exciton has a Bohr radius of ≈10 Å and a binding energy of ≈0.58 eV, slightly larger than values ranging from 0.35 eV to 0.54 eV reported in the literature.[41,44] Increasing interchain interactions mixes the zero-order antisymmetric states in Eq. (8) with increasing α' (involving one or more vibrational quanta), the equivalent of inter-band mixing in Frenkel aggregates.[45]

Figure 5(a) shows the k-dependent energies corresponding to the eigenstates of H_1 for a single, ordered chain, evaluated numerically within the aforementioned multiparticle basis set. Several bound states are observed to split off the free-polaron continuum, the lowest of which ($\alpha = 1$) corresponds to the 1^1B_u exciton which is dominated by admixtures with

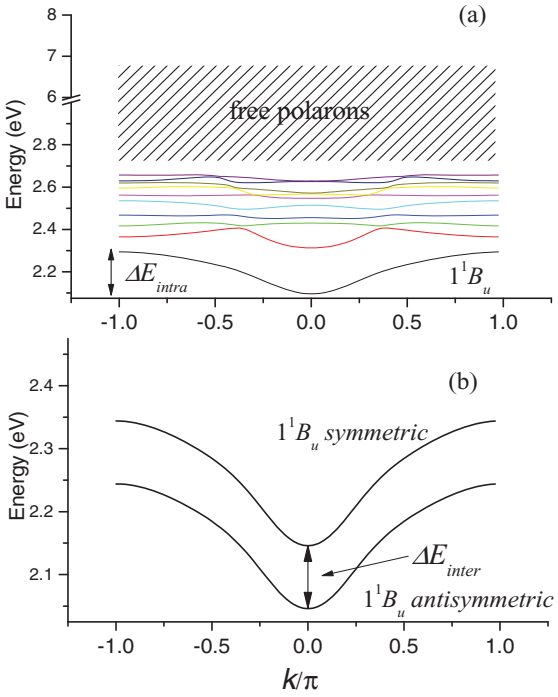

FIG. 5. (a) Dispersion curves for the ten lowest energy excitons in a single MEH-PPV parameterized chain: $U = 1$ eV, $V_1 = 0.5$ eV, and $t = 0.5$ eV, $e_e + e_h = 4.31$ eV. The energy of the effective vibrational mode is 0.175 eV with HR factors: $\lambda_0^2 = 2$, $\lambda_+^2 = \lambda_-^2 = 1.5$. Note the break in the vertical scale: the total bandwidth including also the free polarons is quite large, approximately 4 eV. (b) Interchain interactions (with $J_{inter} = 250$ meV) cause a splitting of the 1^1B_u band. Absorption is allowed only to the symmetric band. A higher energy symmetric state is characteristic of H-aggregates.

Frenkel-like and CS states containing on average almost no vibrational quanta. Such states contribute to the first vibronic (0-0) peak in the absorption spectrum. The next higher energy band ($\alpha = 2$) corresponds to excitons similar to the 1^1B_u exciton but containing an average of close to one vibrational quanta. Such states give rise to the second vibronic peak in the absorption spectrum (0-1),[46] but are too high in energy to contribute significantly to emission. Figure 5(a) shows that the associated bandwidth, ΔE_{intra}, for the ($\alpha = 1$) 1^1B_u exciton is approximately $\Delta E_{intra} = 0.2$ eV, reflecting the strength of the intramolecular coupling as mediated by t and modulated by the narrowing influence of vibronic coupling. ΔE_{intra} is far smaller than the full bandwidth of ≈4 eV which also includes the unbound intrachain polarons (note the axis break in Fig. 5(a)).

Through-space Coulombic coupling within the dimer splits the 1^1B_u band into a low-energy antisymmetric ($\varepsilon_{k,-,\alpha=1}$) band and a higher-energy symmetric ($\varepsilon_{k,+,\alpha=1}$) band, as depicted in Fig. 5(b). For the simplified form of the Coulombic coupling in Eq. (5), the band splitting, ΔE_{inter}, is approximately independent of k when the excitonic coupling within the chain is strong, i.e., the high energy dispersion curve is vertically displaced by ΔE_{inter} relative to the low-energy band. The interchain coupling, J_{inter}, within the MEH-PPV dimer leads to the exciton splitting, as depicted in Fig. 5(b). As shown in Ref. 22, the splitting is given by

$$\Delta E_{inter} \approx 2F\phi_0 J_{inter}. \tag{9}$$

The splitting ΔE_{inter} is not simply $2J_{inter}$ but is substantially reduced by an additional factor of $F\phi_0$. The factor ϕ_0 arises because the Frenkel-exciton coupling in Eq. (3) depends on the probability (ϕ_0) of the electron and hole being on the same unit cell. Our calculations using the parameters which best describe MEH-PPV (see caption of Fig. 5) give $\phi_0 \approx 0.4$. The factor F is a generalized FC factor accounting for vibronic coupling and ranges from $\exp[-\lambda_0^2]$ in the weak exciton coupling limit to unity in the strong exciton coupling limit. Since coupling is dominant within the chain, F can be approximated by using the single-chain value, $F \approx 0.5$. Hence, Eq. (9) gives a splitting, $\Delta E_{inter} \approx 0.4 J_{inter}$, in MEH-PPV dimers.

V. ABSORPTION IN MEH-PPV DIMERS

The main effect of introducing site disorder H_{dis} in Eq. (7) is to mix the various k-states within the two lowest energy bands in Fig. 5(b). The result is primarily an increase of the line width corresponding to the $|G\rangle \rightarrow 1^1B_u$ exciton transition (the 0-0 transition), as well as higher energy vibronic transitions (i.e., 0-1). However, because the calculated intrachain bandwidth, $\Delta E_{intra} = 200$ meV, is considerably larger than the measured line width σ (≈30 meV at T = 80 K), we might expect motional (or "exchange") line narrowing to be important. Such narrowing is one of the hallmark signatures of J-aggregates and has been extensively studied by Knapp[47] and Fidder *et al.*[48] for linear Frenkel aggregates (without vibronic coupling). When the exciton bandwidth, W, satisfies, $W \gg N^{3/2}\sigma_{dis}/\pi^2$, the absorption spectral line width is reduced to $\sigma_{dis}/\sqrt{N}$, where σ_{dis} is the width of the inhomogeneous (Gaussian) distribution of chromophore site energies and N is the number of chromophores in the aggregate. For increasing N, the inequality eventually cannot be satisfied and the line width converges to a value between σ_{dis} and $\sigma_{dis}/\sqrt{N}$.

Although our model Hamiltonian in Eq. (2) is not of the simple Frenkel exciton form, motional narrowing due to exciton delocalization over the $2N$ monomers comprising the MEH-PPV dimer remains operative. Recently, motional narrowing of the environmental disorder has been demonstrated in MEH-PPV and its oligomers.[49] Since intrachain exciton coupling is so much larger than the interchain coupling in MEH-PPV, the main effect of motional narrowing can be obtained through analysis of a single chain using the uncorrelated inhomogeneous distribution of electron and hole energies in Eq. (6). Unfortunately, the basis set necessary to obtain a converged absorption spectrum for a chain containing more than eight repeat units is so large that averaging over the thousands of configurations of disorder needed to obtain a good signal to noise ratio is not feasible. Therefore, to estimate the impact of motional narrowing we made the approximation that disorder couples only states within the *same* vibronic band. For a single chain, we determine the impact of motional narrowing by expressing H_{dis} in Eq. (7) in a basis set consisting of all N excitons in the lowest energy band (1^1B_u band) of Figure 5(a). Such a procedure gives a single, inhomogeneously broadened (0-0) peak absorption spectrum from which the line narrowing can be determined. Our goal was to determine what value of σ_{dis} is necessary to obtain a line width which best describes the spectra of Sec. III, $\sigma \approx 32$ meV. The latter is slightly larger than the value deduced from our FC fit, but accounts for the extra asymmetric broadening found in the measured spectrum. Our choice of σ_{dis} will also reproduce the measured PL line width (see below). From such an analysis, we found a very significant motional narrowing of about a factor of 2.8 in the large N limit; in other words, the calculated line width is $\sigma = \sigma_{dis}/2.8$, so that $\sigma_{dis} = 90$ meV is necessary to reproduce the measured line width (32 meV). The N dependence of the calculated line width σ is depicted in Fig. 6. σ follows the predicted $1/\sqrt{N}$ dependence up to $N = 7$, thereafter converging to approximately the experimental value, $\sigma_{dis}/2.8$.

We checked our approximate treatment of disorder by comparing it to exact calculations involving small chains with up to six repeat units (2000 configurations), and the line widths calculated by both methods are in excellent agreement. We also note that in our small oligomer calculations the relative intensities of the various vibronic bands, in particular the 0-0/0-1 ratio of oscillator strengths, was not affected by disorder, so that disorder primarily affects the line widths, as anticipated. Thus, in order to obtain the absorption spectral line shape for large chains and dimers thereof, we evaluate transition strengths from *disorder-free* chains and broadened each transition using a Gaussian line shape function with a width of 32 meV. This "homogeneous" approximation precludes the time-costly averaging procedure allowing one to work with large-N chains. Moreover, in the homogeneous limit, the absorption spectrum depends only on the totally symmetric states, i.e., the $k = 0$ excitons which are

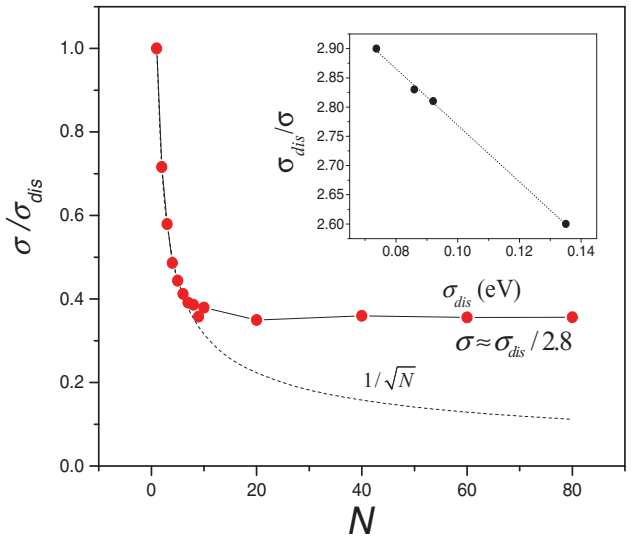

FIG. 6. Calculated width of the 0-0 absorption line as a function of the number of repeat units in a single MEH-PPV chain. The width of the Gaussian distribution of electron and hole energies was set to $\sigma_{dis} = 90$ meV. The parameters characterizing the MEH-PPV chain are the same as those in Fig. 5. Inset shows the large-N narrowing factor as a function of σ_{dis}.

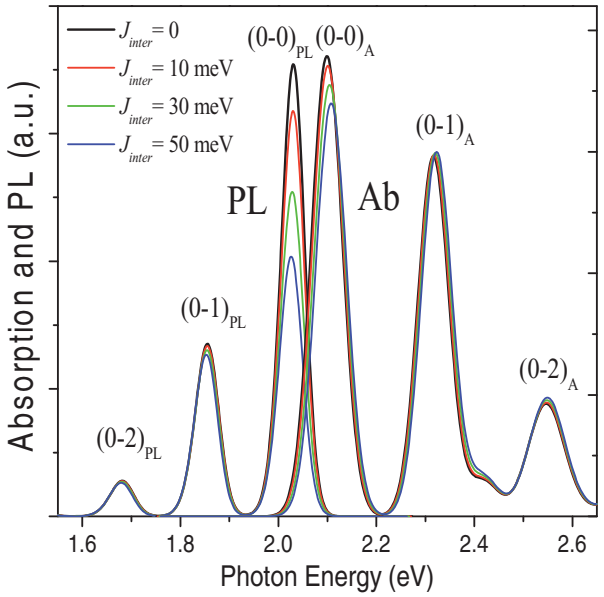

FIG. 7. Numerically calculated absorption and PL spectra using Eqs. (10) and (15) respectively, for MEH-PPV dimers consisting of two cofacial chains of 80 repeat units each and for several values of the interchain coupling, J_{inter}. The single-chain parameters are given in the caption of Fig. 5. The PL spectra are calculated using Eq. (15) for a disordered dimer at T = 80 K with $\sigma_{dis} = 90$ meV (see text). The line width used in Eq. (10) is $\sigma = 32$ meV $= (\sigma_{dis}/2.8)$.

symmetric (+) with respect to the reflection plane dividing the two chains.

The absorption spectrum is obtained using the expression

$$A(\omega) = \sum_{\alpha} f_{k=0,+,\alpha}\Gamma(\omega - \omega_{k=0,+,\alpha}) \tag{10}$$

with the oscillator strength given by

$$f_{k=0,+,\alpha} \equiv \omega_{k=0,+,\alpha}|\langle G|\hat{\mu}|\Psi_{k=0,+,\alpha}\rangle|^2. \tag{11}$$

Here, $\omega_{k,+,\alpha} \equiv \varepsilon_{k,+,\alpha}/\hbar$, and $\hat{\mu}$ is the dipole moment operator,

$$\hat{\mu} \equiv \mu_0 \sum_{s=1,2}\sum_{n}(c^{\dagger}_{n,s}d^{\dagger}_{n,s} + d_{n,s}c_{n,s}), \tag{12}$$

with μ_0 equal to the $S_0 \rightarrow S_1$ transition dipole moment of the phenylene-vinylene monomer unit, polarized mainly along the polymer backbone. In Eq. (11), $|G\rangle$ is the vibrationless ground state of the polymer,

$$|G\rangle \equiv |g\rangle \otimes |0, 0, \ldots, 0\rangle, \tag{13}$$

where $|0, 0, \ldots, 0\rangle$ indicates that there are no vibrational quanta in the monomer S_0 (unshifted) nuclear potentials (the vacuum state). Finally, Γ is a line shape function, chosen here to be a peak-normalized Gaussian,

$$\Gamma(\omega) = \exp(-\omega^2/2\sigma^2), \tag{14}$$

with a width, $\sigma = 32$ meV.

Fig. 7 shows calculated absorption spectra for cofacial MEH-PPV dimers consisting of 80-monomer chains ($N = 80$). Several values of the interchain coupling, J_{inter}, are shown. The spectrum consists primarily of a dominant 0-0 peak, corresponding to the 1^1B_u exciton absorption, and its first side band (0-1). The ratio of the oscillator strengths of the 0-0 and 0-1 peaks, $R_{abs} \equiv I_A^{0-0}/I_A^{0-1}$, ranges from 1.25 for isolated chains ($J_{inter} = 0$) to about 1.1 for the largest interchain coupling shown ($J_{inter} = 50$ meV), in good agreement with the experimentally determined ratio from Fig. 1(b).[27] The *decrease* in R_{abs} with increasing interchain interaction is characteristic of H-aggregates as discussed in detail in Ref. 18, and is ultimately traced back to the positive sign of J_{inter}.

For a *single* chain, the value of $R_{abs} \approx 1.25$ is substantially larger than the value of 0.5 which arises from an *isolated* monomer (phenylene vinylene unit), as follows from the usual Poissonian distribution, $I^{0-v}_{mon} \approx \lambda_0^{2v}\exp(-\lambda_0^2)/v!$ using $\lambda_0^2 = 2$. The more than doubling of R_{abs} when the coupling, t, between repeat units is activated ($t = 0.5$ eV) can be viewed as a decrease in vibronic coupling due to the delocalization of the exciton over the entire chain.[21] An increasing R_{abs} with electronic coupling is also a defining signature of J-aggregates.[18] Increasing t to 1 eV (not shown) in a single chain leads to a very large increase in R_{abs} to almost 3, thereby justifying our choice of $t = 0.5$ eV for MEH-PPV. Overall, the absorption spectrum of aggregated MEH-PPV responds like a J-aggregate with respect to intrachain coupling and a H-aggregate with respect to interchain coupling.

Careful inspection of the absorption spectra in Fig. 7 shows that the spectral separation between the first two vibronic peaks in the absorption spectrum is slightly larger than a single vibrational quantum. We have verified that the dilation is mainly due to truncating the basis set at the three-particle level. Inclusion of four-particle states in evaluating the absorption spectra of small oligomers reduces the spectral gap to a single vibrational quantum and, most importantly, shows a less than 5% change in the relative oscillator strengths.[50]

VI. EMISSION FROM DISORDERED MEH-PPV DIMERS

Unlike in the absorption spectrum, the relative intensities of the vibronic peaks within the PL spectrum depend very strongly on disorder. As a simple example, consider a disorder-free H-aggregate at T = 0 K. In this limit, the 0-0 emission peak is entirely absent from the vibronic progression due to a total destructive interference between emission from the two chains.[22] The 0-0 line strength increases with increasing disorder as the symmetry is broken. Hence, in order to properly evaluate the PL line shape in MEH-PPV dimers, one must deal with the full Hamiltonian in Eq. (2), and average the spectra over an ensemble of electron and hole site-energy configurations.

The emission spectrum for a distribution of disordered dimers at temperature T is evaluated using the expression

$$S(\omega) = \sum_{v_t=0,1,\ldots} \langle (\omega_\alpha - v_t\omega_0)^3 I_\alpha^{0-v_t}\, \Gamma_{\rm hom}(\omega - \omega_\alpha + v_t\omega_0)\rangle_{C,T}. \tag{15}$$

The sum in Eq. (15) represents a vibronic progression involving transitions terminating on ground electronic states (all repeat units with a filled HOMO) with a total of v_t vibrational quanta distributed amongst the associated $2N$ monomeric S_0 potentials. α designates the αth eigenstate of H in Eq. (2) for a disordered dimer identified by the configuration of electron and hole site energy deviations, $(\Delta_1^e, \Delta_1^h, \ldots, \Delta_{2N}^e, \Delta_{2N}^h)$, with $\alpha = 1,2,\ldots$ in order of increasing energy, $\hbar\omega_\alpha$. Although not indicated, the line strengths $I_\alpha^{0-v_t}$ and energies $\hbar\omega_\alpha$ all depend on the particular disorder distribution. The exact expression for $I_\alpha^{0-v_t}$ can be found in Ref. 22. The symbol $\langle\ldots\rangle_{C,T}$ indicates a configurational average over the many realizations of disorder, as well as a thermal (Boltzmann) average over the lowest thermally populated excitons within each disordered dimer. The thermal average is discussed in greater detail in Ref. 22. In what follows, the averaged line strength of the 0–v_t transition is designated as, $I_{PL}^{0-v_t} \equiv \langle I_\alpha^{0-v_t}\rangle_{C,T}$. Finally, the homogeneous line shape function in Eq. (15) is taken to be Gaussian, $\Gamma_{\rm hom}(\omega) = \exp(-\omega^2/2\sigma_{\rm hom}^2)$, with the homogeneous line width $\sigma_{\rm hom} = 14$ meV.

Fig. 7 also shows the numerically calculated PL spectra using Eq. (15) for several values of J_{inter}. Averages were performed over 10^4 configurations of disorder. All of the spectra are evaluated at T = 80 K (needed for the Boltzmann average) and for the disorder width, $\sigma_{dis} = 90$ meV, which reproduced the line widths of the vibronic peaks in the absorption spectrum (see Sec. V). The figure shows that the impact of J_{inter} on the PL spectrum is far more dramatic than on the absorption spectrum, with most of the changes confined to the 0-0 line strength. The substantial drop in the PL 0-0 peak intensity with increasing interchain coupling is characteristic of H-aggregates and is due to more effective destructive interference between the emitting chains. Interestingly, the side-bands are far less sensitive, only slightly decreasing with J_{inter}. The 0-0/0-1 PL ratio matches the measured value in the red-phase spectrum (see Fig. 1) when $J_{inter} = 30$ meV. Note that our calculations also reproduce the measured 0-2/0-1 ratio quite well. Fig. 7 further shows that the 0-2/0-1 ratio is practically independent of J_{inter}. We have shown that this ratio is far more sensitive to the intrachain bandwidth, where it *decreases* with increasing ΔE_{intra}.[51] Interestingly, the 0-2/0-1 ratio is more than twice as large in P3HT films, reflecting a smaller intrachain bandwidth in P3HT vs MEH-PPV.

The vibronic linewidths in the calculated PL spectra in Fig. 7 are significantly narrower than the width, σ_{dis}, of the Gaussian distribution from which the site energies are drawn. In fact, the emission lines are about 30% narrower than the already motionally narrowed 0-0 absorption line width with $\sigma = 32$ meV; the calculated inhomogeneous line width for the 0-0 PL line is only $\sigma = 21$ meV, which nicely agrees with the experimentally determined line width of 22 meV from Fig. 2.

The significant Stokes shift observed in Fig. 7 of approximately 60 meV is in good agreement with the measured value of approximately 50 meV from Fig. 1(b). The Stokes shift is due to spectral relaxation within the disordered density of states consistent with our assumption made in Fig. 7 that emission occurs only from the lowest energy thermally populated states within a given (disordered) dimer. This also leads to the aforementioned enhanced narrowing in the PL vibronic lines vs the absorption vibronic lines.[7] Although the measured PL spectrum continues to red-shift with further decreases in temperature (see Fig. 4), this cannot unambiguously be attributed to an increasing Stokes shift since we have not measured the absorption spectrum at lower temperatures due to scattering of the sample below the glass transition temperature of MeTHF. In fact, in P3HT films a significant red-shift in the absorption spectral origin of several hundred wave numbers is observed upon cooling from room temperature to 10 K,[7] possibly due to a reduction of intermolecular contact distances and an associated increase in the red-shifting, non-resonant dispersion interactions.

We now turn to the temperature dependence of the PL line strength ratios. Fig. 8 shows how the calculated line strength ratio, $I_{PL}^{0-0}/I_{PL}^{0-1}$ varies with temperature for three MEH-PPV dimers characterized by $J_{inter} = 0$, 10 meV, and 30 meV in panels (a)–(c), respectively. Within each panel, the temperature-dependent ratio is calculated for three levels of disorder, with $\sigma_{dis} = 0$ meV, 11 meV, and 22 meV. Let us first consider the behavior of isolated chains ($J_{inter} = 0$) with no disorder (top panel, triangles) where $I_{PL}^{0-0}/I_{PL}^{0-1}$ varies with T in accordance with what is expected for disorder-free linear J-aggregates.[8,17] The PL ratio is largest at lowest temperature, reaching a value of almost 25 at T = 0 K, about an order of magnitude larger than the measured value from Fig. 2, but decreasing steadily with increasing temperature. In Ref. 8, the ratio at T = 0 K for disorder-free polymer chains was shown to satisfy

$$I_{PL}^{0-0}/I_{PL}^{0-1} = \kappa N/\lambda_0^2. \tag{16}$$

The prefactor, κ, accounts for the impact of vibronic coupling on charge separated states. κ is exactly unity in the limit of Frenkel chains (no charge separation),[8,17] but generally deviates from unity for Wannier-like excitons, where it must be determined numerically.[8] For MEH-PPV, the parameters listed in the caption of Fig. 5 give $\kappa \approx 0.62$ for the lowest energy, $k = 0$ exciton ($1B_u$ exciton).[8] When temperature is increased or disorder added, N in Eq. (16), is replaced by the coherence number, N_{coh}.[8,17] Hence, the PL ratio can be used to

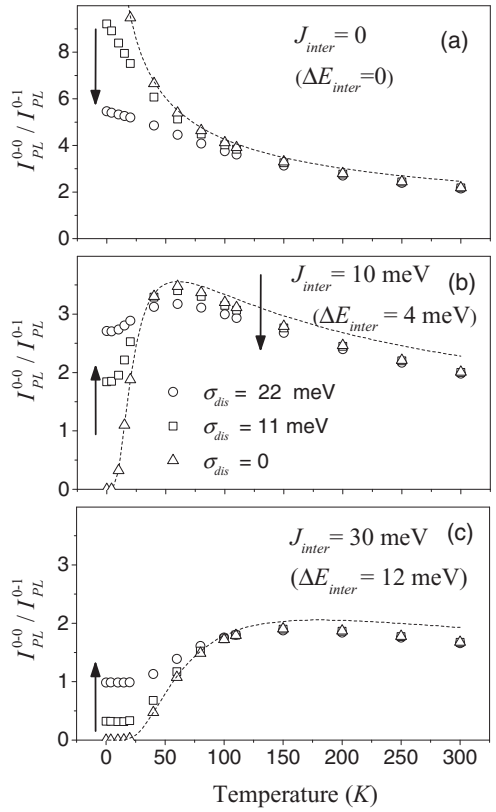

FIG. 8. (a)–(c) Numerically calculated 0-0/0-1 PL ratio as a function of temperature for MEH-PPV dimers for three values of the interchain coupling, J_{inter}. Within each panel the Gaussian line widths, σ_{dis}, are taken to be 0 (no disorder, triangle), 11 meV (square), and 22 meV (circle). The electronic parameters chosen for MEH-PPV are the same as those reported in Fig. 5. The dashed curves are obtained using Eq. (19) with $\kappa = 0.62$, $\omega_c = 0.12$ eV, and the interchain splittings, ΔE_{inter}, as calculated from Eq. (9) and reported in the figure inset. Equation (19), which assumes no disorder, closely agree with the numerical results for disorder-free dimers. The arrows point in the direction of increasing disorder.

directly extract the exciton coherence size in isolated polymer chains (as well as linear J-aggregates). In the thermodynamic limit (where N is sufficiently large so that many levels exist within k_bT), the PL ratio for noninteracting chains scales as the inverse square-root of the temperature, according to[8,17]

$$I_{PL}^{0-0}/I_{PL}^{0-1} \approx \frac{\kappa}{\lambda_0^2}\sqrt{\frac{4\pi\hbar\omega_c}{k_bT}}. \tag{17}$$

ω_c is the band curvature, $\omega_c \equiv (1/2\hbar)d^2E/dk^2$, evaluated at the bottom of the exciton band where $k = 0$ (k is the dimensionless wave vector ranging from $-\pi$ to π). From the 1^1B_u dispersion curve shown in Fig. 5(b), the curvature is estimated to be $\omega_c \approx 0.12eV/\hbar$. The dashed curve in Fig. 8(a) shows the single chain result using Eq. (17). The latter does an excellent job in describing the attenuation of the PL ratio with temperature for hypothetical disorder-free MEH-PPV chains.

The impact of interchain interactions on the PL spectrum of disorder-free ($\sigma_{dis} = 0$) chains is quite dramatic (triangles in Figs. 8(b) and 8(c)) and discussed at great length in Ref. 22. Once interchain interactions are activated the PL ratio for disorder-free chains drops exactly to zero at T = 0 K, as is required by symmetry for H-aggregates. This arises because the antisymmetric exciton in Fig. 5(b) has no transition dipole moment to the vibrationless ground state. Subsequent increases in temperature lead to thermal activation of the higher-energy symmetric state and an associated increase in $I_{PL}^{0-0}/I_{PL}^{0-1}$, whereupon the ratio peaks at the "HJ" transition temperature, T_p, and thereafter drops with temperature like a J-aggregate. The peak (transition) temperature is simply proportional to the interchain splitting, ΔE_{inter}[22]

$$T_P \approx 1.3\Delta E_{inter}/k_b, \tag{18}$$

where ΔE_{inter} is given in Eq. (9). The overall behavior of the PL line strength ratios in *disorder-free* dimers is captured in the analytical expression[22]

$$I_{PL}^{0-0}/I_{PL}^{0-1} \approx \frac{\kappa}{\lambda_0^2}\frac{2e^{-\Delta E_{inter}/k_bT}}{1+e^{-\Delta E_{inter}/k_bT}}\sqrt{\frac{4\pi\hbar\omega_c}{k_bT}}, \quad N > \sqrt{4\pi\hbar\omega_c/k_bT}, \tag{19}$$

valid in the thermodynamic limit defined by the inequality. Equation (19) reduces exactly to the single chain result in Eq. (17) when $\Delta E_{inter} = 0$.[8] The dashed curves in Figs. 8(b) and 8(c) are obtained using Eq. (19). The agreement with the fully numerically calculated curves is excellent.

We now turn to the effect of disorder on the T-dependent PL ratio in coupled chains. Figs. 8(b) and 8(c) show that the ratio increases with σ_{dis} at low temperatures, as is characteristic of H-aggregates, and decreases with σ_{dis} at high temperatures (beyond T_p), as is characteristic of J-aggregates. This is especially evident in Fig. 8(b). The overall effect of disorder is therefore to flatten out the temperature dependence of $I_{PL}^{0-0}/I_{PL}^{0-1}$. Interestingly, Figs. 8(b) and 8(c) show that the changeover from H to J behavior based on the response to disorder does not occur exactly at T_p but at slightly lower temperatures. At such "changeover" temperatures, disorder apparently has no effect on the PL ratio.

In Fig. 9, the calculated temperature-dependent PL ratios are shown for several interchain interactions using the physically relevant value of σ_{dis} (= 90 meV) deduced from the absorption analysis in Sec. V. The increased disorder over the values used in Fig. 8 induces practically T-independent behavior for all values of J_{inter}. Also shown are the measured values of the PL ratio, obtained by dividing the 0-0 intensity by the sum of the mode 2 and mode 3 sideband intensities. Agreement between theory and experiment is quite good when J_{inter} is 30 meV.

A. Radiative decay rate

As shown in Ref. 22, the temperature dependence of the radiative decay rates in disorder-free dimers roughly tracks the T-dependence of $I_{PL}^{0-0}/I_{PL}^{0-1}$. Fig. 10 shows that this also remains true in the presence of substantial disorder. The figure shows the calculated radiative decay rates for a disordered distribution of MEH-PPV dimers as a function of temperature using

$$k_{rad}/k_{mon} = \sum_{v_t=0,1,2,..} I_{PL}^{0-v_t}(1 - v_t\,\omega_0/\omega_{em})^3,$$

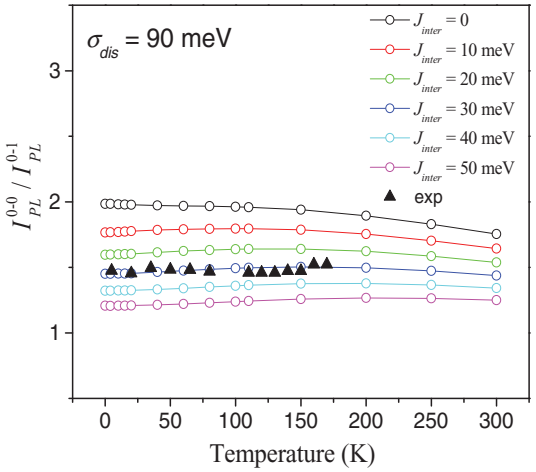

FIG. 9. Numerically calculated 0-0/0-1 PL ratio as a function of temperature for disordered MEH-PPV dimers with $\sigma_{dis} = 90$ meV and for several values of the interchain coupling, J_{inter}. Also shown are the measured values (triangles). The electronic parameters chosen for MEH-PPV are the same as those reported in Fig. 5.

where k_{mon} is the decay rate for a hypothetical repeat unit, $k_{mon} \equiv n^3 \omega_{em}^3 \mu_0^2 / 3\pi\varepsilon_0 \hbar c^3$, having the same emission frequency as the dimer complex. k_{rad} is practically independent of temperature, consistent with the measured temperature-independent PL lifetimes shown in Fig. 3(b). Of course, this assumes that the nonradiative decay rates also do not depend on temperature, but this is expected since for singlet states in solution, the non-radiative decay is largely dominated by the temperature-independent internal conversion process. Fig. 10 also shows that k_{rad} decreases with increasing interchain interactions, due to a more effective destructive interference between emission from the two chains, as is characteristic of H-aggregates.

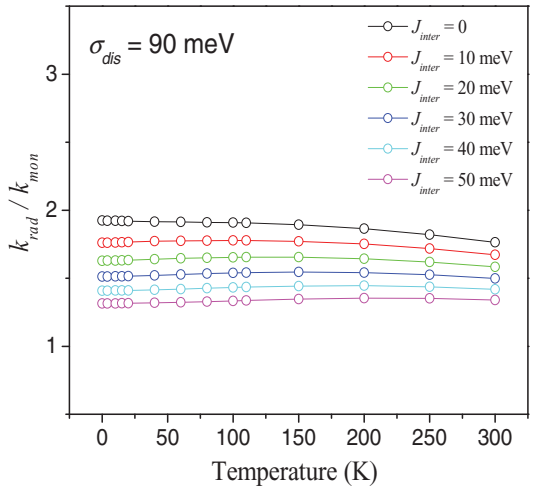

FIG. 10. Numerically calculated relative radiative decay rates as a function of temperature for disordered MEH-PPV dimers with $\sigma_{dis} = 90$ meV for several values of the interchain coupling, J_{inter}. The electronic parameters chosen for MEH-PPV are the same as those reported in Fig. 5.

VII. EXCITON COHERENCE

We conclude our investigation with an evaluation of exciton coherence in MEH-PPV dimers.[52] As shown in Refs. 7 and 53, all information regarding exciton coherence is contained in the ensemble-averaged coherence function,

$$\bar{C}(\boldsymbol{r}) \equiv \langle \langle \Psi^{(em)} | \sum_{\boldsymbol{n}} B_{\boldsymbol{n}}^{\dagger} B_{\boldsymbol{n}+\boldsymbol{r}} | \Psi^{(em)} \rangle \rangle_{C,T}. \tag{20}$$

In Eq. (20), $B_{\boldsymbol{n}}^{\dagger} \equiv |\boldsymbol{n}; vac\rangle \langle g; vac|$ creates a Frenkel-like exciton on the monomer unit located at position $\boldsymbol{n}$. $|\boldsymbol{n}; vac\rangle$ represents the state in which the monomer at $\boldsymbol{n}$ is excited electronically with zero vibrational quanta in all $2N$ S_0 nuclear potentials, and $|g; vac\rangle$ is the dimer electronic/vibrational ground state. $\langle \ldots \rangle_{C,T}$ represents a dual configurational and thermal (Boltzmann) average over the lowest-energy emitting states, $|\Psi^{(em)}\rangle$. From $\bar{C}(\boldsymbol{r})$, one obtains the total number, N_{coh}, of coherently connected chromophores[7,17]

$$N_{coh} = \bar{C}(0)^{-1} \sum_{\boldsymbol{r}} |\bar{C}(\boldsymbol{r})|. \tag{21}$$

The coherence number diminishes with increasing disorder and/or temperature as the exciton localizes.[7,17] In a π-stack, one can further identify the coherence *lengths* along the polymer backbone ($L_{||}$) and along the stacking axis ($L_{\perp}$).[51] For the dimer, we are mainly interested in $L_{||}$, which is given by

$$L_{||}/d \equiv \left\{ \bar{C}(0)^{-1} \sum_{\boldsymbol{r} \in chain} |\bar{C}(\boldsymbol{r})| \right\} - 1, \tag{22}$$

where d is the length of a phenylene-vinylene repeat unit and the sum is restricted to values of $\boldsymbol{r}$ connecting two repeat units within the *same* chain (including $\boldsymbol{r} = 0$).

In Fig. 11, the exciton coherence length *along* the chain is plotted as a function of temperature for disordered MEH-PPV dimers composed of 80-mer chains using the disorder width deduced from the absorption analysis in Sec. V. The value of $L_{||} \approx 7d$ at T = 0 K deduced from Fig. 11 is substantially smaller than the total chain length, $(N-1)d$, due to the disorder-induced localization. The corresponding coherence number of ≈8 at T = 0 K agrees surprisingly well with the conjugation length of approximately 8 repeat units obtained by De Leener *et al.*[54] using quantum chemical techniques. Increasing temperature leads to a reduction in $L_{||}$ as the exciton undergoes additional thermally induced localization, similar to what happens in Frenkel chains.[17] The figure also shows a very interesting effect due to interchain coupling: increasing J_{inter} leads to an increase in $L_{||}$. We believe this arises from the ability of excitons to "side-step" deep traps along the chain, by hopping to the neighboring chain.

Comparison between Figs. 11 and 9 reveals that despite the existence of a nearly temperature-independent PL ratio for disordered, interacting chains, the coherence length is temperature dependent. However, a direct proportionality between $I_{PL}^{0-0}/I_{PL}^{0-1}$ and the coherence length *is strictly valid only for J-aggregates,* or, in the current application, for single MEH-PPV chains. Indeed, when $J_{inter} = 0$, Figs. 9 and 11 show that both $I_{PL}^{0-0}/I_{PL}^{0-1}$ and $L_{||}$ decrease by roughly the same relative amounts with temperature, reflecting single-chain J-like properties. Only when J_{inter} is activated do the temperature

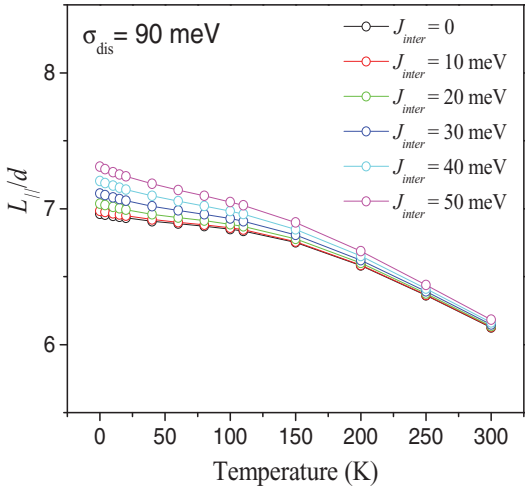

FIG. 11. Exciton coherence length along the polymer chain evaluated disordered MEH-PPV dimers with $\sigma_{dis} = 90$ meV using Eqs. (20) and (22). Electronic and vibrational parameters are the same as in Fig. 5.

dependences between $I_{PL}^{0-0}/I_{PL}^{0-1}$ and $L_{||}$ begin to differ due to the destructive interference between emission from the two chains.

The coherence length $L_{||}$ of the MEH-PPV 1^1B_u exciton measured along the chain (see Eq. (22)) is conceptually different from the commonly referred to conjugation length. The latter is based on the planarity of the individual chains, so that one could say that in a perfectly planar chain (with no other sources of disorder) the conjugation length is equal to the chain length. This is not so for $L_{||}$ because it depends on disorder *and* temperature. Generally, $L_{||}$ shrinks with increasing temperature and can therefore be substantially smaller than the chain length, even on a totally planar chain, or more generally, even when there is no disorder.[55,56] This is easiest to appreciate in a density matrix formalism where a thermal distribution of emitting excitons is represented by a diagonal density matrix expressed in the "k-space" eigenbasis (assuming no disorder). Canonical transformation to the site basis gives rise to spatial coherences which extend over a narrower distribution of sites as temperature is increased.

Normally, the conjugation length is associated with the red-shift of the emission origin, rationalized using a particle-in-a-box type approach.[27] Our estimate of the conjugation length of about eight repeat units (coherence length at T = 0 K) from Fig. 11 is somewhat smaller than the estimates of about 15 or so repeat units based on spectral shifts made in Ref. 22 using the Kuhn model. The discrepancy is likely due to our assumption of spatially uncorrelated disorder. Adding spatial correlation along the polymer chain enhances resonance between neighboring monomers thereby extending coherence.

VIII. DISCUSSION/CONCLUSION

The aggregate red-phase of MEH-PPV is characterized by weakly coupled HJ-aggregates in which the interchain splitting, ΔE_{inter}, is roughly an order of magnitude smaller than the (0-0) intrachain 1^1B_u exciton bandwidth, ΔE_{intra}. For the parameters which best reproduce the measured absorption and PL spectral line shapes, we obtain $\Delta E_{intra} \approx 0.2$ eV and $\Delta E_{inter} \approx 0.012$ eV. Generally, the photophysical response results from a competition between intrachain interactions which promote J-like behavior, and interchain interactions which promote H-like behavior.

In red-phase MEH-PPV, the measured ratio, $I_{PL}^{0-0}/I_{PL}^{0-1}$, as well as the PL lifetime is practically independent of temperature in the range from 5 K–160 K. This is in stark contrast to the strong temperature dependence predicted by the HJ-aggregate model when disorder is absent (see Figs. 8(b) and 8(c)).[22] In the absence of disorder ($\sigma_{dis} = 0$), the PL ratio is exactly zero at T = 0 K due to destructive interference between the emission occurring from each chain, as expected for H-aggregates. The ratio increases with temperature as the higher-energy symmetric exciton is populated (see Fig. 5(b)), peaks when kT is approximately equal to the interchain splitting, ΔE_{inter}, and subsequently decreases with further temperature increases, as expected for J-aggregates. The radiative decay rate follows a similar pattern.[22] Adding static disorder has a profound effect on the temperature dependence.[57] In our model, the disorder is due to a Gaussian distribution of spatially uncorrelated electron and hole site energies, where a "site" is defined as a single phenylene-vinylene repeat unit within a given polymer chain. Disorder *increases* the PL ratio at low temperatures, as the symmetry required for perfect destructive interference inherent to H-aggregates is destroyed, and *decreases* the PL ratio at high temperatures, as is characteristic of J-aggregates. The overall impact of disorder is to level off the temperature dependence of both the PL ratio and radiative decay rates. When Gaussian disorder width, σ_{dis}, is chosen such that the motionally narrowed line width matches the measured absorption spectral line width ($\sigma_{dis} = 90$ meV), the PL ratio and radiative decay rates become essentially temperature independent. Agreement with experiment is excellent for $J_{inter} = 30$ meV.

Our calculations show that a *single*, disordered MEH-PPV chain depicted by the $J_{inter} = 0$ curves in Figs. 9–11, behaves like a J-aggregate with respect to the following vibronic signatures.[18] (1) The PL ratio $I_{PL}^{0-0}/I_{PL}^{0-1}$ increases with the exciton coherence length, approximately consistent with Eq. (16) with N replaced by N_{coh}. The PL ratio for a polymer is about four times larger than the value of $1/\lambda_0^2$ ($= \frac{1}{2}$) for a single repeat unit because exciton coherence is spread over approximately eight repeat units. (2) $I_{PL}^{0-0}/I_{PL}^{0-1}$ decreases with increasing temperature and (3) increasing disorder as the exciton localizes. (4) The ratio of oscillator strengths in the absorption spectrum, I_A^{0-0}/I_A^{0-1}, is larger than the value (=1/2) for a single repeat unit. Our spectroscopic measurements for the red-phase of MEH-PPV are consistent with properties 1 and 4 if we compare the measured PL and Ab ratios (both greater than one) to the significantly smaller values found in small oligomers such as stilbene.[31] Property (3) is difficult to test experimentally since disorder is not easily controlled. As for Property (2), the calculated (slight) decrease in the PL ratio in Fig. 9 with temperature ($J_{inter} = 0$ curve) is difficult to distinguish from the measured temperature-independent PL ratio from Fig. 2. However, the *magnitude* of the calculated line strength ratio, $I_{PL}^{0-0}/I_{PL}^{0-1}$, for a single chain (≈2) does

not agree with our measured value of approximately 1.5 (see Fig. 9). One needs interchain interactions with $J_{inter} \approx 30$ meV in order to reduce $I_{PL}^{0-0}/I_{PL}^{0-1}$ to the measured value. Hence, the red-phase of MEH-PPV is best described as a disordered HJ-aggregate. This is consistent with measurements of the "red" single-chromophore emitters found in single molecule spectroscopy of MEH-PPV by Yu and Barbara,[31] where the spectrum strongly resembles the red-phase PL spectrum presented here, but with a slightly larger value of $I_{PL}^{0-0}/I_{PL}^{0-1}$. HJ-aggregates of red-phase of MEH-PPV therefore spectrally resemble single, elongated chains, but for the reduced 0-0/0-1 PL ratio.

We should point out that our estimation of the interchain coupling, J_{inter}, is likely a lower limit. This follows because we have omitted spatial correlation between electron (and hole) site energies in the disorder distribution in Eq. (6). Inclusion of spatial correlation along the chain enhances the exciton coherence length and the single-chain 0-0/0-1 PL ratio. As the latter increases, a larger value of J_{inter} is needed to bring the PL ratio back down to the measured value. (Interestingly, spatial correlation has minimal effect on the absorption ratio, as this ratio is mostly sensitive to the exciton bandwidth and not the coherence length.)

One way to better appreciate how the competition between interchain and intrachain interactions impacts the PL ratio is in the limit of relatively weak disorder, $\sigma_{dis} \lesssim 22$ meV, where the *maximum* PL ratio in Fig. 8 (occurring at $T = T_p$) does not significantly differ from the disorder-free value. Hence, we can use the simple analytical formula in Eq. (19), which was derived strictly for ordered chains in Ref. 22, to obtain the maximum PL ratio in the limit of weak disorder. This is determined by evaluating Eq. (19) at the peak (HJ-transition) temperature, $T = T_p$. Substitution of Eq. (18) into Eq. (19) gives

$$\left(I_{PL}^{0-0}/I_{PL}^{0-1}\right)_{\max} \approx 2\frac{\kappa}{\lambda_0^2}\sqrt{\frac{\hbar\omega_c}{\Delta E_{inter}}}. \tag{23}$$

Equation (23) shows how the competition between intra- and interchain interactions manifests in the size of the PL ratio. The maximum PL ratio increases with the curvature ω_c of the exciton band (ω_c is strongly correlated to the intrachain bandwidth ΔE_{intra}) and decreases with the interchain splitting (ΔE_{inter}). The fascinating property of Eq. (23) is that it places no limit on how large the PL ratio may get, given that the thermodynamic limit is maintained. Moreover, since the sideband intensities are practically independent of temperature,[22] it is the 0-0 intensity that is mostly responsible for changes in the PL ratio. Hence, polymer dimers can even be superradiant (when compared with the monomer unit decay rate, k_{mon}) in cases where the intrachain curvature (or bandwidth) significantly exceeds the interchain bandwidth. Equation (23) shows how fundamentally different a polymer dimer is compared with a dimer composed of small oligomers. The latter is an example of a classic H-aggregate of Kasha and co-workers,[9–12] which is strictly nonfluorescent if vibronic coupling is absent ($k_{rad} = 0$) or weakly fluorescent (assuming $k_{rad} \ll k_{nonrad}$) with a substantially attenuated 0-0 peak, when vibronic coupling is included.[18] The possibility that polymer dimers can have a dominant 0-0 PL band and can even superradiate is completely at odds with what is expected of conventional H-aggregates.

Equation (23) shows that the emergence of J-like behavior is due to a dominance of the intrachain vs interchain exciton bandwidths. The J-like rise in $I_{PL}^{0-0}/I_{PL}^{0-1}$ has been observed in other polymers such as P3HT when going from spin cast films to solution grown nanofibers.[23] The likely explanation involves changes in morphology: increased torsional disorder in spin cast films reduces the intrachain exciton bandwidth while enhancing the interchain bandwidth. The latter effect is a result of shorter conjugation lengths which leads to larger interchain interactions.[58–61] We believe that J-dominant effects are operative also in polyfluorene polymers, where the β-phase is also characterized by a substantial increase in $I_{PL}^{0-0}/I_{PL}^{0-1}$. This is evident when comparing the room temperature absorption and emission spectra of the polyfluorene β-phase[62] with the 10 K spectra,[63] as well as when comparing, at 10 K, the Huang-Rhys factors of the disordered phase polyfluorene with β-phase polyfluorenes.[63] The resulting $I_{PL}^{0-0}/I_{PL}^{0-1}$ ratios range from 0.53 to 0.73 for the disordered phase, depending on film preparation conditions, while values of 1.72 are typical for the β-phase in polyfluorene.

Finally, we point out that the substantial increase in $I_{PL}^{0-0}/I_{PL}^{0-1}$ when the blue-phase is converted to red-phase MEH-PPV is due to an enhanced coherence length along the chain ($L_{\|} > 7$ repeat units) associated with chain elongation. When the unit cell transition dipole moments are aligned *within the coherence length*, the 0-0 transition strength is constructively enhanced by N_{coh}, as occurs in linear J-aggregates. This follows from the uniquely coherent nature of the 0-0 PL transition as opposed to the largely incoherent sidebands.[8,17,18] In the coiled blue-phase, the transition dipole moments are more randomly oriented within smaller coherence lengths, thereby degrading the 0-0 transition intensity (as well as $I_{PL}^{0-0}/I_{PL}^{0-1}$). Hence, in a coiled conformation one has to contend with (at least) two sources of disorder: the usual site-energy disorder as well as transition dipole alignment disorder. We are currently considering PL in the blue-phase morphology in greater detail as well as the applicability of our model to other emissive conjugated polymers.

ACKNOWLEDGMENTS

A.K. and C.S. gratefully acknowledge support from the research training group GRK1640 "photophysics of synthetic and biological multichromophoric systems" of the Deutsche Forschungsgemeinschaft (DFG). F.C.S. is supported by the National Science Foundation (NSF), Grant No. DMR-1203811.

[1] A. J. Heeger, Chem. Soc. Rev. **39**(7), 2354–2371 (2010).
[2] S. Gunes, H. Neugebauer, and N. S. Sariciftci, Chem. Rev. **107**(4), 1324–1338 (2007).
[3] R. H. Friend, R. W. Gymer, A. B. Holmes, J. H. Burroughes, R. N. Marks, C. Taliani, D. D. C. Bradley, D. A. D. Santos, J. L. Bredas, M. Logdlund, and W. R. Salaneck, Nature (London) **397**, 121–128 (1999).
[4] F. C. Spano, J. Chem. Phys. **122**, 234701 (2005).
[5] J. Clark, C. Silva, R. H. Friend, and F. C. Spano, Phys. Rev. Lett. **98**(20), 206406 (2007).

[6]J. Clark, J. F. Chang, F. C. Spano, R. H. Friend, and C. Silva, Appl. Phys. Lett. **94**(16), 163306 (2009).
[7]F. C. Spano, J. Clark, C. Silva, and R. H. Friend, J. Chem. Phys. **130**(7), 074904 (2009).
[8]H. Yamagata and F. C. Spano, J. Chem. Phys. **135**, 054906 (2011).
[9]M. Kasha, H. R. Rawls, and M. A. El-Bayoumi, *Molecular Spectroscopy* (Butterworths, London, 1965), pp. 371–392.
[10]R. M. Hochstrasser and M. Kasha, Photochem. Photobiol. **3**, 317–331 (1964).
[11]M. Kasha, Radiat. Res. **20**(1), 55–70 (1963).
[12]E. G. McRae and M. Kasha, J. Chem. Phys. **28**, 721–722 (1958).
[13]B. Khachatryan, T. D. Nguyen, Z. V. Vardeny, and E. Ehrenfreund, Phys. Rev. B **86**(19), 195203 (2012).
[14]F. Dubin, R. Melet, T. Barisien, R. Grousson, L. Legrand, M. Schott, and V. Voliotist, Nat. Phys. **2**(1), 32–35 (2006).
[15]M. Schott, in *Photophysics of Molecular Materials: From Single Molecules to Single Crystals*, edited by G. Lanzani (Wiley-VCH, Weinheim, 2006), pp. 49–145.
[16]R. Lecuiller, J. Berrehar, J. D. Ganiere, C. Lapersonne-Meyer, P. Lavallard, and M. Schott, Phys. Rev. B **66**(12), 125205 (2002).
[17]F. C. Spano and H. Yamagata, J. Phys. Chem. B **115**(18), 5133–5143 (2011).
[18]F. C. Spano, Acc. Chem. Res. **43**(3), 429–439 (2010).
[19]J. Cornil, D. Beljonne, C. M. Heller, I. H. Campbell, B. K. Laurich, D. L. Smith, D. D. C. Bradley, K. Mullen, and J. L. Bredas, Chem. Phys. Lett. **278**, 139–145 (1997).
[20]Z. Shuai, J. L. Bredas, and W. P. Su, Chem. Phys. Lett. **228**(4–5), 301–306 (1994).
[21]R. Chang, J. H. Hsu, W. S. Fann, K. K. Liang, C. H. Chiang, M. Hayashi, J. Yu, S. H. Lin, E. C. Chang, K. R. Chuang, and S. A. Chen, Chem. Phys. Lett. **317**(1–2), 142–152 (2000).
[22]H. Yamagata and F. C. Spano, J. Chem. Phys. **136**(18), 184901 (2012); **137**, 249901 (2012).
[23]E. T. Niles, J. D. Roehling, H. Yamagata, A. J. Wise, F. C. Spano, A. J. Moule, and J. K. Grey, J. Phys. Chem. Lett. **3**(2), 259–263 (2012).
[24]T. W. Hagler, K. Pakbaz, and A. J. Heeger, Phys. Rev. B **51**(20), 14199 (1995).
[25]B. J. Schwartz, Annu. Rev. Phys. Chem. **54**, 141–172 (2003).
[26]C. J. Collison, L. J. Rothberg, V. Treemaneekarn, and Y. Li, Macromolecules **34**, 2346–2352 (2001).
[27]A. Kohler, S. T. Hoffmann, and H. Bassler, J. Am. Chem. Soc. **134**(28), 11594–11601 (2012).
[28]H. Z. Lin, R. P. Hania, R. Bloem, O. Mirzov, D. Thomsson, and I. G. Scheblykin, Phys. Chem. Chem. Phys. **12**(37), 11770–11777 (2010).
[29]O. Mirzov and I. G. Scheblykin, Phys. Chem. Chem. Phys. **8**, 5569–5576 (2006).
[30]P. F. Barbara, A. J. Gesquiere, S.-J. Park, and Y. J. Lee, Acc. Chem. Res. **38**(7), 602–610 (2005).
[31]Z. H. Yu and P. F. Barbara, J. Phys. Chem. B **108**(31), 11321–11326 (2004).
[32]J. K. Grey, D. Y. Kim, B. C. Norris, W. L. Miller, and P. F. Barbara, J. Phys. Chem. B **110**(51), 25568–25572 (2006).
[33]F. A. Feist and T. Basche, J. Phys. Chem. B **112**(32), 9700–9708 (2008).
[34]F. A. Feist, M. F. Zickler, and T. Basche, ChemPhysChem **12**(8), 1499–1508 (2011).
[35]Y. Ebihara, S. Habuchi, and M. Vacha, Chem. Lett. **38**(11), 1094–1095 (2009).
[36]Y. Ebihara and M. Vacha, J. Phys. Chem. B **112**(40), 12575–12578 (2008).
[37]D. H. Hu, J. Yu, K. Wong, B. Bagchi, P. J. Rossky, and P. F. Barbara, Nature (London) **405**(6790), 1030–1033 (2000).
[38]P. K. H. Ho, J.-S. Kim, N. Tessler, and R. H. Friend, J. Chem. Phys. **115**, 2709–2720 (2001).
[39]S. J. Strickler and R. A. Berg, J. Chem. Phys. **37**(4), 814 (1962).
[40]L. A. Peteanu, G. A. Sherwood, J. H. Werner, A. P. Shreve, T. M. Smith, and J. Wildeman, J. Phys. Chem. C **115**(31), 15607–15616 (2011).
[41]M. W. Wu and E. M. Conwell, Phys. Rev. B **56**(16), R10060–R10062 (1997).
[42]H. Bassler, Phys. Status Solidi B **107**, 9 (1981).
[43]A. Stradomska, W. Kulig, M. Slawik, and P. Petelenz, J. Chem. Phys. **134**(22), 224505 (2011).
[44]J. W. van der Horst, P. A. Bobbert, M. A. J. Michels, and H. Bassler, J. Chem. Phys. **114**(15), 6950–6957 (2001).
[45]F. C. Spano, Chem. Phys. **325**, 22–35 (2006).
[46]To remain consistent with Secs. II and III we label the absorption vibronic peaks as 0-0, 0-1,0-2,... in order of increasing energy, not to be confused with a similar labeling scheme for the PL progression.
[47]E. W. Knapp, Chem. Phys. **85**, 73–82 (1984).
[48]H. Fidder, J. Knoester, and D. A. Wiersma, J. Chem. Phys. **95**(11), 7880–7890 (1991).
[49]S. T. Hoffmann, H. Bassler, and A. Kohler, J. Phys. Chem. B **114**(51), 17037–17048 (2010).
[50]See supplementary material at http://dx.doi.org/10.1063/1.4819906 for the absorption spectra of small oligomers calculated using the n-particle approximations (n = 1,2,3,4).
[51]F. Paquin, H. Yamagata, N. J. Hestand, M. Sakowicz, N. Bérubé, M. Côté, L. X. Reynolds, S. A. Haque, N. Stingelin, F. C. Spano, and C. Silva, "Two-dimensional spatial coherence of excitons in semicrystalline polymeric semiconductors: The effect of molecular weight," Phys. Rev. B (submitted).
[52]E. Collini and G. D. Scholes, Science **323**(5912), 369–373 (2009).
[53]F. C. Spano, S. C. J. Meskers, E. Hennebicq, and D. Beljonne, J. Am. Chem. Soc. **129**, 7044–7054 (2007).
[54]C. De Leener, E. Hennebicq, J. C. Sancho-Garcia, and D. Beljonne, J. Phys. Chem. B **113**, 1311–1322 (2009).
[55]H. Kuhn, Angew. Chem. **71**, 93 (1959).
[56]F. Bär, W. Huber, G. Handschig, H. Martin, and H. Kuhn, J. Chem. Phys. **32**, 470 (1960).
[57]We are assuming that the disorder is independent of temperature, consistent with the observation that in many emissive conjugated polymer films the absorption line width does not dramatically change with temperature.
[58]J. Gierschner, Y. S. Huang, B. Van Averbeke, J. Cornil, R. H. Friend, and D. Beljonne, J. Chem. Phys. **130**(4), 044105 (2009).
[59]W. Barford, J. Chem. Phys. **126**(13), 134905 (2007).
[60]J. Cornil, D. A. dos Santos, X. Crispin, R. Silbey, and J. L. Bredas, J. Am. Chem. Soc. **120**, 1289 (1998).
[61]E. S. Manas and F. C. Spano, J. Chem. Phys. **109**, 8087 (1998).
[62]J. Peet, E. Brocker, Y. H. Xu, and G. C. Bazan, Adv. Mater. **20**(10), 1882–1885 (2008).
[63]A. L. T. Khan, P. Sreearunothai, L. M. Herz, M. J. Banach, and A. Kohler, Phys. Rev. B **69**(8), 085201 (2004).

8 Revealing Structure Formation in PCPDTBT by Optical Spectroscopy

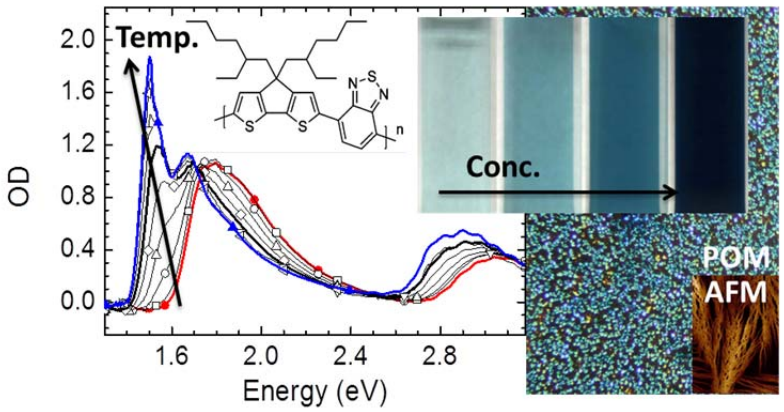

Christina Scharsich, Florian S. U. Fischer, Kevin Wilma,

Richard Hildner, Sabine Ludwigs, Anna Köhler

Prepared for submission

Revealing structure formation in PCPDTBT by optical spectroscopy

Prepared for submission

Christina Scharsich[1,2], Florian S. U. Fischer[3], Kevin Wilma[1,4], Richard Hildner[1,4], Sabine Ludwigs[3]*, Anna Köhler[1,2]*

[1] Bayreuth Institute of Macromolecular Research (BIMF), University of Bayreuth, Bayreuth 95440, Germany.

[2] Experimental Physics II, University of Bayreuth, Bayreuth 95440, Germany.

[3] IPOC-Functional Polymers, University of Stuttgart, Stuttgart 70569, Germany

[4] Experimental Physics IV, University of Bayreuth, Bayreuth 95440, Germany

*Corresponding authors:

e-mail: *sabine.ludwigs@ipoc.uni-stuttgart.de*
anna.koehler@uni-bayreuth.de

Abstract

The low band-gap polymer PCPDTBT (poly{[4,4-bis(2-ethylhexyl)-cyclopenta-(2,1-b;3,4-b')dithiophen]-2,6-diyl-alt-(2,1,3-benzo-thiadiazole)-4,7-diyl}) is widely used for organic solar cell applications. Here, we present a comprehensive study of the optical properties as a function of temperature for PCPDTBT in solution and in thin films with two distinct morphologies. Using absorption and photoluminescence spectroscopy as well as Franck-Condon analyses, we show that PCPDTBT in solution undergoes a phase transition (critical temperature: 300 K) from a disordered to a truely aggregated state upon cooling. The saturation value of aggregates in solution is reached in PCPDTBT thin films at any temperature. In addition, we demonstrate that the photophysical properties of the aggregates in films are similar to those in solution and that a low percentage of thermally activated excimer-like states is present in the films at temperatures above 200 K.

1 Introduction

The tendency of a conjugated polymer material to aggregate is a key factor in controlling both the charge carrier mobility as well as the ability of excited states to dissociate when combined with an electron accepting material.[1-3] In this way, the aggregation process controls the performance of a polymer in solar cell applications as well as in field-effect transistors.[3-5] The interdependence of device performance and thin film morphology has been extensively studied in particular for the polymer poly(3-hexylthiophene) (P3HT).[2,4,6-8] The conformation of P3HT chains in thin films of neat materials or when blended with an electron acceptor such as PCBM can be controlled by a range of methods such as thermal annealing, solvent annealing and spin-coating from solvents containing high boiling point additives. The reason why P3HT is so amenable to these processing techniques lies in the semicrystalline nature of P3HT. While it adopts a randomly coiled chain conformation in a good solvent, planarization and concomitant crystallization occurs when the solvent quality is deteriorated.[9,10] Similar effects have been reported for other homopolymers such as the poly(*p*-phenylene-vinylene) derivative MEH-PPV and for poly(fluorene).[11-14]

While solar cells with high efficiencies have been obtained by optimizing the morphology of P3HT/PCBM blends, the lower energy part of the sun's irradiation spectrum is not used by this polymer/acceptor combination. An alternative that is more matched to the incident photon flux consists in the use of low-bandgap polymers.[15-17] Low optical gaps can be obtained by combining electron-rich and electron-deficient moieties to donor-acceptor co-polymers.[18] Examples for such co-polymers that have been employed for solar cell applications are cyclopentadithiophene based polymers such as PCPDTBT, carbazole-based polymers such as PCDTBT, diketopyrrole-based polymers such as PDPP-TPT, thienothiophene-benzodithiophene-based polymers such as PTB7 and many more (see Supporting Information for full chemical names).[19] Like for P3HT, the performance of bulk heterojunction solar cells made with these polymers depends critically on the processing conditions and the resulting thin film morphology. Consequently, great effort is made to understand and control the bulk heterojunction morphologies, e.g. by thermal annealing, solvent annealing and spin-coating from solvents containing additives.[2,20-25] While the blends used for solar cell applications are studied intensively, less attention is paid to the aggregation properties of the individual blend components. Knowledge of what controls the conformation and assembly of an individual low-bandgap polymer, however, is a prerequisite to understand its behavior in composites.

Here, we have therefore studied the formation of aggregates in solution and neat films of the widely used low-bandgap polymer PCPDTBT. PCPDTBT reaches power conversion efficiencies up to 5.5% in bulk heterojunction cells with PCBM,[24,26] yet the properties of structure formation in PCPDTBT themselves are not well understood,

and few studies address the properties of the pure polymer.[27-30] Initial structural studies indicated PCPDTBT to form apparently amorphous films that cannot be made to crystallize upon thermal annealing.[31] It has been considered as "marginally crystallizable", quite in contrast to derivatives with the same backbone yet different side chains that readily form ordered structures.[32-34] Subsequent work, however, demonstrated that PCPDTBT forms randomly oriented aggregates of about 40 nm size that are arranged in a lamellar stacking, similar to P3HT, when films are spin-coated from chlorobenzene solution.[27] When spin-coating from solvents containing additives such as diiodooctane or octanedithiol, the amount of aggregates in the film increases as evidenced by changes in the absorption spectra, yet the structure of the aggregates remains. These laminar stacks may even form fibrils.[31] A different crystal structure containing polymer dimers in a herringbone arrangement was recently reported for PCPDTBT films prepared by solvent vapor annealing.[35]

Here, we present a detailed study on the process of aggregation in PCPDTBT using steady-state absorption and photoluminescence spectroscopy as well as time-correlated single photon counting. First, we investigate PCPDTBT in solution where high degree of conformational freedom allows for facile structure formation. Next, we compare the optical properties of the polymer in solution to the properties in thin films of two different morphologies where structure formation is more constraint. One type of films was spun using the high-boiling point additive diiodooctane (DIO), the second type was solvent annealed with chlorobenzene after spin-coating according to Fischer et al.[35]

The temperature-dependent measurements of PCPDTBT in solution reveal a phase transition to occur from the disordered, coiled state to an ordered, aggregated state with extended, planarized chains. The according critical temperature of the phase transition is at about 300 K. Thus, PCPDTBT in solution tends to form pre-aggregates that affect the aggregation process of solution-processed thin films and devices.

In the photoluminescence of PCPDTBT thin films, a similar planarized structure as in solution is found at low temperatures. At room temperature and at temperatures with efficiently extended diffusion lengths, however, relaxation to trap sites takes place. We show that spectral diffusion within the aggregates evolves as expected for individual chromophores and that the populated trap sites can be understood to be excimer states as typically formed at grain boundaries and interfaces in the solid state.[36] In addition, we show that there is a nearly temperature independent fraction of about 40% of aggregates within the films in accordance with the saturation value of aggregates in solution.

2 Results

PCPDTBT in solution

Earlier work has shown that PCPDTBT can adopt different morphologies.[27,35] In order to investigate the self-assembly process in PCPDTBT, we first concentrate on solutions of the polymer. In a solution, the chain experiences less external constraints than during the process of film preparation, where interfaces (substrate-solution, solution-air), sheer forces (during spin-coating or swelling) and kinetic aspects impact on the self-aggregation process. By cooling the cuvette, the quality of the solvent can be modified gradually from a good solvent to a poor solvent without changing the chemical structure. Optical spectroscopy in solution is thus a convenient tool to study the self-assembly process in a controlled fashion.[9,11,37] First, we investigated PCPDTBT in a MTHF solution with concentration c = 0.25 mg/ml. For both, absorption and emission, we observe a clear change of the spectra with temperature (Figure 1a). At elevated temperatures (340 K), the absorption spectrum features a broad and unstructured band peaking at about 1.8 eV. At higher energies, the second absorption band has a center peak at about 3.05 eV. Upon cooling, the first absorption band shifts continuously to red. At 300 K, an additional low energy shoulder appears at about 1.55 eV. This shoulder grows in intensity with decreasing temperature, forming a sharp maximum at 1.50 eV at 180 K. The spectral range from 1.60 to 2.00 eV is examined in more detail in Figure 1b. It can clearly be seen how the absorption shifts to lower energies from 340 K to 280 K. From 280K onwards, the spectra form an isosbestic point at 1.705 eV. The integrated intensity of the first absorption band increases linearly by 23 per cent upon cooling the solution from 340 K to 180 K. The absorption of the second absorption band (2.5 - 3.2 eV) shifts similarly to the red and increases with decreasing temperature.

These changes in the absorption spectrum – a bathochromic shift, an isosbestic point and an increase in intensity - are similar to those observed for the polymers P3HT and MEH-PPV.[9,11,37] Accordingly, we attribute the initial redshift upon cooling to a swelling-up of the polymer chain that leads to increased conjugation length and thus lower energy absorption. The isosbestic point is clear evidence for the transition between two phases. The lower energy of this band, its dominant 0-0 peak and the associated clear vibrational structure indicate a planarized conformation of the lower-energy phase with concomitant longer conjugation length.

In the photoluminescence spectra of the PCPDTBT solution (Figure 1c), we observe a similar evolution. At high temperatures, the emission maximum is centered at 1.6 eV, with decreasing temperature the intensity of this emission decreases and a second emission emerges at 1.42 eV dominating the photoluminescence spectrum below 260 K. The second emission at lower energies shows higher 0-0 peaks and is

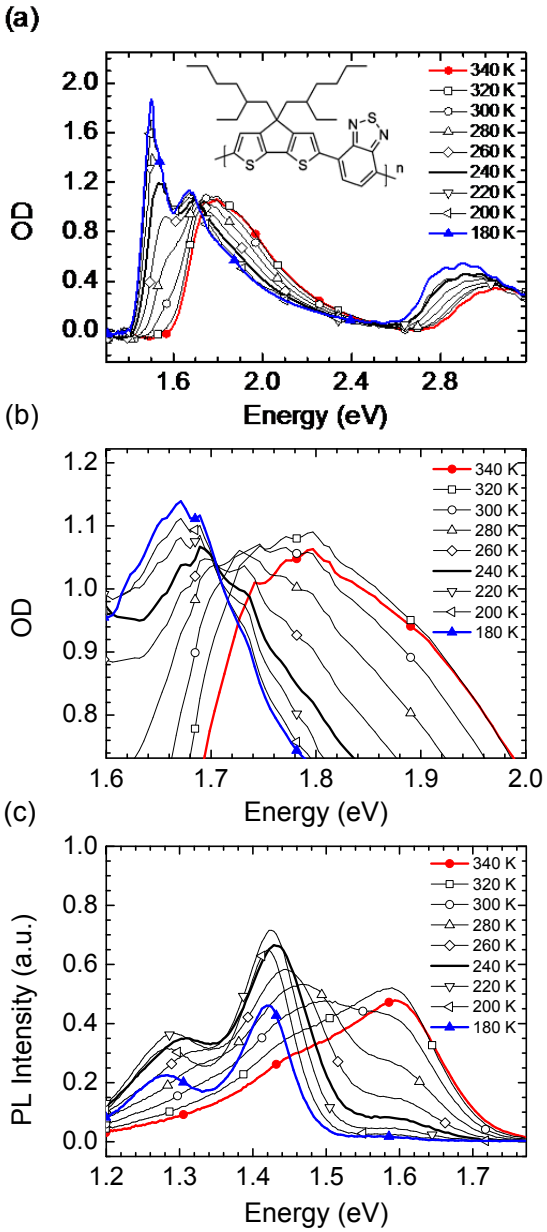

Figure 1: PCPDTBT in solution (c = 0.25 mg/ml in MTHF) for different temperatures between 340 K and 180 K: (a) optical density as measured, (b) optical density illustrating the isosbestic point, (c) intensity of the photoluminescence as measured.

more structured than the high energy emission. We assign the high energy emission to the PCPDTBT coiled phase in which more geometric disorder is present after excitation than in the planarized phase. In contrast, the more structured low energy emission indicates more ordered and planarized chains.

In order to explore whether these spectral changes are associated merely with planarized conformations of individual chains or whether they actually indicate the formation of aggregated planar chains, we measured the absorption and photoluminescence at room temperature as a function of concentration (Figure 2). Upon raising the concentration by factors of $\sqrt{10}$ from 0.025 mg/ml to 0.79 mg/ml, we

observe the increase of a shoulder at 1.6 eV in the absorption spectrum, indicating that increased concentration assists the formation of the low-energy band. The same trend is observed in room temperature photoluminescence. For the lowest concentration, 0.025 mg/ml, we still observe two features, one shoulder centered at 1.6 eV and a peak centered at about 1.45 eV. With increasing concentration, the high

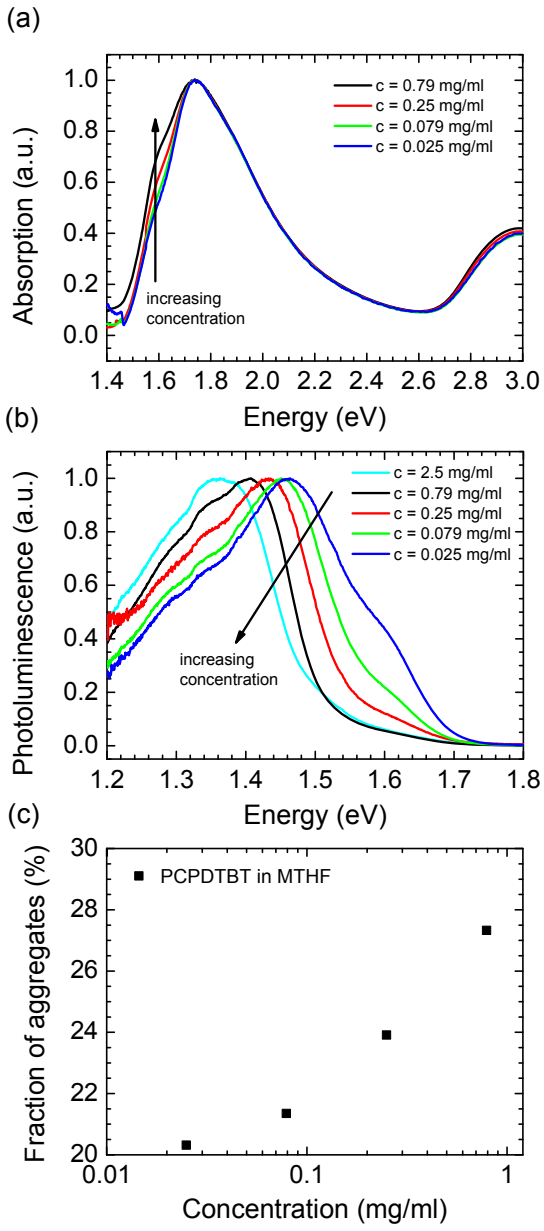

Figure 2: (a) Absorption of PCPDTBT in MTHF with concentrations of 0.025 mg/ml, 0.079 mg/ml, 0.25 mg/ml, and 0.79 mg/ml, respectively. Arrows indicate increasing concentration. Inset: solutions of above mentioned concentration in 1mm- quartz cuvettes. (b) Photoluminescence of PCPDTBT in MTHF with different concentrations. (c) Fraction of aggregates in solution as a function of concentration (PCPDTBT in MTHF) as determined from absorption spectra by means of Franck-Condon analysis.

energy shoulder disappears and the low energy peak shifts to even lower energies. This evolution is similar to that observed when lowering the temperature at a fixed concentration. This concentration dependence clarifies that the low-energy transition is associated not only with *planarized* chains but rather with *aggregated* chains. Figure 2c demonstrates how the fraction of aggregates formed increases with concentration. This fraction has been determined from the absorption spectra as described in detail further below in the context of Figure 6.

It is possible to separate the measured spectra into the spectra arising from the aggregated phase and the coiled phase by employing a thorough Franck-Condon analysis according to Eqs. 3 and 4 (see Exp. methods) for absorption and photo-luminescence, respectively. The multi-mode Franck-Condon analysis was based on five modes with the following energies: 62 meV, 106 meV, 136 meV, 167 meV, 190 meV. The 62 meV mode is assigned to torsional relaxation, the other modes are effective vibrational modes taken from Raman measurements (see Supporting Information). The refractive index of the surrounding medium was assumed to be constant over the considered spectral range. Figure 3 shows the normalized photoluminescence and absorption of PCPDTBT

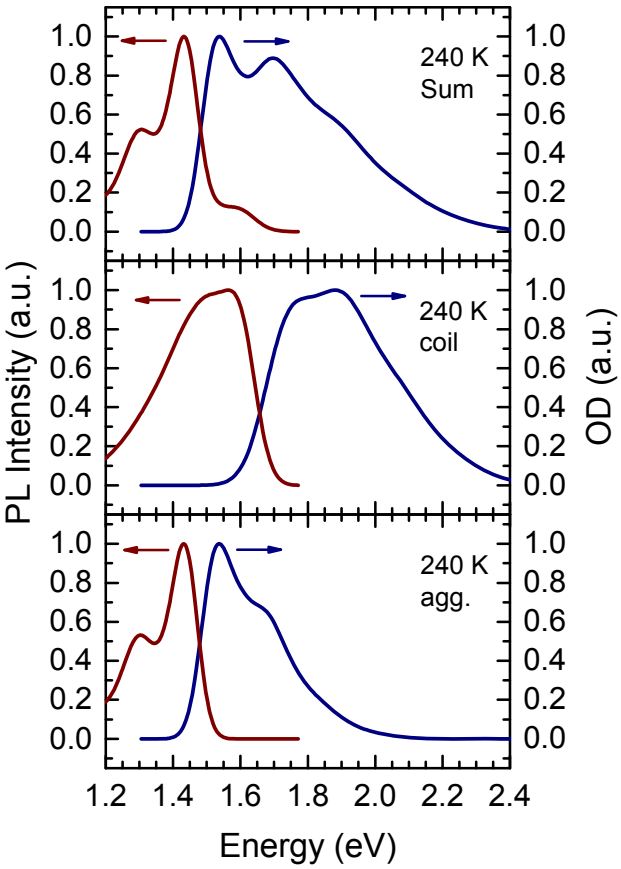

Figure 3: Normalized photoluminescence and optical density of PCPDTBT in solution at 240 K: (top) spectra as measured, (middle) spectra of coiled phase, (bottom) spectra of aggregated phase.

in solution measured at 240 K as well as the normalized underlying spectra of coiled and aggregated phase that were obtained from the Franck-Condon analysis. The Franck-Condon fits and their comparison against the measured spectra are detailed in the Supporting Information. This decomposition of the spectra into the two phases shows that photoluminescence and absorption of the coiled phase intersect at 1.66 eV whereas for the aggregated phase this intersection point is at 1.48 eV. Thus, the spectra associated with two distinct phases are 180 meV apart.

In this manner, we decomposed the absorption spectra in the temperature range from 320 K to 180 K. The obtained absorption spectra for the aggregated PCPDTBT phase are shown in Figure 4a. The associated photoluminescence spectra (Figure 4b) were found by subtracting the coiled phase photoluminescence (as measured at 340 K yet normalized to match the high energy shoulder) from the photoluminescence spectrum measured at an arbitrary temperature. We see that in absorption, the aggregate spectrum shifts continuously by about 150 meV to lower energies (up to 1.495 eV)

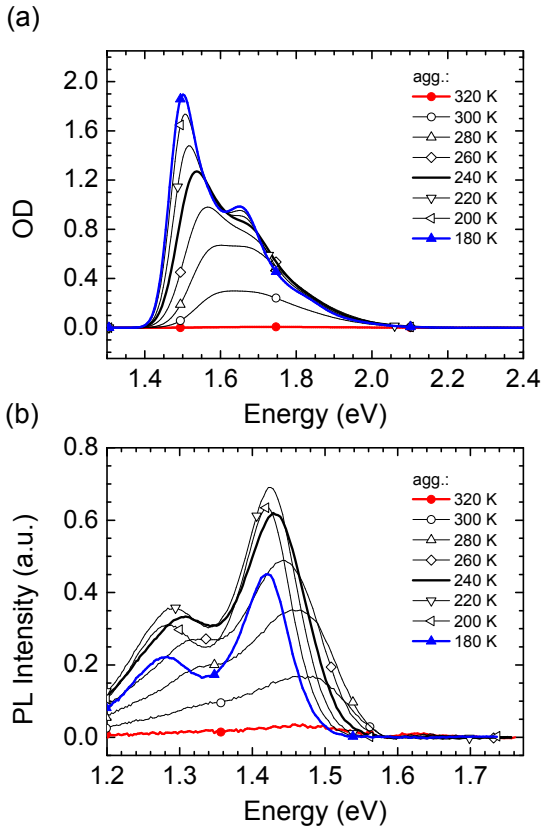

Figure 4: PCPDTBT in solution (c = 0.25 mg/ml in MTHF): (a) optical density of aggregated phase as result of Franck-Condon analysis of the first absorption band, (b) photoluminescence intensity of the aggregated phase resulting from subtracting the coiled phase photoluminescence (as measured at 340 K yet normalized to match the high energy shoulder) from the photoluminescence spectrum measured at an arbitrary temperature.

and narrows with decreasing temperature. Moreover, the ratio of the 0-0 to the 0-1 absorption peak increases. In photoluminescence, the spectrum of the aggregates shifts only by about 50 meV in a continuous way to the red (1.420 eV) and becomes narrower.

The parameters of the Franck-Condon analysis are summarized in Table 1 including the position of the 0-0 transition E_0, the standard deviation of the Gaussian line width σ, the peak ratio of the 0-0 and 0-1 transition $I_{0\text{-}0}/I_{0\text{-}1}$ and the relative contribution of the aggregates to the total spectra. For the peak ratio, the 0-0 intensity was calculated as the sum of all Huang –Rhys parameters of the above mentioned modes. In Table 1, the Franck-Condon fits are listed for spectra dominated by the aggregated phase (180 K), dominated by the coiled phase (340 K), and one spectrum exemplarily containing both, aggregated and coiled phase (240 K) with roughly equal weights in absorption. The actual spectra and fits are presented in the Supporting Information in Figure S2.

Table 1: Fitting parameters of the Franck-Condon analyses for the photoluminescence and absorption spectra of the aggregated phase (agg.) and the coiled phase (coil) of PCPDTBT in solution with f the relative contribution of the phase to the total spectrum, E_0 the position of 0-0 transition, σ the Gaussian standard deviation, and $I_{0\text{-}0}/I_{0\text{-}1}$ the peak ratio of the 0-0 line and the 0-1 line, the latter calculated as the sum of all Huang-Rhys parameters of the present modes with the following energies: 62 meV, 106 meV, 136 meV, 167 meV, 190 meV.

		Photoluminescence				**Absorption**			
FC parameter		f	E_0	σ	$I_{0\text{-}0}/I_{0\text{-}1}$	f	E_0	σ	$I_{0\text{-}0}/I_{0\text{-}1}$
unit		%	eV	meV		%	eV	meV	
180 K	agg.	100	1.420	30	0.94	67	1.495	33	1.06
180 K	coil	0	-	-	-	33	1.720	60	0.70
240 K	agg.	86	1.434	37	0.98	57	1.520	40	0.94
240 K	coil	14	1.598	46	0.76	43	1.720	63	0.66
340 K	agg.	0	-	-	-	0	-	-	-
340 K	coil	100	1.614	46	0.76	100	1.720	63	0.76

Whereas for the aggregated phase, the $I_{0\text{-}0}/I_{0\text{-}1}$ ratio is about 1.0, this value is about 0.7 for the coiled phase, indicating a stronger geometric distortion of the excited states. The disorder parameter σ is around 35±5 meV for the aggregated phase, yet 55±9 meV for the coiled phase, with the lower value pertaining to the photoluminescence spectra. These data support the notion of a higher energy phase with more conformational disorder and a lower energy phase where the chains adopt a more planar geometry so that the excited states are more delocalized and conformationally induced energetic disorder is reduced. From Table 1 and Figure S2 we also see that the contribution of the aggregates to the steady state spectra is much stronger in emission than in absorption for the spectra taken below 340 K. Obviously, there is energy transfer from the coiled phase to the aggregated phase, implying that at the concentration used (c = 0.25 mg/ml) the two phases are reasonably adjacent.

PCPDTBT thin films

Knowing the characteristics of PCPDTBT in solution, we expanded our studies to PCPDTBT thin films since films are most relevant to device applications.[24,26,35,38] We focused on two different preparation conditions. The first type of films was spin-coated with 2 wt% DIO in chlorobenzene ("CB/DIO"). The second type of films was spun from chloroform and afterwards annealed with chlorobenzene ("CB annealed").

Figure 5 compares the absorption spectra of the two PCPDTBT films for temperatures between room temperature and about 500 K to PCPDTBT in solution. Whereas in solution, the low energy peak appears suddenly from 300 K onwards and there is an isosbestic point from 280 K onwards, the film spectra show no isosbestic point and the low energy peak evolves gradually, yielding peak positions of 1.56 eV and 1.67 eV at room temperature for the CB/DIO film and the CB-annealed film, respectively. Furthermore, the 0-0 peak is less pronounced in the thin film spectra than in the solution spectra.

The absorption spectra of the films at room temperature are compared with the spectra of the solution at low temperature (240 K) in Figure 5d. We see that the solution spectrum and the spectrum belonging to the CB/DIO film coincide with regards to the energetic position as well as the 0-0/0-1 peak ratio. In contrast, the spectrum of the CB-annealed film is shifted to higher energy (140 meV to the blue), is broader and shows a high energy shoulder at about 2.05 eV. From this, we infer that the aggregates in the CB/DIO film may be structurally similar to the aggregates found in solution upon cooling whereas the aggregates formed in the CB annealed film differ in their structure.

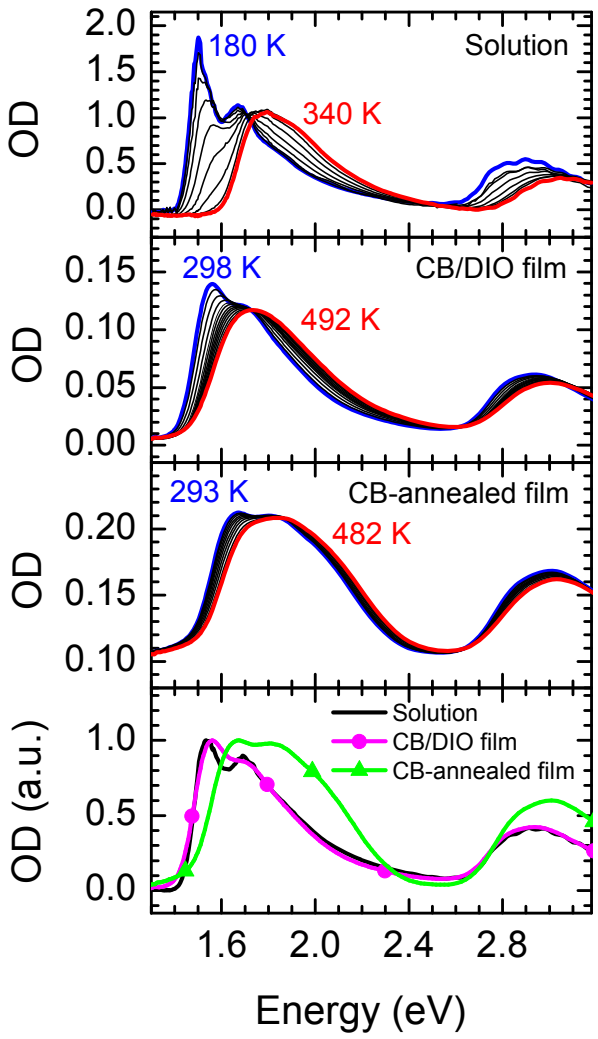

Figure 5: Optical density of PCPDTBT for different temperatures: (from top to bottom) solution (c = 0.25 mg/ml), CB/DIO film, and CB-annealed film. (Bottom) Normalized absorption of PCPDTBT in solution at 240 K (black line) and absorption of CB/DIO film (pink line) and CB-annealed film (green line) at room temperature.

Analogous to the absorption spectra measured in solution, it is possible to separate the thin film absorption spectra into a superposition of two spectra using a Franck-Condon analysis on the basis of the Raman spectra. This spectral decomposition is shown in the Supporting Information (Figure S3). Note that a Franck-Condon-analysis of the experimental spectra under the assumption of a single emitting excited state is *not* possible, consistent with our interpretation of there being two phases, namely a disordered phase and an aggregated phase. From the spectral decomposition, we can determine the fraction of aggregates present in the films. This requires to correct the fraction of aggregate absorption observed in the absorption spectra in order to account for the change in oscillator strength that takes place upon aggregation. This change in oscillator strength can be obtained - following the procedure by Clark et al.[39] - from the absorption spectra of PCPDTBT in solution since, in solution, there is an isosbestic point. Thus, we compared the additional contribution of absorption of the

aggregated phase with the reduction in absorption of the coiled phase when going from 280 K to 240 K in solution. From this we find the oscillator strength of the aggregated chains to be 1.45 ± 0.10 higher than the oscillator strength of the coiled chains. This factor is in good agreement with relative oscillator strengths found for transition of coiled to aggregated chains in poly(3-hexylthiophene)(P3HT) solution and thin films.[9,39] The fraction of aggregates in the film can then be obtained by dividing the fraction of aggregate absorption observed in the spectra by the relative change in oscillator strength. The resulting fraction of aggregates for PCPDTBT thin films and solution is shown in Figure 6. In solution, the fraction of aggregates increases with decreasing temperature until a saturation value of about 45% is reached at temperatures below 200 K. In PCPDTBT thin films, the fraction of aggregates does not significantly depend on temperature. For the CB-annealed film, the aggregate fraction stays constantly at 38%. In the CB/DIO film, the aggregate fraction slightly rises from 40% to 45% with decreasing temperature. Thus, both film morphologies show similar fractions of aggregates compared to the saturation value in solution.

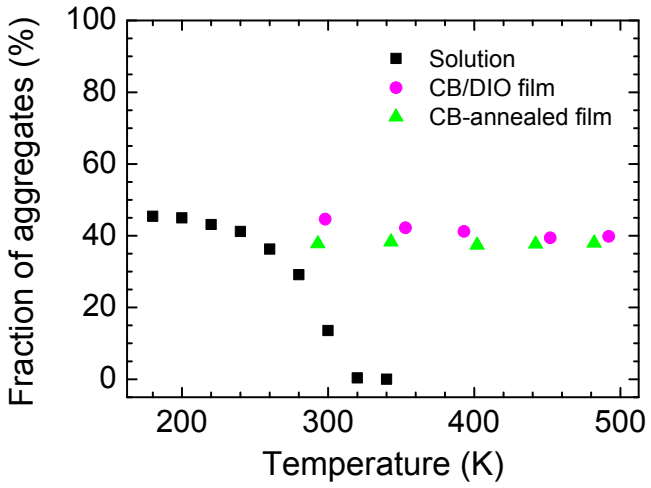

Figure 6: Fraction of aggregates as function of temperature for PCPDTBT solution (squares), CB/DIO film (circles) and CB-annealed film (triangles). Determined by calculating the fraction of aggregate absorption and the relative change in oscillator strength for coiled and planarized chains via Franck-Condon analysis.

The photoluminescence spectra of the two films are compared with the photoluminescence in solution in Figure 7. Whereas in solution emission is observed from both, the disordered phase (at 1.60 eV) and the aggregated phase (at 1.42 eV), the thin film spectra show only one emission with a 0-0 peak at 5 K centered at 1.40 eV for the CB/DIO film and at 1.43 eV for the CB-annealed film. The photoluminescence spectra of the films shift continuously to the red from 400 K to 5 K, the shift being 60 meV (CB/DIO film) and 47 meV (CB-annealed film), respectively, as determined from the 0-0 peak positions obtained by Franck-Condon analysis.

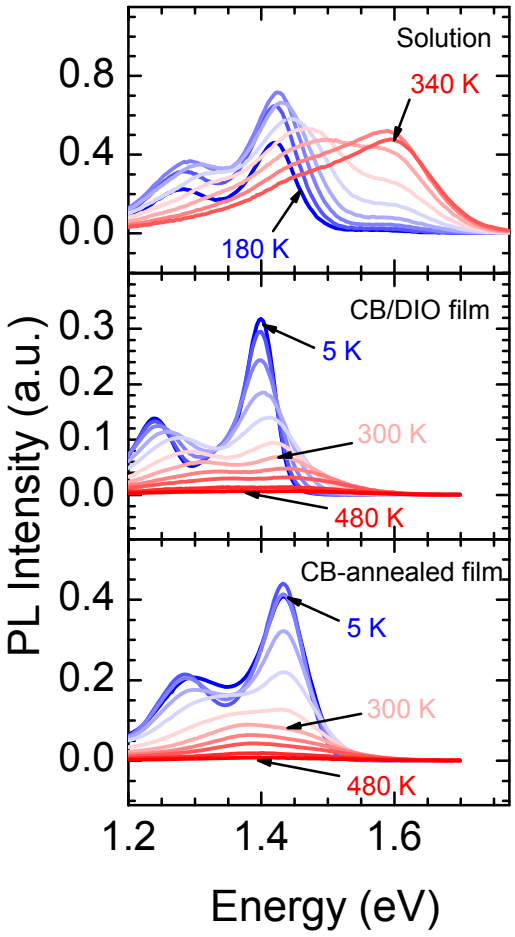

Figure 7: Intensity of photoluminescence of PCPDTBT for different temperatures: (from top to bottom) solution (c = 0.25 mg/ml), CB/DIO film, and CB-annealed film.

Concomitantly, the shape of the spectra changes with temperature. Figure 8a shows the temperature dependent photoluminescence normalized such that the 0-0 transition as determined by the Franck-Condon analysis (shown in the Supporting information) is at unity. The solution spectra are also displayed for ease of comparison. Evidently, in all spectra, the Gaussian linewidth broadens with increasing temperature from values around 30 meV to about 55 meV. In addition, for the films, roughly 100 meV below the 0-0 peak, a Gaussian peak increases strongly in intensity upon heating above 150 K. The evolution with temperature for the PL spectra in solution can be modelled well by convoluting the 180 K solution spectrum with a Gaussian linewidth function of increasing linewidth, as displayed in Figure 8b. This is not possible for the film spectra. The change in the thin film spectra with temperature can only be reproduced if one of the two following approaches is used. One option is to presume a single emitting state and to model the spectra using a Franck-Condon analysis according to Eq. 2. To account for the spectral changes with temperature, one needs to presume a modified, reduced intensity of the 0-0 peak and a strong increase (from S=0.16 to S=0.63) of the vibrational mode at 136 meV (1096 cm^{-1}) from 100 K

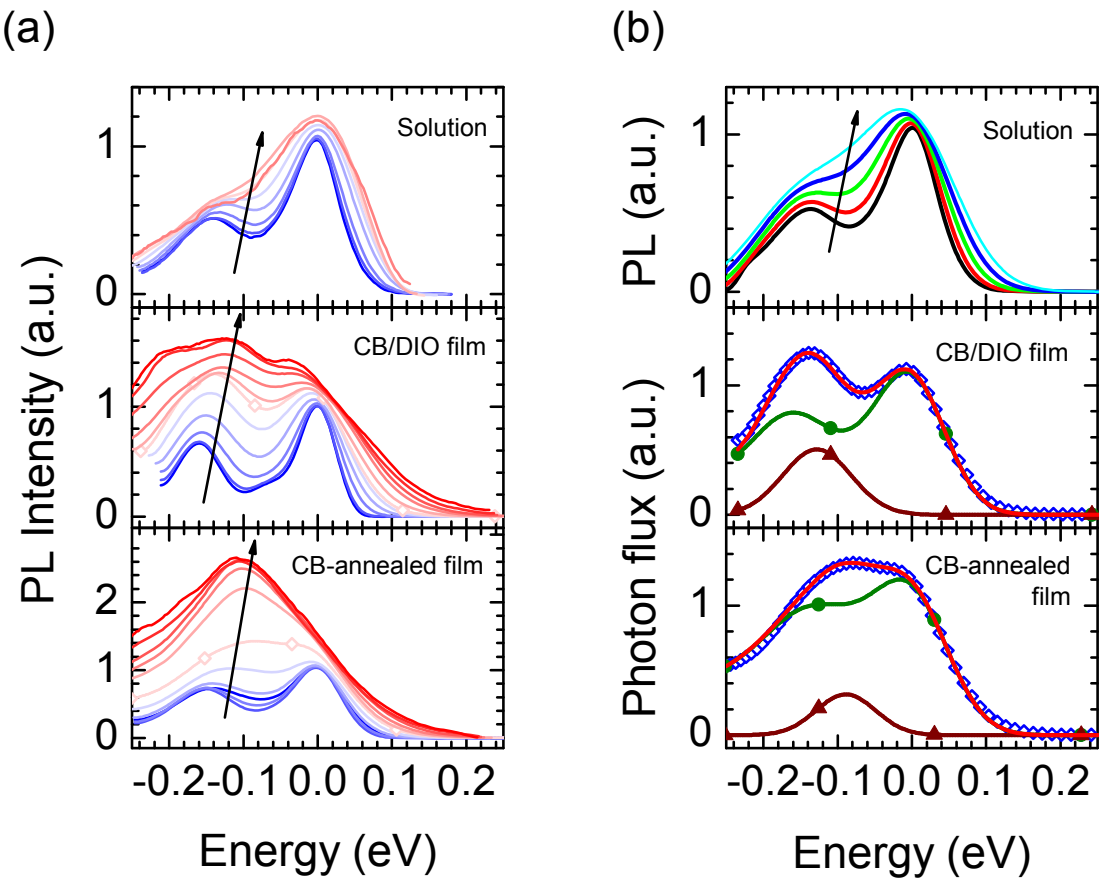

Figure 8: (a) Photoluminescence spectra of PCPDTBT thin films and in solution normalized to 0-0 transition as determined by Franck-Condon analysis. The energy axis is shifted to show the position of the 0-0 transition at 0 eV. The temperature ranges from 180 K to 320 K for solution and from 5 K to 480 K for films, arrows indicating direction of increasing temperature. (b) (top) 180 K PL spectrum convoluted with Gaussian line of standard deviation σ = 10, 20, 30, 40, and 50 meV. Arrow indicating the direction of increasing σ. (center/bottom) Photon flux, i.e. PL intensity/energy^3, of 250 K PL film spectra (blue squares) and Franck-Condon fits (red line) comprising a FC progression of the aggregated phase (green line with filled circles) and a Gaussian-shaped emission (wine line with triangles).

onwards. This is shown in the Supporting Information. The second possibility is to postulate two emitting states. One can then reproduce the spectra by superimposing a usual FC-progression (Eq. 3) with a broad Gaussian peak at 70 meV to 130 meV below the 0-0 peak. The standard deviation σ of this additional peak is comparable with σ of the corresponding FC-progression. The intensity of the Gaussian increases with temperature, while the Huang-Rhys parameters of the FC-progression remains essentially unaffected. Figure 8b shows this superposition exemplarily for the film spectra at 250 K. In addition, we measured the photoluminescence decay of the PCPDTBT thin films at room temperature and found a single exponential decay with lifetimes of τ = 250 ps for both films (see Supporting Information). The quantum yield ϕ of both films is less than 0.1% at room temperature (below measuring limit). The

radiative decay rate k_r and the non-radiative decay rate k_{nr} can be calculated according to

$$\Phi = k_r \cdot \tau = \frac{k_r}{k_r + k_{nr}} \quad (1)$$

resulting in $k_r = 0.004\ ns^{-1}$ and $k_{nr} = 4.0\ ns^{-1}$ for $\phi = 0.1\%$.

3 Discussion

Two phases in PCPDTBT solution

Several semiconducting polymers are known to show a transition from a disordered phase consisting of randomly coiled chains to a mixed phase where ordered aggregates are embedded in a disordered, amorphous matrix of coiled chains. This has been shown extensively for P3HT, yet also for MEH-PPV and PFO. In solution, the transition can be induced by reducing the solvent quality or temperature.[9,11,40-44] As shown in exemplary fashion for low polydispersity P3HT, the transition from the fully disordered form to the phase containing aggregates proceeds in a sequence of three steps upon lowering the temperature of the solution.[37] First, the absorption and emission spectra of the coiled form shift to slightly lower energies and the oscillator strength increases slightly. This has been interpreted to indicate an increase in conjugation length due to planarization of the polymer backbone. Next, an isosbestic point can be observed that has been taken to indicate the transformation from coiled chains to aggregated chains. Finally, a continuous bathochromic shift of the 0-0 peak of the aggregate absorption indicates an ongoing further planarization that leads to a longer conjugation length. These observations are also made for PCPDTBT upon cooling the solution (Figure 1). In addition, the measurements of absorption and emission as a function of concentration (Figure 2) demonstrate that the lower energy absorption and emission results from the interaction of polymer chains with each other. It is thus clear that PCPDTBT can exist in two phases, namely a fully disordered phase and a phase containing aggregated chains, consistent with earlier observations by Peet et al.[28] As revealed by Figure 3, the S_1 excited state of the coiled form and the aggregated form differ by 180 meV. This shift is consistent with the energy differences between emission from coiled and aggregated chains in P3HT (200 meV, Panzer et al.[37]), PPV (180 meV, Ho et al.[45]), MEH-PPV (120 meV, Köhler et al.[11]) and PFO (110 meV, Peet et al.[12], Ariu et al.[14]; 100 meV, Khan et al.[46]).

The phenomenon of a disorder-order transition is often regarded as specific to P3HT. It is well known that it plays a major role in controlling the efficiency of bulk heterojunction solar cells of P3HT with a fullerene. Evidently, this disorder-order

transition can be found in a range of chemically different polymers, and it proceeds in an analogous manner for P3HT, MEH-PPV and PCPDTBT. Existing differences relate to the temperature at which the disorder-order transition proceeds, the sharpness of the temperature dependent transition, the maximum fraction of aggregation obtained and the predominance of H- or J-type character in the spectra.

Whereas MEH-PPV and P3HT show transition temperatures at about 200 K and 250 K, respectively, PCPDTBT shows the phase transition already at room temperature. Clearly this has a strong impact on films prepared at room temperature for applications of PCPDTBT in organic semiconductor devices. Considering the sharpness of the disorder-order transition, Figure 6 shows that for our PCPDTBT with a molecular weight of 23 kDa and a PDI of 1.7, the phase transition extends from 320K to 260 K, i.e. over a range of about 60K. This is the same temperature range as observed for polydisperse, commercial MEH-PPV and for P3HT with a molecular weight of 19kD and a PDI of 2.0.[11,37] Note that when using a P3HT with same molecular weight yet lower PDI of 1.1, the transition range reduces to only 25K. With respect to the saturation fraction of aggregates, the saturation value of 40% of aggregates in solution that we observe for PCPDTBT is consistent with the similar values found for P3HT and MEH-PPV.[9,11,37]

P3HT and MEH-PPV are known to form weakly interacting aggregates with either H-type or J-type character, depending on the detailed conditions in the solutions (with respect to solvent mixture, solvation process, molecular weight of the polymer, polydispersity etc.).[11,37,47-53] Whether H-type or J-type character prevails, depends on the relative orientation of adjacent chains to each other as well as the amount of energetic disorder that is present in the sample and that may arise from variations in structure or in polarization of the environment.[54,55] Upon cooling solutions with THF or MTHF, low to medium molecular weight P3HT usually forms H-type aggregates, whereas MEH-PPV adopts a mixed H/J-character.[56,57] As evidenced by Figure 2, PCPDTBT is clearly an aggregate. Its vibrational structure, however, can be reproduced without need to suppress or enhance the 0-0 peak relative to the remaining vibrational progression. Thus, PCPDTBT has neither a predominant H-type character nor an eminent J-type nature. Evidently, the inherent energetic disorder is large compared to the amount of coupling between chromophores, so that the signatures of a prevailing H- or J-type character are masked.[57] The PCPDTBT aggregates are perhaps best described as a strongly disordered H/J-aggregates.

Aggregate formation in PCPDTBT thin films

When studying the formation of the low energy β-phase in PFO thin films, Khan et al. showed that small aggregates present in the solution act as nucleation sites during the spin-coating process.[13,46] Here, we have evidence for PCPDTBT aggregates in a MTHF

solution at room temperature and we have shown that the formation of aggregates depends on the concentration of the solution. Thus, we consider that preexisting aggregates act as nucleation sites when the film formation takes place in the presence of a slowly evaporating solvent as is the case when spin-coating a film from a CB/DIO solution. The aggregates formed in solution and those formed in a CB/DIO spin-coated film seem to be identical. This can be inferred from the nearly identical absorption spectra of aggregates in solution at 240 K and in CB/DIO film at room temperature (Figure 5), as well as the close similarity of the photoluminescence spectra at 180 K in solution and at 5 K in CB/DIO film (Figure 7).

It is well known that aggregate formation can also be induced by swelling a film in a solvent vapor (solvent annealing). The films prepared in this manner for PCPDTBT (CB-annealed films) also show clear evidence for aggregates, yet their spectral signature differs, indicating an altered structure. For example compared to the CB/DIO film, the absorption in the CB-annealed film is shifted hypsochromically (Figure 5) and the photoluminescence spectra evolve differently with temperatures (Figure 8).

The fraction of aggregates found in the two differently prepared films is comparable to the saturation value obtained in solution, suggesting that aggregate formation has been optimized by both preparation methods. This fraction of aggregates is in very good agreement with aggregate content of 45% that was reported for the low-bandgap copolymer P(NDI2OD-T2).[58] The lack of an isosbestic point when cooling a film, in contrast to its presence when cooling a solution, is remarkable. We attribute this to the change in environmental polarization upon cooling. In solution, the polymer chains are surrounded by solvent molecules, whose polarization does not change significantly upon cooling. In contrast, in film, the chains are embedded in neighboring chains, whose conjugation length, overall density and thus polarization changes with temperature. The associated shift in polarization energy thus masks any isosbestic point.

Energy transfer in PCPDTBT thin films

If we decompose the absorption spectra into absorption from non-interacting chains and absorption from aggregated chains, we find similar fraction of aggregates for solution below the transition temperature regime as for thin films. The amount of aggregates present in the films corresponds to the saturation value in solution (Figure 6). In contrast, in PL we observe differences. The PL spectra of PCPDTBT in solution show emission from both, coiled chains and aggregated chains, whereas the film spectra show only aggregate emission. In thin films, energy transfer can take place efficiently by exciton diffusion, i.e. a multistep hopping process with each hopping occurring by Förster transfer.[46,59-61] We attribute the fact that we see only aggregate emission in thin films containing 60% of amorphous material to exciton

diffusion from amorphous parts of the film to aggregated parts. This also implies that the approximate diameter of any amorphous phase is less than twice the exciton diffusion length at the respective temperature.

The analysis of the spectra has already shown that the chromophores constituting the aggregate are only weakly interacting, so that the spectra retain the vibrational structure that is characteristic for non-interacting chromophores. In this context, one may question whether the exciton dynamics, i.e. the diffusion of excitations, in weakly interacting aggregates differs from that typically found for amorphous films. In

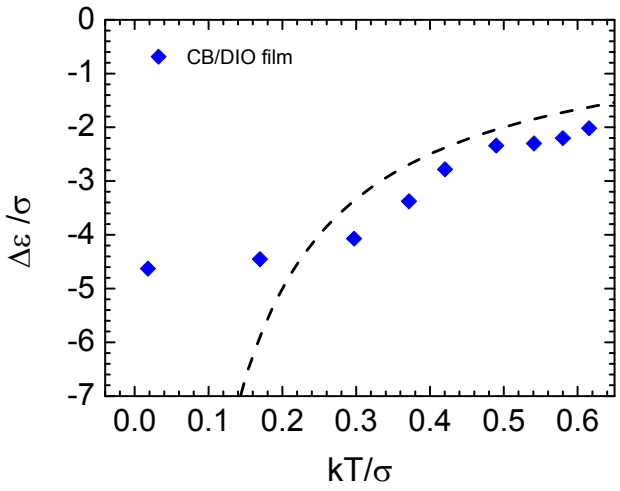

Figure 9: (Solid symbols) Energetic difference Δε between the position of the 0-0 transition in the photoluminescence and the center of the density of states (DOS) normalized to the standard deviation σ versus kT/σ for the CB/DIO film. Δε was determined by Franck-Condon analysis of the absorption spectra. (Dashed line) The theoretical dependence: Δε(T)/σ(T)=-σ(T)/kT.

Figure 9 we plotted the spectral shift Δε between the position of the 0-0 transition in the photoluminescence and the center of the density-of-states (DOS) normalized to the Gaussian line width σ versus kT/σ as determined via Franck-Condon analysis of absorption and photoluminescence spectra (see Supporting Information for absorption spectra at low temperatures). Compared to the theoretical dependence $\Delta\varepsilon(T)/\sigma(T)=-\sigma(T)/kT$[62-64], we see good agreement between theory and experimental data for kT/σ >0.3 (above 150 K). At lower temperatures, saturation of Δε/σ occurs since the life time of the excitation limits the relaxation progress within the density-of-states, as is well established for this process of spectral diffusion.[62] Thus, we found from the analysis of the steady-state spectra that the temperature-dependent dynamics in these weakly interacting aggregates does not differ from that of non-interacting chromophores.

Temperature-induced structural changes

In contrast to the absorption spectra (Figure 5), the photoluminescence spectra show significant differences in their evolution with temperature between the spectra taken in solution and those taken in thin films (Figure 8). In solution, the spectral shape reflects temperature-induced linewidth broadening. This is likely to arise from increased torsional motion since torsional motion has also been shown to be the source of temperature-induced linewidth broading for MEH-PPV in MTHF.[65] In contrast, in the films, an increased intensity in the red tail of the photoluminescence adds to the broadening. As mentioned above, this may be accounted for by a temperature-induced increase of the 136 meV vibration or by the temperature-induced population of a lower-energy emissive state. We consider that the latter is the most likely explanation for the following reasons:

- Modelling the spectra as resulting from only one emitting state requires the use of a modified FC-analysis with a suppressed 0-0 intensity (see Supporting Information) from about 150 K onwards, suggesting a different chain orientation and order at higher temperatures. For the solution spectra, this is not necessary. It is not plausible why in a film, where chain movement is constraint compared to solution, such a reorientation should occur while it is absent in solution. In addition, the spectra considered are emission spectra. The vibrational peaks observed relate to the vibrations induced in the molecule in the ground state, when the nuclei want to return to their ground state equilibrium position after the vertical electronic transition from the excited state. It is not obvious why raising the temperature should change the intensity of a particular ground state vibrational mode. Thus, we discard this approach as physically unlikely.

- The model of two emitting states, in contrast, allows reproducing the spectra with the same FC-analysis as used for solution, without need for suppressing the 0-0 peak. A temperature-induced population of a lower energy emissive state is possible. As demonstrated by Mikhnenko et al, exciton diffusion becomes temperature-activated from about 150 K onwards.[66] If a very low amount of red emitting sites were incorporated in a film, the amount of emission from those sites would thus increases with temperature from 150 K onwards, consistent with the observation in our data. Note that if low-energy sites are formed in solution, the lack of efficient diffusion across the solution prevents them to be sufficiently populated for detection.

While we can assign the spectral changes with temperature to red emissive trap sites, we are not able to unambiguously identify the nature of these sites merely on the basis of the spectroscopic data. The broad emission shape would be consistent with excimer-like sites, forming to a low percentage in the film, as a possible origin.[67,68] In polycrystalline samples, excimers have been demonstrated to form in particular at

grain boundaries as a result of structural dislocations. Thus, excimer formation comprising structural trapping is promoted by small domain sizes, a large amount of interfaces and fast exciton diffusion.[36] To assess, whether the optical data are consistent with an excimer-like origin, we compare the radiative decay rate k_r and the non-radiative decay rate k_{nr} obtained for the PCPDTBT films at room temperature with typical values for molecular assemblies and solids collected by Gierschner and Park.[69] For excimer emission of disytrylbenzene derivatives in the solid state, Gierschner and Park find a quantum yield of 0.01, a lifetime of 8.3 ns and a radiative decay rate of 0.001 ns^{-1}. This results in a non-radiative decay rate of 0.12 ns^{-1}. The radiative decay rate is comparable to the value we found for PCPDTBT thin films (k_r = 0.004 ns^{-1}), whereas our values for the non-radiative decay rates (k_{nr} = 4.0 ns^{-1}) is 30 times higher. However, the disytrylbenzene derivative investigated by Gierschner and Parks emits at 3.3 eV while our material emits at 1.4 eV. Since the non-radiative decay rate in polymers increases drastically with decreasing energy gap between ground and excited state, a factor of 30 is fully consistent with the energy gap law.[70] Thus, we tentatively attribute the low-energy emissive state in PCPDTBT thin films to a low percentage of excimer states present whose population is thermally activated.

Correlation to structural analysis

Information on the structure of PCPDTBT has only become available in recent years. On the basis of grazing incidence wide-angle X-ray experiments, Nelson et al., Bazan et al. and Russel et al. could show that PCPDTBT forms lamellar structures with a distance of about 4Å between the plane of the backbone that allows for π-stacking in two polymorphs.[31,71,72] This applies to PCPDTBT films prepared by spin-coating from neat chlorobenzene solution and from chlorobenzene solution containing additives such as dioiodooctane or octanedithiol. These lamellar aggregates extending over about 40 nm are randomly oriented in the film. Figure 10a shows an image taken by atomic force micrcoscopy (AFM).[35] This is the structure that prevails in our CB/DIO films.

For the CB-annealed films, AFM and polarizing microscopy indicate the formation of extended aggregates (Figures 10b and c). Recent structural investigations by Fischer et al.[35] have identified the formation of crystallites with the c-axis of the unit cell arranged at an angle of about 45° or at 90° to the substrate, thus leading to spherulite and terrace-like structures, respectively. In this crystal structure, the polymers assemble in dimers with a distance of about 7Å between the two backbone planes. Adjacent dimers arrange in a herringbone structure. While the lamellar structure with the π-stacking found for the CB/DIO films is akin to the structure of P3HT-aggregates, the herringbone-dimer structure observed for the CB-annealed films that does not exhibit long-range π-interaction is similar to that reported for polyfluorene.[73]

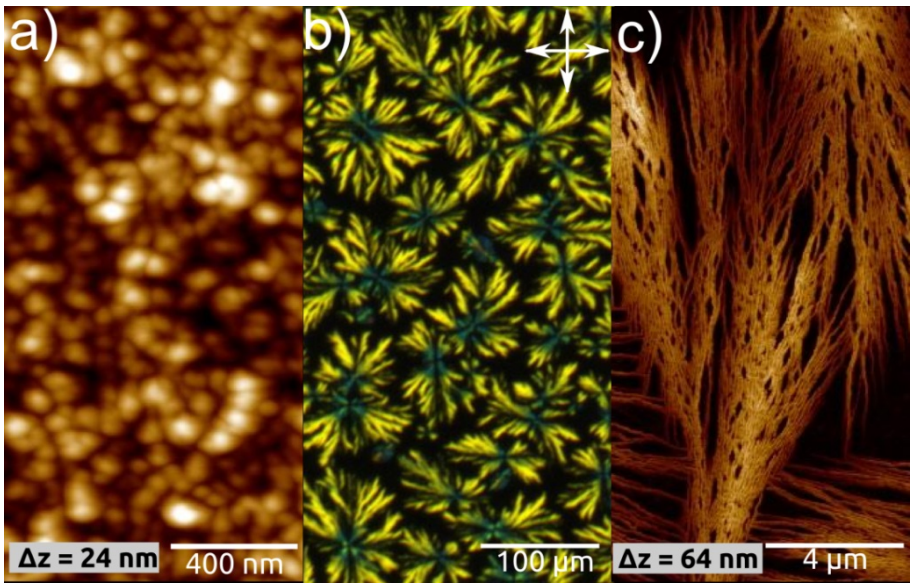

Figure 10: AFM-height images of a CB/DIO film (a) and a CB-annealed film (c). (b) Polarized microscopy image of a CB-annealed film.

The absorption and emission in the CB/DIO film closely resemble the spectra and energetic positions obtained in solution (Figures 5 and 7). Thus it appears likely that PCPDTBT may also prevail in lamellar assemblies of comparable size (~ 40 nm) in solution. This would also account for the similar percentage of 40% aggregates observed in both, solution and CB/DIO films. More remarkable, however, is that the same value is also found for the CB-annealed films.

From the spectral separation of the absorption into the contributions from the aggregated chains and from the disordered chains by Franck-Condon analysis (Figure S3) one learns that the 0-0 position of the disordered chains is hypsochromically shifted in the CB-annealed films compared to the CB/DIO films, suggesting a shorter average conjugation length of the coiled chains in the CB-annealed films. It seems that the formation of extended crystalline structures such as spherulites and terraces in the CB-annealed film constraints the conformations of the chains in the amorphous phase thus reducing the average conjugation length. As demonstrated in Figure 5, the aggregated phase is also hypsochromically shifted in the CB-annealed films compared to the CB/DIO films, suggesting a reduced polarization of the surrounding medium for the polymer chains in the CB-annealed films. This is consistent with the larger distance between the backbone planes that is found in the CB-annealed films compared to the CB/DIO films in the structural studies.[35]

4 Conclusion

The low-bandgap copolymer PCPDTDT that is frequently used for solar cell applications undergoes a phase transition, like P3HT and MEH-PPV, upon cooling in solution. Above the critical temperature T_c for the transition, the polymer prevails in a non-aggregated manner in a randomly coiled conformation. Below T_c , up to about 40-45% of the polymer chains aggregate and adopt a more planarized conformation. For PCPDTBT, the critical temperature T_c at which the phase transition takes place in MTHF is around 300 K. Comparison to structural investigations suggest that lamellar aggregates prevailing in solution at room temperature serve as nucleation points during the process of spin-coating, thus resulting in films containing randomly oriented lamellar aggregates. In contrast, solvent annealing a chloroform-spun film using chlorobenzene vapor induces a herringbone dimer structure. We show that using suitable processing the maximum fraction of about 42% aggregates can also be obtained in thin films of PCPDTBT. In these films, a small percentage of low-energy trap states prevails that are populated by exciton diffusion for temperatures above 150 K. The emission characteristics of these states are consistent with an origin from excimers resulting from structural defects such as grain boundaries.

5 Experimental – materials and methods

(i) Sample preparation

The PCPDTBT (poly{[4,4-bis(2-ethylhexyl)-cyclopenta-(2,1-b;3,4-b')dithiophen]-2,6-diyl-alt-(2,1,3-benzo-thiadiazole)-4,7-diyl}) was purchased from 1-material and has a molecular weight M_w of 23 kD with a polydispersity of 1.7 (HT-SEC, 160°C, trichlorobenzene, against PS standards).The solvents (p.a. grade) chloroform ($CHCl_3$), chlorobenzene (CB) and 2-Methyltetrahydrofuran (MTHF) as well as the processing additive 1,8-Diiodooctane (DIO) were bought from Sigma Aldrich. For temperature dependent solution measurements, the PCPDTBT was dissolved in the low melting-point solvent MTHF with a concentration of 0.25 mg/ml. Concentration dependent solution measurements were done with PCPDTBT in MTHF. Solutions were stirred at about 50 °C for at least 15 min and exposed shortly to ultrasonic sound before further dilution and measurements.

Film preparation was done under nitrogen atmosphere. Spectrosil B quartz substrates were cleaned with a CO_2 snow jet followed by exposure to oxygen plasma (*Diener Femto* 100 W) for at least 300 s. Two different techniques were used. (i) Films were spin-coated onto the quartz substrate at 1000 rpm for 240 seconds from 3 mg/ml solution of chlorobenzene containing 2 wt% of DIO. We refer to these films as CB/DIO-

films (ii) Films were also prepared by first continuously stirring a 3 mg/ml $CHCl_3$ solution for 1 to 2 hours at elevated temperatures (50-60°C). From this solution, spin-coating took place at 1000 rpm for 30 s within 24 h after preparation of the solutions. Subsequently, these films were exposed to controlled chlorobenzene vapor by placing the spin-coated substrates, held at 42°C, in a chamber with the vapor atmosphere set to 50°C. The films were first swollen to a solution-like state and then recrystallized by slowly decreasing the vapor pressure as previously described.[74] We shall call these films CB-annealed films. In addition, films for Raman measurements were prepared by spin-coating from the 3 mg/ml $CHCl_3$ solution onto a gold surface that had been evaporated on top of a silicon wafer.

(ii) Microscopy

The atomic force microscopy (AFM) was performed on a *Dimension Icon AFM* from *Bruker* operated in tapping mode under ambient air. The polarized microscopy images (POM) were captured with an *Axio Imager.A1* from *Zeiss* using crossed polarizers as indicated by arrows in the POM images.

(iii) Optical spectroscopy

The home-built setup for temperature-dependent absorption and photoluminescence measurements of solution and thin films includes a monochromator (*CVI Instruments Digikrom 240*) with Si-photodiode (by Thorlabs) and lock-in technique (*Standford Research Systems, Model SR830 DSP Lock-In Amplifier*) for signal detection, a Xe-lamp (*LAX 1530 by Müller GmbH Elektronik - Optik*) with monochromator (*LTI by Amko Light Technology Instruments*) for illumination (absorption) and a *Compass* continuous wave 405nm diode laser by *Coherent* for excitation (photoluminescence). During the measurement, the sample (the film on the quartz substrate or a 1mm quartz cuvette with the MTHF solution) is held in a continuous flow Helium cryostate, with the temperature controlled by a *ITC503 Oxford instruments* temperature controller. To measure the absorption for different concentrations, we used a *Varian Carry 5000* UV/Vis spectrometer in a standard double-beam transmission alignment. Photoluminescence of the concentration series was measured in front geometry using a home-built setup that includes a *Compass* continuous wave 405nm diode laser by *Coherent* for excitation and an *iDus* CCD camera from *Andor Technology* combined with a *MS125* spectrograph by *Newport* for signal detection. Spectral correction was determined by means of a *SESSL-1-5* calibrated spectral flux standard by *SphereOptics*. Temperature dependent absorption of PCPDTBT thin films was measured using a *Zeiss* spectrometer with *MCS621VIS II* detector combined with a *HotStage THMS600* by *Linkam* for heating. Photoluminescence lifetime was measured on a home-built confocal microscope using TCSPC. The excitation light (532 nm, 20 MHz, <80 ps pulse

duration; *LDH-P-FA-530L*, *PicoQuant*) was directed via a dichroic beam splitter (*z532 RDC, AHF Analysentechnik AG*) to an infinity-corrected oil-immersion objective (60x, *PlanApo*, NA = 1.45, *Olympus*) and focused onto PCPDTBT films. The photoluminescence was collected by the same objective, passed suitable dielectric long-pass filter, and was detected by single-photon sensitive photodiode (*Micro Photon Devices*). The *Micro Photon Devices*'s electrical signal was used to start a TCPC module (*Timeharp 200, PicoQuant*). The quantum efficiency of PCPDTBT in MTHF (c = 0.25 mg/ml) was measured with a *FP-8600* fluorescence spectrometer by *JASCO Analytical Instruments*. The excitation wavelength was 405 nm. For Raman measurements a *Jobin Yvon HR800* confocal Raman microscope from *Horiba* with a He-Ne-Laser (500:1 polarization, 632.82 nm, 20 mW) was used. Films were measured in air for 60 s (laser power: 2 μW).

(iv) Franck-Condon-Analysis

For an appropriate analysis of the spectra, Franck-Condon (FC) fits were carried out by modelling the absorption and photoluminescence spectrum as a sum of Franck-Condon transitions based on several intramolecular vibrational modes, i. In the harmonic approximation, vibrational frequencies ω remain constant for both, ground and excited state. Thus, the intensity of individual emission and absorption lines is determined by the Huang-Rhys parameter S,

$$S = \frac{M\omega}{2\hbar}(\Delta Q)^2 , \qquad (2)$$

with M the reduced mass of a single oscillator and ΔQ the configurational displacement between ground and excited state. The intensities $I_{0\text{-}m}$ of the vibronic transitions 0-m_i of mode i are related to the Huang-Rhys parameter via $I_{0-m_i} = e^{-S_i} S_i^{m_i} / m_i!$. We modeled the photoluminescence spectra, $PL(\hbar\omega)$, and the absorption spectra, $A(\hbar\omega)$, according to[45]

$$PL(\hbar\omega)/n^3 \cdot (\hbar\omega)^3 = \sum_{m_i} \prod_i I_{0-m_i} \Gamma\delta[\hbar\omega - (\hbar\omega_0 - \sum_i m_i \hbar\omega_i)] \text{ and} \qquad (3)$$

$$A(\hbar\omega)/n \cdot (\hbar\omega) = \sum_{m_i} \prod_i I_{0-m_i} \Gamma\delta[\hbar\omega - (\hbar\omega_0 + \sum_i m_i \hbar\omega_i)] \qquad (4)$$

where n is the refractive index of the surrounding medium, m_i=0,1,2,3,… being the vibration quantum number of the ith vibrational mode , $\hbar\omega_0$ is the energetic position of the 0-0 line, and Γ denotes the Gaussian line shape function with constant standard deviation σ. The normalization term $n^3(\hbar\omega)^3$ and $n(\hbar\omega)$ arise from accounting for the photon density-of-states in the surrounding medium effecting the emitter's emission and absorption coefficient, respectively.[45,57,75]

Acknowledgements

We thank Heinz Bässler for fruitful discussions and Fabian Panzer for assistance with the spectroscopic setup. Funding by the Graduiertenkolleg 1640 of the Deutsche Forschungsgemeinschaft, by the Free State of Bavaria in the context of the program „Solar Technologies go Hybrid“ and of the program “Bayerisches Programm zur Förderung der Chancengleichheit für Frauen in Forschung und Lehre” are gratefully acknowledged.

References

(1) Li, L. G.; Lu, G. H.; Yang, X. N. *J. Mater. Chem.* **2008**, *18*, 1984.
(2) Zhao, Y.; Xie, Z. Y.; Qu, Y.; Geng, Y. H.; Wang, L. X. *Appl. Phys. Lett.* **2007**, *90*.
(3) Schubert, M.; Dolfen, D.; Frisch, J.; Roland, S.; Steyrleuthner, R.; Stiller, B.; Chen, Z. H.; Scherf, U.; Koch, N.; Facchetti, A.; Neher, D. *Adv. Energy Mater.* **2012**, *2*, 369.
(4) Zen, A.; Pflaum, J.; Hirschmann, S.; Zhuang, W.; Jaiser, F.; Asawapirom, U.; Rabe, J. P.; Scherf, U.; Neher, D. *Adv. Funct. Mater.* **2004**, *14*, 757.
(5) Virkar, A. A.; Mannsfeld, S.; Bao, Z. A.; Stingelin, N. *Adv. Mater.* **2010**, *22*, 3857.
(6) Yang, X. N.; Loos, J.; Veenstra, S. C.; Verhees, W. J. H.; Wienk, M. M.; Kroon, J. M.; Michels, M. A. J.; Janssen, R. A. J. *Nano Lett.* **2005**, *5*, 579.
(7) Chirvase, D.; Parisi, J.; Hummelen, J. C.; Dyakonov, V. *Nanotechnology* **2004**, *15*, 1317.
(8) Liu, J. S.; Tanaka, T.; Sivula, K.; Alivisatos, A. P.; Frechet, J. M. J. *J. Am. Chem. Soc.* **2004**, *126*, 6550.
(9) Scharsich, C.; Lohwasser, R. H.; Sommer, M.; Asawapirom, U.; Scherf, U.; Thelakkat, M.; Neher, D.; Köhler, A. *J. Polym. Sci. Pt. B-Polym. Phys.* **2012**, *50*, 442.
(10) Johnson, C. E.; Boucher, D. S. *J. Polym. Sci. Pt. B-Polym. Phys.* **2014**, *52*, 526.
(11) Köhler, A.; Hoffmann, S. T.; Bässler, H. *J. Am. Chem. Soc.* **2012**, *134*, 11594.
(12) Peet, J.; Brocker, E.; Xu, Y. H.; Bazan, G. C. *Adv. Mater.* **2008**, *20*, 1882.
(13) Khan, A. L. T.; Banach, M. J.; Köhler, A. *Synth. Met.* **2003**, *139*, 905.
(14) Ariu, M.; Lidzey, D. G.; Sims, M.; Cadby, A. J.; Lane, P. A.; Bradley, D. D. C. *J. Phys.-Condes. Matter* **2002**, *14*, 9975.
(15) Konarka press release, Feb 28, 2012.
(16) Polyera press release, Feb 1, 2012.
(17) Dou, L. T.; You, J. B.; Yang, J.; Chen, C. C.; He, Y. J.; Murase, S.; Moriarty, T.; Emery, K.; Li, G.; Yang, Y. *Nat. Photonics* **2012**, *6*, 180.
(18) Havinga, E. E.; Tenhoeve, W.; Wynberg, H. *Polym. Bull.* **1992**, *29*, 119.
(19) Liu, F.; Gu, Y.; Jung, J. W.; Jo, W. H.; Russell, T. P. *J. Polym. Sci. Pt. B-Polym. Phys.* **2012**, *50*, 1018.
(20) Ma, W. L.; Yang, C. Y.; Gong, X.; Lee, K.; Heeger, A. J. *Adv. Funct. Mater.* **2005**, *15*, 1617.
(21) Kim, Y.; Choulis, S. A.; Nelson, J.; Bradley, D. D. C.; Cook, S.; Durrant, J. R. *Appl. Phys. Lett.* **2005**, *86*.
(22) Li, G.; Shrotriya, V.; Yao, Y.; Huang, J. S.; Yang, Y. *J. Mater. Chem.* **2007**, *17*, 3126.
(23) Hoven, C. V.; Dang, X. D.; Coffin, R. C.; Peet, J.; Nguyen, T. Q.; Bazan, G. C. *Adv. Mater.* **2010**, *22*, E63.
(24) Lee, J. K.; Ma, W. L.; Brabec, C. J.; Yuen, J.; Moon, J. S.; Kim, J. Y.; Lee, K.; Bazan, G. C.; Heeger, A. J. *J. Am. Chem. Soc.* **2008**, *130*, 3619.

(25) Etzold, F.; Howard, I. A.; Forler, N.; Cho, D. M.; Meister, M.; Mangold, H.; Shu, J.; Hansen, M. R.; Mullen, K.; Laquai, F. *J. Am. Chem. Soc.* **2012**, *134*, 10569.
(26) Peet, J.; Kim, J. Y.; Coates, N. E.; Ma, W. L.; Moses, D.; Heeger, A. J.; Bazan, G. C. *Nat. Mater.* **2007**, *6*, 497.
(27) Fischer, F. S. U.; Tremel, K.; Saur, A. K.; Link, S.; Kayunkid, N.; Brinkmann, M.; Herrero-Carvajal, D.; Navarrete, J. T. L.; Delgado, M. C. R.; Ludwigs, S. *Macromolecules* **2013**, *46*, 4924.
(28) Peet, J.; Cho, N. S.; Lee, S. K.; Bazan, G. C. *Macromolecules* **2008**, *41*, 8655.
(29) Fazzi, D.; Grancini, G.; Maiuri, M.; Brida, D.; Cerullo, G.; Lanzani, G. *Phys. Chem. Chem. Phys.* **2012**, *14*, 6367.
(30) Marin, L.; Penxten, H.; Van Mierloo, S.; Carleer, R.; Lutsen, L.; Vanderzande, D.; Maes, W. *J. Polym. Sci. Pol. Chem.* **2013**, *51*, 4912.
(31) Gu, Y.; Wang, C.; Russell, T. P. *Adv. Energy Mater.* **2012**, *2*, 683.
(32) Niedzialek, D.; Lemaur, V.; Dudenko, D.; Shu, J.; Hansen, M. R.; Andreasen, J. W.; Pisula, W.; Mullen, K.; Cornil, J.; Beljonne, D. *Adv. Mater.* **2013**, *25*, 1939.
(33) Wang, S. H.; Kappl, M.; Liebewirth, I.; Muller, M.; Kirchhoff, K.; Pisula, W.; Mullen, K. *Adv. Mater.* **2012**, *24*, 417.
(34) Tsao, H. N.; Cho, D. M.; Park, I.; Hansen, M. R.; Mavrinskiy, A.; Yoon, D. Y.; Graf, R.; Pisula, W.; Spiess, H. W.; Mullen, K. *J. Am. Chem. Soc.* **2011**, *133*, 2605.
(35) Fischer, F. S. U.; Trefz, D.; Back, J.; Kayunkid, N.; Tornow, B.; Albrecht, S.; Yager, K.; Singh, G.; Karim, A.; Neher, D.; Brinkmann, M.; Ludwigs, S. *Adv. Mater.* **2014**, DOI: 10.1002/adma.201403475.
(36) Gierschner, J.; Luer, L.; Milian-Medina, B.; Oelkrug, D.; Egelhaaf, H. J. *J. Phys. Chem. Lett.* **2013**, *4*, 2686.
(37) Panzer, F.; Bässler, H.; Lohwasser, R.; Thelakkat, M.; Köhler, A. *J. Phys. Chem. Lett.* **2014**, *5*, 2742.
(38) Chen, H. P.; Hsiao, Y. C.; Hu, B.; Dadmun, M. *Adv. Funct. Mater.* **2014**, *24*, 5129.
(39) Clark, J.; Chang, J. F.; Spano, F. C.; Friend, R. H.; Silva, C. *Appl. Phys. Lett.* **2009**, *94*.
(40) Dias, F. B.; Morgado, J.; Macanita, A. L.; da Costa, F. P.; Burrows, H. D.; Monkman, A. P. *Macromolecules* **2006**, *39*, 5854.
(41) Cossiello, R. F.; Susman, M. D.; Aramendia, P. F.; Atvars, T. D. Z. *J. Lumines.* **2010**, *130*, 415.
(42) Sherwood, G. A.; Cheng, R.; Smith, T. M.; Werner, J. H.; Shreve, A. P.; Peteanu, L. A.; Wildeman, J. *J. Phys. Chem. C* **2009**, *113*, 18851.
(43) Kitts, C. C.; Vanden Bout, D. A. *Polymer* **2007**, *48*, 2322.
(44) Inganäs, O.; Salaneck, W. R.; Osterholm, J. E.; Laakso, J. *Synth. Met.* **1988**, *22*, 395.
(45) Ho, P. K. H.; Kim, J. S.; Tessler, N.; Friend, R. H. *J. Chem. Phys.* **2001**, *115*, 2709.
(46) Khan, A. L. T.; Sreearunothai, P.; Herz, L. M.; Banach, M. J.; Köhler, A. *Phys. Rev. B* **2004**, *69*.
(47) Niles, E. T.; Roehling, J. D.; Yamagata, H.; Wise, A. J.; Spano, F. C.; Moule, A. J.; Grey, J. K. *J. Phys. Chem. Lett.* **2012**, *3*, 259.
(48) So, W. Y.; Hong, J. Y.; Kim, J. J.; Sherwood, G. A.; Chacon-Madrid, K.; Werner, J. H.; Shreve, A. P.; Peteanu, L. A. *J. Phys. Chem. B* **2012**, *116*, 10504.
(49) Zhou, R. T.; Chen, W.; Jiang, X. Y.; Wang, S. F.; Gong, Q. H. *Appl. Phys. Lett.* **2010**, *96*.
(50) Roque, A. P.; Mercante, L. A.; Scagion, V. P.; Oliveira, J. E.; Mattoso, L. H. C.; De Boni, L.; Mendonca, C. R.; Correa, D. S. *J. Polym. Sci. Pt. B-Polym. Phys.* **2014**, *52*, 1388.
(51) Chao, K. P.; Biswal, S. L. *Langmuir* **2014**, *30*, 4236.
(52) Crotty, A. M.; Gizzi, A. N.; Rivera-Jacquez, H. J.; Masunov, A. E.; Hu, Z. J.; Geldmeier, J. A.; Gesquiere, A. J. *J. Phys. Chem. C* **2014**, *118*, 19975.
(53) Martin, T. P.; Wise, A. J.; Busby, E.; Gao, J.; Roehling, J. D.; Ford, M. J.; Larsen, D. S.; Moule, A. J.; Grey, J. K. *J. Phys. Chem. B* **2013**, *117*, 4478.
(54) Kasha, M. *Radiat. Res.* **1963**, *20*, 55.
(55) Spano, F. C.; Silva, C. *Annu. Rev. Phys. Chem.* **2014**, *65*, 477.
(56) Clark, J.; Silva, C.; Friend, R. H.; Spano, F. C. *Phys. Rev. Lett.* **2007**, *98*.

(57) Yamagata, H.; Hestand, N. J.; Spano, F. C.; Köhler, A.; Scharsich, C.; Hoffmann, S. T.; Bässler, H. *J. Chem. Phys.* **2013**, *139*.
(58) Steyrleuthner, R.; Schubert, M.; Howard, I.; Klaumunzer, B.; Schilling, K.; Chen, Z. H.; Saalfrank, P.; Laquai, F.; Facchetti, A.; Neher, D. *J. Am. Chem. Soc.* **2012**, *134*, 18303.
(59) Albuquerque, R. Q.; Hofmann, C. C.; Köhler, J.; Köhler, A. *J. Phys. Chem. B* **2011**, *115*, 8063.
(60) Bagnich, S. A.; Im, C.; Bässler, H.; Neher, D.; Scherf, U. *Chem. Phys.* **2004**, *299*, 11.
(61) Herz, L. M.; Silva, C.; Grimsdale, A. C.; Müllen, K.; Phillips, R. T. *Phys. Rev. B* **2004**, *70*.
(62) Hoffmann, S. T.; Bässler, H.; Koenen, J. M.; Forster, M.; Scherf, U.; Scheler, E.; Strohriegl, P.; Köhler, A. *Phys. Rev. B* **2010**, *81*.
(63) Bässler, H. *Phys. Status Solidi B-Basic Res.* **1993**, *175*, 15.
(64) Athanasopoulos, S.; Hoffmann, S. T.; Bässler, H.; Köhler, A.; Beljonne, D. *J. Phys. Chem. Lett.* **2013**, *4*, 1694.
(65) Hoffmann, S. T.; Bässler, H.; Köhler, A. *J. Phys. Chem. B* **2010**, *114*, 17037.
(66) Mikhnenko, O. V.; Kuik, M.; Lin, J.; van der Kaap, N.; Nguyen, T. Q.; Blom, P. W. M. *Adv. Mater.* **2014**, *26*, 1912.
(67) Egelhaaf, H. J.; Gierschner, J.; Oelkrug, D. *Synth. Met.* **2002**, *127*, 221.
(68) Gierschner, J.; Egelhaaf, H. J.; Oelkrug, D.; Müllen, K. *J. Fluoresc.* **1998**, *8*, 37.
(69) Gierschner, J.; Park, S. Y. *J. Mater. Chem. C* **2013**, *1*, 5818.
(70) Wilson, J. S.; Chawdhury, N.; Al-Mandhary, M. R. A.; Younus, M.; Khan, M. S.; Raithby, P. R.; Köhler, A.; Friend, R. H. *J. Am. Chem. Soc.* **2001**, *123*, 9412.
(71) Agostinelli, T.; Ferenczi, T. A. M.; Pires, E.; Foster, S.; Maurano, A.; Muller, C.; Ballantyne, A.; Hampton, M.; Lilliu, S.; Campoy-Quiles, M.; Azimi, H.; Morana, M.; Bradley, D. D. C.; Durrant, J.; Macdonald, J. E.; Stingelin, N.; Nelson, J. *J. Polym. Sci. Pt. B-Polym. Phys.* **2011**, *49*, 717.
(72) Rogers, J. T.; Schmidt, K.; Toney, M. F.; Kramer, E. J.; Bazan, G. C. *Adv. Mater.* **2011**, *23*, 2284.
(73) Brinkmann, M. *Macromolecules* **2007**, *40*, 7532.
(74) Crossland, E. J. W.; Rahimi, K.; Reiter, G.; Steiner, U.; Ludwigs, S. *Adv. Funct. Mater.* **2011**, *21*, 518.
(75) Strickler, S. J.; Berg, R. A. *J. Chem. Phys.* **1962**, *37*, 814.

Supporting Information to

Revealing structure formation in PCPDTBT by optical spectroscopy

Christina Scharsich[1,2], Florian S. U. Fischer[3], Kevin Wilma[1,4], Richard Hildner[1,4], Sabine Ludwigs[3]*, Anna Köhler[1,2]*

[1] Bayreuth Institute of Macromolecular Research (BIMF), University of Bayreuth, Bayreuth 95440, Germany.

[2] Experimental Physics II, University of Bayreuth, Bayreuth 95440, Germany.

[3] IPOC-Functional Polymers, University of Stuttgart, Stuttgart 70569, Germany

[4] Experimental Physics IV, University of Bayreuth, Bayreuth 95440, Germany

email: sabine.ludwigs@ipoc.uni-stuttgart.de, anna.koehler@uni-bayreuth.de

1 Raman spectroscopy

In addition to the energetic position of the 0-0 transition and the Gaussian line width, the vibrational frequencies coupling to the transition from ground to first excited state are essential parameters for Franck-Condon fitting. Therefore, we have measured the Raman energies of PCPDTBT spin-coated from chloroform using a *Jobin Yvon HR800* confocal Raman microscope from *Horiba* with a He-Ne-Laser. Figure S1 shows the resulting Raman spectrum.

The following four Raman modes were used for Franck-Condon fitting in addition to a low energy mode at 500 cm^{-1} (62 meV) that we associate with a torsional mode: 857 cm^{-1}, 1096 cm^{-1}, 1347 cm^{-1}, 1535 cm^{-1} (106 meV, 136 meV, 167 meV, 190 meV). These modes are used as effective modes for energetically adjacent vibrations.

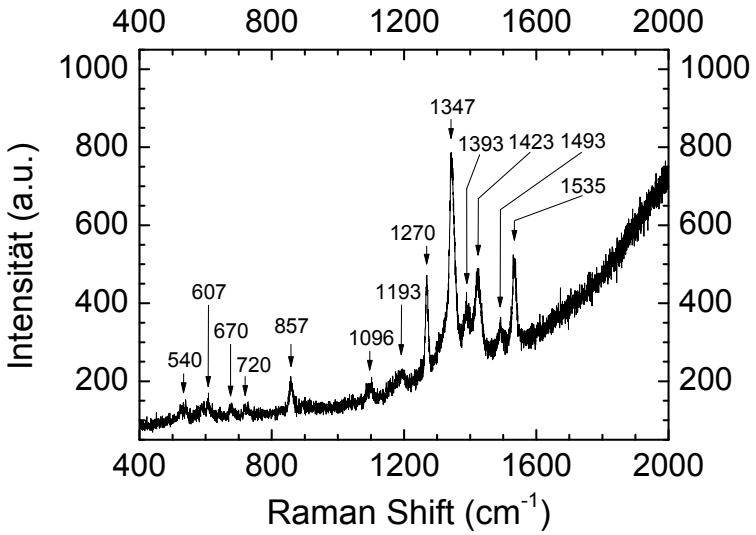

Figure S1

Raman spectrum of PCPDTBT with peak positions labeled in cm^{-1}.

2 Franck-Condon analyses in PCPDTBT solution

Franck-Condon analyses for photoluminescence and absorption spectra were carried out according to Equations 3 and 4 from the manuscript, respectively. Prior to fitting, normalizations were done via $n^3(\hbar\omega)^3$ and $n(\hbar\omega)$ accounting for the photon density-of-states in the surrounding medium effecting the emitter's emission and absorption coefficient, respectively. The refractive index n was taken to be constant over the fitted spectral range. Our multi-mode Franck-Condon fitting procedure is based on the Raman frequencies enumerated in the above section and executes fits for two phases simultaneously.

We separated the spectra into spectra of low energy, aggregated, phase and spectra of high energy, coiled, phase. Figure S2 shows exemplarily the results for 180 K, 240 K and 340 K.

At 180 K, the photoluminescence spectrum shows only aggregated phase, in absorption both phases, aggregated and coiled, are present. At 240 K, both phases are present in absorption as well as in photoluminescence. At 340 K, only coiled phase is present in both photoluminescence and absorption. Therefore, the 180 K and 340 K photoluminescence FC fits were used as starting points for successive two phase analysis for the whole temperature range from 180 K to 340 K. In absorption, the 340 K FC fit was used as a starting point for fits at different temperatures.

The separation of the spectra yields in addition to the spectral shape of the pure aggregated and coiled phases the fraction of absorption for each phase. The latter can

be used to determine the actual fraction of aggregated phase present in the solution. In order to do so, an isosbestic point is mandatory for determination of the change in oscillator strength when going from coiled to aggregated polymer chain. Since the temperature dependent absorption spectra of PCPDTBT show a perfect isosbestic point below 280 K, we were able to extract the fraction of aggregates (see Figure 6, manuscript) following the procedure presented in the Supporting Information of Scharsich et al. 2012.[1]

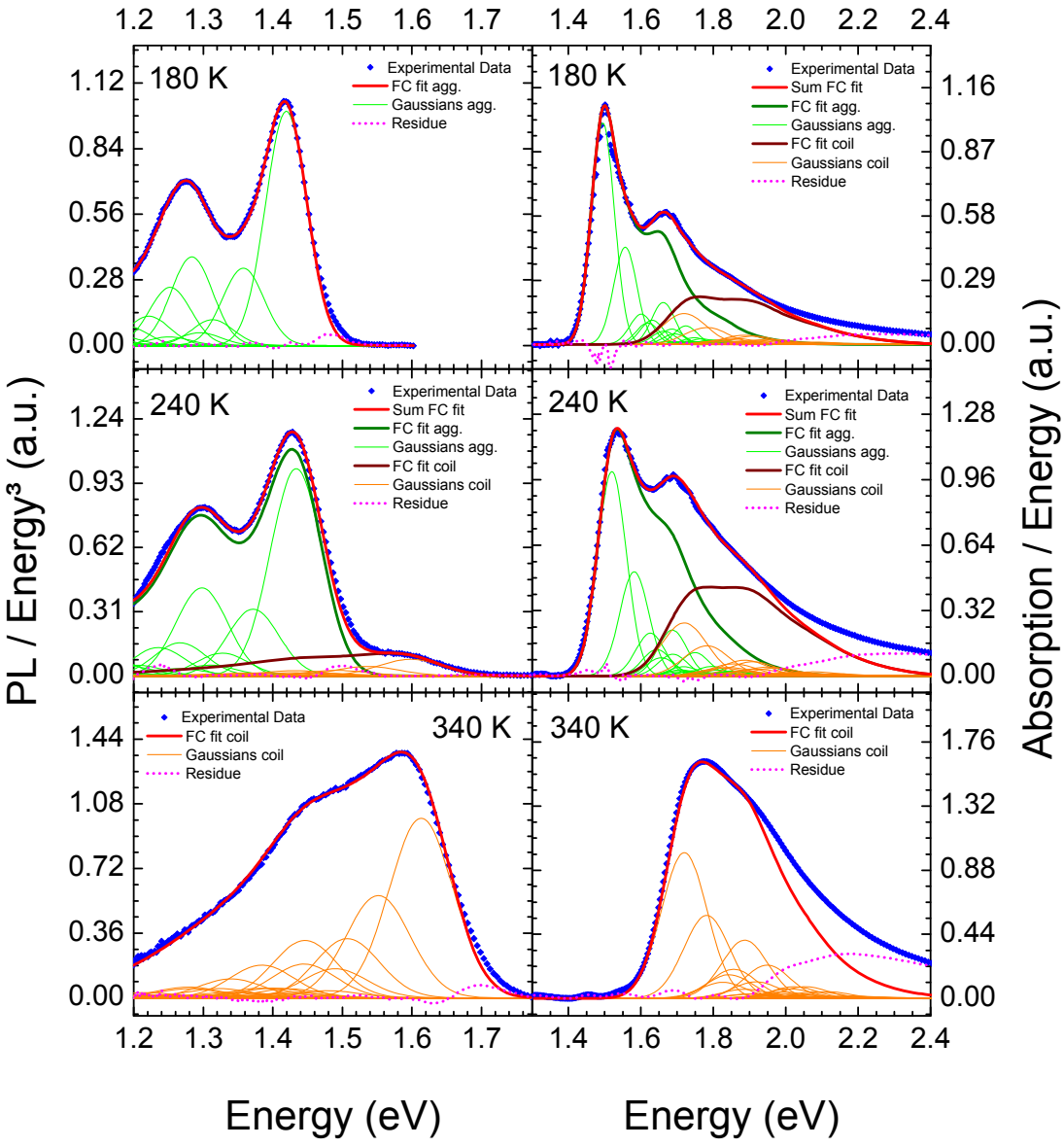

Figure S2

Multi-mode Franck-Condon fits of photoluminescence (left) and absorption (right) spectra of PCPDTBT in solution for the temperatures 180 K (top), 240 K (middle), 340 K (bottom). The spectra were normalized according to Equations 3 and 4 (see the manuscript) prior to fitting and scaled yielding normalization to the 0-0 transition line of the lowest energy phase present.

3 Franck-Condon analyses in PCPDTBT thin films

The multi-mode Franck-Condon analyses of PCPDTCT thin film absorption spectra were done analogously to the above mentioned routine for fitting solution spectra. In this case, the Franck-Condon fit of the absorption spectrum of PCPDTBT in solution at 180 K was used as a starting point for fitting the film spectra. For the considered temperature range of room temperature up to approximately 500 K, we varied mainly the line width σ combined with only slight changes in Huang-Rhys parameters. Figure S3 shows the resulting absorption FC fits for PCPDTBT CB/DIO film and PCPDTBT CB-annealed film at room temperature and at about 500 K. Table S1 shows the corresponding FC fitting parameters.

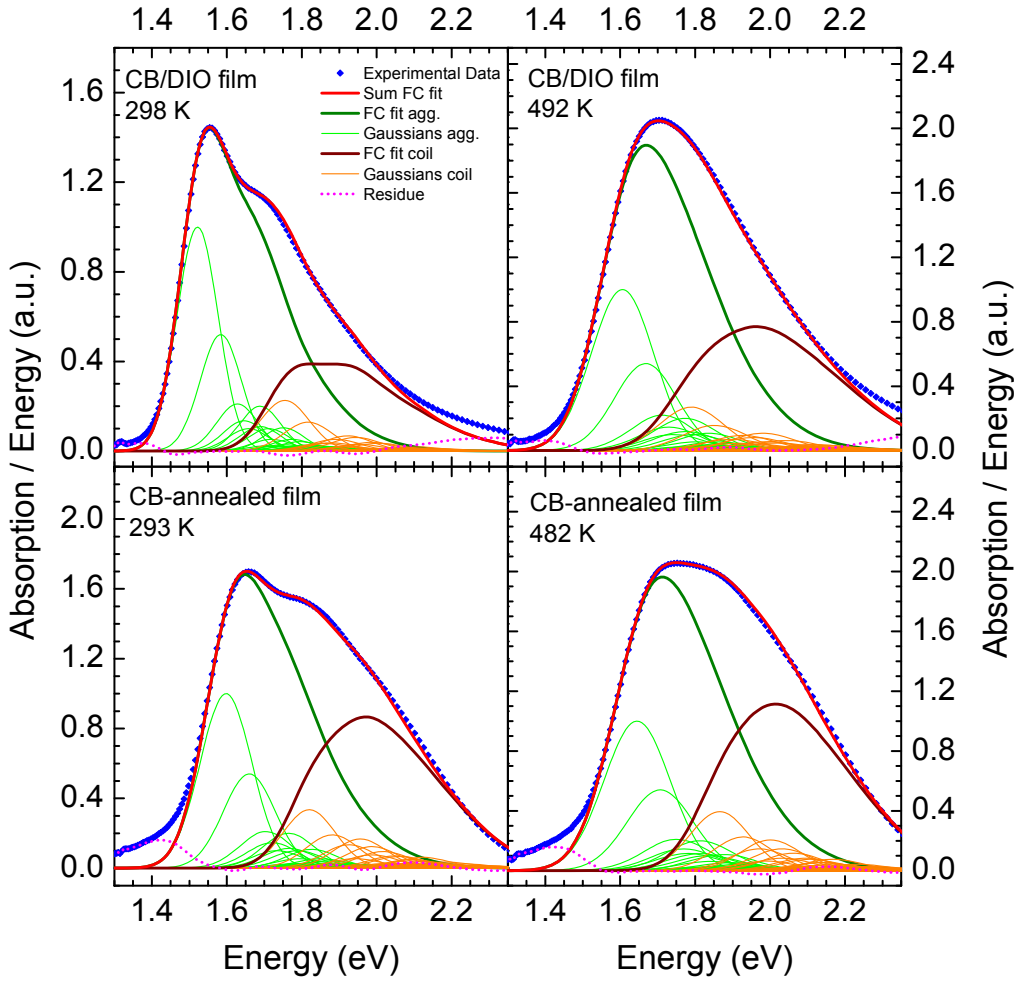

Figure S3

Multi-mode Franck-Condon fits containing aggregated and coiled phase of absorption spectra for PCPDTBT thin films: CB/DIO film (top) and CB-annealed film (bottom) at room temperature (left) and at about 500 K (right), respectively. The spectra were normalized according to Equation 3 and 4 (see the manuscript) prior to fitting and scaled yielding normalization to the 0-0 transition line of the lowest energy phase present.

Table S1

Fitting parameters of the Franck-Condon analyses for absorption spectra of the aggregated phase (agg.) and the coiled phase (coil) of PCPDTBT thin films with E_0 the position of 0-0 transition and σ the Gaussian standard deviation.

FC parameter			**E_0 in eV**	**σ in meV**
CB/DIO film	298 K	agg.	1.522	55
	298 K	coil	1.755	65
	492 K	agg.	1.606	83
	492 K	coil	1.790	85
Film CB annealed	293 K	agg.	1.598	69
	293 K	coil	1.850	70
	482 K	agg.	1.645	88
	482 K	coil	1.865	79

Again, we used the Franck-Condon analysis of the absorption spectra to determine the fraction of aggregates (see Figure 6, manuscript) assuming the relative oscillator strength equals the one in solution.

One possibility to model the photoluminescence spectra of PCPDTBT thin films is a modified Franck-Condon fit involving a variable 0-0 line strength according to

$$\mathrm{PL}(\hbar\omega)/\mathrm{n}^3 \cdot (\hbar\omega)^3 = \alpha \cdot \Gamma\delta[\hbar\omega - \hbar\omega_0] + \sum_{m_i=1} \prod_i I_{0-m_i} \Gamma\delta[\hbar\omega - (\hbar\omega_0 - \sum_i m_i \hbar\omega_i)]$$

with *n* being the refractive index of the surrounding medium, m_i*=1,2,3,4…* being the vibration quantum number of the *i*th vibrational mode , $\hbar\omega_0$ being the energetic position of the 0-0 line, Γ denoting the Gaussian line shape function with constant standard deviation σ and α being the scaling factor for the 0-0 line. Figure S4 shows the modified Franck-Condon fits of the photoluminescence spectra of PCPDTBT thin films for exemplary temperatures. The used vibrational modes are the above mentioned (see section Raman spectroscopy). For clarity, the fits are shown only up to the first vibration quantum number for each mode. Note, that for temperatures of 150 K and above it's necessary to increase strongly the 136 meV mode to fit the experimental data.

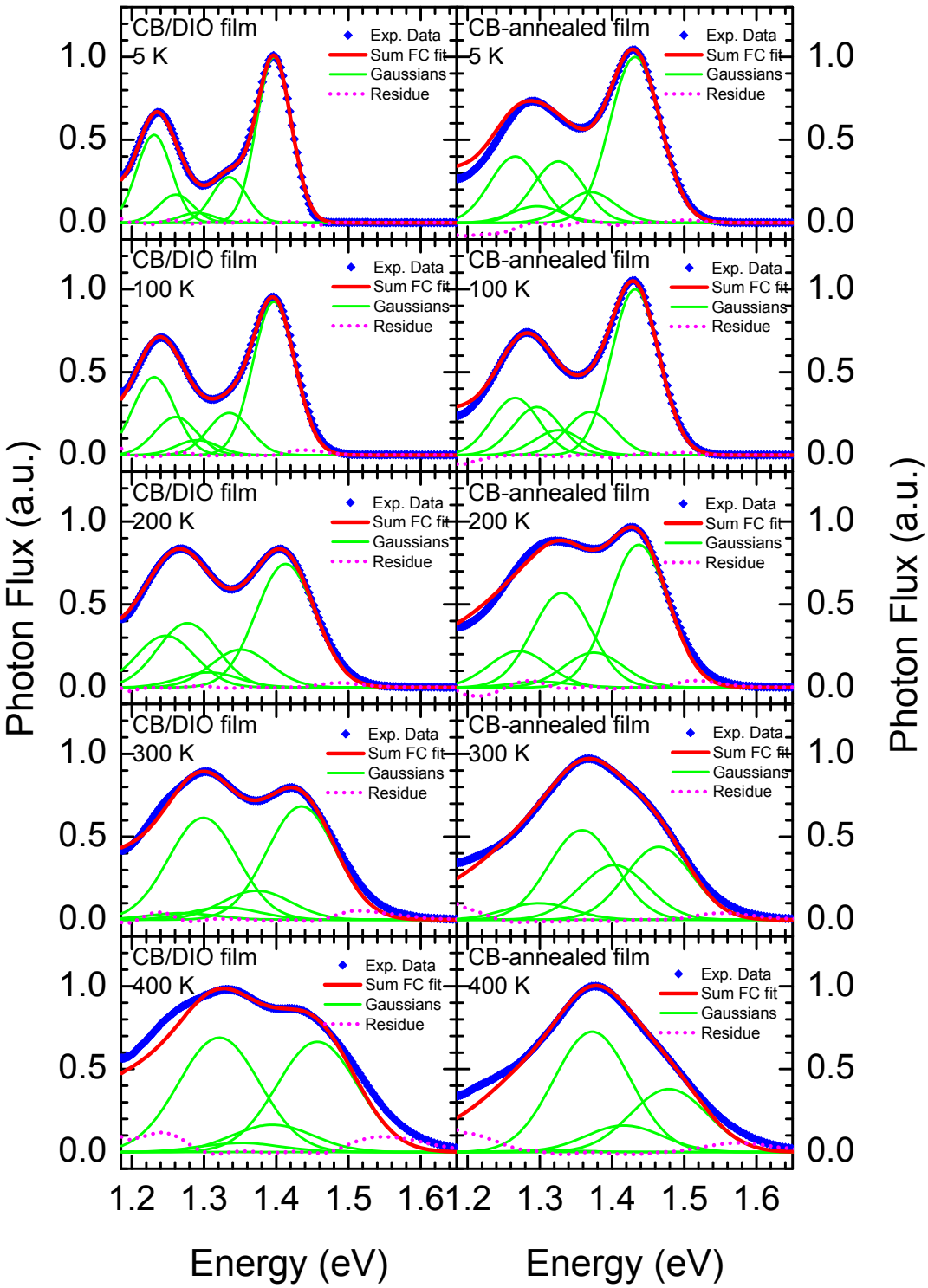

Figure S4

Modified Franck-Condon fits of the photoluminescence of PCPDTBT thin films allowing for variable 0-0 line intensity: CB/DIO film (left column), CB-annealed film (right column) at exemplary temperatures.

4 Spectral diffusion

In Figure S5, we show the underlying absorption spectra of Figure 9, manuscript, for PCPDTBT CB/DIO film for the temperature range of 5 K to 400 K. The spectra were measured using a Xe-lamp with monochromator for illumination and a monochromator with Si-photodiode and lock-in technique for signal detection.

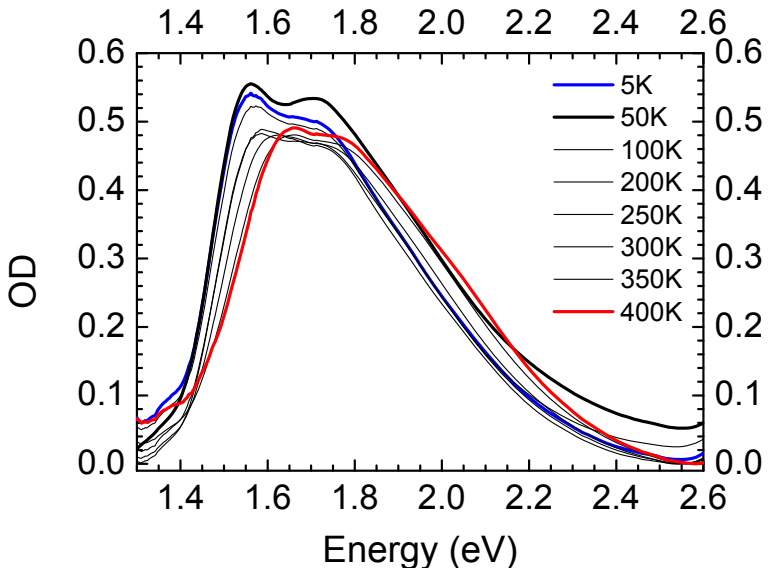

Figure S5

Optical density of PCPDTBT CB/DIO film for temperatures between 5 K and 400 K. Data were smoothed and corrected for offset.

The analysis of the PCPDTBT photoluminescence and absorption spectra concerning spectral diffusion requires the exact knowledge of center energy of the density of states (DOS). When an exciton relaxes to lower energy sites in the DOS where it emits yielding the measured photoluminescence, the energy difference between the center of DOS and the relaxation site, $\Delta\varepsilon$, normalized by the line width σ, should obey the theoretical law $\Delta\varepsilon(T)/\sigma(T)=-\sigma(T)/kT$.[2] We determined the center energy of the DOS as the energy of the 0-0 transition line via Franck-Condon analysis of the temperature dependent absorption spectra shown in Figure S5. The corresponding energy of the 0-0 line in photoluminescence resulting from FC analysis yields the temperature dependent energy difference $\Delta\varepsilon(T)$. The line width $\sigma(T)$ was taken from FC fits to the photoluminescence spectra. The resulting plot of $\Delta\varepsilon(T)/\sigma(T)$ against $kT/\sigma(T)$ is shown in Figure 9, manuscript.

5 Lifetime measurements of PCPDTBT thin films

For the PCPDTBT thin films, we measured lifetimes using time-correlated single photon counting (TCSPC) as described in detail in the manuscript. Figure S6 shows exemplarily the data and the corresponding fit for the CB-annealed film. The analysis and fitting of the decay curves were done with the program *PicoQuant FluoFit 4.1.1*.

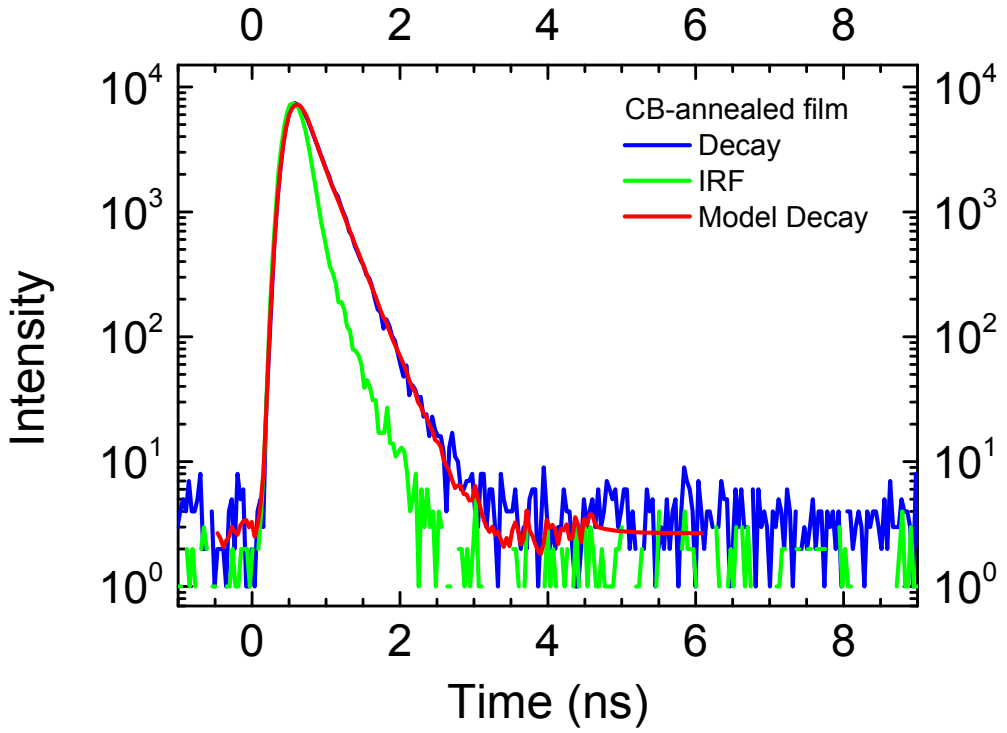

Figure S6

TCSPC decay curve of the photoluminescence of the CB-annealed film (blue line), instrument response function (IRF) (green line) and the monoexponential, reconvoluted model decay (red line).

The model used for fitting was monoexponential and reconvoluted with the instrument response function (IRF). Table S2 shows the fitting parameters for the decay curves of both films. The fits were calculated according to

$$I(t) = \int_{-\infty}^{t} IRF(t')Ae^{-\frac{t-t'}{\tau}}dt'$$

with *I(t)* being the intensity of the decay signal at time *t*, *IRF(t')* being the intensity of the IRF at time *t'*, *A* being the amplitude of the decay at time zero and τ being the lifetime.

Table S2

Fitting parameters for the decay fits as yielded by analysis with *PicoQuant FluoFit 4.1.1: A* is the amplitude at time zero, τ is the lifetime.

Parameter	CB/DIO film	CB-annealed film
A	(7140 ± 180) counts	(9260 ± 110) counts
τ	(0.2619 ± 0.0040) ns	(0.2576 ± 0.0020) ns

6 PCPDTBT film spin-coated from chloroform

In addition, we investigated a third type of PCPDTBT films spin-coated from chloroform ($CHCl_3$). The samples were prepared from 3 mg/ml $CHCl_3$ solutions by continuously stirring the solutions for 1 to 2 hours at about 50 to 60°C. The films were then prepared by spin-coating at 1000 rpm for 30 s within 24 h after preparation of the solution. These films are the precursor films for the vapor annealed films presented in the manuscript. Their morphology is unproved.

Figure S7 shows the absorption and photoluminescence spectra for a temperature range of 293 K to 493 K and 5 K to 480 K, respectively. In absorption, the spectrum shifts to the red continuously and evolves a low energy peak that shifts at room temperature up to 1.62 eV. Thus, it lies energetically between the CB/DIO film and the CB-annealed film shifting up to 1.56 eV and 1.67 eV, respectively, at room temperature. The low energy peak is less pronounced than in the CB/DIO film but higher when compared to the CB-annealed film. The spectral shape in absorption is similar to the one of the CB/DIO film missing as well the pronounced high energy shoulder of the CB-annealed film.

In photoluminescence, the film spun from CHCl3 spectra shows one emission as the two other film types do. The photoluminescence shifts continuously to the red with decreasing temperature by 65 meV. At 5 K, the photoluminescence of the CB/DIO film is at 1.40 eV and for the CB-annealed film at 1.43 eV, the film spun from $CHCl_3$ is again in between at 1.42 eV.

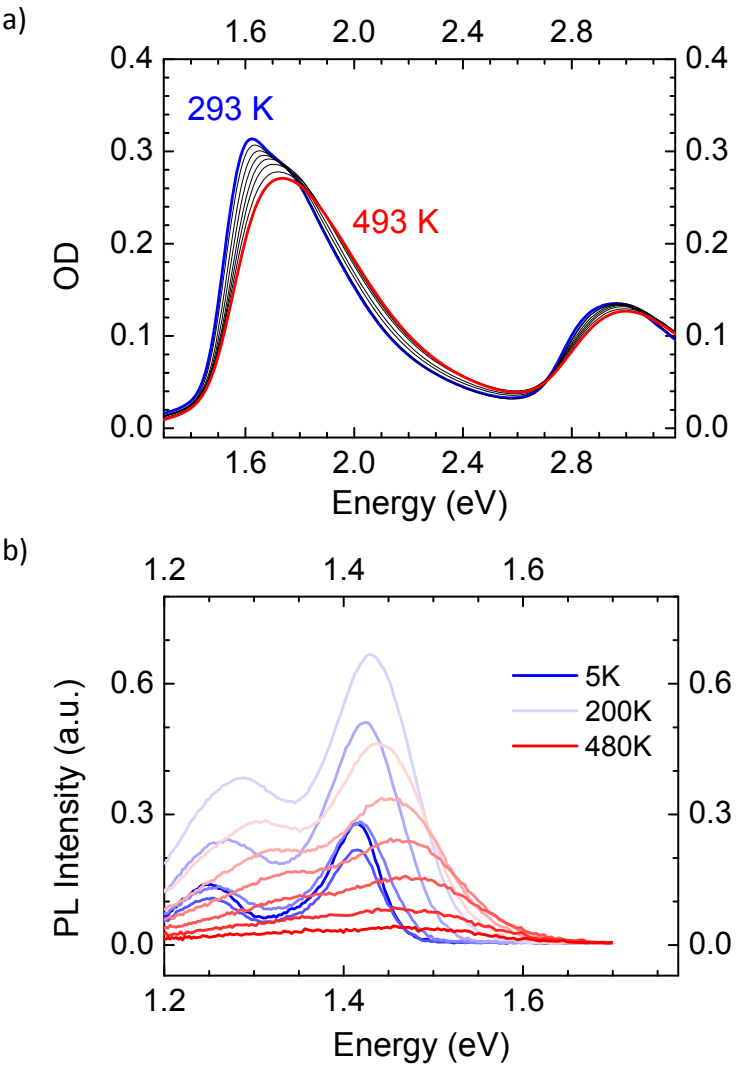

Figure S7

PCPDTBT film spin-coated from chloroform (a) optical density for temperatures between 293 K and 493 K, (b) photoluminescence for temperatures between 5 K and 480 K.

7 Full chemical names of materials from the manuscript

Table S3

Abbreviations and names of materials as mentioned in the manuscript (left) together with their full chemical names (right).

dioodooctane	1,8-diiodooctane
chloroform	trichloromethane
distyrylbenzene	1,4-distyrylbenzene
MEH-PPV	poly[2-methoxy-5-(2-ethylhexyloxy)-1,4-phenylenevinylene]
octanedithiol	1,8-octanedithiol
P3HT	poly(3-hexylthiophene-2,5-diyl)
PCBM	[6,6]-phenyl C61 butyric acid methyl ester
PCDTBT	poly[N-9′-heptadecanyl-2,7-carbazole-alt-5,5-(4′,7′-di-2-thienyl-2′,1′,3′-benzothiadiazole)]
PCPDTBT	poly{[4,4-bis(2-ethylhexyl)-cyclopenta-(2,1-b;3,4-b′)dithiophen]-2,6-diyl-alt-(2,1,3-benzo-thiadiazole)-4,7-diyl}
PDPP-TPT	poly[{2,5-bis(2-hexyldecyl)-2,3,5,6-tetrahydro-3,6-dioxopyrrolo[3,4-c]pyrrole-1,4- diyl}-alt-{[2,20-(1,4-phenylene)bis-thiophene]-5,50-diyl}]
PFO	poly(9,9-di-n-octylfluorenyl-2,7-diyl)
PPV	poly(*p*-phenylene vinylene)
PTB7	poly({4,8-bis[(2-ethylhexyl)oxy]benzo[1,2-b:4,5-b′]dithiophene-2,6-diyl}{3-fluoro-2-[(2-ethylhexyl)carbonyl]thieno[3,4-b]thiophenediyl})

References

(1) Scharsich, C.; Lohwasser, R. H.; Sommer, M.; Asawapirom, U.; Scherf, U.; Thelakkat, M.; Neher, D.; Köhler, A. *J. Polym. Sci. Pt. B-Polym. Phys.* **2012**, *50*, 442.
(2) Hoffmann, S. T.; Bässler, H.; Koenen, J. M.; Forster, M.; Scherf, U.; Scheler, E.; Strohriegl, P.; Köhler, A. *Phys. Rev. B* **2010**, *81*.

Danksagung

An dieser Stelle möchte ich mich herzlich bei allen bedanken, die mich auf meinem bisherigen wissenschaftlichen Weg begleitet und unterstützt haben.

Daher danke ich zuallererst meiner Biologie- und Chemielehrerin Ute Drews dafür, dass sie mir gezeigt hat, dass jede Frage es wert ist, sie zu stellen.

Ein großer Dank geht an meine Betreuerin Prof. Anna Köhler, die mich mit diesem spannenden Forschungsthema bekannt gemacht und gefesselt hat. Danke für die Unterstützung und das Vertrauen. Danke für die Möglichkeit, Teil dieser Arbeitsgruppe zu sein. Vielen Dank auch an Prof. Heinz Bässler für sein offenes Ohr und die guten Diskussionen.

Ohne die freundschaftliche Atmosphäre in unserer Arbeitsgruppe wären die letzten sechs einhalb Jahre nur halb so schön gewesen. Deshalb herzlichen Dank an die Freunde und Kollegen für die stete Hilfsbereitschaft, den Humor und, nicht zu vergessen, die vielen Kicker-Runden.

Großer Dank geht auch an unsere Techniker, die mir stets mit Rat und Tat zur Seite standen. Besonders möchte ich hier Irene Bauer danken für die unablässige Hilfe und Unterstützung, vorallem während meiner Schwangerschaft.

Vielen Dank an das Graduiertenkolleg 1640 für die Interdisziplinarität, die guten Tutorien und die lehrreichen Diskussionen mit den Doktoranden und Professoren.

Vielen Dank auch an meine Projektpartner für die gute und produktive Zusammenarbeit.

Für die finanzielle Unterstützung danke ich dem DFG Graduiertenkolleg 1640 und dem Bayerischem Programm zur Förderung der Chancengleichheit für Frauen in Forschung und Lehre.

Abschließend möchte ich meiner Familie herzlich für die fortwährende Unterstützung danken. Vorallem danke ich meiner Frau, ohne deren Hilfe, Verständnis und Liebe Vieles nicht möglich gewesen wäre.

Erklärung

Hiermit erkläre ich mich einverstanden, dass die elektronische Fassung meiner Dissertation unter Wahrung meiner Urheberrechte und des Datenschutzes einer gesonderten Überprüfung hinsichtlich der eigenständigen Anfertigung der Dissertation unterzogen werden kann. (§ 8 S. 2 Nr. 6 PromO)

Hiermit versichere ich eidesstattlich, dass ich die Dissertation selbständig verfasst und keine anderen als die von mir angegebenen Quellen und Hilfsmittel benutzt habe. (§ 8 S. 2 Nr. 8 PromO)

Hiermit erkläre ich, dass ich nicht bereits versucht habe eine Dissertation einzureichen oder mich einer Doktorprüfung zu unterziehen. (§ 8 S. 2 Nr. 9 PromO)

Hiermit erkläre ich, dass ich bisher keine Hilfe von gewerblichen Promotionsberatern bzw. Promotionsvermittlern in Anspruch genommen habe und diese auch künftig nicht in Anspruch nehmen werde. (§ 8 S. 2 Nr. 10 PromO)

Bayreuth, den 15.01.2015

. . . . . .

Christina Scharsich